

ELECTROSTATIC PROPULSION BEAM DIVERGENCE EFFECTS ON SPACECRAFT SURFACES

VOLUME II FINAL REPORT

TRW NO. 11985-6002-RU-00

DAVID F. HALL

17 JANUARY 1973

CONTRACT NO. 952350

This work was performed for the Jet Propulsion Laboratory, California Institute of Technology, sponsored by the National Aeronautics and Space Administration under Contract NAS7-100.

**Prepared for
JET PROPULSION LABORATORY
CALIFORNIA INSTITUTE OF TECHNOLOGY
PASADENA, CALIFORNIA**

TRW
SYSTEMS GROUP

ACKNOWLEDGMENT

The technical work reported herein was accomplished by the following individuals:

Chemistry	Howard E. Green
Metallurgy	R. A. Mendelson
Thermophysics	L. R. Kelley E. E. Luedke
Surface and Vacuum Physics	D. F. Hall

Substantial support was provided by W. Goldstein and P. Faville. The JPL Technical Manager was J. R. Womack. He was aided by W. Carroll.

ABSTRACT

The third phase of a program to develop understanding of and tolerance-level criteria for the deleterious effects of electrostatic rocket exhaust (Cs , Cs^+ , Hg , Hg^+) and materials of rocket construction impinging on typical classes of spacecraft (S/C) surfaces has been completed. The first phase was completed under Contract No. NAS7-575. The second phase was completed under the present contract and reported in Volume I. This report (Volume II) presents models of ion engine effluents and models describing the degradation of S/C surfaces by these effluents. Experimental data from previous phases are summarized and Phase II data and analysis are presented in detail. The spacecraft design implications of ion engine contaminants are discussed.

CONTENTS

	Page
1. INTRODUCTION	1-1
1.1 Background	1-1
1.2 Program Scope and Approach	1-1
1.3 Program Status	1-2
1.4 Report Organization	1-2
1.5 References (Section 1)	1-3
2. SPACECRAFT DESIGN IMPLICATIONS OF ION ENGINE CONTAMINANTS	2-1
2.1 Ion Engine Contamination Particles	2-1
2.2 Degradation Mechanisms	2-2
2.2.1 Deposition of Films	2-3
2.2.2 Chemical and Metallurgical Reaction	2-4
2.2.3 Surface Erosion by Sputtering	2-4
2.2.4 Radiation Damage	2-4
2.3 Potential Solutions to Contamination Problems	2-5
2.3.1 Spacecraft Configuration	2-5
2.3.2 Thruster Baffles	2-5
2.3.3 Electrical Biasing and Deflecting	2-6
2.3.4 Choice of Materials	2-6
3. ION THRUSTER EFFLUENTS	3-1
3.1 Propellant Atoms	3-2
3.2 Propellant Ions	3-3
3.2.1 Groups 1 and 2 Propellant Ions	3-3
3.2.2 Group 4 Propellant Ions	3-10
3.3 Thruster Material	3-10
3.3.1 Accelerator Grid Atoms	3-10
3.3.2 Accelerator Grid Ions	3-12
3.4 Discharge Neutralizers	3-13
3.5 References (Section 3)	3-13
4. DEPOSITION AND EFFECTS OF THIN FILMS	4-1
4.1 Types of Film Deposition	4-1
4.1.1 Propellant Condensation	4-1
4.1.2 Thruster Material Deposition	4-4
4.1.3 Sputtered Spacecraft Materials	4-4
4.2 Mechanisms of Film Removal	4-5
4.3 Effects of Metal Film Deposition	4-5
4.3.1 Deposition of Thrust Material on Solar Cells	4-5
4.3.2 Propellant Condensation on Solar Arrays	4-31

CONTENTS (Continued)

	Page
4.3.3 Electrical Effects of Thin Films	4-35
4.4 References (Section 4).	4-37
5. ION EROSION	5-1
5.1 Introduction	5-1
5.2 Experimental Procedure	5-1
5.2.1 Test Facility	5-1
5.2.2 Sample Coupons	5-1
5.2.3 Sample Holder	5-2
5.2.4 Exposure Sequence	5-3
5.2.5 Post Exposure Inspection	5-4
5.2.6 Erosion Measurement Techniques	5-4
5.2.7 Data Analysis	5-6
5.3 Results and Discussion	5-7
5.3.1 Measurements	5-7
5.3.2 Discussion	5-7
5.4 Conclusions and Recommendations	5-19
5.5 References (Section 5)	5-19
6. CHEMICAL EFFECTS OF PROPELLANTS	6-1
6.1 Introduction	6-1
6.2 Cesium Immersion Tests	6-1
6.2.1 Paints	6-1
6.2.2 Kapton	6-3
6.3 Mercury Ion Beam Tests	6-5
6.3.1 Chemical Analysis	6-6
6.3.2 Results and Discussion	6-6
6.4 Conclusions and Recommendations	6-13
6.5 References (Section 6)	6-15
7. METALLURGICAL EFFECTS OF PROPELLANTS	7-1
7.1 Metallurgical Effects of Propellants	7-1
7.2 Test Design and Results (Early Series)	7-1
7.3 Tests with Milled Fillet Samples	7-5
7.3.1 Immersion Tests	7-5
7.3.2 Mercury Beam Tests	7-7
7.3.3 Comparison Between Beam and Immersion Tests	7-11
7.4 Conclusions and Recommendations	7-14
7.4.1 Cesium/Solder (Phase II)	7-14
7.4.2 Mercury/Silver (Phase II)	7-14
7.4.3 Mercury/Solder	7-14

CONTENTS (Continued)

	Page
7.5 References to Section 7	7-15
8. DAMAGE OF THERMAL CONTROL COATINGS	8-1
8.1 Introduction	8-1
8.2 Experimental Approach	8-1
8.3 Thermal Control Coating Degradation Measurements	8-3
8.3.1 Effect of Mercury Ions (Early Experiments) . . .	8-3
8.3.2 Effect of Mercury Ions (Recent Experiments) . .	8-12
8.3.3 Effect of Mercury Atoms (Early Experiments)	8-31
8.3.4 Effect of Mercury Atoms (Recent Experiments)	8-34
8.4 Comparisons to Data From Other Laboratories	8-47
8.4.1 Total Property Damage	8-47
8.4.2 Spectral Damage	8-47
8.4.3 Summary	8-49
8.5 References (Section 8)	8-50
9. OVERALL CONCLUSIONS AND RECOMMENDATIONS FOR FUTURE WORK	9-1
9.1 Introduction	9-1
9.2 Spacecraft Design Implications	9-1
9.3 Ion Engine Effluents	9-1
9.4 Deposition and Effects of Thin Films	9-1
9.5 Ion Erosion	9-2
9.6 Chemical Effects of Propellants	9-2
9.7 Metallurgical Effects of Propellants	9-2
9.8 Damage of Thermal Control Coatings	9-2
10. NEW TECHNOLOGY	10-1
APPENDICES	
A. EXPERIMENTAL FACILITY	A-1
B. THERMOPHYSICS INSTRUMENTATION	B-1

ILLUSTRATIONS

		Page
2-1.	Schematic of the Classes of Particulate Contaminants Associated with Ion Engines	2-2
3-1.	Schematic of Ion Categories Emitted by an Ion Engine	3-2
3-2.	Geometry for Simple Ion Beam Representations	3-4
3-3.	Simplified Representation of Axial Ion Current Density (Normalized to Initial Value) as a Function of Distance from Thruster Exit Plane	3-5
3-4.	Ion Beam Profile Data from Several Different Mercury Bombardment Ion Engines with Conventional Grids.	3-8
3-5.	Photograph of 15 cm Diameter NASA/Lewis-Type Electron Bombardment Thruster	3-11
4-1.	Bulk Accumulation Regions for Mercury and Cesium Atoms on Surfaces Where Absorbed Monolayers Already Exist	4-3
4-2.	Effects of Deposition of a Uniform Film of Aluminum on the Illuminated (Front) Surface of a Solar-Cell Panel	4-17
4-3.	Effects of Uniform Aluminum Film Deposition on Nonilluminated (Rear) Surface	4-18
4-4.	Effects of Equal and Uniform Aluminum Film Deposition on Both Front and Rear Surfaces	4-19
4-5.	Effects of Uniform Molybdenum Film on Illuminated (Front) Surface of Solar-Cell Panel	4-20
4-6.	Effects of Uniform Molybdenum Film Deposited on Nonilluminated (Rear) Surface of Solar-Cell Panel	4-21
4-7.	Effects of Molybdenum Film Deposited on Both Front and Rear Surfaces of Solar-Cell Panel	4-22
4-8.	Dependence of the Transmittance and Reflectance on Film Thickness ($\lambda = 8$ - - - - - , $\lambda = 500$ m_____).	4-25
4-9.	Transmittance as a Function of Film Thickness of Thin Metallic Films	4-26
4-10	Comparison of Transmittance-Time Curves of Flight Tests, Ground Tests, and Theoretical Predictions.	4-28

ILLUSTRATIONS (Continued)

	Page
4-11. Neutral Mercury (a) and Cesium (b) Atom Arrival Rates Necessary to Sustain Opaque Condensation on Boeing Solar Cell Array	4-33
5-1. Photograph of Four Aluminum Sample Substrates and Reworked Stainless Steel Mounting Screw	5-2
5-2. Photograph of Loaded Sample Holder	5-2
5-3. Alternate Erosion Depth Measurement Schemes, Method C was Used for Most Samples	5-5
5-4. Erosion Rate of Various Spacecraft Surface Materials by 3 kev Mercury Ions as a Function of Ion Incidence Angle	5-8
5-5. Erosion Rate of Various Spacecraft Surface Materials by 1 kev Mercury Ions as a Function of Ion Incidence Angle	5-10
5-6. Erosion Rate of Teflon FEP by 1 and 3 kev Mercury Ions and Poly (Vinyl Acetate) by 3 kev Hg^+ as a Function of Ion Incidence Angle	5-12
5-7. Ion Dose Density Required to Produce 1-mil Erosion versus Sputtering Yield for Three Target Densities	5-13
5-8. Sixty-degree Quartz Surface at (a) 10X and (b) 400X Following ~21 Hours of 3 kev Hg^+ Exposures	5-16
5-9. Polished Aluminum Samples (a) Prior to Exposure; (b) 0-Degree; and (c) 45-Degree Following 39 Hours of 3 kev Hg^+	5-18
6-1. Full Set of 5-mil Teflon FEP Samples After ~1 Hour of 3 kev Hg^+ (2.6X).	6-9
6-2. Sixty-degree Coupon With 5-mil Thick Teflon FEP After ~2 Hours Exposure to 3 kev Hg^+ (10X)	6-9
7-1. Design of Soft Solder Lap Joint Tensile Test Specimens	7-2
7-2. Soft Solder Lap Shear Specimens Mounted on QCM Fixture Prior to Hg Beam Exposure	7-3
7-3. Sixteen Double Lap Shear Solder Joint Specimens Mounted on QCM Fixture Prior to Mercury Atom Beam Exposure	7-9

ILLUSTRATIONS (Continued)

	Page
8-1. Spectral Reflectance of Cold and Z93 White Paint versus Wavelength Before and After Exposure to 3 kev Mercury Ions	8-8
8-2. Degradation of Z93 White Paint from Exposure to Various Mercury Ion Beams.	8-14
8-3. Degradation of S13G White Paint from Exposure to Various Mercury Ion Beams	8-15
8-4. Degradation of PV100 White Paint from Exposure to Various Mercury Ion Beams	8-16
8-5. Degradation of RTV41 White Silicon Rubber from Exposure to Various Mercury Ion Beams	8-17
8-6. Degradation of Polished Aluminum (6061-T6) from Exposure to Various Mercury Ion Beams	8-19
8-7. Spectral Distribution of Z93 White Paint Before and After Mercury Ion Beam Exposure	8-24
8-8. Spectral Distribution of S13G White Paint Before and After Mercury Ion Beam Exposure	8-25
8-9. Spectral Distribution of PV100 White Paint Before and After Mercury Ion Beam Exposure	8-26
8-10. Spectral Distribution of RTV41 White Silicone Rubber Before and After Mercury Ion Beam Exposure.	8-27
8-11. Spectral Distribution of Polished Aluminum (6061-T6) Before and After Mercury Ion Beam Exposure.	8-28
8-12. Spectral Distribution of PV100 White Paint Before and After Exposure to a Mercury Atom Beam (7) and Immersion in Liquid Mercury (8)	8-42
8-13. Spectral Distribution of RTV41 White Silicon Rubber Before and After Exposure to a Mercury Atom Beam (7) and Immersion in Liquid Mercury (8)	8-43
8-14. Spectral Distribution of S13G White Paint Before and After Exposure to a Mercury Atom Beam (7) and Immersion in Liquid Mercury (8)	8-44
8-15. Spectral Distribution of Z93 White Paint Before and After Exposure to a Mercury Atom Beam (7) and Immersion in Liquid Mercury (8)	8-45

ILLUSTRATIONS (Continued)

		Page
8-16.	Spectral Distribution of Polished Aluminum Before and After Exposure to a Mercury Atom Beam (7) and Immersion in Liquid Mercury (8)	8-46
8-17.	Change in Solar Absorptance ($\Delta\alpha_s$) as a Function of Proton Integrated Dose for ZnO/K ₂ SiO ₃ Paints (After Reference 19) and Change in Absorptance ($\Delta\alpha_x$) of Z93 by Hg ⁺	8-48

TABLES

	Page
2-1. Potential Degradation of Spacecraft Systems by Ion Engine Effluents	2-3
4-1. Typical Measured Values for Opaque Samples	4-6
4-2. Aluminum - Solar Region - on Glass $n = 1.8$, $k = 7.12$, $\lambda = 0.75 \mu m$	4-7
4-3. Aluminum - Solar Region - on Fluorespar Measured by Walkenhorst, $\lambda = 0.500 \mu m$	4-8
4-4. Niobium - Solar Region - on Glass $n = 1.8$, $k = 2.11$, $\lambda = 0.579 \mu m$	4-8
4-5. Molybdenum - Solar Region - on Glass $n = 3$, $k = 4.$, (Extrapolated Values) $\lambda = 0.82 \mu m$	4-9
4-6. Niobium - Solar Region - on Solar Cell	4-11
4-7. Molybdenum - Solar Region - on Solar Cell	4-12
4-8. Aluminum - Solar Region - on Solar Cell	4-12
4-9. Aluminum - Infrared Region - on Quartz	4-13
4-10. Input Values for Computation of Film Properties	4-23
4-11. Surface Thermal Properties of Opaque Hg and Cs	4-31
5-1. Sputtering Yields of Polycrystalline Metal Samples Positioned Normal to 1 and 3 keV Hg ⁺ Beam	5-13
6-1. Cesium Exposure of Thermal Control Coatings	6-2
6-2. Chemical Effects of Cs, Cs ⁺ , Hg and Hg ⁺ on Typical Spacecraft Materials	6-14
7-1. Hg/Soft Solder Lap Shear Tensile Test Data (Natural Fillet)	7-4
7-2. Tensile Strength of Milled Fillet Soft Solder Lap Shear Specimens of Mercury Quick Immersion Test	7-6
7-3. Tensile Strength of Milled Fillet Soft Solder Lap Shear Specimens of Mercury Atom Beam Test	7-8
7-4. Tensile Strength of 45-degree Milled Fillet Soft Solder Lap Shear Specimens of Mercury Atom Beam Test	7-10
8-1. Surface Thermal Degradation Test Results, Mercury Ions	8-4

TABLES (Continued)

	Page
8-2. Summary of Nominal Test Conditions	8-12
8-3. Thermal Annealing Experiment Results	8-22
8-4. Comparison of In Situ and Ex Situ Total Absorptance Data	8-29
8-5. Surface Thermal Degradation Test Results, Mercury Neutrals	8-32
8-6. Surface Thermal Degradation Test Results, Mercury Neutrals	8-33
8-7. In Situ Results, Test Series 7 (Mercury Neutrals)	8-35
8-8. Comparison of Thermal Property Changes	8-39
8-9. Summary Comparison of Ex Situ Delta α_x at Various Wavelengths	8-41

1. INTRODUCTION

1.1 BACKGROUND

Electrostatic rockets (ion engines) emit particles of propellant and their materials of construction into at least 2π steradians. Spacecraft (S/C) designers therefore require tolerance-level criteria for the almost inevitable interception of these particles by S/C surfaces. During Phase I of this program, under Contract NAS 7-575, a systematic analytical study and literature search was made of the deleterious effects of Hg, Hg^+ , Cs, and Cs^+ on spacecraft surfaces¹. Sufficient information was available or generated analytically regarding some effects, but many were found to require experimental study. The Phase I work was summarized and extended, first in a presentation to the electric propulsion community², and then in an archival publication.³

During Phase II, experimental fabrication was completed and exploratory measurements were made. This work was summarized in an AIAA paper⁴ and reported in detail in Volume I of this report.⁵

1.2 PROGRAM SCOPE AND APPROACH

The integration of an electric propulsion subsystem into a spacecraft requires knowledge of the particulate effluents and electromagnetic radiations of the propulsion subsystem so that rates and energies of particle impingement and intensities and frequencies of radiation interception at potentially vulnerable S/C surfaces and subsystems may be predicted. Secondly, knowledge of the effects of these contaminants on the surfaces and subsystems is required. This program has been limited to consideration of particulate (or mass transport) type interactions. Furthermore, although some effort has been made to collect and analyze the ion engine effluent data available in the literature so that estimates of impingement may be made, such activity has represented a minor portion of the effort and has not included any experimental measurements. Most of the work has been addressed to measuring, understanding, and predicting the effects of impinging particles, given their species, impingement rate and energy. Much experimental work must be done before high angle effluent predictions can be made with confidence, and the entire subject area of

electromagnetic interactions is in need of attention. These problems were outside the Work Statement scope.

Since the fields of electric spacecraft design and component construction are constantly evolving, the program approach was to develop physical models of degradation effects and extrapolatable data rather than to conduct a series of engineering material tests. This body of knowledge could then be used as the bases for tradeoff calculations and consideration of new materials and designs.

The program was performed with support from four groups of technical specialization. The metallurgy group was charged with elucidating reactions between the propellants and S/C metals. The chemistry group was responsible for reactions between the rocket efflux and non-metallic S/C materials. The thermophysics group determined the surface thermal changes which occur in various thermal control coatings as a result of particle interception. The low thrust propulsion group conducted the sputtering experiments, operated the primary facility in which most experiments were performed, and provided program management.

1.3 PROGRAM STATUS

The goals of Phase III were met. Substantial quantities of basic experimental data were obtained and analyses made regarding the effects of propellant and materials of thruster construction on S/C surfaces. These results were summarized for the technical community.⁶⁻⁹

Phase IV of the program is currently in progress and not covered in this report. It is an experimental examination of the compatibility of the ATS-F Ion Engine Experiment¹⁰ with engineering subsystems and other experiments on the ATS-F spacecraft. The first cesium atom and ion beams experiments have been conducted during Phase IV; previously beam experiments had been done with mercury.

1.4 REPORT ORGANIZATION

This report begins in Section 2 with a general discussion of the kinds of particulate contamination problems encountered in the use of ion engines on spacecraft, and where the solutions to these problems may lie. Section 3 is a review of the present knowledge of ion engine particulate emissions. Section 4 discusses sources and effects of film deposition.

Section 5 reports measurements of surface erosion by ion sputtering. Sections 6 and 7 recount experiments and theory of propellant reactions with non-metallic and metallic spacecraft materials, respectively. Section 8 describes measurements of thermal control coating property damage by mercury ion and atom beams. Each section contains detailed conclusions and recommendations. In Section 9, these conclusions and recommendations are highlighted. Section 10 presents new technology developed during the contract. Appendix A is a description of the vacuum test facility developed during the program and used in all the beam tests. Appendix B describes how the thermophysical property measurements of thermal control coatings were made.

1.5 REFERENCES (SECTION 1)

1. D. F. Hall, "Evaluation of Electric Propulsion Beam Divergence Effects on Spacecraft," 08965-6013-RO-00, Final Report, Contract No. NAS7-575, TRW Systems, Redondo Beach, Calif., September 1969.
2. D. F. Hall, B. E. Newnam, and J. R. Womack, "Electrostatic Rocket Exhaust Effects on Solar-Electric Spacecraft Subsystems," AIAA Paper No. 69-271, 1969.
3. D. F. Hall, B. E. Newnam, and J. R. Womack, "Electrostatic Rocket Exhaust Effects on Solar-Electric Spacecraft Subsystems," Journal of Spacecraft and Rockets, Vol. 7, No. 3, pp. 305-312, March 1970.
4. D. F. Hall, and L. R. Kelley, "Experimental Techniques to Determine Electrostatic Rocket Exhaust Effects on Spacecraft Surfaces," AIAA Paper No. 70-1144, September 1970.
5. D. F. Hall, "Electrostatic Propulsion Beam Divergence Effects on Spacecraft Surfaces," Final Report, Vol. 1, JPL Contract 952350, Doc. No. 11985-6001-RO-00, TRW Systems, Redondo Beach, Calif., August 1970.
6. R. F. Kemp, et al., "Effects of Electrostatic Rocket Material Deposited on Solar Cells," AIAA Paper No. 72-447, April 1972.
7. D. F. Hall, and H. E. Green, "Erosive and Chemical Effects of Energetic Mercury Ions Bombarding Spacecraft Surface Materials," AIAA Paper No. 72-446, April 1972.

8. L. R. Kelley, E. E. Luedke, and D. F. Hall, "Damage of Thermal Control Coating Properties by Energetic Mercury Ion Bombardment," AIAA Paper No. 72-445, April 1972.
9. D. F. Hall and W. C. Lyon, "Low Thrust Propulsion System Effects on Communication Satellites," AIAA Paper No. 72-519, April 1972.
10. E. J. Worlock, et al., "A One Millipound Cesium Ion Thruster System," AIAA Paper No. 70-1149.

2. SPACECRAFT DESIGN IMPLICATIONS OF ION ENGINE CONTAMINANTS

In designing a spacecraft which will carry an electric propulsion system, one should be aware of the various kinds of particulate contamination the system will produce, the mechanisms by which these particles may degrade the performance of subsystems which receive them, and potential solutions to problems encountered. These three subjects are discussed below.

2.1 ION ENGINE CONTAMINATION PARTICLES

The various classes of contamination particles associated with ion engine operation are shown schematically in Figure 2-1. Propellant (mercury or cesium) ions and atoms, and atoms of thruster material (molybdenum or aluminum) are emitted at large (as well as small) angles from the thruster exit plane. In addition, the primary thrust beam is a source of high angle thruster material and propellant ions which may even escape the exhaust hemisphere (defined by the engine exit plane), as indicated by the figure. These ion engine effluents are discussed in more detail in Section 3.

Figure 2-1 shows a spacecraft surface arbitrarily located within the exhaust hemisphere. It is subjected to impingement by the contaminant particles mentioned above, and may be detrimentally affected in one or more of the ways described in the following section. It also becomes a (secondary) source of contaminants which can proceed to other S/C surfaces, including surfaces outside the exhaust hemisphere. These secondary particles are (1) re-evaporated propellant atoms, (2) surface atoms sputtered by propellant ions, and, perhaps, (3) thruster atoms first deposited on and then sputtered from the receiving surface. Propellant evaporation is discussed in Section 4 and sputtering in Section 5.

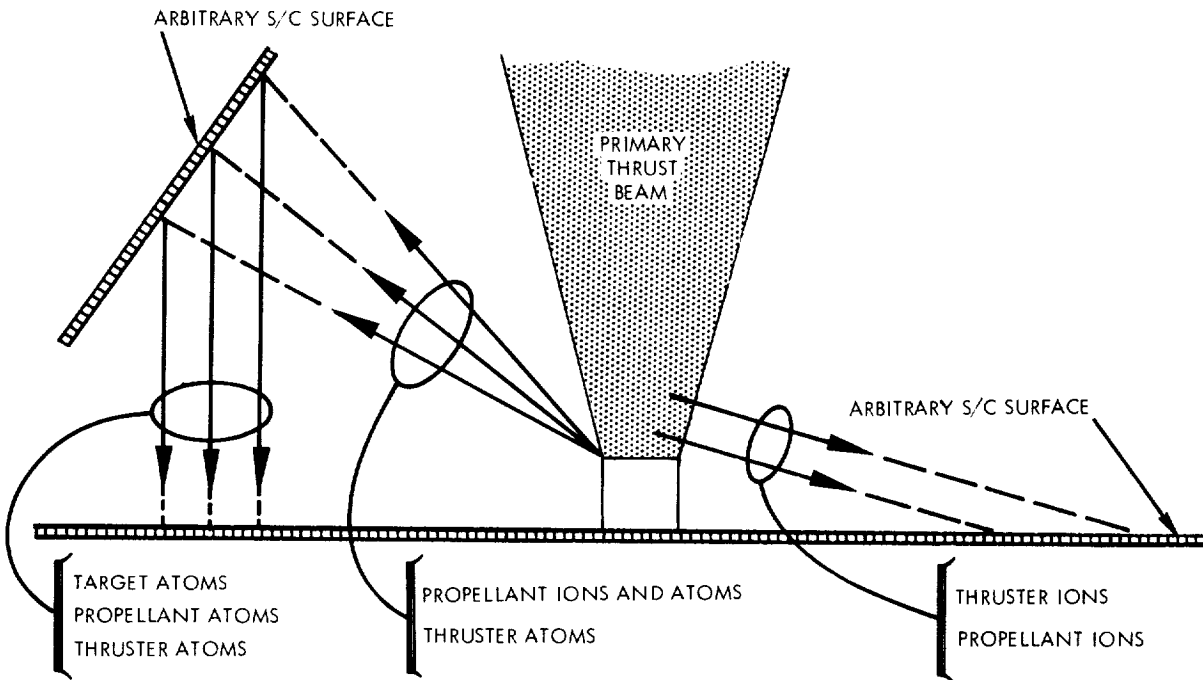


Figure 2-1. Schematic of the Classes of Particulate Contaminants Associated with Ion Engines

2.2 DEGRADATION MECHANISMS

Given the arrival at a spacecraft surface of a flux of one or more of the classes of particles discussed above, in what ways might the surface be degraded? This depends critically on the purpose of the receiving surface.

Table 2-1 lists five degradation "mechanisms" arising from the effluents discussed above and seven spacecraft "systems" potentially affected by these mechanisms. For perspective, a problem area rating scale of 0 to 3 has been used to suggest the degree to which each system is inherently sensitive to the various degradation mechanisms. Of course, in any particular spacecraft design, a potentially "serious problem" area may become an "improbable problem" area.

These mechanisms are briefly discussed below. They are discussed at length and quantitatively in later sections of this report.

Table 2-1. Potential Degradation of Spacecraft Systems by Ion Engine Effluents

DEGRADATION MECHANISM	SPACECRAFT SYSTEMS AFFECTED						
	THERMAL CONTROL COATINGS	SOLAR ARRAYS	OPTICAL SYSTEMS	COMMUNICATION SYSTEMS	STRUCTURAL MATERIALS	ELECTRICAL INSULATORS	MOVING JOINTS
DEPOSITION OF FILMS	3	3	3	2	0	2	0
CHEMICAL REACTION	3	2	0	0	1	0	1
METALLURGICAL REACTION	2	2	0	0	1	0	1
SPUTTERING EROSION	2	2	2	0	1	0	0
RADIATION DAMAGE	3	0	0	0	0	0	0

PROBLEM AREA RATING SCALE: IMPROBABLE (0) TO POTENTIALLY SERIOUS (3)

2.2.1 Deposition of Films

Film deposition can occur in three ways: condensation of un-ionized propellant and low energy propellant ions, deposition of thruster material, and deposition of material sputtered from other spacecraft surfaces. If a film of sufficient thickness is deposited on a thermal control coating, the coating will acquire the thermophysical properties of the film. A film on a solar array or optical sensor lens will reduce optical transmittance and affect component temperature. As indicated in Table 2-1, the forementioned systems are inherently quite sensitive to films. Metal films can also degrade electrical insulators and, in the case of the propellants, promote high voltage breakdown across electrode gaps. Thus, the first S/C design implication of ion engine contaminants is: Minimize the deposition of films on thermal control coatings, solar arrays, optical elements, electrical insulators, and electrode gaps. Estimate the degradation of these subsystems over the mission life and determine if it is acceptable.

2.2.2 Chemical and Metallurgical Reaction

Soft solder is the spacecraft material most sensitive to reaction with mercury. Solder finds extensive use in solar cell-to-interconnect bonds, and bond breakage is a major cause of solar array failure (with or without the presence of ion engines). However, the mercury/solder tests described in Section 7 suggest that although immersion of solder in liquid mercury produces dramatic results, soldered joints may be able to withstand reasonably large fluxes of impinging mercury atom beams.

Vacuum immersion of soft solder, Teflon FEP and Kapton (H-Film) in cesium also produced serious reactions, as described in Sections 7.4.1 and 6.2. Since Kapton is commonly employed as the foundation of lightweight, rollout solar array designs and aluminized Kapton is a popular thermal control coating, tests which are more representative of actual spacecraft conditions are desired. Phase IV of this program will include some Kapton/cesium beam experiments. The design implication is: Avoid mercury and cesium impingement on solder joints, and cesium impingement on Teflon and Kapton. With the aid of the latest experimental results (e.g., Phase IV reports) determine if the estimated arrival rates are excessive.

2.2.3 Surface Erosion by Sputtering

When high velocity particles, such as some of the high angle propellant ions, impact a surface, some surface atoms are removed. However, the measurements of typical erosion rates presented in Section 5 and typical ion arrival rates computed from information in Section 3 indicate that total erosion depths will be small, even for long total thrust periods. Thus, thin films, such as lens and solar cell cover glass coatings, and some thermal control surfaces may be endangered; however, most spacecraft surfaces will not be significantly eroded. The design implication is: Avoid placing thin targets where they will receive significant fluxes of energetic propellant ions. Estimate the total erosion which will occur on any vulnerable surface.

2.2.4 Radiation Damage

The solar absorptance of many thermal control coatings, particularly white paints, degrades under bombardment by the energetic

particles in the space environment (electrons, protons, photons, micro-meteoroids, etc.). Measurement of the effects of energetic mercury ion bombardment described in Section 8 demonstrate a similar dose-dependent increase in absorptance. In general, little change occurs to any commonly-used paints prior to accumulating 10^{15} ions/cm², and several can tolerate 10^{16} or more. Infrared emittance properties were not seen to change with ion doses as large as 4×10^{19} . The design implication is: Limit the total dose of energetic mercury ions arriving at white paint surfaces to an amount which produces a tolerable absorptance increase. For cesium ion engines, refer to Phase IV data.

2.3 POTENTIAL SOLUTIONS TO CONTAMINATION PROBLEMS

2.3.1 Spacecraft Configuration

By definition, if a spacecraft surface is located where there can be no primary particle impingement, it has no particle contamination problem. It will be seen in Section 3 that the greater the angle between the thruster axis and the surface, and the greater the distance between the thruster exhaust plane and the surface, the smaller the arrival rate of contaminants at the surface. Unfortunately, however, it is not possible at this time to specify an angle beyond which the particle distributions are all zero - the necessary experimental data are lacking. However, the "appearance" angle is probably greater than 90 degrees. Fortunately, it is often possible to devote a cone with 45 degrees or more half angle exclusively to the thruster exhaust and to choose relatively insensitive materials for the surfaces which do receive thruster contaminants.

2.3.2 Thruster Baffles

A potential solution to contamination of S/C surfaces located at high angles with respect to the thruster axis is to deploy an intervening baffle. This technique has not been studied, but several baffle design considerations may be listed.

First, the baffle should be large enough and oriented so as to be effective in shielding all sensitive spacecraft surfaces which otherwise would receive contamination. Second, it should meet the usual mechanical requirements of flight hardware regarding weight and vibration tolerance. Taken together these two requirements imply a baffle location near the

thruster. However, in most instances the baffle will receive energetic ion impingement, and therefore will become a source of secondary particles which may reach S/C surfaces or adversely affect thruster performance or life. For example, the discharge neutralizer or thruster cathode might become clogged with material sputtered from the baffle or insulators might become coated. A baffle will also act as a heat shield and may significantly affect the thruster temperature. It will increase the propellant atom density in the vicinity of the exhaust plane leading to increased production of engine contaminants and decrease engine operating life. If propellant is allowed to condense on the baffle and then the baffle undergoes an upward temperature transient, the sudden desorption of propellant could damage the thruster or its power processor. Further, questions related to thruster vectoring, gimbaling, and clustering, if any, must be considered during baffle design. Most of these baffle problems are reduced if the baffle need not consist of a full cylinder. Even so, baffles only represent a potential solution to contamination problems. They will require detailed analysis and operational testing before they may be accepted as innocuous and effective.

2.3.3 Electrical Biasing and Deflecting

Often low energy ions (known as Group 4) are a contaminant of major concern. It should be possible to prevent these particles from arriving at a conductive surface by either electrically biasing: (1) the surface itself, (2) a nearby deflecting electrode or electrodes, or (3) the thrust beam neutralizer. However, a system which repels ions necessarily attracts electrons, so consideration of the power dissipated at the collecting surface and the capacity of the neutralizer to supply current in excess of the ion beam current is necessary.

2.3.4 Choice of Materials.

In some instances it is possible to substitute an insensitive surface for a sensitive surface at locations receiving impingement. For instance, second surface quartz mirrors or polymers might be substituted for white paint when a low α/ϵ surface is required at a location receiving a large flux of energetic ions. The subsequent sections of this report provide information regarding the sensitivity of various commonly used spacecraft materials to ion engine contaminants.

3. ION THRUSTER EFFLUENTS

Exhaust from an ion thruster contains collimated propellant (cesium or mercury) ions, uncollimated propellant ions, propellant atoms and small quantities of ionized and un-ionized thruster material. The collimated ions, which constitute most of the exhaust, have high energy (500 to 3000 ev) and are primarily contained within an envelope defined by a small semi-angle (~15 degrees). These ions, referred to as primary or Group 1 ions, do not interact with a spacecraft unless something is placed directly in the beam.

Group 2 ions, which are formed by charge exchange within the thruster, also travel in approximately straight lines. However, they depart with angles greater than 15 degrees and perhaps as great as 90 degrees.¹

It should be emphasized that the ion current density distribution of Groups 1 and 2 ions is a function not only of the electrical operating characteristics of a particular engine, but also of its mechanical design and fabrication tolerances. Since the distribution is important not only to the subject of exhaust effects on spacecraft surfaces, but also to thruster efficiency and thrust vector precision, such data should be taken on all flight hardware thrusters.

Another class of propellant ions, referred to as Group 4, exist which are uncollimated because they are formed within the thrust beam¹ and proceed radially outward under the influence of small electric fields both within and outside the beam. The fields within the primary beam are probably about normal to its envelope. If so, these 10 to 50 ev, Group 4 ions should depart at an average angle of approximately 115 degrees from the thrust axis and will invade regions upstream of the thruster exit plane. Figure 3-1 shows schematically the three ion groups discussed above.

Some propellant (1 to 20 percent depending on thruster type) leaves the thruster un-ionized with 500° to 1400°K thermal velocity. As a first approximation, the spatial distribution of this flux is that of an extended cosine source.

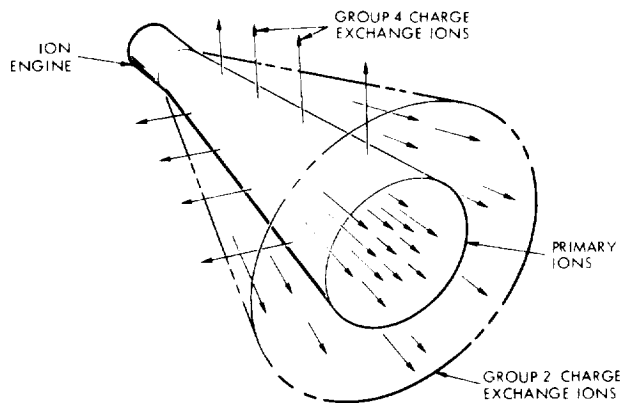


Figure 3-1
Schematic of Ion Categories
Emitted by an Ion Engine

Traces of the metal of thruster construction (molybdenum or aluminum) are also emitted. Nearly all are emitted in an approximately cosine distribution of neutral atoms superimposed on the propellant atom distribution, but some ion flux, analogous to Group 4 propellant ions, is also produced.

Finally, the source of plasma neutralizing electrons (the "neutralizer") can be a source of contaminant particles.

In the following sections, these various classes of ion engine effluents are discussed in more detail and, wherever possible, mathematical descriptions of the particle spatial distributions are given.

3.1 PROPELLANT ATOMS

The neutral atom efflux fraction ranges from ~1 percent in the cesium contact engines² to 5 to 25 percent for electron bombardment (EB) thrusters.^{3, 4} This efflux has been experimentally shown² to follow approximately a cosine distribution for the cesium contact rocket (thermal velocity ~1400°K); the electrode geometry of EB rockets also leads to the expectation of an approximately cosine distribution (thermal velocity ~500°K). Therefore, the angular distribution of atoms from all circular ion engines may be approximated by that of an extended cosine source (see geometry of Figure 3-2).

$$\Gamma(z, \theta) = \Gamma_0 (r^2/z^2) \cos \theta [1 + (2r^2/z^2) \cos \theta + (r^4/z^4)]^{-1/2} \quad (3-1)$$

While Equation (3-1) is not appropriate for values of (z, θ) with $z < r$, this restriction is of no consequence, because objects are not normally placed within one thruster radius of the exhaust plane. Reynolds⁵ has discussed calculation of the arrival rate of particles Γ_{ar} at arbitrarily located and oriented spacecraft surfaces, including those outside of line-of-sight to the thruster.

3.2 PROPELLANT IONS

As mentioned earlier, three classes of propellant ions are emitted by ion engines, Groups 1, 2 and 4. In the following subsections means of estimating their distributions are discussed.

3.2.1 Groups 1 and 2 Propellant Ions

The primary (or Group 1) ion beam of all ion engines is essentially similar. It consists of an approximately geometrically expanding beam, ~94 percent of which is singly ionized atoms⁶⁻⁸ with velocities in the 3×10^4 m/sec range, whose "boundaries" form angles of 15 to 20 degrees with the beam axis. For cesium contact ionization rockets, ion current densities may be as large as 10 or 20 ma/cm² at the exit plane, while electron bombardment rockets are operated in the 1 to 4 ma/cm² range.

The primary beam may be approximated by a cone, having uniform current density in any plane P, and which appears to originate from some focal point O' located upstream of the exhaust plane, as shown in Figure 3-2. Then the ratio of ion current density at a downstream point to that at the exit plane is

$$\frac{j(z)}{j_0} = \left[1 + \frac{2z}{r} \tan \beta + \left(\frac{z}{r} \tan \beta \right)^2 \right]^{-1} \quad (3-2)$$

The angle β is the characteristic divergence angle of the beam, obtained by integration of the thrust components of all beam ions over a plane such as P. It may be defined in the thrust-efficiency formula

$$\eta_T = \eta_0 \cos^2 \beta \quad (3-3)$$

where η_0 is the efficiency which would be obtained with zero beam divergence. Equation (3-2) is plotted in Figure 3-3 for commonly encountered values of β .

Group 2 ions have divergence angles greater than β . Little experimental data have been published on the spatial distribution of these ions beyond 20 degrees. Reynolds⁹ has discussed an empirical mathematical representation of both Groups 1 and 2 ion beam profile data obtained in the far field, e.g., at distances greater than ~8 thruster radii. He presents several examples where the values of the two constants of his formula have been determined from experimental data. Four of the examples [Figures

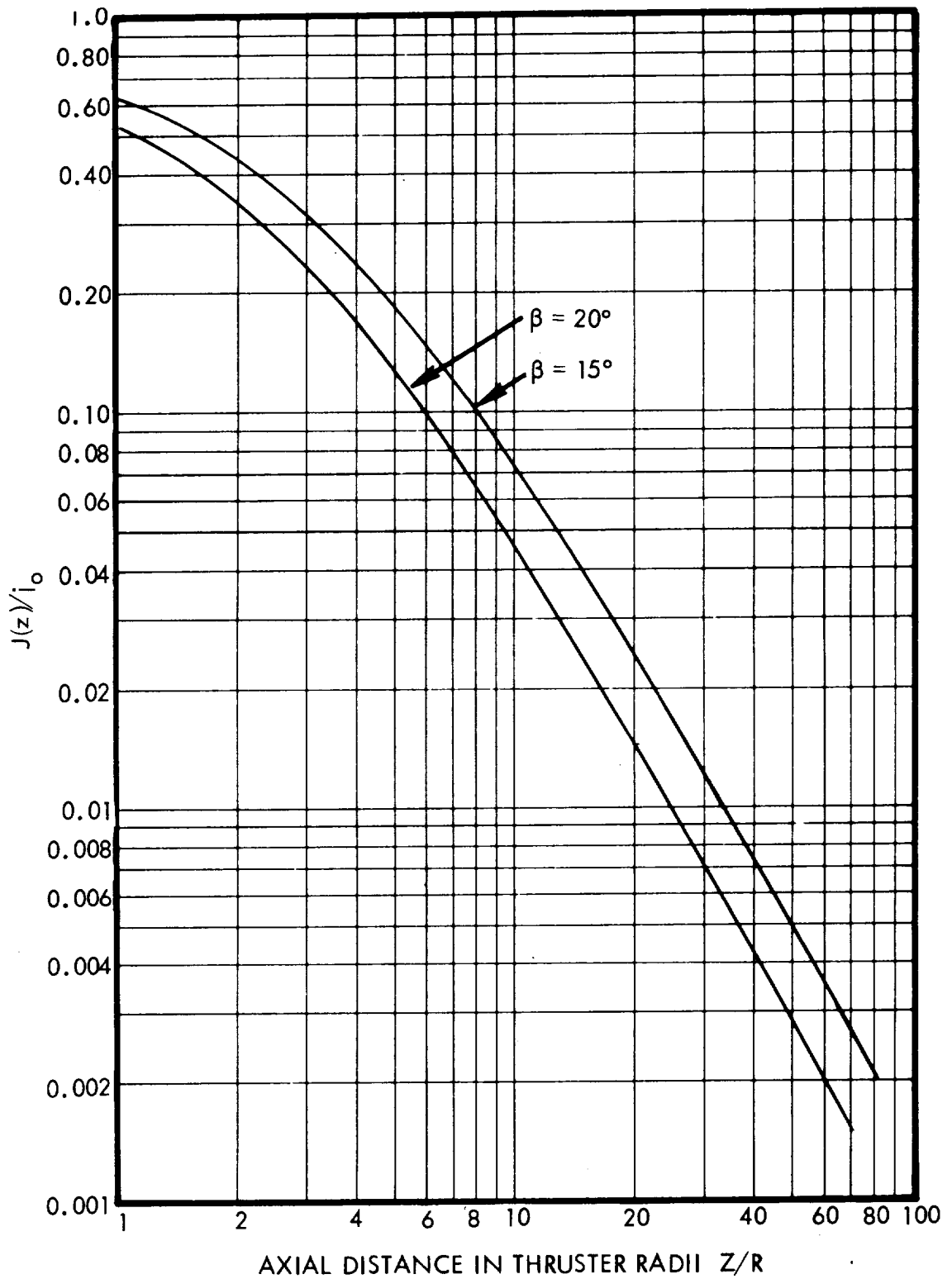


Figure 3-3. Simplified Representation of Axial Ion Current Density (Normalized to Initial Value) as a Function of Distance from Thruster Exit Plane. Electron bombardment thrusters with conventional grids typically have beam divergence half angles, β , between 15 and 20 degrees.

3(a), 3(b), 3(c), and 3(g) of Reference 9] use data from mercury bombardment ion thrusters with a single metallic/dielectric composite grid. To date, composite grid systems have exhibited severely limited operating lifetimes and therefore must be regarded as experimental rather than prototypical of flight hardware thrusters. (It is noteworthy that these profiles are much more divergent than is typical of conventional two-grid systems.) Reynolds' other examples are discussed below.

Figure 3(e) of Reference 9 shows data from a 2.54 cm diameter cesium contact ionizer with a close-spaced accelerator cross grid of fine tungsten wire. This is an ion source useful for plasma experiments, but its grid life is severely limited when operated with continuously applied high voltages as would be typical of thruster operation. Its ion optics are quite different from two-grid bombardment thrusters, so its ion current density profile cannot be regarded as typical of bombardment-type thrusters.

However, measurements of a beam from a laboratory cesium contact source by Sellen, et al.,¹⁰ are still the most extensive available. These included detailed mapping of beam density (over more than two decades in density in a given plane), local plasma potential, and electron temperature, in planes extending from 0.9 to 1598 source radii downstream. They resulted in a far-field description of the thrust beam as a central core surrounded by a region of ion density which decreases exponentially with distance from the beam axis. The more limited data available from practical thrusters are consistent with this description.

Sellen's measurements also included scans of the beam very close to the exit plane (uniform density core with very steep edges) and at several planes in the transition region. From these and other data, a good "rule-of-thumb" seems to be that the far-field description from Reference 10 is essentially valid at downstream distances greater than about 10 thruster radii. Reynolds' analysis is consistent with this experimental result.

Inasmuch as it is the high angle particles which are of interest in evaluating the potential effects of ion engine effluents on spacecraft surfaces, the apparent exponential dependence of ion current density on distance from the beam axis outside the core noted by Sellen provides a basis for a simpler, though less elegant, Group 2 model than that of Reynolds. As discussed below, the exponential model is also more conservative in

that it predicts higher Group 2 fluxes at high angles, where no experimental data are available to indicate which model is more accurate. Further, means will be discussed whereby the exponential far-field model may be adapted in a simple way to provide flux estimates nearer the thruster.

The exponential relationship has the form

$$\frac{j(y/z)}{j(z)} = c_2 \exp(-y/zc_1) \quad (y/z \geq 0.4) \quad (3-4)$$

where

- y = radial distance from beam axis
- z = axial distance from thruster exhaust plane
- j(z) = ion current density on beam axis at distance z
- c₁ = e-folding constant for (y/z)
- c₂ = initial value of exponential
- j(y/z) = ion current density through a point (z, y)

The nomenclature of Figure 3-2 has been retained in Equation (3-4). The equation gives the ratio of the current density at point p (z, y) in a plane P to that where the beam axis intersects the plane P. Note that ion current density at point p is defined as ions per second per unit area in the plane P. The constants c₁ and c₂ are obtained from a best fit to experimental data. The value j(z) may be obtained from Equation (3-2) or from Figure 3-3.

Equation (3-4) is found to be a good analytical representation of most conventional grid bombardment thruster beam data for $\theta \geq 20$ degrees and $z \geq 10r$, where $\theta = \arctangent(y/z)$ and $r = \text{thruster radius}$. Figure 3-4 shows three sets of beam profile data from conventional grid mercury ion engines found in the literature and one set obtained at TRW on a 20 cm thruster. In each case but the last, a single straight line fits the $\theta \geq 20$ -degree data well, demonstrating the applicability of Equation (3-4) over the range of the data.

The data of Figure 3-4 deserves some discussion. The 5 cm engine data are those of Nakanishi¹¹ and are erroneously described as from a "glass grid" engine and attributed to Reference 12 in the caption of Figure 3d, Reference 9. In fact, the data are from conventional grids and the authors report that it represents about the minimum beam spreading which they obtained.

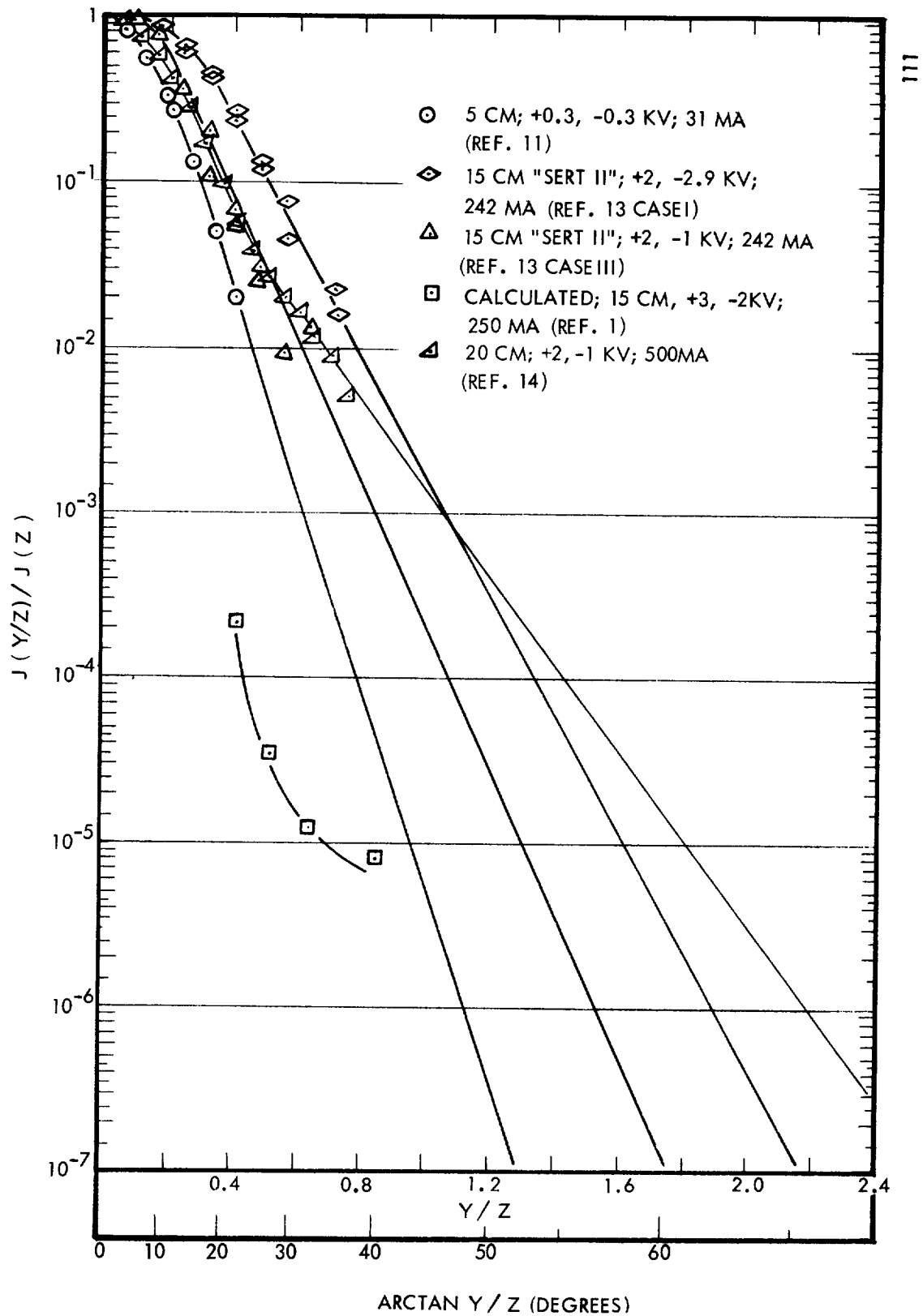


Figure 3-4. Ion Beam Profile Data from Several Different Mercury Bombardment Ion Engines with Conventional Grids

The two 15 cm engine profiles are from the work of Byers.¹³ Unfortunately, because of experimental difficulties, neither profile was taken at the normal operating point for the thruster, which is +3 kv screen potential and -2 kv accelerator potential. However, the two cases presented bracket this normal total-to-net accelerating potential ratio of 1.66, and therefore the profiles probably bracket the one which would have been obtained at normal operating potentials.

The data on the 20 cm engine are that of Sellen.¹⁴ The engine accelerating potentials are normal, but the beam current is throttled to 50 percent of the maximum rated value. It is not known why the data beyond 30 degrees have a different slope from those between 20 and 30 degrees.

Finally, four computer-calculated values by Staggs, et.al.,¹ are shown. This was pioneering work, but the use of these values as representative of the Group 2 ion distribution is not recommended.

Figure 3-4 demonstrates that most available high angle ($\theta > 20$ degrees) data can be represented by an expression of the form of Equation (3-4) with suitably chosen values of the constants C_1 and C_2 . Reynolds⁹ has shown that these same data may be well represented by an expression of the form

$$\frac{j(y/z)}{j(z)} = e^{-\lambda(1 - \cos \theta)^n} \quad (3-5)$$

where λ and n are suitably chosen constants. However these two analytical representations do predict different current density ratios for values of θ beyond the range of the experimental data. Equation (3-4) predicts the larger values of the two; the larger θ the greater their divergence. Equation (3-4) is favored at TRW for use in ion engine/spacecraft interactions calculations for this very reason; assumption of a large distribution is more conservative. Note, too, that had Sellen¹⁴ terminated data taking by 30 degrees, as others have usually done, lower high angle fluxes would be predicted by Equation (3-4) than were actually measured. Thus, the values from Equation (3-4), though larger than those from Equation (3-5), may still underestimate the values which would be measured. In any case, the need for higher angle Group 2 data from representative ion engines is obvious.

Neither Equation (3-4) nor (3-5) can be expected to correctly predict ion arrival rates at locations so near the thruster that it fails to approximate a point source. If the far-field definition $\theta' = \arctan(y/z)$ is retained, the predicted values will be too small. Reynolds has derived an integral expression suitable for computer-aided calculations in the near field.⁹ A crude but mathematically much simpler approach is to use Equation (3-2) but substitute $y' = y-r$ for y . This is equivalent to measuring θ from the nearest thruster periphery (point E in Figure 3-2) instead of from its center (point O in Figure 3-2).

3.2.2 Group 4 Propellant Ions

In addition to Groups 1 and 2, ion engines emit Group 4 charge exchange ions. These are particles which leave the thruster as neutrals but subsequently undergo "near-miss" collisions with primary ions in which the original ion recombines with an electron from the neutral. The resulting particles are a fast neutral with the velocity (direction as well as speed) that the primary ion had at the time of collision, and a slow ion which is subjected to any electric fields present. At this time, there are insufficient data regarding the resultant trajectories of Group 4 ions to make reliable ion engine/spacecraft interactions calculations; again, experimental data are required.

It is possible to calculate the production rate of Group 4 ions given the appropriate charge exchange cross section. For (3 Kev) $\text{Hg}^+ + \text{Hg}^0$, a value of $5 \text{ or } 6 \times 10^{-15} \text{ cm}^2$ is often taken, based on extrapolation of the data of Paliukh and Sena¹⁵ (reprinted in Brown¹⁶) or the measurements of Zuccaro.¹⁷ For (0.5 Kev) $\text{Cs}^+ + \text{Cs}^0$, a value of $2.4 \times 10^{-14} \text{ cm}^2$ has been used,¹⁸⁻¹⁹ based on measurements by Zuccaro,²⁰ Marino,²¹⁻²² and Perel.²³ Charge exchange production rate calculations have been discussed by Staggs,¹ Lyon,^{18, 19, 24} and Reynolds²⁵ and will not be reviewed here.

3.3 THRUSTER MATERIAL

3.3.1 Accelerator Grid Atoms

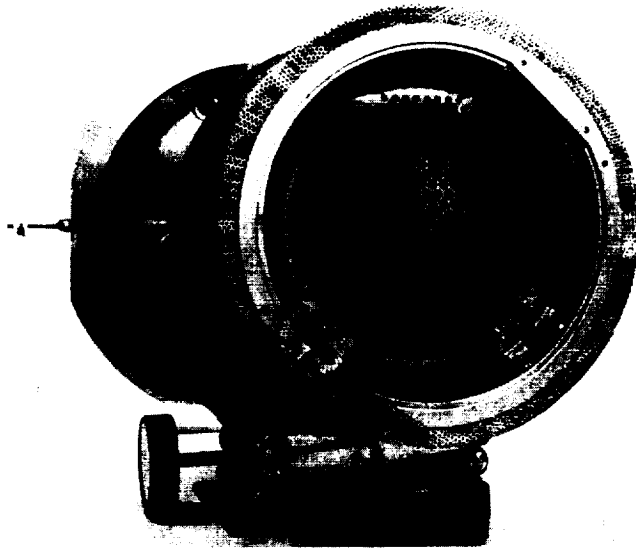
During normal thruster operation the negatively biased accelerator electrode is bombarded by a small ion current. In electron bombardment type thrusters, the accelerator electrode consists of holes in a molybdenum or aluminum plate and forms the exit plane of the thruster, as shown in

Figure 3-5. Propellant (Group 3) ions which are formed downstream of the thruster between the accelerator grid and the neutralization plane by charge exchange are attracted by the electrode's large negative potential. The impinging ions appear as accelerator "drain" current in the accelerator power supply, and after a few hundred hours of operation, sputtering patterns are clearly visible on the downstream face of this electrode (see Figure 3-5). The magnitude of the resulting flux of molybdenum atoms may be estimated from the drain current and sputtering yield data:

$$\Gamma_o = S \Gamma_+ = S I_+ (qA)^{-1}$$

where

- Γ_o = flux density of Mo atoms leaving the accelerator grid, atoms/cm²-sec
- S = number of Mo atoms released per incident ions, atoms/ion
- I_+ = accelerator drain current, amps
- q = 1.6×10^{-19} coul/electron
- A = area of accelerator grid, cm²
- Γ_+ = flux of propellant (Group 3) ions impinging on accelerator grid, ions/cm²-sec.



75690-70

Figure 3-5. Photograph of 15 cm Diameter NASA/Lewis-Type Electron Bombardment Thruster. Charge exchange ion sputtering pattern on screen electrode is visible.

Electron bombardment thrusters typically have accelerator drain currents of the order of 1 percent of the beam current, or $1 \text{ to } 3 \times 10^{-5} \text{ A/cm}^2$ drain current density. The sputtering yield of polycrystalline molybdenum by 2 Kev Hg^+ is ~ 2 and of polycrystalline aluminum by 500 ev Xe^+ is 0.8 (Reference 26). Therefore $\Gamma_o \approx 10^{14} \text{ atoms/cm}^2 \text{-sec.}$

To first order, the spatial distribution of this flux should be cosine. Since the distribution of un-ionized propellant flux from the thruster is also approximately cosine, the two fluxes may be directly compared. Taking the example above, it is found that the flux of accel grid atoms arriving at any location will be approximately 1/10 the corresponding propellant atom flux. However, mercury and cesium have high vapor pressures and therefore will reevaporate at a significant rate. In contrast, molybdenum, aluminum, and any other conceivable grid material have a very low vapor pressure, so virtually all accelerator grid atoms arriving at a spacecraft surface will be permanently deposited there. This means that in many situations sputtered accelerator grid material is more important than un-ionized propellant as a potential contaminant.

3.3.2 Accelerator Grid Ions

The primary ion beam passes through part of the population of sputtered accelerator grid atoms. There is a finite probability of charge exchange collisions between the propellant ions and grid atoms, resulting in Group 4 grid material ions. This flux is of particular interest as a contaminant in that it has nearly the same spacial distribution as the Group 4 propellant ions and the deposition permanence of accelerator grid material. (Compared to the propellant ion distribution, the grid ion distribution is expected to be shifted slightly away from the thruster because the sputtered atoms have approximately 5 ev of initial kinetic energy, generally in the downstream direction, whereas the propellant atoms have much less.)

Calculation of Group 4 accelerator grid ion production rate is identical to calculation of Group 4 propellant ions, except that the appropriate charge exchange cross sections must be employed. However, these values have not been found in the literature. Hall²⁷ made a crude estimate of the 3 (kev) $\text{Hg}^+ + \text{Mo}^0$ of $1 \times 10^{-15} \text{ cm}^2$. Dugan²⁸ has made sophisticated estimates of the upper limit of $\text{Hg}^+ + \text{Mo}^0$ and $\text{Cs}^+ + \text{Al}^0$ cross sections. He obtains $\sim 8 \times 10^{-16} \text{ cm}^2$ maximum for 3 kev Hg^+ and $\sim 6 \times 10^{-16} \text{ cm}^2$ maximum for 500 ev Cs^+ . If the cross sections are indeed this large, Group 4

accelerator grid efflux will often be significant in ion engine/spacecraft interactions. Furthermore, Dugan warns that charge exchange between Group 4 propellant ions and accelerator grid atoms can also be important because the cross sections for low relative velocity collisions may be much larger than in the 500 to 3000 ev range.

3.4 DISCHARGE NEUTRALIZERS

Ion engine systems include an electron source located an inch or two downstream of the engine exit plane and outside the primary beam. This neutralizer supplies a current of electrons to the thrust beam to provide charge neutrality of the thrust plasma and equality of the negative and positive particle currents leaving the spacecraft.

The best performing electron sources for this task are of the discharge (or plasma bridge) type. A review of the discharge neutralizer as a source of spacecraft contamination was given in Volume I of this report. It was concluded that in a cone about the neutralizer axis propellant particle fluxes may be comparable to those from the thruster at high angles. However, the recent trend is to orient the neutralizer so that its axis is nearly parallel to the thrust axis rather than the earlier practice of placing it nearly perpendicular. In the parallel orientation, the importance of the neutralizer as a contamination source is diminished.

3.5 REFERENCES (SECTION 3)

1. J.F. Staggs, W.P. Gula and W.R. Kerslake, "The Distribution of Neutral Atoms and Charge-Exchange Ions Downstream of an Ion Thruster," *Journal of Spacecraft and Rockets*, Vol. 5, No. 2, February 1968, pp. 159-164.
2. D.F. Hall, Alfred Y. Cho and H. Shelton, "An Experimental Study of Porous Metal Ionizers," *AIAA Preprint No. 66-218*, AIAA Fifth Electric Propulsion Conference, March 1966.
3. W.R. Kerslake, R.G. Goldman and W.C. Nieberding, "SERT II: Mission, Thruster Performance, and In-Flight Thrust Measurements," *Journal of Spacecraft and Rockets*, Vol. 8, No. 3, March 1971, pp. 213-224.
4. E. James, et al., "A One Millipound Cesium Ion Thruster System," *AIAA Paper No. 70-1149*, August 1970.
5. T.W. Reynolds and E.A. Richley, "Propellant Condensation on Surfaces Near an Electric Rocket Exhaust," *Journal of Spacecraft and Rockets*, Vol. 6, No. 10, October 1969, pp. 1155-1161.

6. R.F. Kemp, J.M. Sellen, Jr., and E.V. Pawlik, "Neutralizer Tests on a Flight-Model Electron-Bombardment Ion Thruster, " NASA TN D-1733, 1963.
7. N.L. Milder, "Comparative Measurements of Singly and Doubly Ionized Mercury Produced by Electron-Bombardment Ion Engine, " NASA TN D-1219, 1962.
8. E.V. Pawlik, R. Goldstein, D.J. Fitzgerald, and R.W. Adams, "Ion Thruster Performance Calibration, " AIAA Paper No. 72-475, April, 1972.
9. T.W. Reynolds, "Mathematical Representation of Current Density Profiles from Ion Thrusters, " AIAA Paper No. 71-693, June 1971.
10. J.M. Sellen, Jr., R.F. Kemp and R.H. Hieber, "Observations of Neutralized Thrust Beams in the 80' NASA Testing Chamber, " Section III-G of "Investigations of Ion Beam Diagnostics, " Final Report, Contract NAS8-1560, TRW Space Technology Laboratories, April 1964.
11. S. Nakanishi, E.A. Richley and B.A. Banks, "High Perveance Accelerator Grids for Low Voltage Kaufman Thrusters, " AIAA Paper No. 67-680, Sept. 1967
12. S. Nakanishi, B.A. Banks, and E.A. Richley, "High-Perveance Accelerator Grids for Low-Voltage Kaufman Thrusters, " Journal of Spacecraft and Rockets, Vol. 5, No. 3, March 1968, pp. 35C-358.
13. D.C. Byers, "Angular Distribution of Kaufman Ion Thruster Beams, " NASA TN D-5844, June 1970.
14. J.M. Sellen, Jr., Private Communication, Contract NAS 2-6940, August 1972.
15. B.M. Paliukh and L.A. Sena, "Charge Exchange in Atoms and Ions of Mercury, " J. Exp. Theoret. Phys (U.S.S.R.), Vol. 20, 1950, p. 481; English Translation, SLA Translation Center 60-18509.
16. S.C. Brown, Basic Data of Plasma Physics, Wiley & Son, N.Y., 1959, p. 38.
17. D.E. Zuccaro, "Measurement of the Resonant Charge Exchange Cross Section of Mercury and Cesium, " AIAA Paper No. 67-682, September 1967.
18. W.C. Lyon, "Thruster Exhaust Effects Upon Spacecraft, " NASA TMX 65427, X-460-70-401, Oct. 1970.
19. W.C. Lyon, "Propellant Condensation on Surfaces near an Electric Rocket Exhaust, " Journal of Spacecraft and Rockets, Vol. 7, No. 12, Dec. 1970 pp. 1494-1496.
20. D. Zuccaro, "Measurement of the Charge Exchange Cross Section of Mercury, " NASA CR-72398 (N68-30824), Hughes Research Laboratories, April 1968.

21. L.L. Marino, A.C.H. Smith, and E. Caplinger, "Charge Transfer Between Positive Cesium Ions and Cesium Atoms," *Physical Review*, Vol. 128, No. 5, p. 2243, December 1, 1962.
22. L.L. Marino, "Charge Transfer Between Alkali-Metal Ions and Cesium Atoms," *Physical Review*, Vol. 152, No. 1, p. 46, December 2, 1966.
23. J. Perel, R.H. Bernon and H.L. Daley, "Measurement of Cesium and Rubidium Charge-Transfer Cross Sections," *Physical Review*, Vol. 138, No. 4A, p. A937, May 17, 1965.
24. W.C. Lyon, "Monopropellant Thruster Exhaust Effects upon Spacecraft," *Journal of Spacecraft and Rockets*, Vol. 8, No. 7, July 1971, pp. 689-701.
25. T.W. Reynolds, "Procedure for Estimating Effects of Ion Beam Interaction with Spacecraft," NASA TM X-68043, April 1972.
26. G. Carter, and J.S. Colligon, Ion Bombardment of Solids, American Elsevier Publishing, Inc., 1968, pp. 310-353.
27. D.F. Hall, "Electrostatic Propulsion Beam Divergence Effects on Spacecraft Surfaces," Quarterly Technical Report October 1970 - January 1971, JPL Contract No. 952350, Feb. 15, 1971, pp. 31-36.

4. DEPOSITION AND EFFECTS OF THIN FILMS

A major mechanism whereby ion engines may affect nearby spacecraft surfaces is the overcoating of these surfaces with engine effluents. Section 4.1 is a discussion of the kinds of overcoating which may take place. Section 4.2 is a discussion of the effects of overcoating with the assumption that no chemical or metallurgical reaction takes place. (Chemical and metallurgical treated separately in Sections 6 and 7, respectively.)

4.1 TYPES OF FILM DEPOSITION

Film deposition on spacecraft surfaces can occur in three ways: condensation of un-ionized propellant (and Group 4 propellant ions), deposition of thruster material, and deposition of material sputtered from other spacecraft surfaces.

4.1.1 Propellant Condensation

Condensed layer formation proceeds in two stages: adsorption of propellant atoms on the spacecraft surface, followed by bulk condensation of atoms on this adsorbate. Desorption and then evaporation (or sublimation) compete with these processes in proportion to $\exp [-E_D/kT_S]$, where T_S is the surface temperature and E_D is the energy binding the atom to the surface. The value of E_D varies with surface composition and cleanliness, adsorbate species, and extent of adsorbate coverage. It affects whether the adsorbate forms as a uniform monolayer or as agglomerates. Usually its value is known precisely only for special substrates, such as atomically clean single crystals and the condensate itself.

Knowledge of the relative value of E_D for the atom-spacecraft surface combination (E_D^o) and the atom-condensate combination (E_D^f) is useful in predicting bulk condensation. When $E_D^o > E_D^f$, adsorption will (1) be more or less uniform on the surface and (2) occur and be sustained at lower Γ_{ar} and/or higher T_S than will subsequent condensation. Thus, condensation rates will be controlled by E_D^f . When $E_D^o < E_D^f$, adsorption will (1) require higher Γ_{ar} and/or lower T_S than will subsequent condensation, and (2) proceed by a nucleation process often leading to macroscopic agglomerates. Thus, calculations based on E_D^f will be

"worst case," since the initial Γ_{ar} must exceed the equilibrium value at a given T_S . Langmuir¹ explains this "critical temperature" phenomenon by observing that if two adatoms are in contact, "... a larger amount of work must be done to evaporate one of these atoms than if the atoms were not in contact" and that the higher the arrival rate, the higher the probability that two or more adatoms will simultaneously occupy adjacent sites on the surface. Another means by which two or more adatoms may come into "contact" is through surface migration². The kinetic energy an atom must acquire to migrate on a surface is typically much lower than the energy needed to leave it.

It is common laboratory experience that cesium wets most surfaces, a good indication of $E_D^o > E_D^f$. According to Holland's review,³ additional evidence for this relation may be found in the literature.

In contrast, it is common laboratory experience that mercury does not wet many surfaces, indicating $E_D^o < E_D^f$. Glass is a notable and important example. Langmuir,^{4,5} has discussed the experiments of R. W. Wood with mercury and cadmium on glass and his own cadmium experiments, in which condensation would not proceed at room temperature unless the surface had been previously cooled with liquid air to start the first monolayer.

Therefore, in the bulk layer growth analysis, one may assume the presence of the initial cesium monolayer. In the case of mercury, the initial monolayer may not be formed without substantially exceeding the arrival rates necessary for subsequent layer growth, and the analysis is "worst case." However, in space, this worst-case condition may well exist because surface contamination may be removed by evaporation and ion sputtering, and insulating surfaces may become charged by impacting ions which may in turn enhance nucleation of droplets.

The bulk condensation of metals as a function of arrival rate and substrate temperature is readily predictable from kinetic theory and vapor pressure data, given an initial uniform coverage a few monolayers thick. Metallic vapors have unity sticking coefficient,^{4,6} so if the neutral

atom arrival rate exceeds the evaporation rate of the metal at a given sample temperature, bulk accumulation will proceed at a rate

$$dx/dt = [\Gamma_{ar} - P(T)(2\pi mkT)^{-1/2}]n^{-1} \quad (4-1)$$

where n and T refer to the condensed layer, and $P(T)$ is its vapor pressure. If, on the other hand, the arrival rate is lower than the evaporation rate, only coverages of a few monolayers or less will result. At some locations in the exhaust the arrival rate of ions is a significant fraction of the total flux. Then it is necessary to calculate an effective Γ_{ar} which accounts for sputtering and ion condensation.

The diagonal lines of Figure 4-1 are obtained from setting $dx/dt = 0$ in Equation (4-1), inserting the appropriate values⁷ for the two propellants of interest, and plotting Γ_{ar} vs $1000/T(^{\circ}K)$. Therefore, these lines are

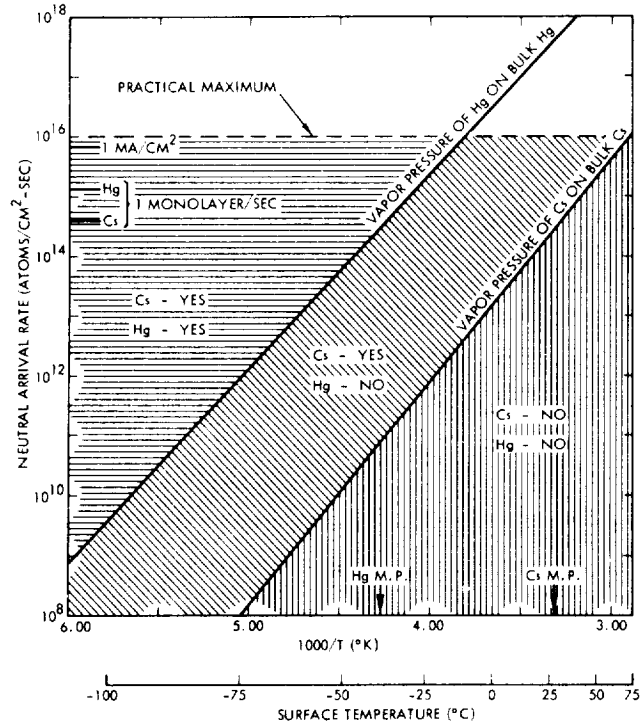


Figure 4-1. Bulk Accumulation Regions for Mercury and Cesium Atoms on Surfaces Where Adsorbed Monolayers Already Exist

the loci (Γ_{ar} , T) which produce no change in condensed layer thickness. Above them, bulk accumulation proceeds. Below them condensed layer thickness decreases until approximately one monolayer or less remains. It is seen that the region permitting bulk condensation of Cs is more extensive than for Hg. Note that in practice Γ_{ar} will not greatly exceed 10^{16} atoms/cm²-sec, which is approximately the neutral flux at the exit plane of a single thruster, and usually will be significantly lower (less than 10^{12}). At 10^7 atoms/cm²-sec, layer growth is ≈ 1 monolayer/1000 days of thrusting even in the absence of reevaporation, so this is a practical lower limit of concern for bulk condensation effects.

4.1.2 Thruster Material Deposition

As discussed in Section 3.4, ion engines emit accelerator grid material, usually a metal such as molybdenum or aluminum. Like the propellants, these metals also have sticking coefficients near unity. However, unlike the propellants, grid materials have very low vapor pressures and thus will not reevaporate from spacecraft surfaces. For this reason, grid material is often more troublesome than propellant, even though the flux emitted by the thruster is much smaller.

4.1.3 Sputtered Spacecraft Materials

This potential source of thin films is highly spacecraft design-dependent. If a spacecraft surface intrudes far enough into the exhaust hemisphere of the thruster, it will receive a significant flux of energetic Group 2 ions. The surface then becomes a secondary source of contaminants — its own materials of construction — as it is slowly eroded by sputtering. These sputtered atoms may then arrive at sensitive spacecraft surfaces.

Section 3.3 presented propellant ion distribution models from which ion arrival rate at spacecraft surfaces may be computed. Section 5 presents data concerning the rate at which surfaces may erode. Literature on sputtering is helpful in estimating the spatial distribution of sputtered atoms. Thus, arrival rates at secondary spacecraft surfaces may be estimated.

4.2 MECHANISMS OF FILM REMOVAL

Once deposited, films on spacecraft surfaces are subject to removal through evaporation, diffusion, propellant ion sputtering and sputtering by particles of the space environment. Evaporation, which is a significant process only for propellants, has been discussed in Section 4.1.1. Significant diffusion rates are also restricted to propellants, and some discussion appears in Section 7.3.3. Film removal by propellant ion sputtering may be estimated with the aid of the models of Section 3.3 and the data of Section 5. Erosion of deposited films by the solar wind, atmospheric particles (low satellite orbits) and micrometeoroid bombardment has not been investigated. It is possible that such particles might keep clean surfaces which receive very small arrival rates of ion engine effluents.

4.3 EFFECTS OF METAL FILM DEPOSITION

4.3.1 Deposition of Thruster Material on Solar Cells

Contaminant coatings on solar cell arrays affect the power output through reduction in surface transparency. Also, by altering the (solar spectrum) absorptance and (infra-red) emittance, they affect the equilibrium temperature of the array and hence, the conversion efficiency of the cells. The following is an analysis of these effects as a function of the thickness of thin films of typical accelerator grid materials deposited on various combinations of solar array surfaces. Calculations have been made using the properties of thin films of materials representative of both conventional and dielectric accelerator grids. These include: molybdenum, niobium (columbium), aluminum, aluminum oxide, and silicon dioxide.

First the thermophysical properties of opaque films of these materials are noted. Then the properties of thin films of these materials by themselves are calculated with the aid of classical optical theory. Next the properties of composite surfaces are discussed, where substrate properties and interreflections have a role. Then, with the aid of expressions for solar array temperature as a function of composite surface properties and array efficiency on array temperature, curves showing optical properties, temperature, and power output as functions of film thickness are compiled. Finally, these results are compared with experimental data derived from ground and flight tests.

4.3.1.1 Opaque Film Properties

Solar absorptance and 300°K emittance values were obtained from data available in the TRW Systems Thermophysics Section for the bulk (opaque) properties. These values, presented in Table 4-1, are used as boundary values in the analysis below:

Table 4-1. Typical Measured Values for Opaque Samples

	Solar Absorptance	300°K Emittance
Aluminum	0.12	0.04
Molybdenum	0.36	0.04
Niobium	0.56	0.13
SiO ₂	0.02	0.80
Al ₂ O ₃	0.02	0.60-0.80

4.3.1.2 Thin Metal Film Properties

Calculation of the optical properties of thin films is discussed in detail in the American Institute of Physics Handbook.⁹ The complex equations given there may be used to calculate theoretical values of the spectral reflectance, absorptance, and transmittance of thin films as functions of index of refraction, n , and extinction coefficient, k . The case (II) of a thin absorbent film which lies between an incident dielectric medium and a massive absorbent substrate is applicable to the problem of accelerator grid material deposited on spacecraft surfaces. Given particular values for refractive indices of the media, and the incident wavelength, a simple machine code for these equations prints tables of reflectance R , transmittance T , and absorptance A versus film thickness.

Optical properties were calculated to a first approximation for various thicknesses of the metals molybdenum, niobium and aluminum using n and k values from the literature. The procedure required for each metal depended upon the amount of data available. The values of n and k at $\lambda = 0.75 \mu\text{m}$ for aluminum ($n = 1.8$, $k = 7.12$) were used to calculate solar reflectance, transmittance and absorptance. This wavelength was used since it is near the median wavelength of the solar power distribution. The results are shown in Table 4-2.

Table 4-2. Aluminum - Solar Region - on Glass
 $n = 1.8$, $k = 7.12$, $\lambda = 0.75 \text{ m}$

Thickness	Reflectance (percent)	Transmittance (percent)	Absorptance (percent)
1 Å	4.3	94.4	1.3
10	9.0	79.6	11.4
30	25.0	52.3	22.7
100	62.9	14.2	22.9
300	76.3	10.0	13.7
1000	87.7	0.	12.3

The 1000 Å thickness value compares well with a typical solar absorptance of vacuum deposited aluminum of 0.12, as shown in Table 4-1.

It is reported in the literature that very thin films ($< 100 \text{ Å}$) do not obey the simple theory¹⁰. The invalid assumption of the theory is that the thin films are uniform and continuous. Actually in the initial stages of the film growth, the atoms tend to form aggregates. The geometry of these nuclei depends upon the various parameters of the deposition such as the rate, angle of incidence, kinetic energy of atoms and the conditions of the substrate such as roughness of the surface and temperature, among others. In general, the nucleation produces films having a higher transmittance and lower reflectance than uniform, continuous films of equal average thickness (assuming a highly absorbing metal film). Thus, the films will actually have higher transmittance and lower reflectance than the simple theory predicts. The effect upon absorptance is not so straightforward, and it is here that more experimental data would be most welcome.

In order to illustrate the deviation of actual films from the simple theory, Table 4-3 presents some experimental data from W. Walkenhorst¹¹ as reprinted in Reference 12.

Table 4-3. Aluminum — Solar Region — on Fluorspar
Measured by Walkenhorst, $\lambda = 0.500\mu\text{m}$

Thickness	Reflectance (percent)	Transmittance (percent)	Absorptance (percent)
1 Å	4	95	1
10	6	85	9
100	66	12	22
1000	88	0	12

These results compare favorably with the calculated values of Table 4-2. The films were carefully prepared to produce as smooth and continuous films as possible.

Values of n and k as functions of wavelength for niobium are much more scarce than those for aluminum. The computer program was used to calculate the properties with one available set of data: $n = 1.8$, $k = 2.11$, $\lambda = 0.579\mu\text{m}$. Using these values, the calculation gave an absorptance for a nearly opaque layer almost the same as the solar absorptance of a sample of bulk niobium. At first glance, this seems strange since $0.579\mu\text{m}$ is considerably below the center of the solar irradiance function. The spectral reflectance of niobium, however, remains fairly constant over a large part of the solar spectrum including $0.579\mu\text{m}$, so that one has input data for calculations which will yield usable engineering values of optical properties. The results are presented in Table 4-4.

Table 4-4. Niobium — Solar Region — on Glass
 $n = 1.8$, $k = 2.11$, $\lambda = 0.579\mu\text{m}$

Thickness	Reflectance (percent)	Transmittance (percent)	Absorptance (percent)
1 Å	4.3	95.2	0.5
10	5.3	89.8	4.9
100	16.8	53.2	30.3
200	27.9	32.6	39.5
1000	41.9	1.0	57.1

The 1000 Å thickness value compares well with the data for bulk niobium, $\alpha_s = 0.56$.

The same procedure was tried with short wavelength data on molybdenum. This time, however, the absorptance value for the opaque layer did not agree with the solar absorptance of bulk molybdenum. Therefore the values of n and k were extrapolated until an opaque film absorptance was obtained which agreed reasonably well with that of bulk molybdenum. The resulting data are shown in Table 4-5.

Table 4-5. Molybdenum - Solar Region - on Glass
 $n = 3$, $k = 4$, (Extrapolated Values)
 $\lambda = 0.82 \mu\text{m}$

Thickness	Reflectance (percent)	Transmittance (percent)	Absorptance (percent)
1 Å	4.2	94.6	1.2
10	6.5	83.2	10.2
30	12.3	64.1	23.6
100	30.7	30.8	38.5
300	57.0	7.4	35.6
1000	62.6	0.1	37.3

The 1000 Å thickness value has been made to compare well with the data for bulk molybdenum: $\alpha_s = 0.36$.

The data presented in Tables 4-2 and 4-5 are for the films on glass. This information is especially useful for evaluating the transmittance of thin films. However, evaluation of the effective value of solar absorptance and infrared emittance of a composite surface, consisting of a semi-transparent film on an opaque substrate, requires that the properties of both the film and the substrate be taken into account. The following describes the required calculational procedures.

4.3.1.3 Composite Surface Properties

The foregoing calculations gave the solar absorptance, reflectance and transmittance for thin films of the metals aluminum, molybdenum and niobium on glass. These results have been combined with the properties of solar cells to obtain the composite properties. The following general equations were used to calculate these values:

We consider a thin metallic film deposited on the surface of a solar cell cover glass. We assume the glass to be transparent, and bonded to an opaque, absorbing substrate. Accordingly, light which passes through the film will undergo reflection and absorption at the film and also at the glass-substrate interface. Reflected rays within the glass are again partially reflected, transmitted and absorbed at the glass-film interface. The total reflectance at the composite surface is then given by

$$R_t = R_1 + T_1^2 R_2 + T_1^2 R_2^2 R_1 + T_1^2 R_2^3 R_1^2 + \dots \quad (4-2)$$

$$= R_1 + T_1^2 R_2 [1 + R_1 R_2 + R_1^2 R_2^2 + \dots] \quad (4-3)$$

$$= R_1 + T_1^2 R_2 \left[\frac{1}{1 - R_1 R_2} \right] \quad (4-4)$$

and the total absorptance is given by

$$A_t = 1 - R_t \quad (4-5)$$

The total absorptance may also be expressed as the sum of the absorptances of the individual elements of the composite surface. Since A_1 of the light is absorbed when it passes through the thin film in either direction, the total absorptance of the film in a composite is:

$$A_{1t} = A_1 + T_1 A_1 R_2 [1 + R_1 R_2 + R_1^2 R_2^2 + \dots] \quad (4-6)$$

$$= A_1 [1 + T_1 R_2 M] \quad (4-7)$$

where

$$M = \frac{1}{1 - R_1 R_2} \quad (4-8)$$

Similarly, the total absorptance of the opaque substrate (including that arising from multiple reflections within the glass) is:

$$A_{2_t} = T_1 A_2 [1 + R_1 R_2 + R_1^2 R_2^2 + \dots] \quad (4-9)$$

$$= T_1 A_2 M \quad (4-10)$$

The total absorptance of the composite must be the sum of the absorptances of its elements:

$$\begin{aligned} A_t &= A_{1_t} + A_{2_t} = A_1 + T_1 M (R_2 A_1 + A_2) \\ &= \alpha_{\text{composite}} \end{aligned} \quad (4-11)$$

The following results (Tables 4-6 through 4-8) were calculated with Equation (4-11) using 0.78 for A_2 , and 0.22 for R_2 , typical absorptance and reflectance values for solar cells:

Table 4-6. Niobium - Solar Region - on Solar Cell

Thickness	α_{Nb}	T_{Nb}	$\alpha_{\text{composite}}$
0 Å			0.780
1	0.005	0.952	0.756
10	0.049	0.898	0.767
100	0.303	0.532	0.770
1000	0.571	0.010	0.581

Table 4-7. Molybdenum - Solar Region - on Solar Cell

Thickness	α_{Mo}	T_{Mo}	$\alpha_{\text{composite}}$
0 Å			0.780
1	0.012	0.946	0.759
10	0.102	0.832	0.759
100	0.385	0.308	0.671
1000	0.373	0.001	0.374

Table 4-8. Aluminum - Solar Region - on Solar Cell

Thickness	α_{Al}	T_{Al}	$\alpha_{\text{composite}}$
0 Å			0.780
1	0.013	0.944	0.759
10	0.114	0.796	0.768
100	0.229	0.142	0.366
1000	0.123	0.0	0.123

Calculations of the infrared emittance of the composite aluminum on quartz were made at two wavelengths, 7 and 12 microns. These wavelengths were selected as being representative for quartz which has a restrahlen at 9 microns. Quartz is representative of solar cell cover glass, and, since $T \approx 0$ in the infrared, also glass covered solar cells, optical lenses, etc. (Table 4-9).

Table 4-9. Aluminum - Infrared Region - on Quartz

Normal Emittance, ϵ_N			
Film Thickness	$\lambda = 7\mu$	$\lambda = 12\mu$	Total*
1 Å	0.93	0.81	0.84
3	0.83	0.71	0.74
10	0.64	0.46	0.50
30	0.24	0.23	0.23
100	0.08	0.07	0.07
300	0.03	0.03	0.03
1000	0.02	0.02	0.02

*Based on a weighted average of 7 and 12 microns data of 25 percent and 75 percent, respectively.

Since no infrared data were found for other metals of interest, further calculations have not been made. However, the present data provide general information which can be used in a qualitative examination of problem areas.

4.3.1.4 Thin Dielectric Film Properties

The possible use of Al_2O_3 or SiO_2 coatings on thruster grids raises the possibility of thin films of these dielectrics being deposited on the spacecraft components.

When these materials are deposited under conditions favoring low contamination, they are nonabsorbing in the solar region. In other words, deposited layers of pure SiO_2 or Al_2O_3 would not affect the solar absorptance, at least under ideal conditions of deposition. If the actual conditions of deposition introduced impurities, as would be the case with dielectric grid sputtering, it is possible that solar absorptance would be affected synergistically. Experimental data would be required to assess the magnitude of such an effect.

The emittance of these dielectrics is high, and would not adversely affect solar cell cover glasses or paints. However, if they were deposited on metals used for their low emittance characteristics, these surfaces would be affected as dielectric thickness increased, since the emittance would increase.

4.3.1.5 Effect of Thin Metal Films on Solar Cell Power

In previous sections calculations were presented indicating the effects of semi-transparent films of thruster (accelerator grid) materials (or metals sputtered from spacecraft surfaces) on the optical and thermo-physical properties of spacecraft surfaces. In particular, changes in the solar absorptance and infrared emittance of glass covered solar cells caused by various thicknesses of Al, Mo, and Nb were considered. For these calculations, the analysis of Hass and Hadley⁹ was used to calculate film properties, and an equation was derived [Equation (4-11)] for the composite solar absorptance, taking into account the effect of multiple reflections within the cover glass. Changes in emittance were calculated from available infrared data for aluminum.

The above functional relationships, together with two functions relating to solar-cell temperature, have been combined in a computer program which calculates solar-cell temperature and maximum available power output as functions of film thickness. The first of these auxiliary functions gives solar array temperature T in °K.

$$T = \left[\frac{G(r)}{\sigma} \cdot \frac{\alpha_f}{\epsilon_f + \epsilon_b} \right]^{1/4} \quad (4-12)$$

where

$G(r)$ is the density of power arriving from the sun
[$1400/r^2$ (watts/meter²)]

σ is the Stefan Boltzmann constant

α_f is the solar absorptance of the illuminated
side of the array

ϵ_f is the hemispherical emittance of the illuminated
side of the array

ϵ_b is the hemispherical emittance of the dark side
of the array

r is the solar distance in astronomical units (AU).

This expression is derived from heat balance considerations and the following assumptions:

- 1) There is no lateral heat conduction in the array.
- 2) There is no radiant heat load from other spacecraft surfaces, or from planets and their atmospheres.
- 3) The array surface is normal to the sun line.
- 4) Illuminated and dark surfaces of the array are at the same temperature.
- 5) The fraction of solar energy that is converted into electrical energy is negligible.

Assumptions (1) and (4) are especially valid for the lightweight arrays likely to be employed on electrically propelled spacecraft. The validity of the first assumption also means that the expected variation in film thickness with distance from the thruster(s) need not be introduced into the analysis; at any given array location the solar cell degradation will be that predicted for arrays with films of that thickness.

With reference to the fifth assumption, solar cell conversion efficiencies are typically 10 percent and therefore negligible at least during the initial stages of analysis.

The second relationship required is the normalized maximum available power from a solar cell as a function of cell temperature. The function used was obtained from data in Reference 13, which is an extensive

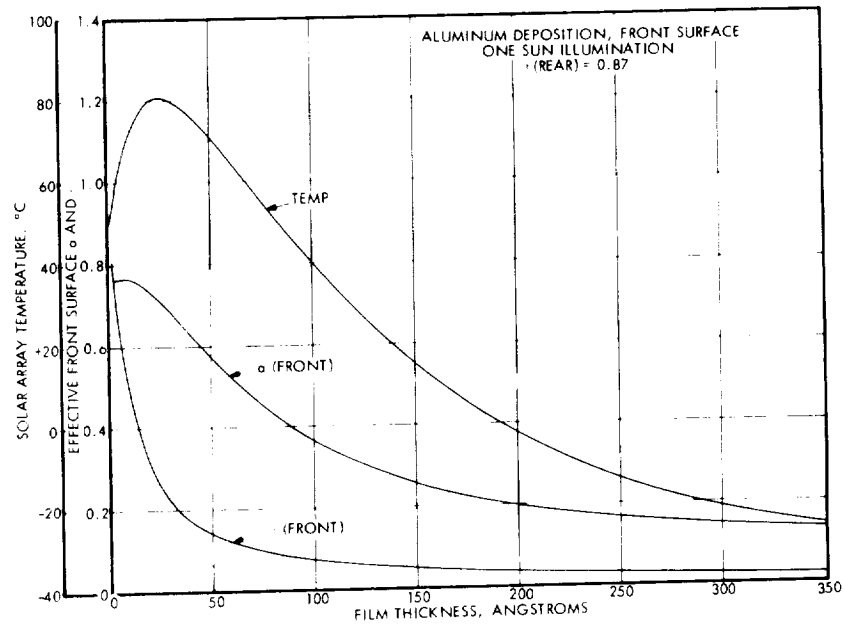
unpublished compilation of laboratory measurements and calculations used in the design of a solar cell array for an extended Pioneer spacecraft mission. A plot was made of maximum power points on the current-voltage curves for a typical solar cell at cell temperatures ranging from 18° to 150°C and "one-sun" illumination. The plot is very nearly a linear function over the range of experimental values, and can be normalized to any point within its interval of definition. It was normalized to 54°C, the equilibrium temperature of the clean array computed with Equation (4-12):

$$\frac{P}{P(54^{\circ}\text{C})} = 1.2734 - 0.0050634 T (^{\circ}\text{C}) \quad (4-13)$$

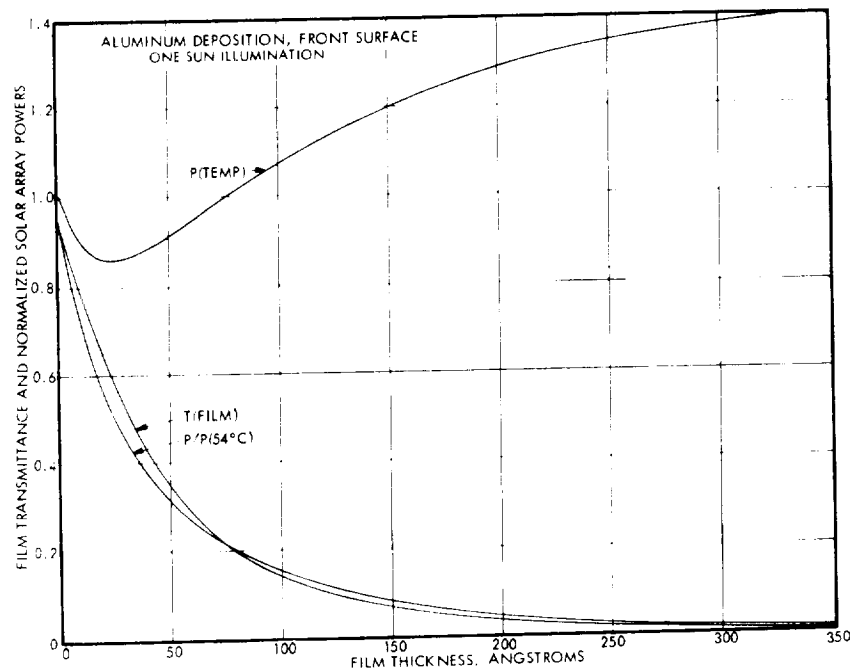
At several values of film thickness, the program computes film properties: reflectance R(FILM), transmittance T(FILM), and absorptance A(FILM), surface emissivities ϵ (FRONT) and ϵ (BACK), composite absorptance α (FRONT), the resulting panel temperature TEMP in °C, normalized power dependence P(TEMP), and finally, the net power $P/P(54^{\circ}\text{C})$ which is the product of the transmittance of the film on the front surface and the P(TEMP) function. These values are all printed out so that the relative importance of the various factors in determining available power may be assessed. Three cases have been run for each of two film materials, aluminum and molybdenum:

- I. Coating on solar-cell surface only
- II. Coating on rear surface of panel only
- III. Coatings of equal thickness on both surfaces.

The results are shown in the curves, Figures 4-2 through 4-7.



(a) Solar absorptance α and infrared emittance ϵ of the front surface, and resultant panel temperature under one-sun illumination



(b) Film transmittance $T(\text{FILM})$, temperature effect on solar cell energy conversion efficiency $P(\text{TEMP})$, and maximum available power $P/P(54^\circ\text{C})$. The latter two are normalized to the zero-film thickness temperature of 54°C .

Figure 4-2. Effects of Deposition of a Uniform Film of Aluminum on the Illuminated (Front) Surface of a Solar-Cell Panel

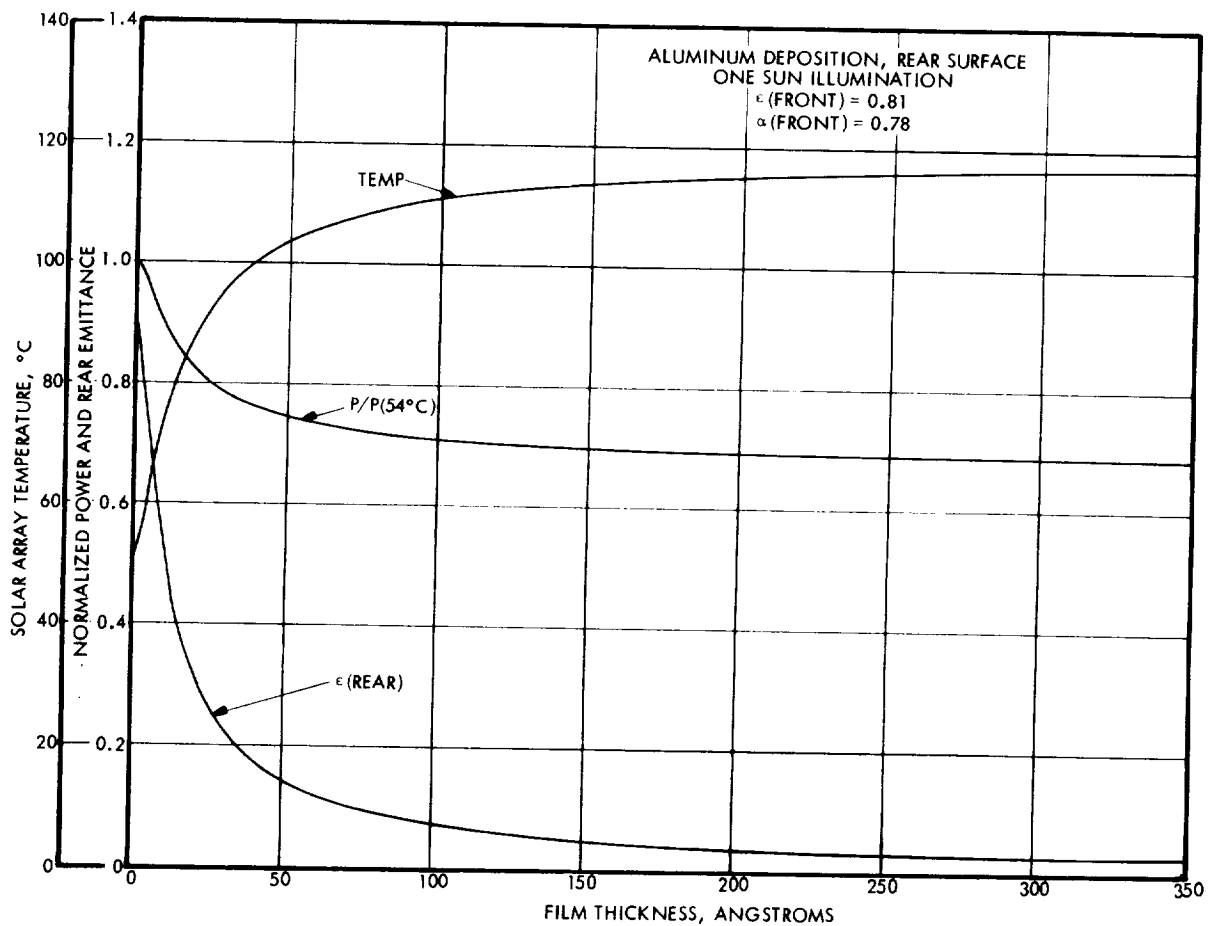
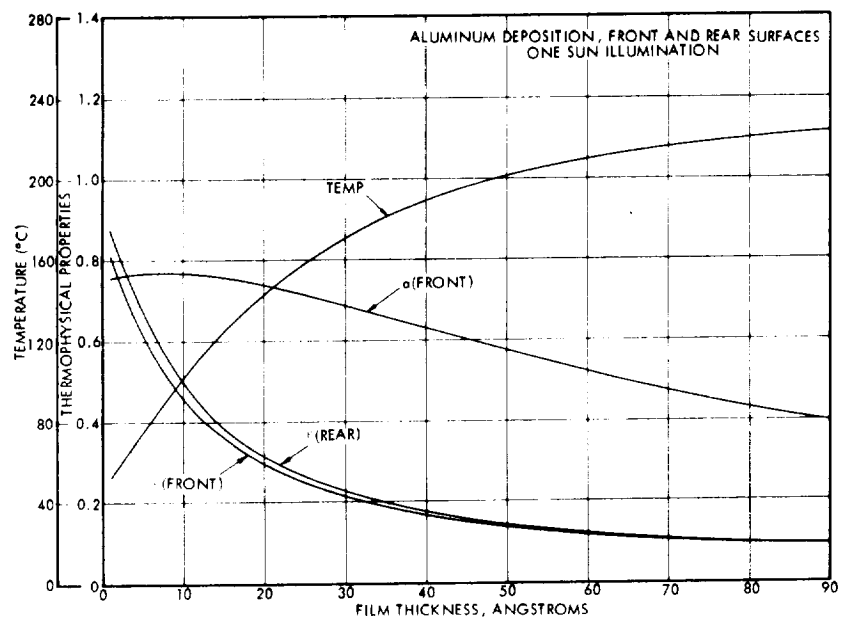
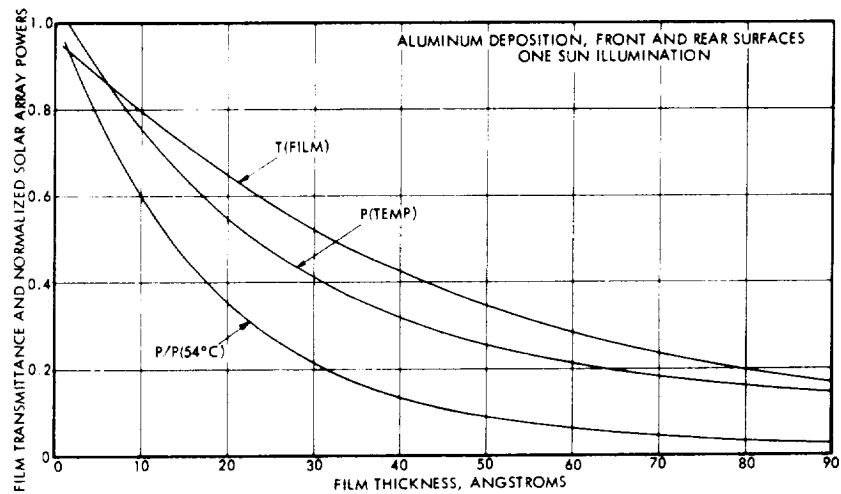


Figure 4-3. Effects of Uniform Aluminum Film Deposition on Nonilluminated (Rear) Surface. The reflective film reduces heat radiation and causes a reduction in power through an increase in solar cell temperature.

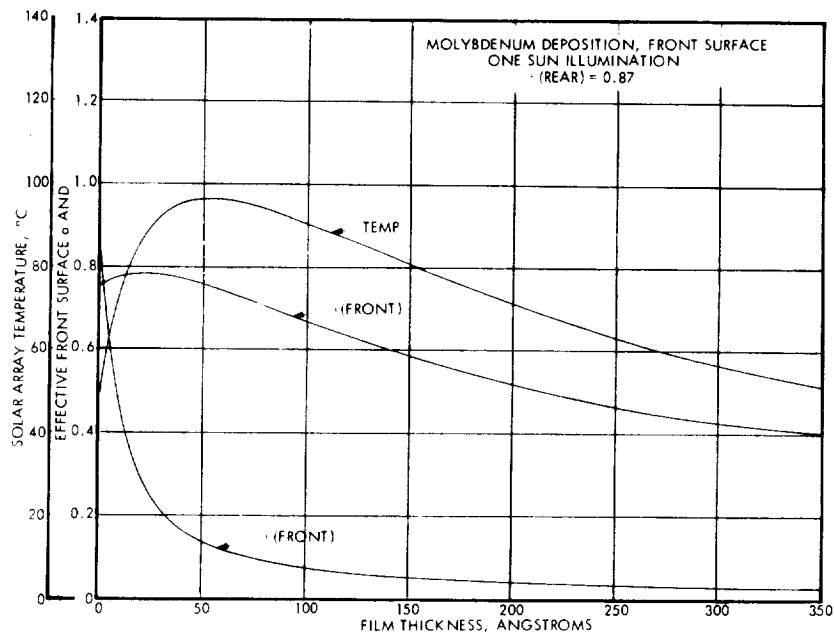


(a)

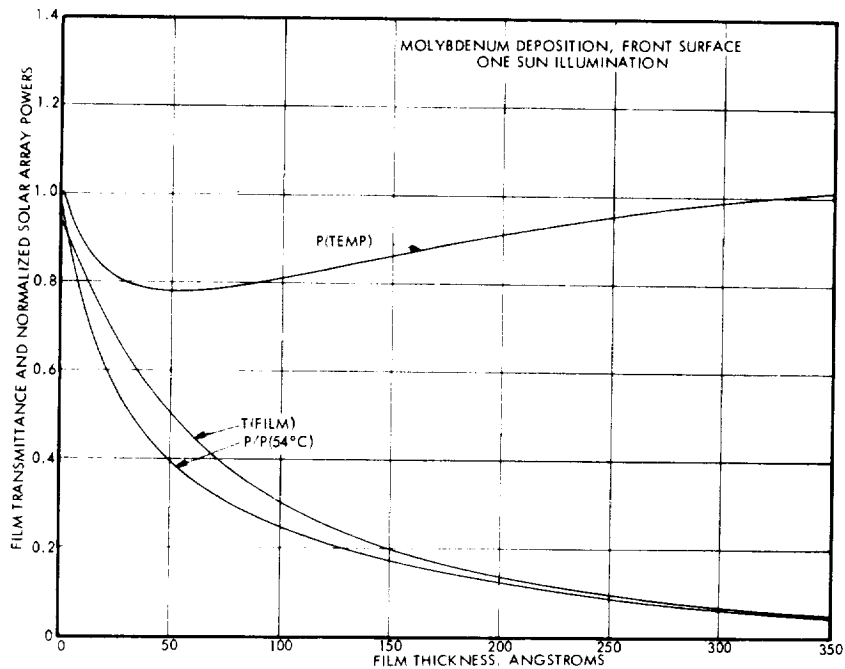


(b)

Figure 4-4. Effects of Equal and Uniform Aluminum Film Deposition on Both Front and Rear Surfaces. This case combines the effects of those in Figures 4-2 and 4-3.



(a)



(b)

Figure 4-5. Effects of Uniform Molybdenum Film on Illuminated (Front) Surface of Solar-Cell Panel. This case may be compared with that of Figure 4-2.

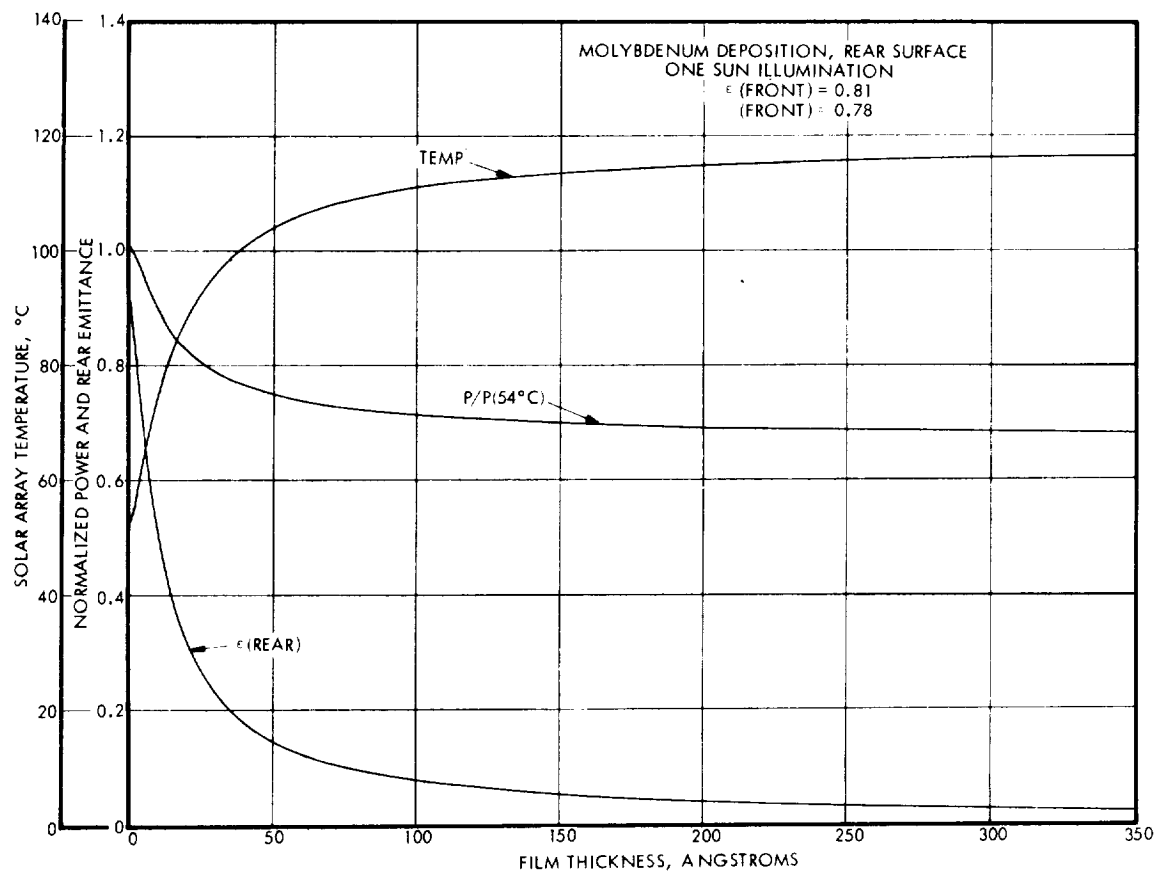
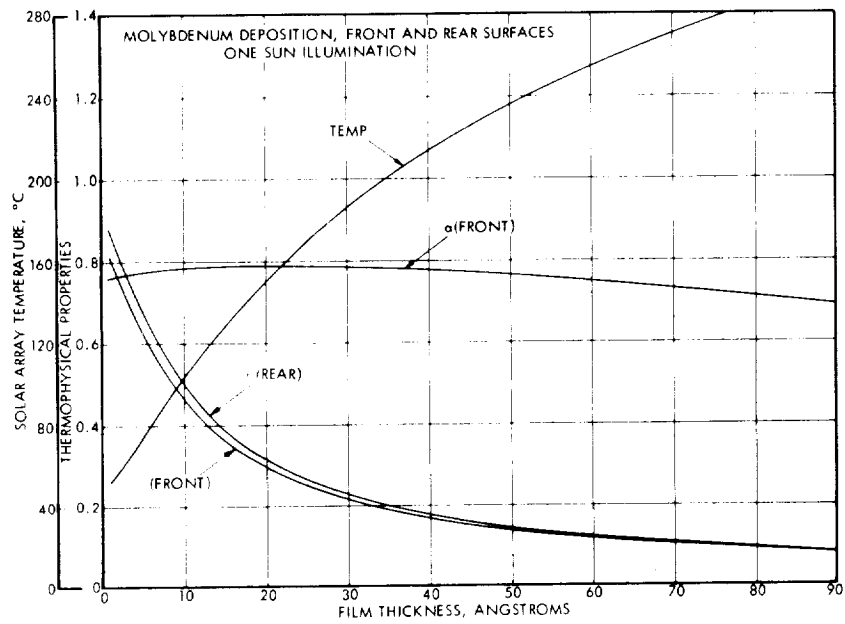
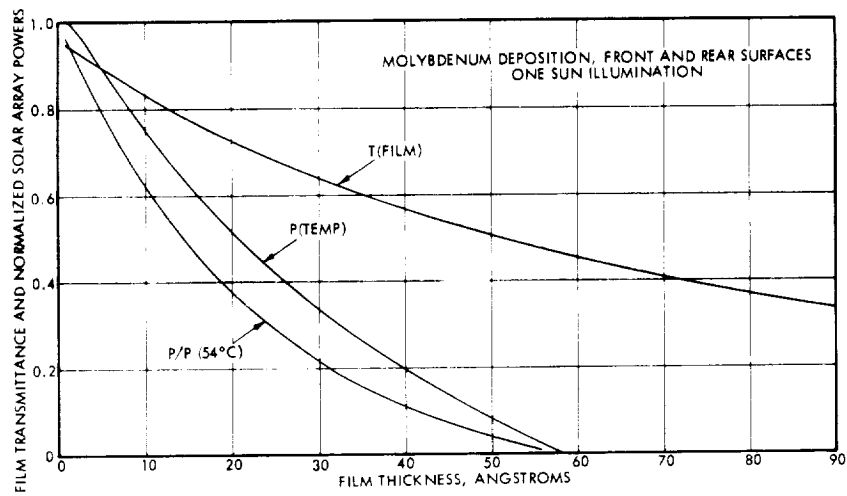


Figure 4-6. Effects of Uniform Molybdenum Film Deposited on Nonilluminated (Rear) Surface of Solar-Cell Panel. Compare with Figure 4-3.



(a)



(b)

Figure 4-7. Effects of Molybdenum Film Deposited on Both Front and Rear Surfaces of Solar-Cell Panel. Compare with Figure 4-4.

In order to achieve a consistent set of results for the calculations, the following input values and assumptions were used: A nominal "one-sun" illumination was assumed throughout.* Input values for the Hass-Hadley function are given in Table 4-10 below, for the several combinations of materials. Absorptance of the glass-covered solar cell in the absence of a contaminating film was taken as 0.78; emittances of the glass surface and of white paint were given values of 0.81 and 0.87, respectively. Accordingly, the equilibrium temperature for the clean solar panel was 54°C, and this temperature was used for normalization of the solar cell power function P(TEMP). Emittances were calculated as for Table 4-9. For the front surface, only the $\lambda=12\mu\text{m}$ aluminum film properties were used and for the back surface averages of the $\lambda=7\mu\text{m}$ and $\lambda=12\mu\text{m}$ properties were used, inasmuch as these functions have the appropriate values in the limit of zero film thickness. Also, in the absence of infrared data for molybdenum, the infrared data for aluminum were used for both film materials. This is considered reasonable for purposes of these calculations, since the total emittance of both materials is similar.

Table 4-10. Input Values for Computation of Film Properties

Material	Wavelength (μm)	Refractive Index				
		Incident Medium n_o	Film n_1	Material k_1	Substrate n_2	k_2
Aluminum	0.75	1.0	1.8	7.12	1.5	0.0
Aluminum	7.0	1.0	17.9	55.3	1.5	0.0
Aluminum	12.0	1.0	33.1	78.0	2.2	0.2
Molybdenum	0.82	1.0	3.0	4.0	1.5	0.0

*These calculations may, in principle, be extrapolated to the case of reduced solar illumination (e.g., a spacecraft more than 1 AU from the sun). However, the data of Reference 13 indicate that at enhanced levels of illumination much above "one sun", the proportionality between maximum power and illumination will be considerably reduced.

The curves clearly show the relative importance of the several effects of a thin-film coating on a solar-cell array in the overall reduction in available power. In the first case, although the emittance is changing more rapidly than the composite absorptance, it is the transmittance of the film which is clearly dominant in reducing the amount of light available for conversion to electrical power. With a film on the rear surface only, the emissivity of the rear surface is the only property affected; hence, the reduction in output is due to the corresponding changes in temperature, and is equal to the $P(\text{TEMP})$ function. This is the least deleterious of the three cases. With both surfaces coated, the effects of emittance dominate by causing a pronounced temperature excursion which drives the cell efficiency down, whereas film transmittance has had a relatively smaller effect on the amount of light available. The combined effects of coatings on both front and back surfaces cause very severe power loss from the cells affected. In comparing the results of front surface coating between the aluminum and molybdenum cases, it is interesting to note that the temperature rise is greater and more persistent with the molybdenum film, but the reduced transparency of aluminum at the same thickness is dominant, so that aluminum causes the more severe power loss.

4.3.1.6 Comparison of Measured and Predicted Thin Film Transmittance

The results of an analysis of the effects of thin films of aluminum and molybdenum on solar cell performance are presented in the previous section. They indicate that films only a few monolayers thick can seriously degrade solar cell output. However, this analysis assumes that the films are uniform and continuous, whereas thin film experiments often indicate that atoms cluster in nuclei during initial stages of film growth¹⁰. Thus, a question is raised about the validity of these results in the region of greatest interest: thickness less than ~ 100 Å.

Few experimental data are available in the literature for comparison with the theoretical analysis. However, thin film transmission data from three papers have been evaluated. These comparisons increase confidence in the engineering value of the theoretical calculations above.

The first paper is that of Walkenhorst¹¹, published in 1941. He measured the transmittance and reflectance of aluminum films; Figure 4-8

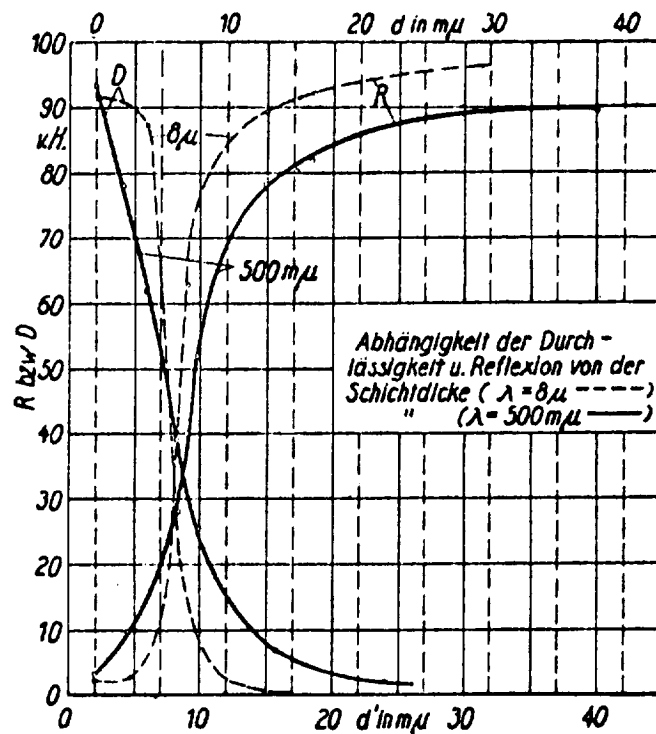


Figure 4-8. Dependence of the Transmittance and Reflectance on Film Thickness ($\lambda = 8\mu$ -----, $\lambda = 500m\mu$ ———). Reprinted from Walkenhorst, Reference 11.

is from his original paper. His results are quoted directly or indirectly in subsequent textbooks, e. g., Heavens¹² and Holland¹⁴ (between whom there is an apparent discrepancy*). Figure 4-9 shows the Walkenhorst curve (vs. d) and our calculated curves for transmittance of both aluminum and molybdenum (from Figures 4-2 and 4-5) plotted on the same scales.

Such curves, either experimental or calculated, should be regarded as approximations, at best, to the total performance of a given contaminant film under solar illumination, inasmuch as they represent film

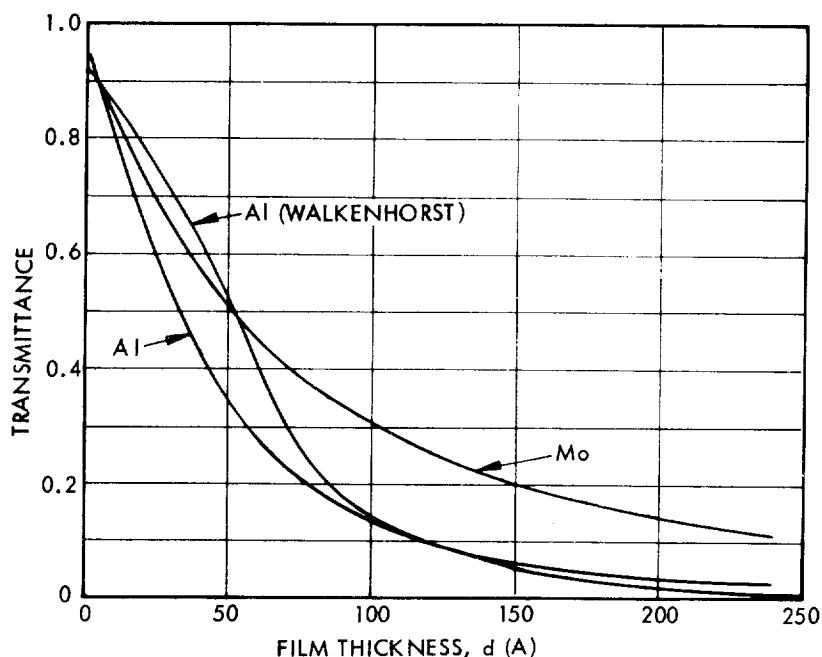


Figure 4-9. Transmittance as a Function of Film Thickness of Thin Metallic Films. The Walkenhorst curve is from experimental data. The curves for aluminum and molybdenum were calculated using the Hass-Hadley equations.

*In Walkenhorst's figure, two abscissa scales, d and d' , are given with an offset of 20 Å, where d is the effective film thickness and d' is the thickness determined from weighing, which includes the oxide layer that forms rapidly on exposure to air. Heavens shows a plot of R and T vs d , whereas Holland has a table of values of R and T vs values of d' .

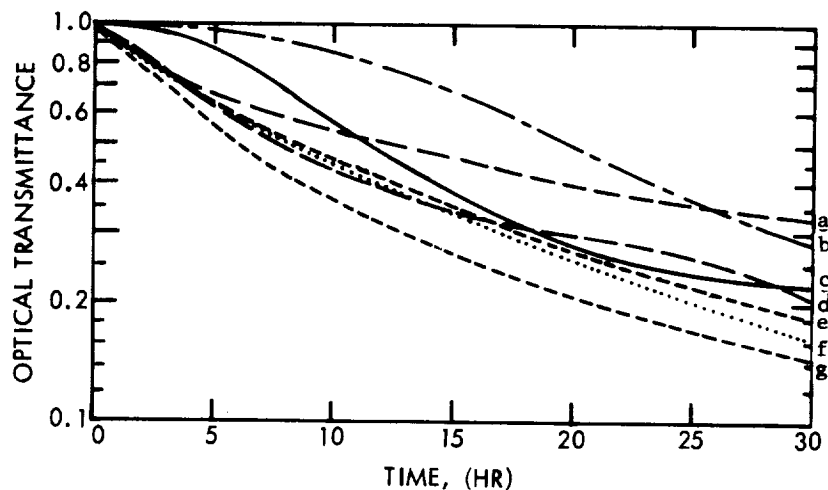
properties for only one wavelength of light and for only one angle of incidence (usually normal). The curves of Figure 4-9 show reasonably good overall agreement and very good agreement between the Mo curve and the Walkenhurst curve for Al at small thicknesses, and between the two Al curves at thicknesses above about 80 angstroms. Nevertheless, the generally good agreement between the Mo curve and the SERT II results, discussed below, is probably the best confirmation to date of the usefulness of the calculated curve for engineering predictions of solar panel performance during the early stages of spacecraft design.

The second and third papers report solar cell degradation experiments. They have been carefully reviewed and their results compared with our analytical predictions. Very good agreement is obtained.

One of the experiments was incorporated in the flight test of the SERT II spacecraft¹⁵. Details and results of the experiment are reported in Reference 16. In brief, the SERT II spacecraft carried two mercury electron-bombardment thrusters. Associated with each thruster were two small arrays of solar cells mounted about 4 thruster radii from each thrust beam axis and about 2 thruster radii downstream, so as to be illuminated by the sun, yet subject to contamination from thruster effluent. For each thruster, one array was held at about -40°C temperature, and the other at about $+60^{\circ}\text{C}$; hence, they were known as the Lo-temp and Hi-temp sensors, respectively. Short-circuit currents of the four arrays were measured as functions of time and were seen to drop to about 50 percent of initial value in 6 to 12 hours of thruster operating time (Curves a, d, e, and g, Figure 4-10).

The other experiment, also a part of the SERT II program, was a ground-test experiment performed at the NASA, LeRC facility in which small solar-cell arrays similar to those used in the space experiment were subjected to contaminant efflux from ion engines. Details of this experiment, and comparison of the results with those from the SERT II flight are given in Reference 17.

Both the ground test and the spaceflight results clearly indicate that degradation in the performance of solar cells, at these temperatures and locations relative to the thruster, was not due to mercury condensation, but to the deposition of molybdenum (or other constituents)



Curve	Source of Curve
a	SERT II result, Lo-temp sensor No. 1, Ref. 16
b	Prediction for SERT II flight based on silver experimental data and arrival rate of 3.4 angstroms/hour, Ref. 16
c	Thruster-solar cell, ground test, NASA/LeRC, Ref. 17
d	SERT II flight, Lo-temp sensor No. 2, Ref. 16
e	SERT II flight, Hi-temp sensor No. 1, Ref. 16
f	Theoretical, this paper (Figure 4-5b) and assumed arrival rate of 6 angstroms/hour
g	SERT II flight, Hi-temp sensor No. 2, Ref. 16

Figure 4-10. Comparison of Transmittance-Time Curves of Flight Tests, Ground Tests, and Theoretical Predictions.

sputtered from the accelerator grid. Assuming a cosine normal distribution of this material, authors of both References 16 and 17 utilize the view factor, $F = \mu/\nu$, which is the ratio of arrival rate of particles at the given surface to emission rate at the source. F is a function of angle from the source normal to the point in the test surface, distance to the surface, and orientation of the surface to the direction of arriving particles. The view factors in both sets of experiments were between 0.016 and 0.019.

Using 0.00327×0.253 amp as the estimated current of charge exchange ions, and a unity sputtering yield, Staskus and Burns¹⁶ predicted an accumulation rate of 1.37 monolayers of molybdenum per hour (3.4 angstroms/hour). Then, using data on optical transmission of silver films¹⁰ they predicted a curve of relative solar-cell output current versus time (Curve b, Figure 4-10).

As discussed below, the 3.4 Å/hr accumulation rate prediction was probably low. Further, the transmission versus thickness relation used had a much smaller slope over the 0 to 50 Å range than do the curves in Figure 4-9. These facts explain why Curve b of Figure 4-10 is above the others.

In Reference 17, Reynolds and Richley compare the results of the laboratory experiment with the SERT II results. Figure 4-10 is taken from Figure 17 of that report; curve c is the relative solar-cell current versus time (Curves b and f have been added here). In their discussion, authors of Reference 17 make several points regarding this comparison:

"There were several differences in operating parameters between the two experiments which probably make any detailed comparisons in performance meaningless. For example, startup procedures, operating current densities, voltages, and acceleration grid material differed. The geometric view factors, however, were similar in spite of the large differences in thruster size. The slow initial drop in transmittance observed in the present experiment may be due to the starting conditions, where the ion beam was on for a considerably smaller fraction of the elapsed time as a result of the initial arcing problems." (Italics added.) This explains why Curve c of Figure 4-9 is initial above all but Curve b (which is discussed above).

"The difference in contamination rates between the high- and low-temperature sensors of the flight experiment probably is due to the higher localized grid sputtering rate in the region of the neutralizer."

The authors then note that in the flight experiment, solar array output decreased to 50 percent of the initial value in 6 to 12 hours, and from this deduce an arrival rate corresponding to 5.8 to 11.6 angstroms/hour. This arrival rate is higher than the 3.4 angstroms/hour estimated by Staskus from Staggs' calculation of charge exchange production rate¹⁸.

Finally, a comparison may be made among the SERT II flight-test data, the ground-test experiment of Reference 17, and solar-cell performance calculations shown in Section 4.2.1.5. One of these curves is almost directly applicable to the SERT II result as follows: The sputtered material deposited on the SERT II sensors was molybdenum.

The sensors were held at constant temperature; hence, power output (or short-circuit current) is a function of film transmittance (illuminating intensity) only. The curve T (film), Figure 4-5b gives the transmittance of molybdenum film as a function of film thickness; this curve is replotted as curve f of Figure 4-10 as a function of time, assuming a constant rate of deposit of 6 angstroms/hour. (For comparison with experimental data, this is to some extent incorrect, inasmuch as the operating schedule of the SERT II thrusters did not provide for constant current versus time, especially during the first few hours of operation.) This curve is a sufficiently good fit to the SERT II data (Curves a, d, e, and g) to suggest that the method outlined in Section 4.2.1.5 may be useful in engineering calculations of solar array performance, particularly in the early phases of spacecraft configuration selection.

It will be recalled that the data used in generating the curve for molybdenum used values of $n = 3.0$ and $k = 4.0$ at $\lambda = 0.82 \mu\text{m}$ (See Table 4-10). This wavelength is well within the spectral sensitivity band of solar cells, and use of this curve as above assumes that the performance of the cell at this wavelength is typical of the cell behavior in general. The agreement cited above is some experimental evidence that this may be so. It is also evident that the question of uniformity versus clustering of atoms in very thin films may be irrelevant, inasmuch as calculations based on the assumption of uniformity give results which agree with experimental data.

4.3.1.7 Conclusions

Theoretical analysis of the effects of semitransparent films of ion engine grid materials on spacecraft optical elements (e.g., lenses, solar cells, and thermal control surfaces) indicates that often films only a few monolayers thick will significantly affect element performance.

Calculations of the degradation in solar cell output caused by depositions of aluminum and molybdenum provide impressive examples of the sensitivity of some spacecraft subsystems to metallic contaminants. They predict that 10 \AA (~ 4 monolayers) of molybdenum on a solar cell at 1 A.U. will degrade its output by approximately 50 percent! Even

depositions as thin as 50 Å on the dark side of an array can reduce the output of the affected area by 25 percent through cell heating effects.

Comparison of these theoretical predictions with available experimental data have shown general agreement, despite the potential inaccuracy of the theory for very thin films.

4.3.2 Propellant Condensation on Solar Arrays

When propellant condenses on a solar array the change in surface thermal properties and resulting change in array temperature greatly affect the propellant re-evaporation rate. The following sections illustrate a first order analytical approach to this effect and conditions which may produce problems.

4.3.2.1 Opaque Propellant Film Properties

The optical properties of Cs and Hg used in the analysis appear in Table 4-11. (They were obtained by a careful review of the experimental literature and available theories.) The solar absorptance of Hg is derived from the Zener-Drude free electron theory of metals,^{19,20} which is in reasonable agreement with the best experimental data at 0.546 μ. The solar absorptance of Cs is based on the data of Ives and Briggs²¹ and Nathanson²² over the 0.25 to 0.7 μ range and an extrapolation of these data to longer wavelengths. The hemispherical emittances of both propellants are calculated from the theory of Parker and Abbott²³. These theoretical values that will be discussed in Section 8.3.4.4 may be in error for propellants arriving at targets below their respective freezing points because of surface roughness.

Table 4-11. Surface Thermal Properties of Opaque Hg and Cs

T, °K	State	ε _H	α _s
Hg 234	Solid	0.055	0.22 ± 0.05
235	Liquid	0.10	0.22 ± 0.05
248	Liquid	0.105	0.22 ± 0.05
298	Liquid	0.12	0.22 ± 0.05
373	Liquid	0.13	0.22 ± 0.05
Cs 248	Solid	0.02	0.25 ± 0.05
301	Solid	0.03	0.25 ± 0.05
302	Liquid	0.04	0.25 ± 0.05
373	Liquid	0.05	0.25 ± 0.05

4.3.2.2 Effects of Condensed Layers on Spacecraft Surfaces

Knowledge of the approximate values of the surface thermal properties of opaque mercury and cesium allows the following analytical description of the boundary conditions for, and rates of condensation, of these metals on various spacecraft surfaces. Only the effects of substituting these new surface thermal values for those of an uncontaminated spacecraft are considered. The Boeing Large Area Solar Array²⁴ has been chosen as a typical spacecraft surface undergoing atom impingement, but the analysis is fairly general, and the method is applicable to many other spacecraft surfaces.

Array temperature is again computed with Equation (4-12). As shown in Figure 4-1, the flux of arriving particles necessary to sustain a condensed layer is strongly dependent on the layer temperature. For the purposes of analysis these equilibrium curves may be expressed by

$$\log_{10} \Gamma_{ar} = -3.17(1000/T) + 28.16 \quad (4-14)$$

for mercury and by

$$\log_{10} \Gamma_{ar} = -3.73(1000/T) + 26.84 \quad (4-15)$$

for cesium. Substitution of Equation (4-12) into Equation (4-14) or (4-15) gives an expression for equilibrium condensation conditions on the array as a function of solar distance and array surface thermal properties. Four "boundary value" cases may be considered without further analysis. They are plotted in Figure 4-11.

To obtain the "No Condensation" curves, the surface thermal values of the Boeing array are used: $\alpha_f = 0.78$, $\epsilon_f = 0.84$, $\epsilon_b = 0.88$. These curves represent the threshold values of Γ_{ar} for condensation. For smaller Γ_{ar} , condensation will not occur, because propellants re-evaporate as rapidly as they are supplied, but if Γ_{ar} exceeds these curves, some condensation will occur.

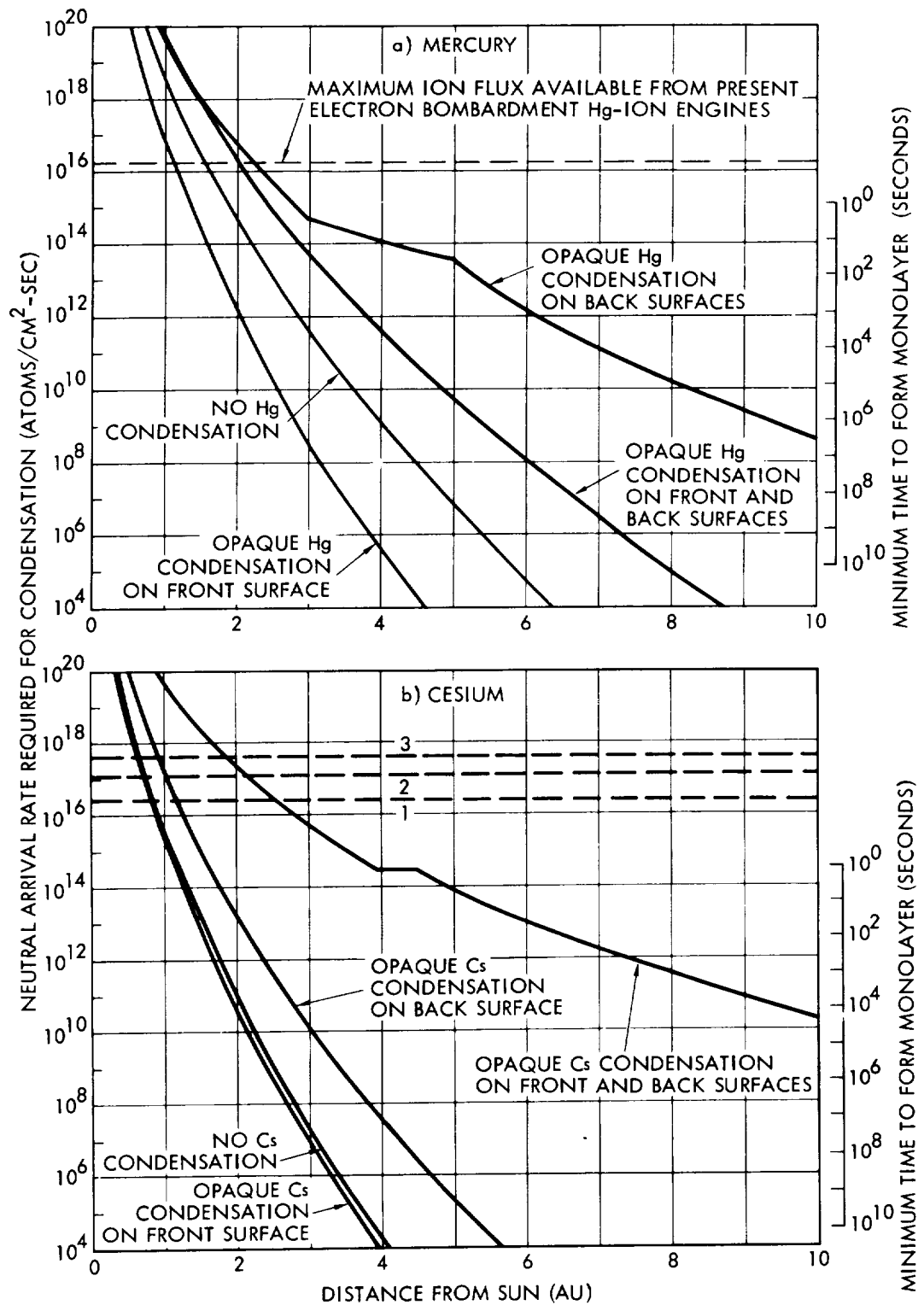


Figure 4-11. Neutral Mercury (a) and Cesium (b)
Atom Arrival Rates Necessary to
Sustain Opaque Condensation on
Boeing Solar Cell Array

The curves labeled "Opaque Condensation on Front Surface" result from using propellant values for α_f and ϵ_f . They represent the equilibrium values of Γ_{ar} which result in constant thickness of an opaque propellant layer condensed on the solar cell side of the array. The formation of an opaque layer on the front surface of the array is ultimately a run-away process: these values of Γ_{ar} are smaller than the "No Condensation" values, because the array temperature is depressed by the presence of the propellant. Obviously, any portion of an array with such an opaque coating would not produce electricity.

The curves for "Opaque Condensation on Rear Surface" result from using propellant values for ϵ_b . Rather high equilibrium values of Γ_{ar} are required to sustain an opaque layer on the rear surface, because the array temperature is increased by the presence of the propellants. Furthermore, unless severe chemical/metallurgical reactions occur between the propellant and substrate, such a condensed layer would not be bothersome at 1 AU and beyond; the array temperature is always acceptably low (less than 400°K) at these distances.

The curves for "Opaque Condensation on Front and Back Surfaces" result from using propellant values for α_f , ϵ_f and ϵ_b . Resulting equilibrium values of Γ_{ar} are very high, making this case academic.

The time scale for these events is roughly indicated by the right-hand scales on Figure 4-11 which express the fact that a monolayer/cm² of mercury is $\sim 1.2 \times 10^{15}$ atoms; of cesium, $\sim 4 \times 10^{14}$ atoms. Careful calculation of the time required to produce opacity must consider ϵ_H and α_s as a function of layer thickness and resulting re-evaporation rates during intermediate semitransparent stages, and layer transmission as a function of layer thickness and radiation wavelength.

When analysis in the foregoing manner indicates potential propellant condensation, several refinements and complicating factors must be considered: (1) the ranges in surface thermal properties of the array and the mercury; (2) heat radiations from the spacecraft and other sources to these locations; (3) layer growth, which will be proportional to the amount by which the arrival rate exceeds the re-evaporation rate, and the

re-evaporation rate is a time-and-layer-thickness-dependent function of temperatures; (4) local cold spots, which might enlarge by lateral heat conduction through the array near the periphery of the spot; and (5) anomalous nucleation of mercury, or formation of the mercury layer as aggregates¹⁰.

4.3.2.3 Conclusions

Spacecraft subsystem degradation from propellant condensation on surfaces can arise even without chemical or metallurgical reaction. A condensed layer on the dark surface of a solar array can affect array temperature (and hence efficiency) by changing the surface emissivity. Condensation on the illuminated side of an array affects array performance through change in surface thermal properties and through attenuation of the light reaching the solar cells. Boundary condition analysis indicates that front surface neutral mercury arrival rates as low as 10^7 atoms $\text{cm}^{-2} \text{sec}^{-1}$ may be of concern at solar distances in excess of 3.5 AU with exposure times of approximately 10^3 days, whereas this flux of cesium may be of concern at 3.0 AU and beyond. At 2.5 AU, arrival rates in excess of 10^{10} Hg atoms $\text{cm}^{-2} \text{sec}^{-1}$ for periods of approximately one day, or 10^9 Cs atoms $\text{cm}^{-2} \text{sec}^{-1}$ for approximately 10 days, require special attention during spacecraft design. At small solar distances the effects of deposited thruster material are likely to predominate over propellant condensation.

4.3.3 Electrical Effects of Thin Films

Electric rocket efflux striking spacecraft surfaces may reduce the resistance of electrical insulators or result in electrical breakdown. Two classes of increased insulator conductivity need be considered: that due to an adsorbed metallic layer on a chemically inert substrate, and that resulting from chemical reaction between metal atom and substrate. The former will be roughly proportional to layer thickness, with departures from this relation occurring for very thin layers when the so-called surface conductivity begins to replace the bulk conductivity of the liquid or solid metal. The effects of electrical power dissipated in the layer must also be considered. Sufficient data are available to make these

calculations. Immersion tests of representative nonmetallic spacecraft surface material in liquid mercury and cesium (Section 6) uncovered two materials whose resistivity was decreased through chemical reaction with cesium — Kapton and Teflon FEP.

Another mechanism for electrical conduction across insulator surfaces is sliding sparks. A fractional monolayer of Cs on insulators (which may occur even in regions of the variables where bulk condensation is not permitted) provides a ready supply of electrons under strong field conditions giving rise to sliding sparks. Even dropwise condensation of Hg, which does not provide a continuous conduction path across insulators, affects this high voltage breakdown in both steady-state and transient conditions. Furthermore, many types of insulators deteriorate after sparking occurs.

The presence of propellant vapors within electrode gaps or the condensation of propellant on electrodes may lead to a variety of breakdown effects which temporarily or permanently damage spacecraft subsystems. Conditions permitting sustained electrical discharges across electrode gaps are not expected. Minimum breakdown in most gases and vapors occurs in the p-d range of 1-10 torr-mm. The equivalent pressure of propellant vapor fluxes of interest is less than 10^{-4} torr. Since spacings between electrodes will probably not exceed 1 m, it is clear that the normal condition will be one or more decades on the vacuum side of the Paschen minimum, and breakdown potentials will be at least a decade higher than the minimum, which is of the order of 300 v. Hence, breakdown through vapors represented by neutral efflux will not occur under normal conditions even for the high voltages used in the thruster.

Transient electrical breakdown could occur on some solar-electric missions. Sudden temperature increases of spacecraft surfaces associated with eclipse termination, vehicle reorientation, start-up of heat-generating equipment, or electrical arcs might desorb enough condensed propellant to raise propellant pressure momentarily into the 10^{-2} torr range. These effects are predictable from Paschen curve data given a specific spacecraft design and mission plan. High voltage (vacuum) arcs are a potential

problem at thruster voltages. These arcs have received extensive study with clean^{25, 26} and cesiated²⁷ electrodes, from which adequate engineering calculations may be made.

4.4 REFERENCES (SECTION 4)

1. I. Langmuir, "The Condensation and Evaporation of Gas Molecules," Collected Works of Irving Langmuir, Vol. 9, edited by C.G. Suits, Pergamon Press, New York, 1961, p. 72.
2. L. Holland, "The Growth, Structure and Physical Properties of Vacuum Deposited Films," Vacuum Deposition of Thin Films, Wiley, 1958, p. 206.
3. L. Holland, "The Growth, Structure and Physical Properties of Vacuum Deposited Films," Vacuum Deposition of Thin Films, Wiley, New York, 1958, p. 203, 223-235.
4. I. Langmuir, "The Condensation and Evaporation of Gas Molecules," Collected Works of Irving Langmuir, Vol. 9, edited by C.G. Suits, Pergamon Press, New York, 1961, pp. 69-74.
5. I. Langmuir, "The Evaporation, Condensation and Reflection of Molecules and the Mechanism of Adsorption," Collected Works of Irving Langmuir, Vol. 9, edited by C.G. Suits, Pergamon Press, New York, 1961, p. 42.
6. I. Langmuir, "The Evaporation, Condensation, and Reflection of Molecules and the Mechanism of Adsorption," Collected Works of Irving Langmuir, Vol. 9, edited by C.G. Suits, Pergamon Press, New York, 1961, p. 43-46.
7. R.E. Honig, "Vapor Pressure Data for the Solid and Liquid Elements," Radio Corporation of America Review, Vol. 23, No. 4, Dec. 1962, pp. 567-586.
8. G. Carter, and J.S. Colligon, Ion Bombardment of Solids, American Elsevier Publishing, Inc., pp. 310-353, 1968.
9. G. Hass, and L. Hadley, "Optical Properties of Metals," Chapter 6g, American Institute of Physics Handbook, pp. 6-103 to 6-121, 1963.
10. R.S. Sennett, and G.D. Scott, "The Structure of Evaporated Metal Films and Their Optical Properties," J. Optical Soc. of America, Vol. 40, No. 4, April, 1950, pp. 203-211.
11. W. Walkenhorst, "Optical Properties of Aluminum Films Deposited in High Vacuum," Z. Techn. Phys. 22 (1941).
12. O.S. Heavens, Optical Properties of Thin Solid Films, N. Y., Academic Press, Inc., 1955.

13. W. Luft, "Extended Pioneer, Final Report on Solar Array," Internal Company Report, TRW Systems, 1 July 1964.
14. L. Holland, Vacuum Deposition of Thin Films, N.Y., John Wiley and Sons, Inc., 1958, p. 323.
15. W.R. Kerslake, et al., "SERT II: Mission and Experiments," Journal of Spacecraft and Rockets, Vol. 7, No. 1, pp. 4-6, January 1970.
16. J.V. Staskus, and R.J. Burns, "Deposition of Ion Thruster Effluents on SERT II Spacecraft Surfaces," AIAA Paper No. 70-1128, September 1970.
17. T.W. Reynolds, and E.A. Richley, "Contamination of Spacecraft Surfaces Downstream of a Kaufman Thruster," NASA TN D-7036, January 1971.
18. J.F. Staggs, W.P. Gula, and W.R. Kerslake, "Distribution of Neutral Atoms and Charge-Exchange Ions Downstream of an Ion Thruster," J. Spacecraft and Rockets, Vol. 5, No. 2, February 1968, pp. 159-164.
19. F. Seitz, The Modern Theory of Solids, McGraw-Hill, New York, 1940, Chap. XVII.
20. N.F. Mott, and H. Jones, The Theory of the Properties of Metals and Alloys, Dover, New York, 1958, pp. 105-125.
21. H. Ives, and H.B. Briggs, "Optical Constants of Rubidium and Cesium," Journal of the Optical Society of America, Vol. 27, 1937, pp. 395-400.
22. J.B. Nathanson, "The Optical Constants of Solid Cesium," Physical Review, Vol. 25, Jan. 1925, pp. 75-84.
23. W.J. Parker, and G.C. Abbot, "Theoretical and Experimental Studies of the Total Emittance of Metals," Symposium on Thermal Radiation of Solids, NASA SP-55, 1965, pp. 11-28.
24. "Large Area Solar Array," DZ-113355-7, Final Report-Phase II, JPL Contract 951934, Oct. 1968, Boeing Co., Seattle, Wash.
25. F.M., Charbonnier, C.J. Bennette, and L.W. Swanson, "Electrical Breakdown Between Metal Electrodes in High Vacuum. I. Theory," Journal of Applied Physics, Vol. 38, No. 2, Feb. 1967, pp. 627-633.

26. C.J. Bennette, L.W. Swanson, and F.M. Charbonnier, "Electrical Breakdown Between Metal Electrodes in High Vacuum. II. Experimental," Journal of Applied Physics, Vol. 38, No. 2, Feb. 1967, pp. 634-640.
27. C.J. Bennette, et al., "Investigation of the Prebreakdown Gap Currents Between Clean and Cesium-Coated Tungsten Electrodes," AIAA Journal, Vol. 3, No. 2, Feb. 1965, pp. 284-290.

5. ION EROSION

5.1 INTRODUCTION

Spacecraft surfaces located downstream of an electrostatic rocket exit plane will be subjected to bombardment by energetic propellant ions.

A literature search revealed little information regarding the rate at which metal surfaces would erode and no information about the erosion rates of nonmetallic targets.

Therefore, an experimental investigation was undertaken to determine the rates at which typical spacecraft surface materials are eroded by mercury ion bombardment. Measurements were made with both 3 and 1 kev Hg^+ .

5.2 EXPERIMENTAL PROCEDURE

5.2.1 Test Facility

The ion erosion measurements were made in the facility described in Appendix A. The use of an ion engine as a beam source was particularly advantageous in these experiments. First, the broad beam permitted exposing many samples simultaneously. Second, the presence of plasma neutralizing electrons in the beam prevented dielectric targets from obtaining a significant surface charge from ion bombardment. As soon as a surface began to accumulate excess positive charge, plasma electrons were attracted and collected. In the 3 kev experiments, secondary electrons from the ion impacts on the collector were used to neutralize the beam. In the 1 kev experiments, a hot wire neutralizer was immersed in the beam near the thruster. The latter technique is recommended.

5.2.2 Sample Coupons

All samples were prepared as 1/4- by 3/4-inch coupons as shown in Figure 5-1. Paints and RTV silicones were applied to aluminum substrates, according to the manufacturer's instructions. Films such as polyimides and microsheet were cemented to aluminum substrates under pressure to minimize cement thickness. Silver and gold were plated on aluminum. Coupons of the other metal samples were machined from solid stock.

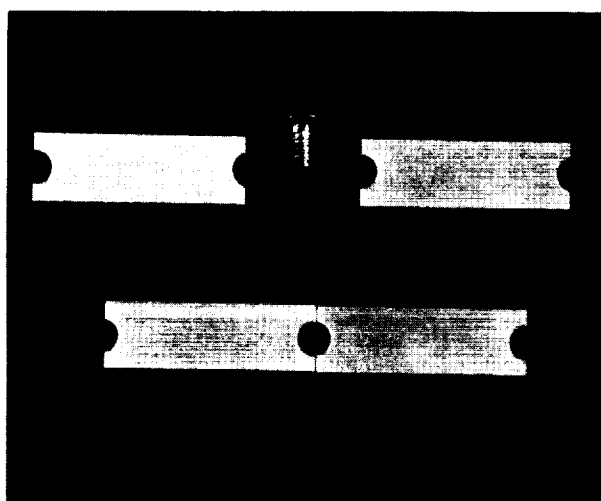


Figure 5-1. Photograph of Four Aluminum Sample Substrates and Reworked Stainless Steel Mounting Screw

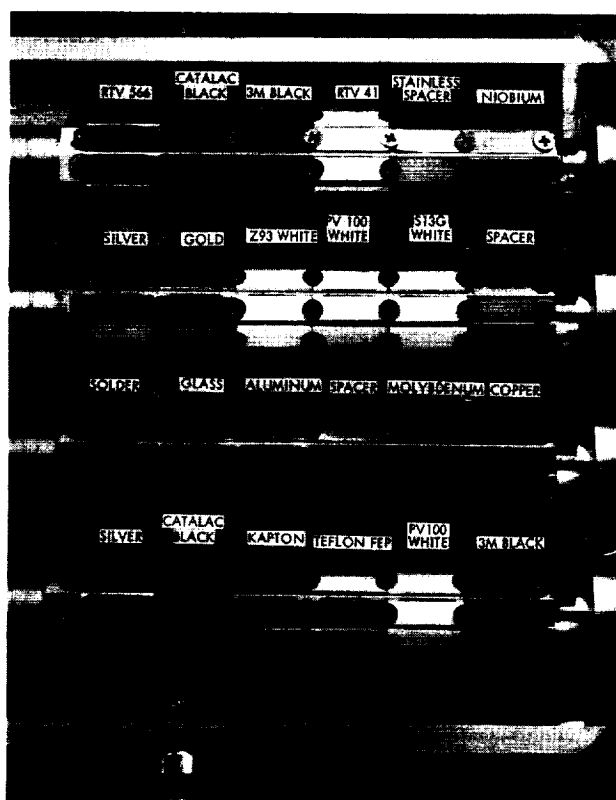


Figure 5-2. Photograph of Loaded Sample Holder

5.2.3 Sample Holder

The coupons were mounted on a multipurpose sample holder, which holds up to 24 sets of samples and permits sample temperature control during exposure. Each sample set contains five samples whose normals form 0, 30, 45, 60 and 75 degree angles with the incident ion beam. Figure 5-2 is a photograph of a typical sample load. The stainless flathead screws serve both to hold the samples to the sample holder pipes and to shield a portion of each end of the sample from the ion beam. These shielded areas are fiducial surfaces for erosion depth measurements. In order to minimize deposition of stainless steel on the samples, each screw head was machined to sharpen its bevel edge.

RTV60 was used as an interface compound between the sample substrates and the sample holder pipes to assure good thermal contact. The temperature of all four pipes was held at approximately 21°C during the exposures by passing city water through the sample pipes. (The pipes are thermally insulated

from each other and can be held at widely different temperatures). All sample holder parts which receive ion bombardment are also water cooled.

T-shaped copper shields are located between the pipes to prevent exchange of sputtered material between adjacent pipes. The top edges of the T are sharpened to minimize sputtering of copper onto the samples.

Each pipe can be removed from the holder for loading, unloading, or microscopic inspection of samples. On each pipe end is a disconnect fitting and the pipe slides in slotted guide plates.

5.2.4 Exposure Sequence

The sample holder loads into the test facility through a side port. A track guides the holder to its position behind the collector cut-out and precisely positions it there. After pump down, chilling the LN_2 liners, and beam stabilization, the sample shutter was opened to begin the exposure. During long exposures the sample shutter was closed periodically to permit beam current density measurements.

An exposure was terminated when the thinnest sample was nearly gone. Then the shutter was closed, the beam shut down, and the test facility let up to nitrogen with the LN_2 liners still cold and the sample's pipes still under temperature control. When the facility was slightly pressurized, the sample holder was withdrawn from the chamber, whereupon it was repumped and the liners allowed to warm, desorbing the mercury and water vapors.

Each sample was then inspected under a binocular microscope while still on its pipe. When a sample was nearly gone, its whole set was removed for erosion depth measurements and chemical analysis. New sets of samples, either of the same or a different type, were placed in the vacant locations. Then the holder was reinserted into the test facility to begin the next exposure sequence.

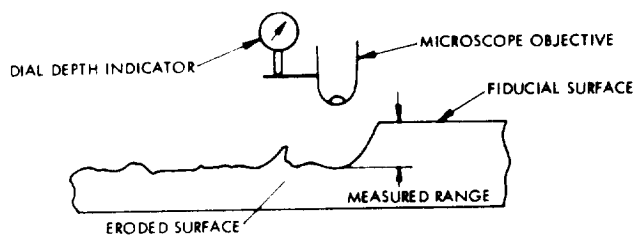
5.2.5 Post Exposure Inspection

After the coupons were removed from the sample holder, each was carefully inspected under a binocular microscope and notes were made regarding surface color and topograph. Most of the samples were also photographed at 10X magnification.

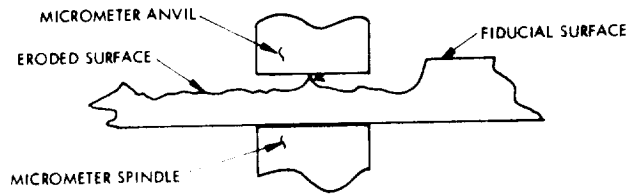
5.2.6 Erosion Measurement Techniques

Three methods were devised to measure sample erosion depth. One was an optical measurement, shown schematically in Figure 5-3a. A toolmaker's microscope was outfitted with a dial depth indicator with 0.00001-inch graduations. The sample was mounted flat on the movable stage, the microscope focused on the sample's fiducial surface, and the indicator reading noted. The stage was then moved and the scope focused on the adjacent eroded surface. The difference in indicator readings at these two locations is a measure of the erosion depth at that end of the sample. The same procedure was used to measure the depth at the other end. The microscope was usually set for 200X magnification and repeated focusing on a flat surface produced indicator readings within ± 0.1 mils. The microscope method of measurement was found to be the most reliable of the methods for rubbery samples, such as RTV41 and RTV566, and samples with very coarse surface topography, such as S13G. Its disadvantages are that it is particularly tedious, and when the surfaces are not very smooth, human judgment is required in choosing the average surface height.

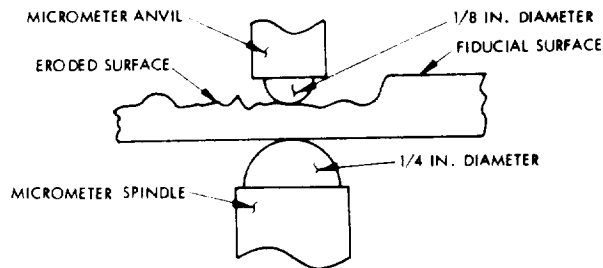
Another measurement method employed a standard 1-inch micrometer with 0.001-inch graduations. The sample was measured in three places on the eroded area and compared with measurements made prior to ion beam exposure at the same three places. The difficulty with this technique is suggested in Figure 5-3b, namely inability to avoid lumps and peaks on the sample surface. None of the data presented was obtained with this method.



(a) Optical Microscope



(b) Standard Micrometer



(c) Bench Micrometer

Figure 5-3. Alternate Erosion Depth Measurement Schemes. Method C was Used for Most Samples.

Most of the data presented below was obtained with a 1-inch bench micrometer with 0.00005-inch graduations and spherical anvils. The advantages of this method are the small contact areas, which, as indicated in Figure 5-3c, allows more precise selection of the area measured, uniformity of micrometer pressure from measurement to measurement, and great precision. A microscope was used to accurately place the small spherical anvil on the desired sample area.

Slightly different techniques were employed with the 3 kev and 1 kev ion eroded samples. In the case of the 3 kev samples, sample thickness was measured at the fiducial surfaces at both ends of the sample, and at the adjacent eroded surfaces. The difference between the fiducial and eroded surfaces was then computed. On the other hand, the thickness of the 1 kev samples was carefully

measured at both ends and the middle prior and subsequent to exposure. These differences were taken as the erosion depth. This method took less time and yielded three measurements per sample as well, which reduced the impact of random measurement errors. Whenever compared, the two methods were in acceptable agreement.

A control sample was maintained for each sample set in the 1 kev group. It was measured in the same manner and at the same time as the other set members, but was not mounted on the sample holder nor exposed to the ion beam. These measurements of the controls suggested that computed erosion depths were generally of the order of ± 10 percent uncertain, although the uncertainty of some measurements were much less and of others much more (e.g., most 75-degree samples) uncertain.

5.2.7 Data Analysis

Sample erosion rate was calculated by dividing erosion depth by the ion dose received by each particular sample. This dose was a function both of the particular exposures during which the sample set had been on the holder and of the angle of ion beam incidence. A remote terminal computer program was then used to find an ion-dose-weighted mean of the erosion rate as calculated from measurements at each location on all samples of a given material and angle of incidence. As a measure of scatter in the data, the program also calculated an approximate standard error according to the formula

$$\sigma_{\bar{x}} = \frac{1}{N(N-1)} \frac{\sum m_i (x_i - \bar{x})^2}{\sum m_i}$$

where

N = Number of data points (two per sample)

m_i = Ion dose associated with data point x_i

\bar{x} = Weighted mean of x_i 's

When the number of data points is very small, this calculation is misleading. For instance, if only one sample is available and the measured erosion depth is the same at both ends, $\sigma_{\bar{x}} = 0$. Obviously this overestimates the repeatability of the data. The ion dose received is uncertain by about ± 5 percent, and therefore all erosion rate data are uncertain by at least ± 5 percent. Nevertheless, "error bars" based on the above equation do provide an estimate of the repeatability of the data, especially when the standard error exceeds 10 percent of the mean.

5.3 RESULTS AND DISCUSSION

5.3.1 Measurements

Forty-four sets of specimens of 21 spacecraft surface materials were eroded by approximately 0.2 ma/cm^2 ($1.25 \times 10^{15} \text{ ions/cm}^2\text{-sec}$) 3 kev ($5.4 \times 10^4 \text{ m/sec}$) mercury ions in a series of 12 exposures totaling 175 hours. In later experiments, thirty-eight sets of specimens of 18 of these materials were eroded by approximately 0.1 ma/cm^2 ($6 \times 10^{14} \text{ ions/cm}^2\text{-sec}$) 1 kev ($3.1 \times 10^4 \text{ m/sec}$) mercury ions in a series of 8 exposures totaling 145 hours. The 3 kev erosion rate measurements are presented in Figures 5-4a through 5-4e and the 1 kev measurements in Figures 5-5a through 5-5f all as a function of angle. Both 1 and 3 kev Teflon FEP data appear in Figure 5-6 along with 3 kev polyvinyl acetate data. Except for those samples noted as having been measured with an optical microscope, erosion depth measurements were made per Figure 5-3c.

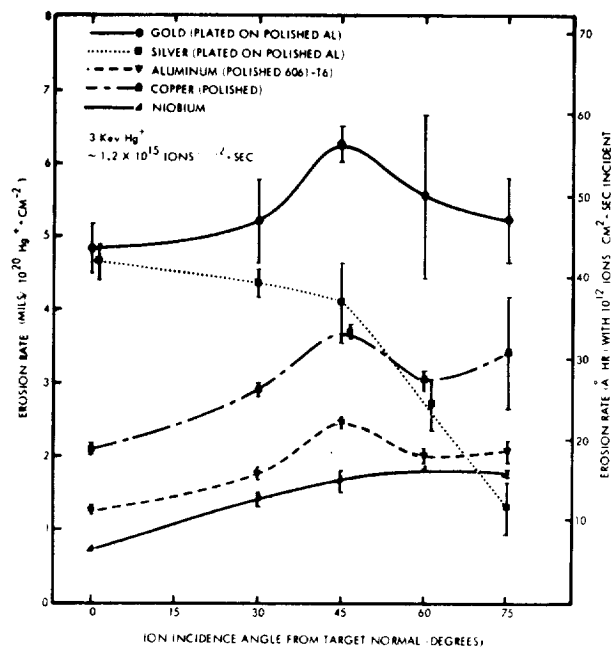
On the left ordinate of these figures, erosion rate is expressed as the number of mils (10^{-3} inches) eroded per incident ion dose of $10^{20} \text{ ions/cm}^2$. This dose was chosen to yield erosion rate values of the order of one mil and represents a much larger dose than would typically be received by a spacecraft surface. For instance, it is unlikely that a spacecraft design would locate a surface closer than 45 degrees from the thrust axis, at which angle ion fluxes near the thruster are in the neighborhood of $10^{12} \text{ ions/cm}^2\text{-sec}$. Thus, typically it would require some 10^5 thrusting hours to accumulate a 10^{20} dose.

On the right-hand ordinate, the measured erosion rates have been expressed as the number of Angstroms of material removed each hour by a $10^{12} \text{ ion/cm}^2\text{-sec}$ flux.

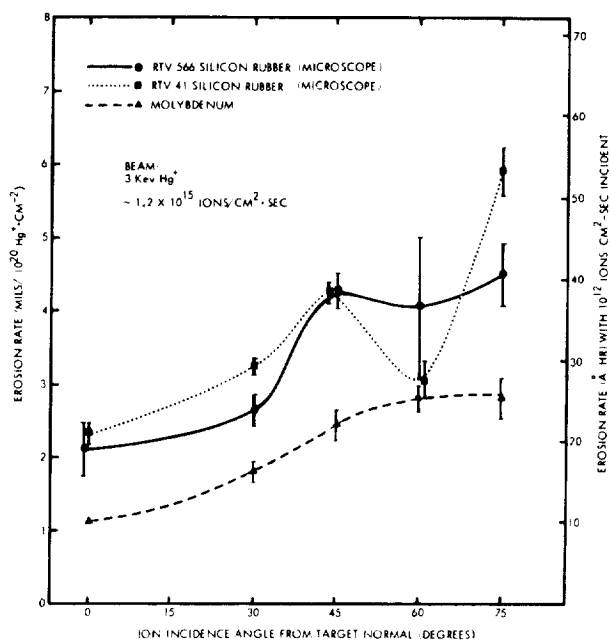
5.3.2 Discussion

5.3.2.1 Equivalent Sputtering Yields

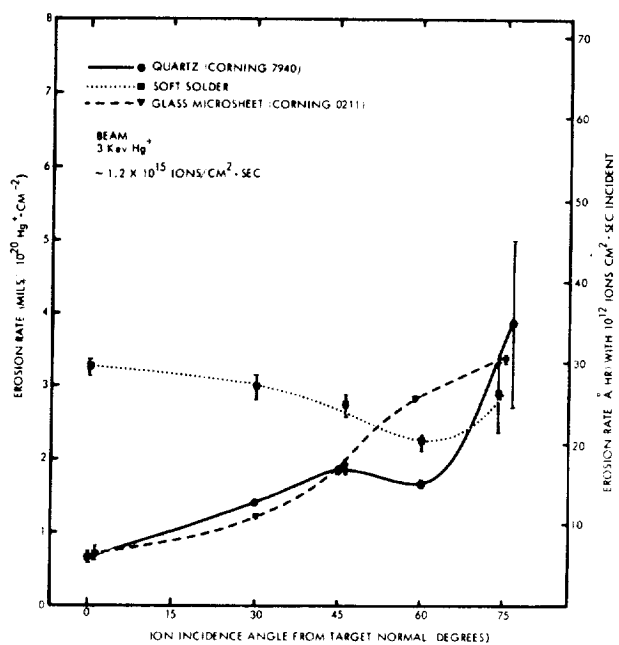
It is of interest to convert the results obtained from metal samples to sputtering yield values.



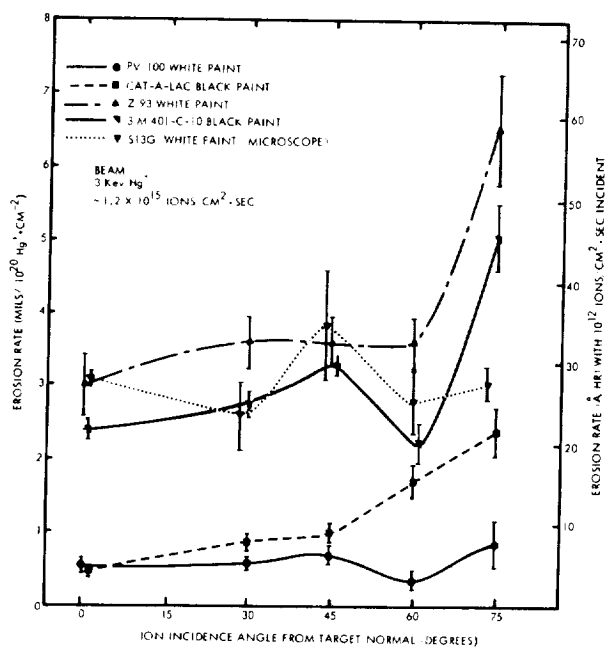
(a)



(c)

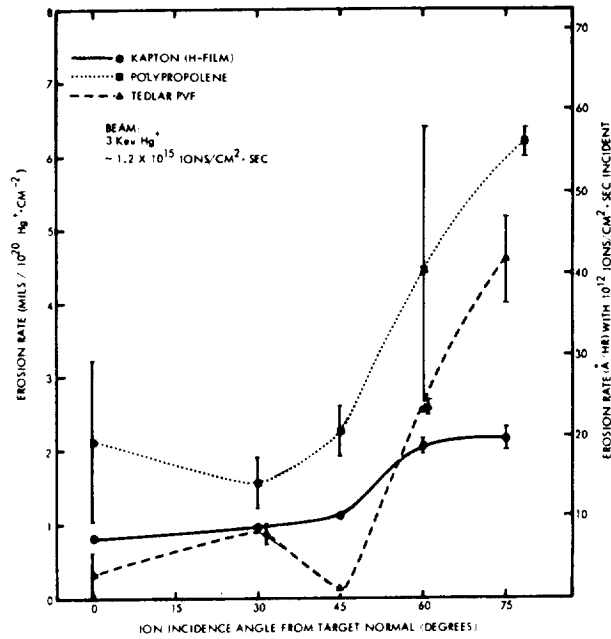


(b)



(d)

Figure 5-4. Erosion Rate of Various Spacecraft Surface Materials by 3 kev Mercury Ions as a Function of Ion Incidence Angle



(e)

Figure 5-4. Erosion Rate of Various Spacecraft Surface Materials by 3 kev Mercury Ions as a Function of Ion Incidence Angle (Continued)

After an initial period, during which the target becomes saturated with propellant atoms, the target erosion rate may be simply expressed:

$$\frac{dx}{dt} = - \frac{\Gamma + S}{n} \left(\frac{\text{cm}}{\text{sec}} \right) \quad (1)$$

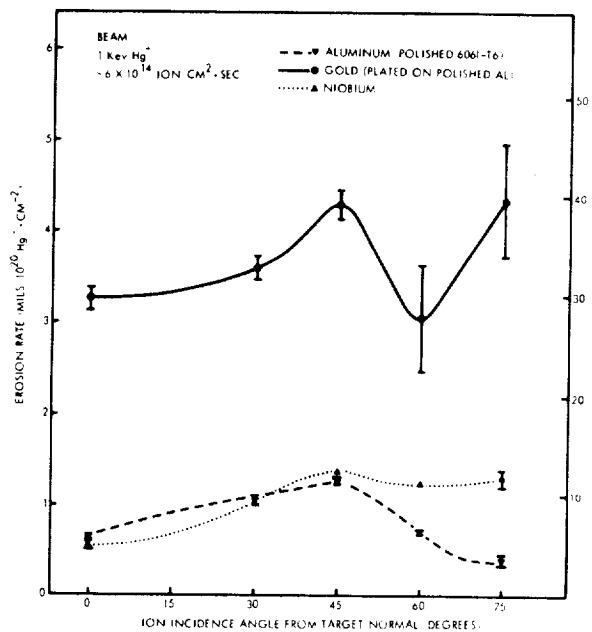
where

$\frac{dx}{dt}$ = time rate at which target thickness changes in cm sec⁻¹

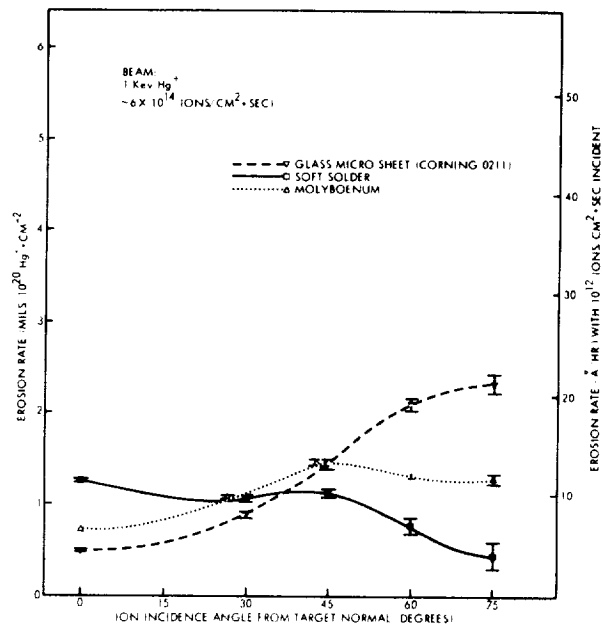
Γ_+ = flux density of bombarding ions in ions cm⁻² sec⁻¹

S = the sputtering yield; i. e., the number of target atoms ejected per incoming ion

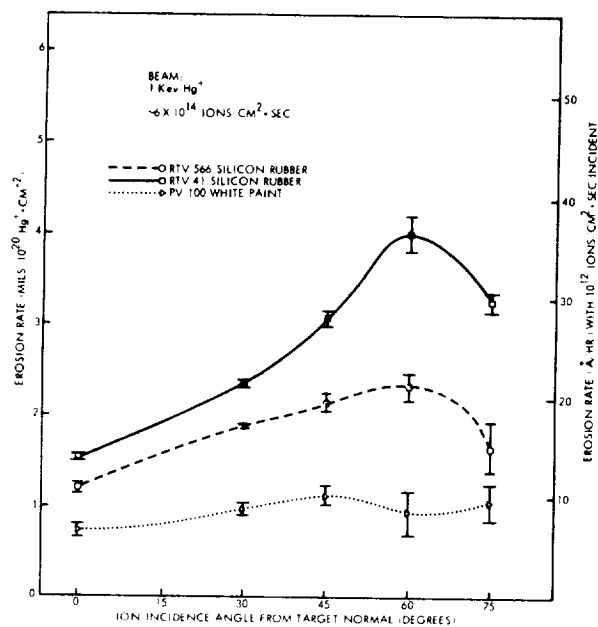
n = the number density of the target in atoms cm⁻³



(a)

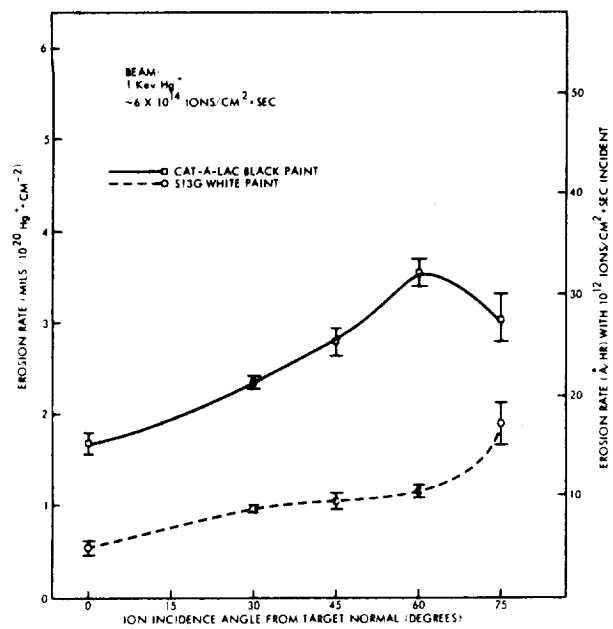


(b)

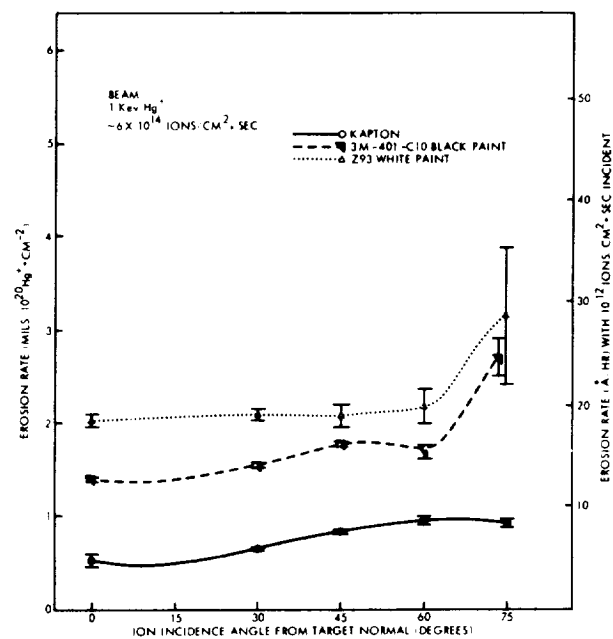


(c)

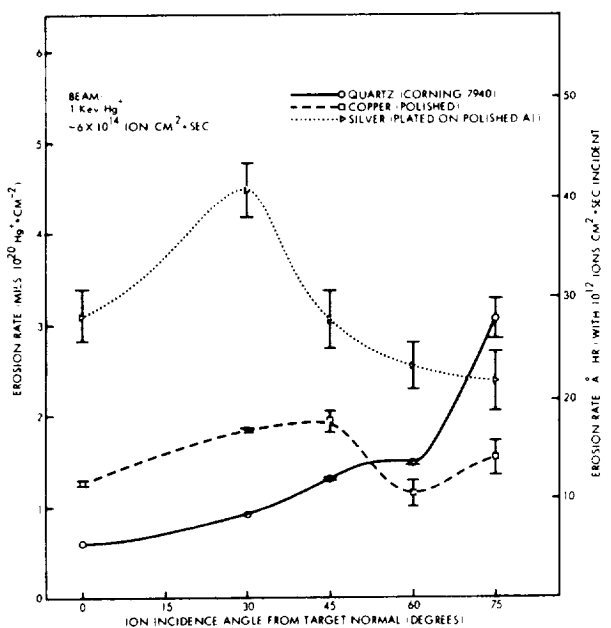
Figure 5-5. Erosion Rate of Various Spacecraft Surface Materials by 1 kev Mercury Ions as a Function of Ion Incidence Angle



(d)



(e)



(f)

Figure 5-5. Erosion Rate of Various Spacecraft Surface Materials by 1 keV Mercury Ions as a Function of Ion Incidence Angle (Continued)

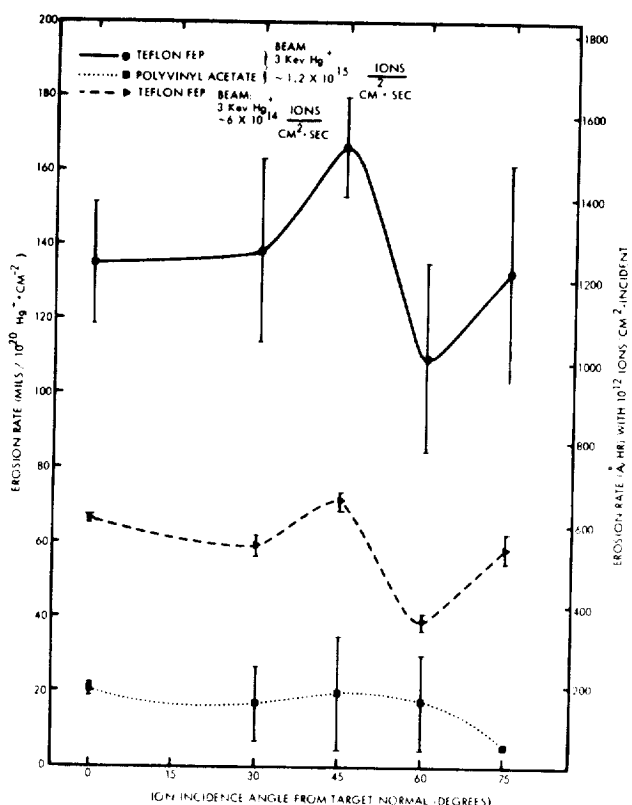


Figure 5-6. Erosion Rate of Teflon FEP by 1 and 3 keV Mercury Ions and Poly (Vinyl Acetate) by 3 keV Hg⁺ as a Function of Ion Incidence Angle

The value of the sputtering yield is dependent on the energy, angle of incidence and species of the incoming ion, as well as on the target material. In these experiments, the quantities $\int dx$ and $\int \Gamma_+ dt$ were measured and their ratio computed. If n is known, then these results may also be expressed as sputtering yields. The atomic densities of metals are well known, and the sputtering yields obtained from the zero degree samples are given in Table 5-1. We compared the present results with those reported by others. No data were found on the nonmetallic samples, and very few measurements have been made of the sputtering yields of polycrystalline metals by Hg⁺ in the 1 to 3 keV energy range. Further-

more, it often happens that yield data reported in other energy ranges by different experimenters are discrepant by 50 percent or more. The data of Table 5-1 are within 50 percent of the values obtained by extrapolating the 4-15 keV measurements of Wehner and Rosenberg.¹ Agreement of this order is also obtained with Magnuson, et al.² on copper and molybdenum.

Table 5-1. Sputtering Yields of Polycrystalline Metal Samples Positioned Normal to 1 and 3 kev Hg⁺ Beam

Sample	Number Density (10 ²² atoms/cm ³)	Sputtering Yield (atoms/ion)	
		1 kev	3 kev
Gold (Plated)	5.9	4.9	7.3
Silver (Plated)	5.9	4.6	6.9
Aluminum 6061-56	6.0	1.0	1.9
Copper	8.5	2.7	4.5
Niobium	5.5	0.8	1.0
Molybdenum	6.4	1.1	2.9

The general relationship between erosion rate, sputtering yield and target density expressed in Equation (1) is illustrated in Figure 5-7. It indicates the integrated ion dose $\int \Gamma^+ dt$ required to erode 1 mil (considered an example coating thickness since thicknesses range between 500 Å and 20 mils) vs S , with target density as the parameter. (Most materials fall between 10²² and 10²³ atoms/cm³. Ion dose is also expressed in terms of constant ion flux for 10⁴ hr. It is seen that even fluxes below 10¹¹ ions/cm²-sec may be troublesome when thrusting times are very long or targets are very thin.

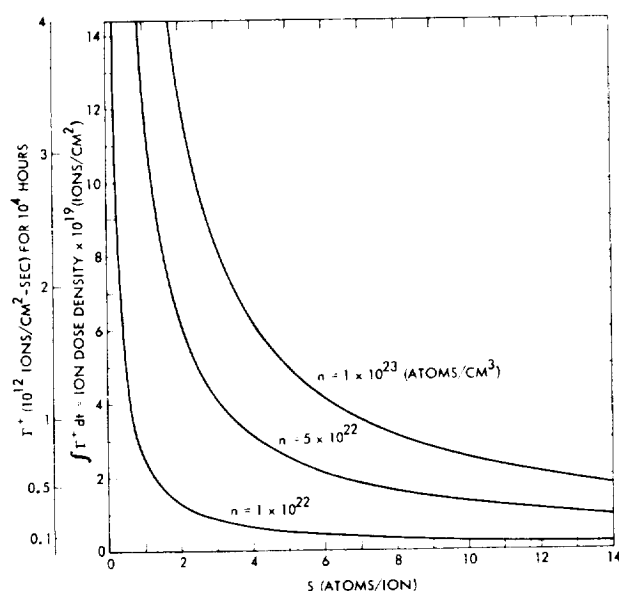


Figure 5-7. Ion Dose Density Required to Produce 1-mil Erosion versus Sputtering Yield for Three Target Densities

5.3.2.2 Dependence on Angle of Incidence

Simple theory leads one to expect that in this energy range the angular dependence of sputtering yield is:

$$S = S_o \frac{1}{\cos \theta} \quad (2)$$

where

S_o = sputtering yield at normal incidence, i.e., at $\theta = 0$

θ = angle between target normal and incoming beam.

The idea is that as a target is tilted, the energy of the bombarding ion is deposited nearer the target surface, and there is a corresponding increase in the probability that part of the energy will be dissipated by ejecting surface atoms. Sputtering experiments confirm that this relationship is roughly correct for many metals out to angles as high as 85 degrees. At grazing incidence ($\theta \rightarrow 90$ degrees), small angle scattering deflects ions out of the target with little or no sputtering, and the yield drops rapidly to zero. Metals such as copper, iron, and molybdenum show even greater increase with angle so that at 45 degrees the yield may be twice that at normal incidence.²⁻⁴

The drop in sputtering yield at grazing angles results in the production of needles and deep holes in the sputtering surface. This is easily seen by recognizing that an acutely angled surface, either a spike or a hole, is self-perpetuating since the steep sides are immune to sputtering and at the same time deflect incident ions toward the base of the spike or hole. Needles were observed on the surface of many of the samples, both metallic and nonmetallic. This same focusing effect will locally increase the erosion rate of the lower of two overlapping surfaces, e.g. a solar cell interconnect where it goes underneath a solar cell.

An interesting thing happens to targets which obey the relationship of Equation (2). As the target is tilted with respect to an incident ion beam the $1/\cos\theta$ increase in sputtering yield is exactly compensated by the reduction in projected target area. Therefore, the erosion rate of a target with this angular dependence of sputtering yield is independent of angle. Inspection of the figures will show that some of the materials tested roughly follow the $1/\cos\theta$ yield dependence while others do not.

There is remarkable similarity between the angular dependence of erosion rate in the 1 and 3 kev cases for most materials. Only S13G and silver have clearly different 1 and 3 kev dependences below 60 degrees.

5.3.2.3 Dependence on Ion Energy

With normal incidence, most of the 1 kev erosion rates are between 0.5 and 0.7 of the corresponding 3 kev erosion rates. A notable exception is PV100, which exhibited a 50 percent higher rate at the lower bombarding energy.

5.3.2.4 Effect on Surface Topography

In addition to eroding sample surfaces, in most cases the surface topography was also affected by the ion beam. Changes in the organic sample surfaces were noted in Section 6. Here we summarize the effects on other samples.

The most important change in surface topography is that the high angle (60 and 75 degrees) quartz and glass microsheet samples became frosty after fairly large ion doses. Figure 5-8a is a 10X photo of a 60-degree Corning 7940 quartz sample following approximately 21 hours of 3 kev Hg^+ exposure. The surface actually consists of thousands of fine spikes oriented along the direction of the incoming ions. Figure 5-8b shows this surface at 400X. The 75-degree quartz sample had large asperities protruding from a smooth base surface. The 30- and 45-degree quartz samples had a cloudy appearance and their surfaces felt slightly rough when lightly scraped with a scalpel. In contrast, the 0-degree samples retained their polished appearance.

The topography of corresponding quartz samples from both the 3 kev and 1 kev experiments were similar. However, the topography of 0211 glass microsheet samples was somewhat different than quartz samples of corresponding angle. The surface of the 75-degree microsheet sample was a dense uniform forest of fine needles. The 60-degree sample appeared as a photographer's ground glass. The 45-degree sample was slightly cloudy, while the 30-degree sample had a definite, fine surface texture. As with the quartz samples, the 0-degree sample was highly polished, even though a significant thickness of glass had been removed.

The fine spikes on the high angle samples conceivable could have been initiated by the arrival of the metal atoms discussed in Section 6, although the erosion rates measured on the quartz and glass are lower than the erosion rates measured on most metals. Electron beam microprobe analysis of the high angle quartz and glass samples failed to indicate a high concentration of metal remaining on the needle tips. Therefore, the phenomenon is probably a genuine property of high angle ion bombardment



(a)



(b)

Figure 5-8. Sixty-degree Quartz Surface at (a) 10X and (b) 400X Following ~21 Hours of 3 kev Hg^+ Exposures

of glass and quartz. In view of the importance of these materials in optical sensors and as solar cell coverglass, measurements of their optical properties should be made as a function of ion dose and angle of exposure.

The metal samples developed a grainy appearance as various crystal faces were preferentially exposed by the sputtering. Figure 5-9a and 5-9(b) show 0- and 45-degree polished aluminum samples after 39 hours of 3 kev Hg^+ exposure. These samples originally had the appearance of the unexposed sample in Figure 5-9c. The 60- and 75-degree aluminum sample had a somewhat smoother texture than the 0-, 30-, and 45-degree samples. The copper and niobium samples were quite similar to those of aluminum. The texture of the gold and silver samples was finer. Dendritic figures were exposed on the 0-, 30-, and 45-degree soft solder samples by the ion beam. No thermophysical measurements were made on these samples, but the infrared emittance of their surfaces probably increased. However, much smaller ion doses failed to affect either the visual appearance or measured emittance of polished aluminum samples in the experiments described in Section 8.

5.3.2.5 Erosion Rates

Perhaps the most notable general feature of the data is that, with the exception of Teflon FEP and the adhesive poly (vinyl acetate), all samples eroded at roughly the same rate (1/2 to 6 mils per $10^{20}\text{Hg}^+\text{cm}^{-2}$). (The high erosion rate of Teflon FEP has been discussed in Section 6.) This means that with an arrival flux of 10^{12} ions/ cm^2 -sec (which might occur at 8 thruster radii and 45 degrees), erosion rates will generally be in the range of 5 to 50 Å per hour. At lower arrival rates (which occur at higher angles, and to a lesser extent, greater distance from the thruster), the rates will be correspondingly lower.

For instance, at 60 degrees and one meter from a 1/2-ampere thruster, the arrival rate of mercury ions would probably be less than 2×10^{10} ions/ cm^2 -sec. If the target erosion rate were "average" -- say 3 mils/ 10^{20} ions cm^{-2} -- the beam would remove $\sim 10^{-2}$ mils (1/4 micron) per year of thrusting. Teflon FEP, the most rapidly eroding material known to us, will disappear at 50 times this rate.

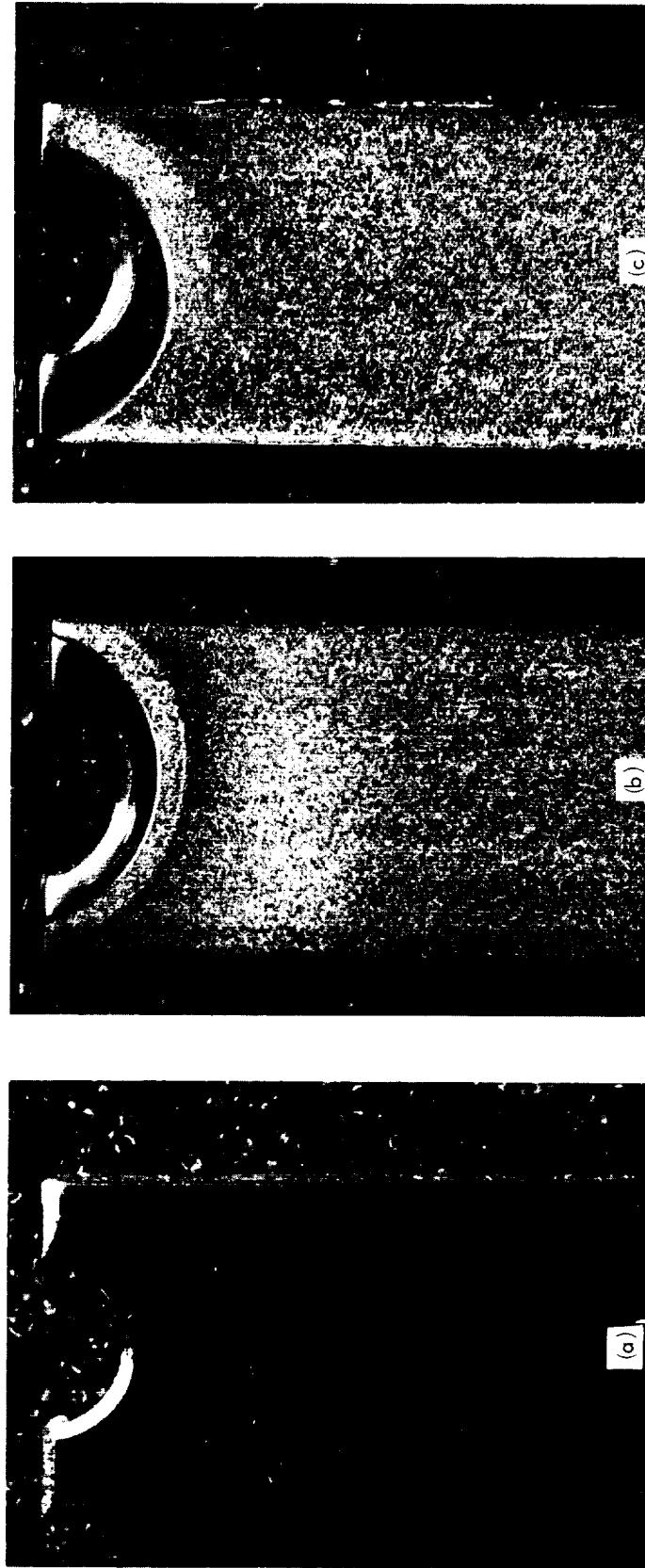


Figure 5-9. Polished Aluminum Samples (a) Prior to Exposure; (b) 0-Degree; and (c) 45-Degree Following 39 Hours of 3 kev Hg^+

5.4 CONCLUSIONS AND RECOMMENDATIONS

The erosion depth per ion dose of 18 materials to 1 and 3 kev Hg^+ at 5 angles of incidence has been measured. Most materials eroded at rates between 1/2 and 6 mils/ $10^{20} \text{Hg}^+ \text{cm}^{-2}$, but Teflon FEP exhibited a remarkable ~140 mils. Most samples eroded in the range of 1/2 to 3/4 the 3 kev rate at 1 kev. These results mean that with the possible exception of Teflon FEP, ion erosion of spacecraft surfaces is mostly of concern insofar as it changes their surface properties (e.g., the optical properties of thermal control coatings and lenses) and the properties of other surfaces intercepting the sputtered atoms. Only very thin films or targets receiving rather large ion doses might be completely removed by sputtering.

Further work is definitely needed on ion bombardment induced changes in the optical properties of lenses and solar cell cover glasses, since the large ion doses in the present experiments produced dramatic topographical effects. Measurements should be made of diffuse and specular transmission as a function of incidence angle and dose. The erosion rates of some additional spacecraft materials are of interest (e.g. DC92-007 and MS-74 white paints, Kynar, and several epoxies). The effects of target temperature are as yet unexplored and might be important in the case of organic materials. Finally, similar measurements with cesium ion beams would be of interest, especially on organic samples where chemical reaction might contribute to a high erosion rate.

5.5 REFERENCES (SECTION 5)

1. G.K. Wehner, and D. Rosenberg, "Mercury Ion Beam Sputtering of Metals at Energies 4-15 kev," Journal of Applied Physics, Vol. 32, No. 5, pp. 887-890, May 1961.
2. G.D. Magnuson, et al., "Sputtering Mechanisms under Ion Propulsion Conditions," GDA-DBE-64-057, Final Report, Contract NAS 3-2591, October 1964, General Dynamics/Astronautics.

3. G.K. Wehner, "Influence of the Angle of Incidence on Sputtering Yields, " Journal of Applied Physics, Vol. 30, No. 11, November 1959.
4. K.B. Cheney, and E.T. Pitkin, Journal of Applied Physics, Vol. 36, No. 11, 1965.

6. CHEMICAL EFFECTS OF PROPELLANTS

6.1 INTRODUCTION

The Phase III chemistry effort was concerned with two principal investigational areas: (1) a continuation of the study, initiated during Phase II, of the effect of cesium metal immersion on selected spacecraft surfaces; and (2) investigation of the effect of high energy mercury ion beams on such surfaces. The studies provided valuable data which will aid in the selection of materials suitable for use on spacecraft surfaces that will be subjected to the environmental effects of cesium or mercury fueled electrostatic thrusters. The results of the cesium immersion and mercury ion beam tests are described below in Sections 6.2 and 6.3, respectively. The implications of these data and those gathered during Phases I and II are described in Section 6.4.

6.2 CESIUM IMMERSION TESTS

The materials tested comprised a group of four thermal control paints and Kapton polyimide film. In view of the unique behavior of Kapton, previously described in Reference 1, the results of the experiments conducted with the polyimide will be discussed separately.

6.2.1 Paints

Weighed samples of PV100, Z93, S13G white, and 3M Velvet black paints on aluminum were each exposed to distilled Cs at room temperature for 48 hours. Each sample was quenched in a benzene-10 percent methanol solution, washed with fresh methanol, and then dried in vacuum. After drying, each sample was reweighed and the surface was inspected for visible damage. Control samples were also given the quenching, washing, and drying treatments to determine their effect on sample weight.

The results are summarized in Table 6-1. With the exception of the 3M Velvet sample there was no visible damage. This sample shows some increase in reflectance (as determined visually) and small pits in one small area of the sample. Cesium did not wet the surface of the Z93 sample.

Table 6-1. Cesium Exposure of Thermal Control Coatings

Sample	Initial Weight gram	Final Weight gram	Weight Change gram	% Change ¹	Comments
S13G	0.2829	0.2718	-0.0111	-3.92	No visible surface damage.
Control	0.1481	0.1478	-0.0003	-0.20	
Z93	0.1829	0.1802	-0.0027	-1.48	No surface damage; Cs did not wet surface.
Control	0.1975	0.1971	-0.0004	-0.20	
3M Velvet	0.3906	0.3834	-0.0072	-1.84	Some whitening and small pits formed.
Control	1.1804	1.1752	-0.0052	-0.44	
PV100	0.3684	0.3660	-0.0024	-0.65 ²	No visible surface damage. Sample lifted from substrate by quench solution.
Control	1.1968	1.1945	-0.0023	-0.19 ²	

1. Based on total weight of sample

2. Percent weight losses were 3.93 percent for the exposed sample and 1.19 percent for the control sample based on substrate-free coating weights of 0.0611 gram and 0.1928 gram, respectively.

The large weight loss incurred by the S13G sample is very likely due to drying of the inorganic pigment. There was no evidence of surface darkening nor degradation of the coating itself.

During the quenching operation on the PV100 sample, the coating was lifted from the aluminum substrate. The same result was obtained when the control sample was subjected to the quenching operation, so the cesium exposure had nothing to do with this result. The samples of this coating were weighed separately and a weight loss based on coating weight alone was determined. This weight loss (associated with cesium exposure) is only 2.74 percent and is probably also due to drying of the coating pigment. However, the possibility of leaching of TiO_2 pigment from the surface of the coating, discussed in Reference 2, should not be discounted completely.

An additional sample of the 3M Velvet black paint was exposed to metallic cesium at room temperature in the manner above. Quenching and handling was also the same. This time, however, sample weight prior to drying was also recorded. The sample was dried by maintaining its temperature at 100°C for 1 hour in vacuum.

<u>Sample</u>	<u>Initial Weight gram</u>	<u>Weight Dried gram</u>	<u>Percent Change</u>	<u>Weight After Exposure, gram</u>	<u>Percent Change</u>
3M Velvet	0.3130	0.3105	-0.80	0.3006	-3.19
Control	0.2934	0.2912	-0.75	0.2912	0

As observed in the previous exposure, the sample surface had changed color, becoming a mottled grey. No pitting was evident this time, however. A small amount of coating had flaked off of the substrate, possibly accounting for the increase in weight loss.

6.2.2 Kapton

During Phase II it was observed that dry Kapton polyimide film (also known as H-Film) turns purple where contacted with cesium metal. This phenomenon was explained in terms of a 1-electron oxidation-reduction

reaction affording a semiconductive, photoconductive salt layer. In addition to this reaction, liquid cesium seriously reduces the tensile strength of Kapton film in the presence of residual water, probably by hydrolysis of the imide linkage.

In order to further investigate the postulated 1-electron oxidation-reduction reaction, two sets of five samples of 2-mil Kapton were exposed to liquid Cs for 48 hours at room temperature and at 100°C, respectively. Cesium was distilled onto each sample under vacuum using the apparatus described in Reference 1. The test vessels of the room temperature samples were back-filled with dry helium and capped for the reaction period, whereas the 100°C samples remained under vacuum.

The samples exposed at room temperature were removed and quenched in a helium filled glove bag. First they were washed with pure benzene in a benzene-5 percent methanol bath. During the quenching operation, two of the five samples were partially destroyed when they caught fire inside of the helium filled glove bag. They were not used. Each of the remaining samples was then dried in vacuum and sealed in an evacuated tube.

A 1-electron oxidation-reduction reaction should result in a reaction product with increased electrical conductivity. As a test of this hypothesis, one of the vacuum ampules was transported to Dr. A. Rembaum of the Jet Propulsion Laboratory, a specialist in the measurement of the electrical properties of organic materials. He measured the film's resistivity in a nitrogen-filled dry box. It was 10^{13} ohm-cm, as compared with the normal Kapton resistivity of 10^{18} ohm-cm.

This 10^5 increase in electrical conductivity is believed to be conservative, since quenching the film in the methanol and benzene solution immediately following its removal from the cesium very likely depleted the surface of the film of current carriers. Thus, the possibility exists that the resistivity before quenching could have been one to several orders of magnitude lower.

Another of the exposed samples was used in a measurement of electron spin resonance (ESR) spectrum. An extremely strong signal was measured at 3325 gauss and 9.36 GHz, with no associated fine structure.

Two possible sources of such a signal are organic free radicals and trapped electrons.

Both the resistivity and ESR measurements support the hypothesis that the deep purpose-red reaction product is formed by one electron oxidation-reduction, or a kind of solid-state solvation of the electron from cesium.

The samples exposed at 100°C had an unexpected property. When the samples were removed from the cesium in the glove bag, they broke into small fragments. Further, several small detonations occurred while trying to handle these fragments with tweezers. Sample handling was suspended for safety reasons.

The three hypotheses listed below have been formulated to explain the detonations. However, no further effort has been expended on understanding this phenomenon.

- Cesium formed a complex with the Kapton film which is more sensitive to the small amount of O₂ remaining in the glove bag.
- Cesium formed a complex with the film which is shock and/or friction sensitive.
- Cesium degraded the film and formed organo-metallic compounds which are shock sensitive.

Since the glove bag had been flushed with helium several times prior to opening the test vessels, it is believed that very little oxygen was present. Furthermore, by the time the 100°C sample vessels were opened, bulk cesium from the other samples was in an open container in the bag which would have removed the O₂ by reacting with it. The appearance of the cesium surface gave no indication of such a reaction and indicates little or none was present.

6.3 MERCURY ION BEAM TESTS

During Phase III ten organic material samples which had been exposed to $\sim 1/4 \text{ ma/cm}^2$ 3 kev Hg⁺ for various time periods were examined. Eight of these samples (Teflon FEP and Kapton films; S13G, Z93, and PV100 white paints; Cat-a-lac and 3M 401C10 black paint; RTV41, Silicone rubber) are representative of many non-metallic materials found on spacecraft surfaces; the remaining two (Tedlar PVF and linear polypropylene) are structurally similar to Teflon FEP and were tested after very high Teflon FEP erosion rates had been detected.

These exposures were made in the facility described in Appendix A, and the experiment was also used to obtain the erosion data presented in Section 5.

6.3.1 Chemical Analysis

Following erosion depth measurement, exposed samples of organic materials were tested for chemical changes which might have resulted from ion bombardment.

The analytical techniques employed on the various samples included: attenuated total reflectance (atr) infrared (ir) spectral analysis, transmission ir spectral analysis, x-ray fluorescence, electron microprobe analysis, and solubility tests.

Infrared spectra obtained using the atr technique record the characteristic bands of functional groups very near the surface of samples, whereas transmission spectra provide information about the functional groups present in the bulk of the samples. The appearance of new, or changes in old, ir bands following Hg^+ beam exposure would denote changes in the structure of the organic molecules present. However, because of the sensitivity limits of the ir spectrophotometer and the nature of the samples, functional groups responsible for altered ir spectra must be present in concentrations greater than 5 percent in order to be observed.

X-ray fluorescence and electron microprobe analysis were used to test for the presence of metallic contaminants. Of the two, the microprobe is the more sensitive instrument and provides the means to accurately determine the location of a metallic contaminant on the surface of a sample.

Solubility tests were performed on appropriate samples to determine if exposure to the Hg^+ beam had resulted in an increase or decrease in solubility due to lowering of molecular weight or cross linking, respectively.

6.3.2 Results and Discussion

We begin with general observations and results that are applicable to some extent to all of the materials tested. Other more specific observations concerned with the individual materials follow.

Representative samples of each of the test materials were subjected to atr and/or transmission ir analysis. Comparison of the spectra of the exposed and unexposed samples of each type of material failed to reveal any important differences in the spectra. These results indicate that no substantial changes have occurred in the molecular structure of the organic portions of the test materials as a result of the mercury ion bombardment. However, the data do not preclude the occurrence of local chain breaking, with volatilization of the fragments produced, and/or cross-linking.

All of the organic materials tested underwent some change in appearance during exposure to the beam. Low absorptance samples were darkened. Surface textures were altered. Many 60- and 75-degree angle samples appear to have received thin deposits of metal from the sampleholder.

Darkening of low absorptance samples, such as white paints and RTV-41, was observed on coupons with all angles. Some of the darkening of the higher angle coupons may have resulted from metallic deposits as discussed below. However, separate measurements have shown that the bombardment of such coatings by energetic particles increases their solar absorptance. These experiments include those with (normally incident) mercury ions discussed in Section 8 and those with photons and noble gas ions performed by other workers³⁻⁷.

In addition to changes in color, changes in surface texture were noted for most of the materials. Samples which were originally smooth (e.g., Teflon FEP and Kapton) were roughened, and materials with a very rough initial texture (e.g., S-13G) were smoothed to some extent.

The apparent accumulation of thin metallic deposits on some high angle samples may be understood from the geometry of the experiment. First, these samples have a "view factor" with unshielded areas of the sample holder sides and back. Second, because they have a small projected area normal to the beam, they receive a smaller flux of ions (which are capable of removing deposits they bombard) than do the low angle samples. It is also noteworthy that extremely thin metallic films are detectable by visual examination. Most metal films 100Å thick are nearly opaque and films of ~10Å thicknesses are usually visible. Thus,

where observed at all, the metallic deposits were probably rather thin. Some shielding improvements were made on the sampleholder to further reduce the arrival of extraneous metals at sample surfaces prior to the 1 kev Hg^+ erosion rate measurements.

6.3.2.1 Teflon FEP

Teflon repeatedly exhibited a remarkably high erosion rate. Its surface topography was also the most dramatically affected of all the samples. Figure 6-1 is a photograph of the five coupons after approximately 1-hour exposure to the 3 kev Hg^+ beam. The original smooth surface shadowed by the flat head screws is visible at each end of the samples. The appearance of the 0-degree sample was mostly that of its aluminum substrate, while the 30- and 45-degree samples showed a modest number of fine needles of Teflon projecting from the surface along the ion beam axis, some of which were 5-mils high. A much greater density of needles was formed on the 75-degree sample. Some of the needles were similar to those on the low angle coupons, but examination at 100X revealed densely packed tiny needles as well. Apparently it is these tiny needles that cause the 75-degree coupon to have such high reflectance. A puzzling observation was made on the 60-degree coupon of a Teflon FEP set exposed for 2 hours. Its surface looked like wet sheep's wool; it had thickly packed, long curved, very small diameter "hair". Figure 6-2 is a closeup of this sample.

It is suspected that these properties derive from Teflon's molecular structure, which is that of a linear addition polymer. This structure may enhance physical sputtering and/or permit various forms of chemical attack.

"Physical" sputtering in this energy regime is the ejection of surface atoms of a target resulting from fast particle impact followed by multiple momentum-transferring collisions between target atoms. It is possible that momentum is more effectively propagated down Teflon FEP's long, relatively independent molecular chains than it is down the cross-linked chains of the other polymers tested or through the crystal lattices of metals. Presumably the momentum remains better focused because of little interaction between adjacent chains. On the other hand, uncross-linked polymers have more rotational degrees of freedom than crosslinked ones, which may provide compensating energy dissipation modes.

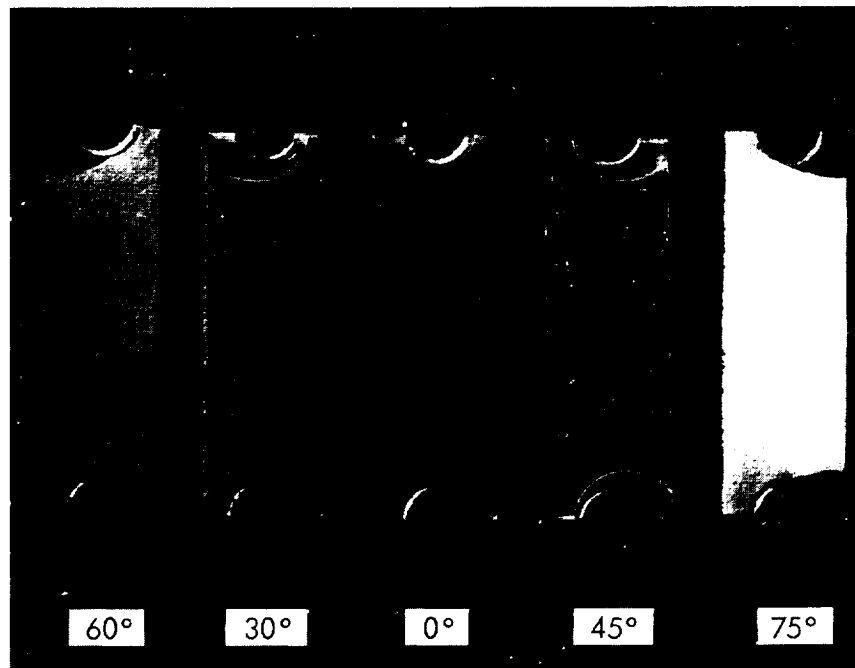


Figure 6-1. Full Set of 5-mil Teflon FEP Samples
After ~1 Hour of 3 kev Hg^+ (2.6X)



Figure 6-2. Sixty-degree Coupon With 5-mil Thick
Teflon FEP After ~2 Hours Exposure
to 3 kev Hg^+ (10X)

Probably a more important medium for rapid mass removal is chain scissions and depolymerization followed by the evolution of monomer gases. Energetically, many (few ev) polymer bonds can be broken by a single 3-kev bombarding particle, and as is shown below, the possibility exists for depolymerization through chemical attack as well.

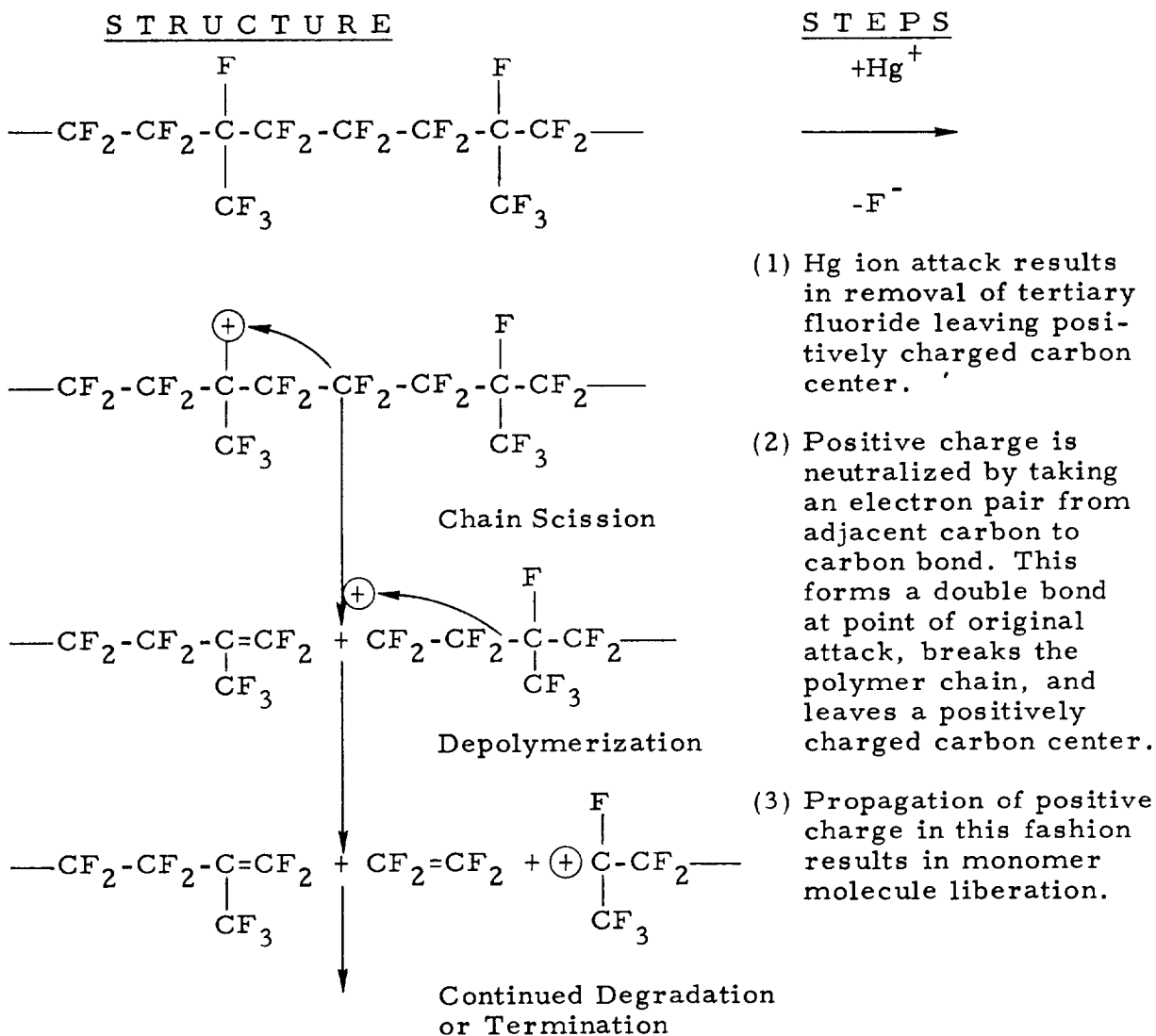
Of the materials originally chosen for test, Teflon FEP is unique in being a linear, fluorine-containing polymer which can undergo both chain scission and depolymerization. Chain scission alone would result in a lowering of molecular weight and a consequent change in mechanical properties. Depolymerization would result in a more drastic reduction of molecular weight and, in the case of Teflon FEP, a volatilization of the polymer into the gases tetrafluoroethylene ($\text{CF}_2=\text{CF}_2$) and hexafluoropropene ($\text{CF}_3\text{CF}=\text{CF}_2$). The other polymeric materials exposed to the ion beam are either highly crosslinked (e.g., silicones and epoxies) and so not subject to loss of molecular weight by random chain scission, or linear (e.g., Kapton polyimide) but not readily depolymerized in the absence of strong bases.

Several modes of chemical attack are possible in addition to the breaking of polymer bonds by kinetic impact from energetic particles. The very high energy of the mercury ion beam ($>69,000$ kcal/mole) renders the assignment of a specific mode of chemical degradation extremely difficult. One likely pathway is outlined in the chemical equations below. This mechanism involves the removal of a fluorine anion by a mercury cation to leave a positively charged carbon atom. The removal of the tertiary fluorine is shown because its carbon-to-fluorine bond is the weakest; however, the very high energy Hg ions are probably not that selective. Neutralization of the carbon ion results in chain scission and the creation of a new positive carbon ion. In the next step a tetrafluoroethylene monomer molecule is liberated (depolymerization) and a new positive carbon ion is produced. The process of depolymerization may continue until terminated by some anion (e.g., F^-) or molecule (e.g., H_2O), by crosslinking, or until the polymer chain is completely degraded.

Under favorable conditions, it would be possible to observe ir bands for the double bonds created in the chain scission step. These bands were not evident in the samples, which indicates that their concentration is

below 5 percent. However, low concentration would be expected since these double bonds are only associated with the end groups on long polymer chains.

POSTULATED DEGRADATION OF TEFLON FEP BY Hg^+



Two organic materials with chemical structures similar to Teflon FEP, i.e., linear addition polymers, were added to the tests after Teflon's high erosion rate was discovered. These were poly (vinyl fluoride) film (Dupont "Tedlar PVF") and linear polypropylene. (Teflon TFE would have been another interesting material; however, a suitable sample was not available.) Both samples exhibited average rather than elevated erosion rates, indicating that, in contrast to Teflon FEP, they

crosslink more rapidly than they depolymerize and that rapid erosion by high energy ions is not a characteristic of all linear addition polymers.

6.3.2.2 White Paints

PV100, Z93 and S13G white paints were darkened as well as eroded. The darkening of the PV100 samples was uniformly distributed across the entire surface of the samples and limited to a thin layer near the surface. The darkening of the Z93 samples was also confined to the surface but was much less uniformly distributed. The zero degree Z93 sample had a "mud flats" appearance and the shiny aluminum substrate could be seen at the bottom of the cracks in the eroded surface. The exposed S13G samples had been smoothed relative to the unexposed surface. The greatest change in its surface texture occurred on the 0-degree sample. The 0- and 30-degree samples had a "shell" or off-white color. The higher angle coupons generally had shiny deposits distributed in spots over the surfaces. These spots occur on the shadow side (relative to the mercury ion beam) of surface projections. All three materials had a larger concentration of dark deposits on the higher angle coupons than on the lower angle ones.

6.3.2.3 Kapton

The films were bonded to the aluminum substrate with poly (vinyl acetate) adhesive. During exposure most of the sample edges curled free of the backing, and one or two were completely unbonded. This is not a surprising result since aromatic polyimides, as a polymer class, do not form good adhesive bonds.

The unbonded sections of Kapton showed evidence of overheating. The well-bonded areas developed a textured appearance. The 60- and 75-degree samples were "frosty" over the entire surface, while the other angle samples had frosty and smooth regions.

6.3.2.4 RTV41

The exposed samples of this white, amine cured silicone coating have uniformly discolored (greyish) surfaces with the exception of some shiny areas on the 60- and 75-degree samples and a number of fairly large pits in the surface of all of the specimens. These pits appear to be bubbles, present in the RTV41 coatings before bombardment, which were exposed by the erosive action of the ion beam.

6.3.2.5 Black Paints

Both Cat-a-lac and 3M 401-C10 velvet black epoxy paints developed surface pits. The 45-, 30- and particularly the 0-degree samples have a greater number of surface pits than the high angle and unexposed (control) samples. These pits are probably responsible for the apparent difference in reflectance between the low angle and unexposed coatings. Differential sputtering of the polymeric binders and the inorganic fillers is a possible cause for these surface changes.

6.4 CONCLUSIONS AND RECOMMENDATIONS

The known and postulated chemical effects of mercury and cesium ion and atom beams on typical spacecraft materials are summarized in Table 6-2.

Immersion of Teflon FEP in liquid cesium, which was reported in Reference 1, produced a black, carbon surface layer through destruction of C-F bonds at the surface. This layer will conduct electricity, and it provides a breakdown path for high voltages. Since Teflon FEP is a popular spacecraft surface material, it should be exposed to cesium ion and atom beams to determine its sensitivity to the limited quantities of cesium to be encountered on an electrically propelled spacecraft. It is also possible that similar but less fluorine-rich materials, (e.g., Kel-F, Tedlar PVF) might be substituted for Teflon FEP. Such substitute materials should be screened by immersion and ion beam exposure tests.

Additional cesium immersion experiments with Kapton were consistent with the results reported in Reference 1. Resistivity and ESR measurements support the hypothesis that the deep purple-red reaction product is formed by 1-electron oxidation-reduction. As with Teflon FEP, beam experiments are clearly indicated, and both materials are under test in Phase IV of this program.

The other organic materials tested appear to be reasonably chemically stable toward both Hg and Cs ions and atoms and the question of their use in spacecraft may be governed by other criteria. The only exception to that statement is the avoidance of materials subject to severe basic hydrolysis (see Table 6-2) in areas where moisture may survive in a space environment for a time after electrostatic thruster operation is initiated.

Table 6-2. Chemical Effects of Cs, Cs⁺, Hg and Hg⁺ on Typical Spacecraft Materials

MATERIAL	TYPE	EXTENT OF DEGRADATION ^a BY			
		Cs	Cs ⁺ , Hg ⁺	CsOH ^b	Hg
H-FILM (KAPTON)	POLYIMIDE	Turns deep purple due to one electron oxidation-reduction; increased electrical conductivity ² (probably photoconductive)	MODERATE ^d	(SEVERE HYDROLYSIS WITH CHAIN SCISSION)	NONE ^c
TEFLON FEP	POLY (PERFLUORO-ETHYLENE PROPYLENE)	Turns black; C & CsF forms at surface ^c	SEVERE, DEPOLYMERIZATION AND VOLATILIZATION ^{d,e}	(NONE)	NONE ^c
RTV41	AMINE CURED SILICONE	(LITTLE OR NONE)	MODERATE ^{d,e}	(MODERATE BY HYDROLYSIS)	(NONE)
3M BLACK	POLYESTER	MOTTLED GREY ^c	MODERATE ^{d,e}	(MODERATE BY HYDROLYSIS)	(NONE)
CAT-A-LAC BLACK	AMINE CURED EPOXY	(LITTLE OR NONE)	MODERATE ^{d,e}	(MODERATE)	(NONE)
PV100	SILICONE-ALKYD RESIN; TiO ₂ PIGMENT	LITTLE OR NONE ^c	MODERATE WITH DARKENING ^d	(MODERATE TO SEVERE DUE TO HYDROLYSIS)	(NONE)
DELFIN	POLYACETAL	LITTLE OR NONE ^c	(MODERATE) ^d	(NONE)	NONE ^c
SYLGARD 182	SILICONE	LITTLE OR NONE ^c	(MODERATE) ^d	(MODERATE)	NONE ^c
SMRD 745	EPOXY	LITTLE OR NONE ^c	(MODERATE) ^d	(LITTLE OR NONE)	NONE ^c
GT-100	POLYESTER	LITTLE OR NONE ^c	(MODERATE) ^d	(SLIGHT TO SEVERE DUE TO HYDROLYSIS)	NONE ^c
EPON 934	AROMATIC EPOXY	(LITTLE OR NONE)	(MODERATE)	(SLIGHT)	(NONE)
RTV-560	POLYMETHYLPHENYL-SILOXANE	(LITTLE OR NONE)	(MODERATE)	(NONE)	(NONE)
EPIALL 1914	EPOXY NOVOLAC	(LITTLE OR NONE)	(MODERATE)	(SLIGHT)	(NONE)
S13G	METHYL SILICONE + ZnO	NONE ^c	MODERATE, WITH DARKENING ^{d,e}	(MODERATE)	(SLIGHT OR NONE)
Z93	POTASSIUM SILICATE + ZnO	NONE ^c	MODERATE, WITH DARKENING ^e	(MODERATE ETCHING)	(SLIGHT OR NONE)
Al ₂ O ₃	-	(SLIGHT TO MODERATE AT STRAIN POINTS)	(SLIGHT)	(SLIGHT ETCHING)	(SLIGHT OR NONE)
BeO	-	(SLIGHT TO MODERATE AT STRAIN POINTS)	(SLIGHT)	(SLIGHT ETCHING)	(SLIGHT OR NONE)
CORNING 7740	PYREX	(SLIGHT TO MODERATE AT STRAIN POINTS)	(SLIGHT TO NONE)	(SLIGHT ETCHING)	(SLIGHT OR NONE)
CORNING 0211	PYREX	(SLIGHT TO MODERATE AT STRAIN POINTS)	SLIGHT TO NONE ^e	(SLIGHT ETCHING)	(SLIGHT OR NONE)

a. INFORMATION IN PARENTHESES IS POSTULATED, BASED ON ANALOGOUS LITERATURE DATA; INFORMATION WITHOUT PARENTHESES IS DATA FROM LITERATURE AND CURRENT WORK.

c. IMMERSION TESTED FOR 48 HOURS.

d. SURFACE CHAIN DEGRADATION AND/OR CROSS-LINKING PROBABLE.

e. EXPOSED TO 3keV Hg⁺

6.5 REFERENCES (SECTION 6)

1. D.F. Hall, "Electrostatic Propulsion Beam Divergence Effects on Spacecraft Surfaces," Final Report, Vol. I, JPL Contract No. 952350, August 1970, TRW Systems, Redondo Beach, Calif.
2. D.F. Hall, "Evaluation of Electric Propulsion Beam Divergence Effects on Spacecraft," 08965-6013-R0-00, Final Report Contract No. NAS7-575, September 1969, TRW Systems, Redondo Beach, Calif.
3. E.R. Streed, "An Experimental Study of the Combined Space Environmental Effects on a Zinc-Oxide-Potassium-Silicate Coating," AIAA Paper No. 67-339, April 1967.
4. S.A. Greenberg, et al., "Damage Mechanisms in Thermal Control Coating Systems," AFML-TR-67-294, September 1967.
5. "Study of Environmental Effects upon Particulate Radiation Induced Absorption Bands in Spacecraft Thermal Control Coating Pigments," Lockheed Report 6-78-68-45, Contract No. NAS 2-4353, Final Report for 22 May 1967 to 27 January 1969.
6. L.B. Fogdall, et al., "Ultraviolet and Electron Radiation Effects on Reflectance and Emittance Properties of Thermal Control Coatings," AFML-TR-70-156, July 1970.
7. J.E. Gilligan, and G.A. Zerlaut, "The Space Environment Stability Problem in White Pigment Coatings," Institute of Environmental Sciences 1971 Proceedings, pp. 447-457, April 26-30, 1971.

—

—

—

7. METALLURGICAL EFFECTS OF PROPELLANTS

7.1 INTRODUCTION

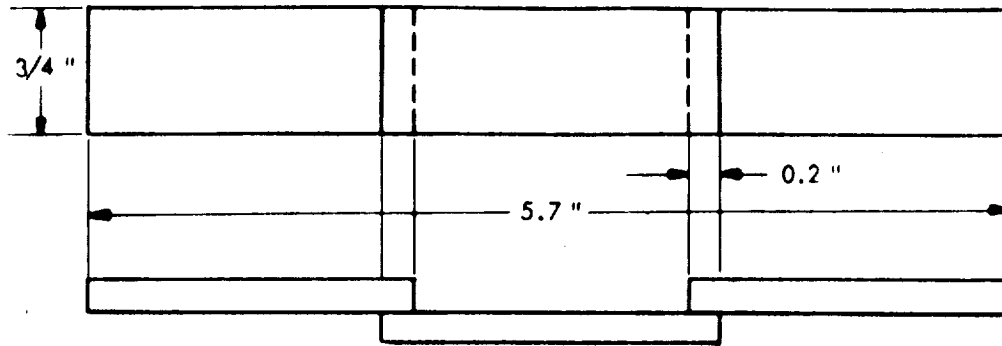
In Reference 1 it was reported that the mechanical properties of solder were markedly affected by immersion and surface coating of samples with mercury. Since the solder "failed" these relatively severe tests, it was recommended that further tests be devised which (1) more closely simulated the conditions of exposure in space, and (2) tested, either directly or indirectly, the effect of mercury on the critical properties of solder in its most common spacecraft surface application, namely, in solar arrays. Exposure to atomic or ionic beam of mercury will satisfy the first mentioned requirement. A brief review of the uses and failure modes of solder in solar arrays was undertaken as the first step in satisfying the second requirement.

Soft solder is used extensively in bonding solar cells to solar cell interconnects. The most common cause of failure of these bonds on deployed solar arrays is differential thermal contraction between silicon and the metal interconnects during temperature cycles, particularly during cooldown. However, it is not the practice of light weight solar array engineers to specify the required or desired strength of cell-to-interconnect solder bonds, apparently because stress levels are neither conveniently calculated nor measured on these tenuous structures.

Nevertheless, solder bond failures do occur, and our previous tests suggest that the mechanical properties of solder are sensitive to even small quantities of mercury. Thus, a simple test of the effects of a mercury beam exposure was designed.

7.2 TEST DESIGN AND RESULTS (EARLY SERIES)

The experimental approach selected was to expose a series of double lap shear tensile test specimens in the facility described in Appendix A. Figure 7-1 shows the detail of the specimen configuration. Brass was chosen because it forms a strong interface bond with solder. Thus, joint failure would occur in the solder itself and test results would reflect the properties of bulk solder rather than a solder interface (see Figure 7-1).



MATERIAL: 3/32 " BRASS

Figure 7-1. Design of Soft Solder Lap Joint Tensile Test Specimens

The initial specimen preparation was as follows. The ends of the as-sheared pieces were cleaned with abrasive cloth to remove any gross oxide and the samples were then vapor degreased. The surfaces to form the lap joint were pretinned by using flux core Sn 62 solder. A thin coating was formed and the surface was wiped to leave a smooth layer of solder. Finally, the 3/4- x 2-inch samples were clamped in a fixture which would produce the desired configuration. The lap area was fluxed and the solder made to flow by resistance heating. The criteria used to determine an acceptable sample were that the solder joint show good wetting and that there was a continuous fillet in the joint. The solder fillets on both sides varied from about 0.020- to 0.040-inch radius. A central mounting hole was drilled in each sample, and the samples were given a final vapor degreasing to remove any residual flux. (This technique was later modified and will be explained in detail in following sections.)

One of two preliminary samples was surface-coated with mercury by brief immersion in the liquid and aged or "soaked" for 3 days at room temperature. The two samples were then tensile tested to determine the effect of mercury on the joint. The exposed sample had a breaking strength of 750 psi while the unexposed sample had a breaking strength of 6100 psi.

Two series of test specimens were prepared for testing. The first series employed mercury atom beam exposures while the second

employed quick immersion of specimens in liquid mercury.

In preparation for the first series, the QCM fixture was modified so that six specimens could be mounted to it and their temperatures controlled during exposure. This was accomplished by fitting the fixture with a metal mounting "bridge" to which specimens were screwed. An RTV interface compound was used. Figure 7-2 is a photograph of the modified and loaded fixture. The quartz crystal is visible between the two sets of three double lap shear specimens.

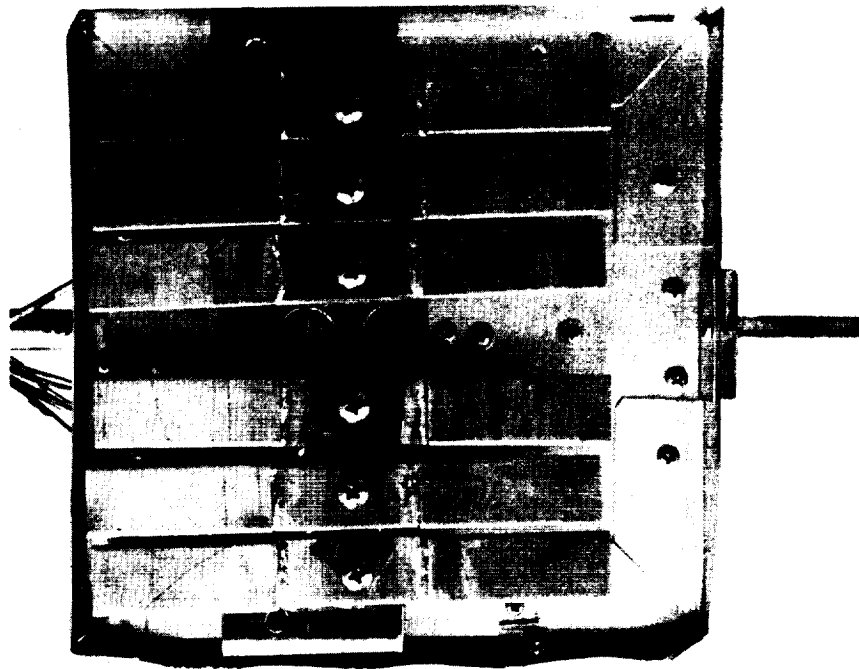


Figure 7-2. Soft Solder Lap Shear Specimens Mounted on QCM Fixture Prior to Hg Beam Exposure

Two exposures of six samples each were made in the experimental facility. In both tests the incident flux of mercury atoms was approximately 6×10^{13} atoms/cm²-sec, the sample temperature 22°C, and the post-exposure "soak" before tensile testing approximately 36 hours. They differed in that Test No. 71-2 was a 36-hour beam exposure and No. 71-3 was a 90-hour beam exposure. The results of these tests and the control group appear in Table 7-1. There was a slight indication of reduced ultimate tensile strength resulting from mercury beam

Table 7-1. Hg/Soft Solder Lap Shear Tensile Test Data (Natural Fillet)

Test No.	Sample Treatment	Ultimate Tensile Strength (psi) x_i	Arithmetic Mean \bar{x}	Standard Error* $\sigma_{\bar{x}}$
71-1	No Exposure (Control Group)	6125 5920 6550 6000 4800	5879	650
71-2	$\Gamma \sim 6 \times 10^{13}$ for 21 hr; 36 hr soak; 22°C	4320 4910 4950 5250 5260 6540	5205	730
71-3	$\Gamma \sim 7 \times 10^{13}$ for 90 hr; 36 hr soak; 22°C	5350 4250 5700 5550 5650 4000	5083	756
71-4	Quick Immersion; 36 hr soak; 22°C	2786 3247 6245 5790	4517	1750
71-5	Quick Immersion; 96 hr soak; 22°C	5300 4860 4000 4450	4652	556

$$* \sigma_{\bar{x}} = \left[\frac{1}{n(n-1)} \sum (x_i - \bar{x})^2 \right]^{1/2} \quad (\text{Reference 2})$$

exposure: the average value of Tests 71-2 and 71-3 is 5144 psi as compared with 5879 psi for the control group. However, since there is presumably only a 68 percent probability that a repetition of these measurements would yield average (\bar{x}) values within $\pm \sigma_{\bar{x}}$ of the \bar{x} values tabulated, this trend is far from conclusive.

These results motivated the second series of tests, which were to more conclusively verify that these specimens were sensitive to quick immersion in liquid mercury, as were the solder tensile bars of Reference 1. As before, the immersion technique was to force the specimens into a cylinder filled with mercury and allow the bouyant force of the mercury to expel the samples. The total time in the mercury was less than 1 second.

A total of eight specimens were treated--four were tested after 36 hours and four after 92 hours. The tensile strength of the samples in Test No. 71-5 is clearly less than those of the control group, indicating that the specimen design is sensitive to quick immersion. However, in a sense Test No. 71-4 is even more significant. Note that the data range for this group is very large; two samples tested at ~3000 psi and two at ~6000 psi. Inspection of the samples revealed that the two low-valued samples had very little solder fillet whereas the fillet on the high-valued samples was larger than average. In contrast, the samples of Test No. 71-5 did not have unusual fillets. It was concluded, therefore, that fillet configuration may have been an important uncontrolled variable in these tests. In all subsequent tests the solder fillet was removed by milling to provide a square corner.

7.3 TESTS WITH MILLED FILLET SAMPLES

7.3.1 Immersion Tests

A number of lap shear specimens with milled fillets were surface-coated with mercury by quick immersion and were divided into four groups. Two groups were "aged" at room temperature for 30 and 120 hours while the other two were aged at 50°C for these time periods.

Tensile tests were performed after the two time periods to determine the effect of both time and temperature on the strength of the solder joint. Table 7-2 presents the tensile results of the treated samples and also shows the results from unexposed samples. Comparison of this data with that obtained from specimens with unmilled fillets (Table 7-1) immediately reveals substantial differences in the size of the standard error in the two control groups. The $\sigma_{\bar{x}}$ of Test No. 71-6 is 1/10 that of Test No. 71-1. Thus, milling the fillet improves sample uniformity significantly.

Both of the sets of 30-hour samples (71-7, 71-8) have higher average tensile values than the control group, although the standard errors are large enough to undermine the significance of this fact somewhat. High tensile strength is consistent with the results of quick

Table 7-2. Tensile Strength of Milled Fillet Soft Solder Lap Shear Specimens of Mercury Quick Immersion Test

Test No.	Sample Treatment	Ultimate Tensile Strength (psi) x_i	Arithmetic Mean \bar{x}	Standard Error $\sigma_{\bar{x}}$
71-6	Control	2070 2260 2050 2313	2173	66.4
71-7	Quick Immersion; Soak 30 hr; 23°C	2294 2683 1810 3450	2559	346.5
71-8	Quick Immersion; Soak 30 hr; 50°C	2500 3650 1677 2315	2535	411.2
71-9	Quick Immersion; Soak 120 hr; 23°C	2550 1252 1717 * *	1840	379.0
71-10	Quick Immersion; Soak 120 hr; 50°C	1135 968 1401 * *	1168	126.0

*Solder joint fractured during test set up.

immersion of soft solder tensile bars¹ and suggests that brittle inter-metallic compounds are formed. Intermetallic compounds are typically brittle. The phase diagrams of mercury with both tin and lead show intermetallic compounds.

Both sets of 120-hour samples (71-9, 71-10) have lower average tensile strengths than the control group. Here the evidence of significant change due to mercury exposure is quite strong. Four of the specimens fractured during set-up in the tensile tester. With one exception, each of the measured values is less than each of the members of the control group. The size of the standard errors in tests 71-6 and 71-10 virtually preclude overlap. Hand flexure of the unbroken end of the double lap specimens showed that the exposed samples were extremely brittle and that they had low tolerance to any bending.

These test results suggest that as the sample aging proceeded a larger and larger percentage of the solder volume became a mercury amalgam. In this model, the brittleness observed is ascribed to the presence of residual intermetallic compounds and low strength to the large percentage of amalgam.

The conclusion of this test is that mercury doses produced by approximately 1-second immersion of soft solder lap shear specimens in liquid mercury are unacceptable if the solder joint must retain mechanical strength. As discussed previously, soft solder bonds between innerconnects and solar cells on solar arrays must retain mechanical strength.

7.3.2 Mercury Beam Tests

The immersion test results reported above encouraged us to undertake another test utilizing a mercury atom beam, which subjects the specimen to a much smaller quantity of mercury. It should be noted, however, that the temperature and/or surface condition of the sample during exposure could be such that all the mercury re-evaporates before it can diffuse into the solder. A technique for dealing with this uncertainty is mentioned below.

An additional 16 solder lap shear specimens were prepared with milled fillets. Six were mounted on the QCM fixture, which provides specimen temperature control during beam exposure, as described previously.

As before, the specimens were positioned normal to the beam axis. Therefore, the view factor between the milled fillets and the beam source was rather small. The mercury arrival rate at the sample plane (normal to the beam) was approximately 10^{14} atoms/cm²-sec. The exposure was 90 hours long and the sample temperature 20°C. Following the exposure, the samples were removed from the vacuum chamber and allowed to "soak" for 120 hours at room temperature. Then they were tensile tested. The other joint of the exposed double lap specimens was tensile tested after 790 hours to determine the effect of a longer "soak" time.

Table 7-3 presents the data for both the control and exposed samples. The exposed samples have slightly higher average tensile values than the control group, but the increase is probably not significant in view of the magnitude of the standard errors. Therefore, it is concluded that this mercury exposure was insufficient to affect the joint strength.

Table 7-3. Tensile Strength of Milled Fillet Soft Solder Lap Shear Specimens of Mercury Atom Beam Test

Test No.	Sample Treatment	Ultimate Tensile Strength (psi) x_i	Arithmetic Mean \bar{x}	Standard Error $\sigma_{\bar{x}}$
71-11a	Beam Exposure	4993	4761	128
	90 hr;	5151		
	10^{14} Hg ^o /cm ² -sec;	4671		
	20°C	4234		
	120 hr soak	4731		
		4787		
71-11b	Beam Exposure	5450	4616	225
	90 hr;	4350		
	10^{14} Hg ^o /cm ² -sec;	4400		
	20°C	5100		
	790 hr soak	4450		
		3950		
71-12	Control	3845	4668	245
		3850		
		5230		
		4546		
		5220		
		5263		
		5703		
		3795		
		3832		
		5402		

In the next test several steps were taken to increase the effective mercury exposure. First, 14 specimens were exposed simultaneously instead of six, providing better experimental "statistics". Second, the specimens were positioned at a 45-degree angle to the beam, which substantially increased the view factor between the milled solder fillet and the beam source, and provided a corresponding increase in mercury atom arrival rate at this surface. Figure 7-3 is a photograph of the mounted specimens. Third, the beam source was operated at a flux level approximately twice previous values, which also served to increase the mercury atom arrival rate at the solder fillet. However,

the exposure duration was approximately one-half previous values, so the total quantity of mercury arriving at a plane normal to the beam was about the same as before. Finally, the exposure was begun by cleaning the specimen surfaces in situ to increase the probability that an absorbed mercury atom would diffuse into the solder rather than be desorbed. This was accomplished by sputtering the surface with $200 \mu\text{a}/\text{cm}^2$ of 3 kev Hg^+ for 12 minutes. Since the ion and atom beam sources are one, the termination of sputtering and commencement of atom beam exposure was accomplished by switching off the thruster potentials.

The ultimate tensile strength of the exposed specimens after approximately 120 hrs of "soak" and of the control group are shown in Table 7-4. The 1500 psi value was so unlike the other values that it has been excluded from the calculation of the mean and standard error. It was probably a poor joint to begin with. Clearly, the beam exposure had not affected the tensile strength of the joints.

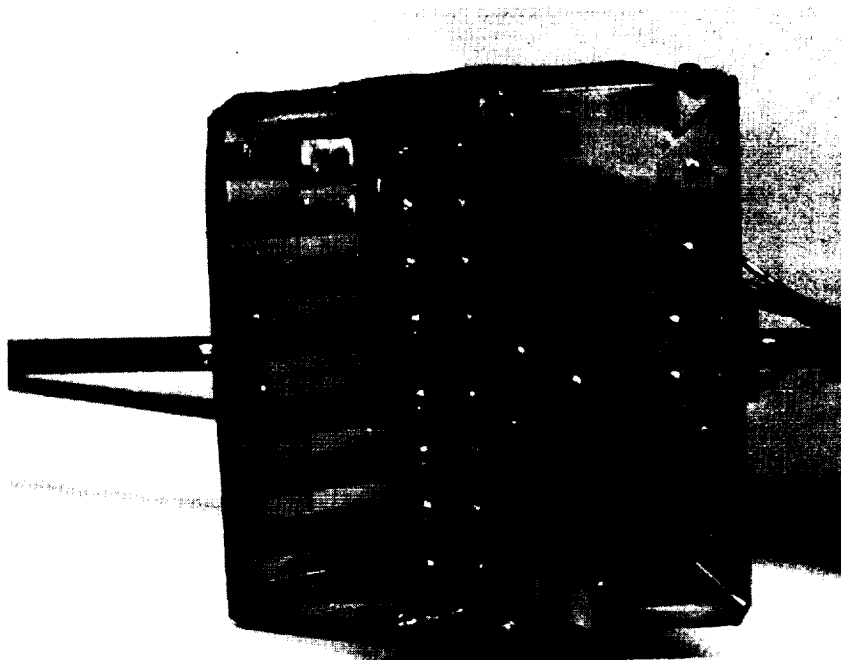


Figure 7-3. Sixteen Double Lap Shear Solder Joint Specimens Mounted on QCM Fixture Prior to Mercury Atom Beam Exposure

Table 7-4. Tensile Strength of 45-degree Milled Fillet Soft Solder Lap Shear Specimens of Mercury Atom Beam Test

Test No.	Sample Treatment	Ultimate Tensile Strength (psi) x_i	Arithmetic Mean \bar{x}	Standard Error $\sigma_{\bar{x}}$
71-13	Control	5300 5000 4900 4750 4650 3300 4350 5100 3700 4450 3150 3150 4700 2600 2700	4120	238
71-14	Beam Exposure after sputter clean- ing: 2×10^{14} $\text{Hg}^0/\text{cm}^2\text{-sec}$ for 45 hr @ 20°C ; 120 hr soak	4550 4350 4850 4600 3550 3550 5000 5000 4000 4000 3950 4350 3150 (1500) (excluded from \bar{x} and $\sigma_{\bar{x}}$)	4223	162

7.3.3 Comparison Between Beam and Immersion Tests

The results of the tests described in the previous sections were that the atom beam exposures had no measurable effect on solder strength whereas quick immersion had a marked effect. In this section, factors which might explain this difference in the results of the two types of tests are discussed.

First, the total number of mercury atoms which arrived at the solder surface in the beam tests is probably less than the quantity of mercury which remains on the surface following a ~1 second immersion. In the absence of any re-evaporation or diffusion, the beam dose would have amounted to an approximately 0.1 mil thick layer. This is perhaps a factor of 10 to 50 less than the quantity remaining on the surface following quick immersion.

Since lead and tin diffuse into mercury rather rapidly, the evaporation rate of the mercury layer acquired by immersion is soon inhibited, increasing the time available for the mercury to diffuse into the solder. However, as discussed below, soon after the commencement of the beam exposures, the situation there is probably just the reverse: most mercury re-evaporating rather than diffusing.

The equations describing the solder surface during mercury beam exposure are:

$$\frac{d\sigma}{dt} = \Gamma_a + \Gamma_{\text{evap}} + \Gamma_{\text{diff}} \quad (1)$$

where

σ = surface density of mercury (atoms/cm²)

Γ_a = arrival rate of mercury per unit area

Γ_{evap} = evaporation rate of mercury per unit area

Γ_{diff} = rate of diffusion of mercury from the surface per unit area

The quantity, Γ_a , is controlled by the experimenter. The quantity, Γ_{evap} , can be expressed as

$$\Gamma_{\text{evap}} = \frac{\sigma}{\tau} \quad (2)$$

where

τ = time constant for evaporation

The quantity, Γ_{diff} , can be expressed as

$$\Gamma_{\text{diff}} = -D \left. \frac{dC}{dx} \right|_{x=0} \quad (3)$$

where

$x = 0$ is the surface on which the mercury beam is impinging
and C is the solution to Fick's Law when the diffusion coefficient is independent of concentration

$$D \nabla^2 C = \frac{dC}{dt} \quad (4)$$

where

D = diffusion coefficient for the component into the system

C = concentration of the diffusing component

t = time

The geometry that most nearly describes that of the experiment is a semi-infinite slab. Therefore, in slab geometry, Equation (4) becomes

$$D \frac{d^2 C}{dx^2} = \frac{dC}{dt} \quad (5)$$

Solutions to this differential equation which are pertinent to the experimental situation may be obtained by proper specification of the boundary conditions. One reasonable assumption is that an equilibrium surface concentration of mercury on the solder is established in time period short in comparison with the exposure times which have been employed (45-90 hrs). A second reasonable assumption is that the location of the mercury/solder interface does not change in time. This will be true if thickness of the mercury layer condensed on the surface is small. Since the evaporation rate of mercury from bulk mercury at 20°C is $\sim 10^{18}$ atoms/cm² · sec and the arrival rate of mercury in the experiment is $\sim 10^{14}$, the equilibrium coverage of mercury is expected to be less than a monolayer.

Therefore we obtain the following solution to Equation (5)

$$C(x,t) = C_o \operatorname{erfc} \left(\frac{x}{2\sqrt{Dt}} \right) \quad (6)$$

where erfc is the complimentary error function and C_o is the density of mercury near the surface and is numerically equal to $\sigma^{3/2}$.

The rate at which mercury is diffusing into the solder per unit area is, from Equation (6)

$$\Gamma_{\text{diff}} = -D \frac{dC}{dx} \Big|_{x=0} = C_o \sqrt{\frac{D}{\pi t}} \quad (7)$$

The total quantity of mercury that has diffused into the solder sample per unit area of exposed surface is

$$S = 2 C_o \sqrt{\frac{Dt}{\pi}} \quad (8)$$

The relative rates of diffusion and evaporation from the surface may now be examined with the use of Equations (2) and (7)

$$\frac{\Gamma_{\text{diff}}}{\Gamma_{\text{evap}}} = \sigma^{1/2} \sqrt{\frac{D}{\tau t}} \quad (9)$$

To estimate an upper bound to the value of this ratio, the expression is evaluated for maximum reasonable values of σ , D and τ are used. A monolayer of mercury is $\sim 1.2 \times 10^{15}$. A large low temperature diffusion coefficient is $10^{-12} \text{ cm}^2/\text{sec}$. A long evaporation lifetime is 1 second. Thus

$$\frac{\Gamma_{\text{diff}}}{\Gamma_{\text{evap}}} < \frac{20}{\sqrt{t}}$$

and within three hours the ratio is less than 0.2.

It is also instructive to estimate the penetration depth of the mercury diffusion into the solder, after say 30 hours of exposure, from the characteristic diffusion length equation

$$d \approx \sqrt{\frac{Dt}{\pi}} \approx 2 \times 10^{-4} \text{ cm}$$

The assumption of infinite solder geometry is consistent with this result.

The conclusion of this analysis is that the quick immersion tests very probably result in a significantly greater quantity of mercury diffusing into the solder. This is because more mercury is applied to the surface and a smaller fraction of the amount applied evaporates rather than diffuses. Thus it is reasonable that the immersion tests affected solder lap joint strength whereas the atom beam tests did not.

7.4 CONCLUSIONS AND RECOMMENDATIONS

In Phase I of the program the metal couples Cs/Au, Cs/solder, Hg/Au, Hg/Ag, and Hg/solder were identified as potentially the most troublesome. However, no metallurgical experiments were planned with gold. (See, however, Sections 5 and 8 for results of mercury beam exposures of silver and gold samples.)

7.4.1 Cesium/Solder (Phase II)

Immersion of eutectic solder in cesium results in rapid, heavy attack. Thus damage rates of solder on warm spacecraft surfaces will be controlled by cesium arrival rates. Lap shear tests such as were performed in Phase III with mercury are recommended.

7.4.2 Mercury/Silver (Phase II)

A metallurgical reaction between silver and mercury has been observed. However, the reaction rate is not rapid and the properties of the reaction products appear to be acceptable.

7.4.3 Mercury/Solder

In Phase II it was concluded that when small quantities of mercury are present in solder, the solder is embrittled, whereas larger concentrations causes solder to become "mushy".

The results of surface coating thin silver solder alloy samples with mercury were identical to that of coating thin silver-free solder samples, indicating that in concentrations of 10 percent or less silver do not significantly reduce degradation of solder strength by mercury.

The Phase III lap shear tests have shown that small quantities of mercury acquired in a 1 second immersion are sufficient to affect joint strength. In contrast rather large atom beam fluxes directed at 20°C samples for periods of several days did not affect joint strength. This latter result is believed to be due, at least in part, to the high re-evaporation rate of mercury at 20°C. Therefore, similar tests at much lower temperatures, i. e., where decreased re-evaporation might more than compensate for the decreased diffusion rate, are recommended.

7.5 REFERENCES TO SECTION 7

1. D. F. Hall, "Electrostatic Propulsion Beam Divergence Effects on Spacecraft Surfaces," Final Report, Vol. I, JPL Contract No. 952350, August 1970, TRW Systems, Redondo Beach, Calif.
2. R. D. Evans, The Atomic Nucleus, McGraw-Hill, p. 762, New York, 1955.

8. DAMAGE OF THERMAL CONTROL COATINGS

8.1 INTRODUCTION

Thermal control coatings are prominent among the classes of solar electric spacecraft surfaces that are sensitive to ion impingement. The complete removal of coatings by sputtering will, of course, significantly affect spacecraft surface temperature. In addition, the ion-bombardment processes which can induce degradation of coatings during their erosion lifetime include: (1) changes in surface topography; (2) implantation of energy within the coating (radiation-type damage); and (3) the chemical/metallurgical reaction of coating materials with implanted ions. Early in Phase I of the program, a literature search was undertaken in an attempt to determine the magnitude of these effects.

The literature search confirmed that optical degradation of spacecraft coatings results from each of the three mechanisms enumerated above¹⁻⁶. In the case of some coatings, the literature suggests qualitative trends regarding the functional dependence of degradation on ion energy, ion species, and ion dose. However, the available information was found to be quite incomplete; no references were found of experiments with Cs or Hg ions, and most of the work reported was at relatively low ion energies. A preliminary experiment performed at TRW with 3 kev Hg^+ on zinc oxide-potassium silicate, a white spacecraft paint, indicated that such coatings are quite susceptible to serious damage by mercury ions.

In view of these various indications that many thermal control coatings will suffer serious damage upon impingement by propellant ions, a carefully controlled experimental technique was devised during Phase I for measuring such degradation.

8.2 EXPERIMENTAL APPROACH

Both the experience in TRW's Thermophysics Section and a review of the open literature⁷⁻⁹ indicated that in some cases bombardment-induced damage to thermal control coatings will "heal" when these coatings are exposed to atmospheric gases. Obviously, healing would not occur at a detectable rate in the high vacuum of deep space where the gas molecules have very low arrival rates. As a consequence, measurements of the

degradation of thermal control coating samples following bombardment by ion beams may be erroneous if the samples are exposed to atmospheric gases prior to measurement.

In addition to errors caused by healing, cesium and mercury atoms implanted near the surface of coatings and metals may react with atmospheric gases and alter surface thermal properties. For these reasons, exposure of damaged samples to the atmosphere represents a potentially serious source of error in laboratory measurements. To avoid this error, the experimental apparatus had to be designed such that the measurement of sample optical properties could be accomplished in situ; i. e., without removal from vacuum. The selected technique employs a constant temperature electrical substitution calorimetric method to provide an absolute measurement of total hemispherical emittance (ϵ_H) and total solar (xenon) absorptance (α_x) in situ before and after the samples are exposed to the ion beam exhaust.

The constant temperature electrical substitution in situ measurements were supplemented with pre- and post-exposure ex situ measurements on spectral and total reflectance laboratory reflectometers for two reasons. First, the ex situ measurements are of known reliability and reproducibility. Pre-exposure ex situ measurements of α_s^* and ϵ_N^* were compared with pre-exposure in situ measurements as a means of calibrating and experimentally ascertaining the accuracy of the in situ test method. The second reason is that differences in the spectral reflectance distributions, before and after exposure to the ion engine exhaust, shed some light on how the ions and atoms affected the samples in spite of atmospheric linked "healing".

Thus, the basic steps followed in measuring the effects of exposure of thermal control surfaces to ion engine exhaust were:

- a) Measure the initial values of α_x (and α_s) and ϵ_N ex situ using the spectral reflectance and total energy instruments of the Thermophysics Laboratory. Apply correction factor to obtain ϵ_H ex situ.
- b) Measure the initial room temperature values of α_x , and ϵ_H in situ in the 4' by 8-foot test (vacuum) chamber while facing the samples into a LN₂-cooled, spectrally black enclosure. (The facility is described in Appendix A, and the in situ instrumentation in Appendix B).

* α_s is "Johnson" solar absorptance; ϵ_N is normal emittance. (See Appendix B, Paragraph 3.)

- c) Bring the samples to the test temperature and remeasure α_x and ϵ_H .
- d) Rotate the samples to face the E-B thruster and expose them to the prescribed ion and/or atom beams.
- e) Rotate the samples back to face into the LN₂-cooled enclosure and measure the post-exposure values of α_x and ϵ_H in situ.
- f) Repeat steps (d) and (e) until the desired particle dose is accumulated. By comparing the values of α_x and ϵ_H measured before and after each exposure, the effect of the ion engine exhaust is obtained.
- g) Remove the samples from the chamber and measure the post-exposure values of α_x and ϵ_H with the laboratory reflectometers.
- h) The effect of atmospheric gases on the values of α_x and ϵ_H was occasionally investigated prior to Step (g) by allowing selective amounts of the ambient gases into the vacuum chamber, repumping down to a proper vacuum ($\leq 10^{-6}$ torr), and remeasuring the in situ thermal radiation properties.

8.3 THERMAL CONTROL COATING DEGRADATION MEASUREMENTS

In situ surface thermal measurements for this program were first performed during Phase II in 1969. The purpose of these early measurements was to make at least a cursory examination of as many of the selected sample materials as possible so as to identify which ones warranted more detailed investigation. These early measurements as well as the more recent and more detailed ones included both mercury ion and mercury atom beam exposures. Before reporting measurements made during Phase III, the results of the Phase II measurements are summarized.

8.3.1 Effect of Mercury Ions (Early Experiments)

Ten sample materials were exposed to various doses of 3 kev mercury ions and the properties were measured in situ. The ion flux used in these tests was approximately 1×10^{15} ions/cm²-sec, and the samples were maintained at approximately 22°C. The results are presented in Tables 8-1a and b. The experimental sequence employed was to pump down the vacuum chamber overnight, cool the LN₂ cold shroud to its steady-state temperature, make in situ pre-exposure measurements of ϵ_H and α_{Xe} (labeled "t=0" in the tables), turn the samples 180 degrees

Table 8-1a. Surface Thermal Degradation Test Results, Mercury Ions
(Sample Temperature $\sim 22^{\circ}\text{C}$, Beam Flux Density $\sim 1 \times 10^{15}$ ions/cm² sec)

Sample Material	Ex Situ Pre Exposure†				In Situ Measurements†										Ex Situ Post Exposure†			
	$\epsilon_S^{(a)}$	$\epsilon_{Xe}^{(a)}$	$\epsilon_N^{(b)}$	$\epsilon_H^{(c)}$	T = 0 hr		T = 0.167 hr		T = 0.667 hr		T = 1.23 hr		Post O ₂		$\epsilon_S^{(a)}$	$\epsilon_{Xe}^{(a)}$	$\epsilon_N^{(b)}$	$\epsilon_H^{(c)}$
					ϵ_{Xe}	ϵ_H	ϵ_{Xe}	ϵ_H	ϵ_{Xe}	ϵ_H	ϵ_{Xe}	ϵ_H	ϵ_{Xe}	ϵ_H				
6-mil Microsheet 2nd Surface V D Aluminum	0.138	0.133	0.842	0.802	0.152 0.170	0.805 0.804		0.187 0.805	0.186 0.1821	0.804 0.8111	0.142	(u)	0.169	0.865	0.166	0.173	0.845	0.804
20-mil Quartz 2nd Surface V D Aluminum	0.118	0.114	0.811	0.778	0.151 0.179	0.779 0.777		0.165 0.779	0.165 0.1591	0.780 0.8031	0.155	0.811	0.147	0.807	—	—	0.809	0.776
3M Velvet Black Paint	0.982	0.982	0.919	0.870	0.888 0.877	0.889 0.885		0.884 0.883	0.876 0.8781	0.886 0.8871	0.900	0.895	0.861	0.889	0.960	0.970	0.915	0.869
RTV-41 Silicone Rubber	0.305	0.265	0.909	0.860	0.244 0.253	0.881 0.878		0.450 0.873	0.446 0.4201	0.874 0.8781	0.486	0.865	0.451	0.857	0.460	0.420	0.909	0.860
Z93 White Paint	0.171	0.117	0.932	0.883	0.147 0.148	0.924 0.904		0.660 0.915	0.762 0.7631	0.915 0.9161	0.841	0.912	0.808	0.912	0.871	0.864	0.935	0.889

(a) Measured on Beckman (modified DK2A).

(b) Measured on Gier Dunkle Quick Emission Inspection Device

(c) Calculated from normal emittance and theoretical correction given in Eckert and Drake, Heat and Mass Transfer, 2nd Edition.

(u) Data unreliable due to instrumentation instability.

† Third figure included to show data trends; not fully significant.

I Remeasured ~ 18 hours later

Table 8-1b. Surface Thermal Degradation Test Results, Mercury Ions
(Sample Temperature ~ 22°C, Beam Flux Density ~ 1×10^{15} ions/cm² sec)

Sample Material	Ex Situ Pre Exposure †			In Situ Measurements ‡										Ex Situ Post Exposure †		
	$\epsilon_S^{(a)}$	$\epsilon_{Xe}^{(a)}$	$\epsilon_N^{(b)}$	T = 0 hr		T = 0.017 hr		T = 0.167 hr		T = 0.667 hr		Post O ₂		$\epsilon_S^{(a)}$	$\epsilon_{Xe}^{(a)}$	$\epsilon_H^{(c)}$
				ϵ_{Xe}	ϵ_H	ϵ_{Xe}	ϵ_H	ϵ_{Xe}	ϵ_H	ϵ_{Xe}	ϵ_H	ϵ_{Xe}	ϵ_H			
Gold Plating on Polished Aluminum	0.220	0.160	0.025	0.135	0.067	(u)	(u)	0.131	(u)	0.126	(u)	—	—	0.203	0.152	0.032
Cat-a-lac Black Paint	0.956	0.956	0.890	0.881	0.862	0.826	0.852	0.868	0.882	0.852	0.890	—	—	0.952	0.955	0.844
P V 100 White Paint	0.188	0.142	0.873	0.165	0.808	0.573	0.802	0.663	0.804	0.632	0.816	—	—	0.562	0.522	0.837
RTV 566 Silicone Rubber	0.652	0.605	0.898	0.575	0.853	0.626	0.848	0.655	0.845	0.649	0.851	—	—	0.698	0.659	0.847
SI3G White Paint	0.190	0.148	0.713	0.163	0.880	0.309	0.872	0.344	0.877	0.338	0.876	—	—	0.331	0.270	0.866

(a) Measured on Beckman (modified DK2A).

(b) Measured on Gier Dunkle Quick Emittance Inspection Device.

(c) Calculated from normal emittance and theoretical correction given in Eckert and Drake, Heat and Mass Transfer, 2nd Edition.

(u) Data Unreliable Due to Instrumentation Instability.

† Third figure included to show data trends; not fully significant.

‡ Based on lens-out spectrum.

for a timed exposure to the ion beam, return the samples to the measurement position and remeasure the properties (labeled "t = X.XXX hr" in the tables), turn and expose again, turn and measure again, and repeat this sequence until the samples had received 3 Hg^+ doses. Throughout these measurements, tank pressure was typically less than 2×10^{-7} torr and consisted of gases not condensed at LN_2 temperatures (mainly CO and H_2).

The second set of measurements shown after 0.667 hour of ion beam exposure of the samples listed in Table 8-1a was made approximately 18 hours following the first set. The excellent agreement between the two sets demonstrates that the sample optical properties were stable in vacuo, even in cases where ion exposure had caused drastic changes in property values.

As seen in Tables 8-1a and b, there were significant changes in some of the test surfaces, notably the Z93; after a 10-minute exposure, its absorptance had increased from 0.15 to 0.66. Two other white paints, PV100 and S13G, and both RTV samples also showed increase in α_{Xe} when exposed to Hg^+ , a trend which was also confirmed by visual inspection. The α_{Xe} of the black paints and the ϵ_{H} of all samples were not significantly affected. Both the quartz and microsheet second surface mirrors exhibited essentially stable properties (within measurement accuracy).

The five samples of Table 8-1a were tested for oxygen-linked recovery. After in situ property measurements were made following the final ion beam exposure, the chamber pressure was raised to approximately 700 torr for approximately 15 minutes. (In addition, pressurization consumed approximately 15 minutes and re-evacuation 48 minutes.) Throughout the entire procedure the LN_2 liners were kept cold to prevent desorption of Hg and H_2 , but above LN_2 temperature to limit condensation of O_2 . At the higher pressures, a thick oxygen fog was produced within the chamber.

As the "Post O_2 " column of Table 8-1a indicates, this procedure had, at most, a very minor effect on the total property values of these samples. This result may or may not be sustained with other sample materials, or sample temperatures, or with other thruster propellants, but it does tend

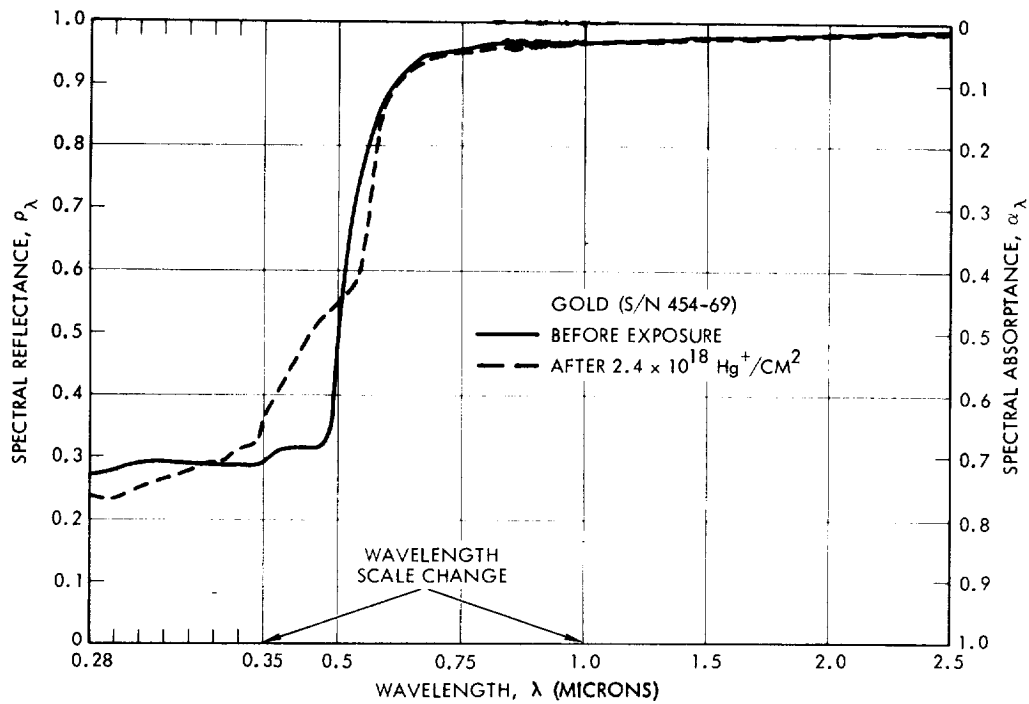
to enhance the value of the ex situ spectral reflectance measurements made for the current series. Pre- and post-exposure spectral reflectance distributions (from ex situ measurements) are therefore presented in Figure 8-1a for gold, all of the tested samples that exhibited noticeable degradation in total properties as measured in situ, and 6-mil microsheet.

The gold sample underwent a visual color change; its post-test appearance could best be described as "coppery". A comparison of pre- and post-exposure spectral reflectance (Figure 8-1a), however, indicates no significant change in total absorptance and the spectral distribution still exhibits the gold characteristics. The surface is most likely a gold-mercury amalgam, but primarily gold.

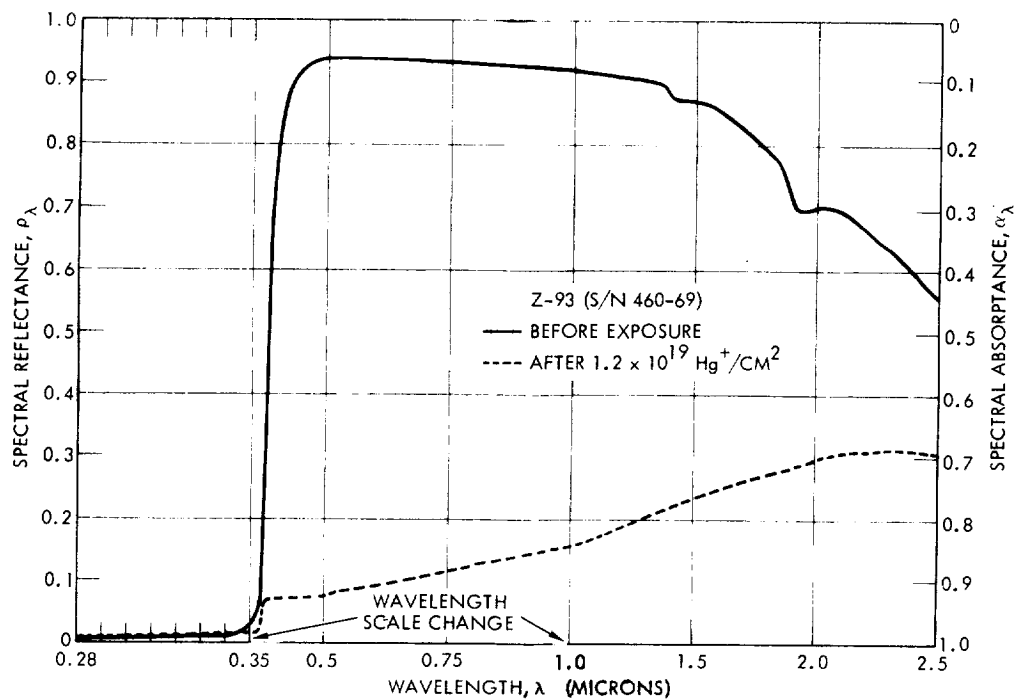
A comparison of pre- and post-exposure Z93 spectral data (Figure 8-1b) is interesting in that the absorptance edge of ZnO is still evident at 0.37 micron even though the surface is nearly "black" at that wavelength. However, this is the only spectral feature remaining. The other two white paints, which suffered less drastic change in α_{Xe} , preserved much more of their spectral features as well, as is seen in Figures 8-1c and d. The spectral signature between 1.0 and 2.5 microns arises from the silicone binder of these paints; it is seen again in Figures 8-1e and f of the silicone based RTV's.

Note that the test results for these early experiments are for greatly accelerated arrival rates. A typical arrival rate of high divergence angle ions to a spacecraft surface might be in the neighborhood of 10^9 ions/cm²-sec as compared with the 10^{15} in these experiments. Furthermore, the Hg⁺ dose was large in comparison to most practical missions. A 10^9 arrival rate during a 10^4 hour thrust period corresponds to a 4×10^{16} ions/cm² dose, whereas in these experiments 6×10^{16} ions/cm² arrive in 1 minute. The effects of flux rate are examined and discussed in the next section of this report which deals with more recent mercury ion experiments.

The following tentative conclusions were drawn from the early tests of thermal control coatings and were the basis for planning the more recent and detailed mercury ion degradation experiments discussed in the following sections.

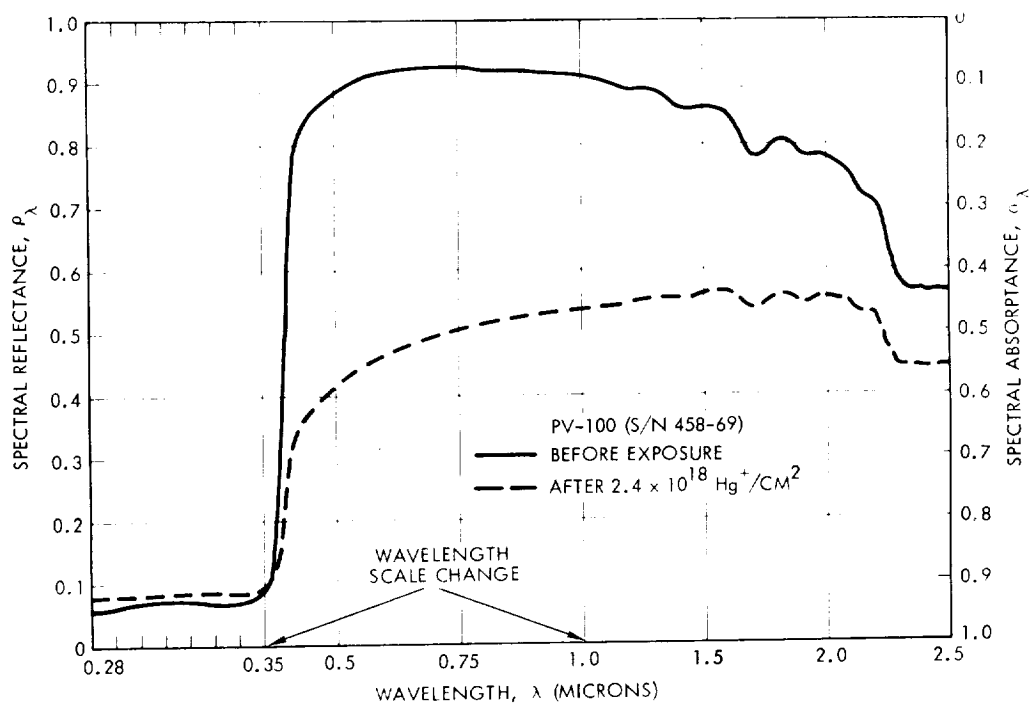


(a)

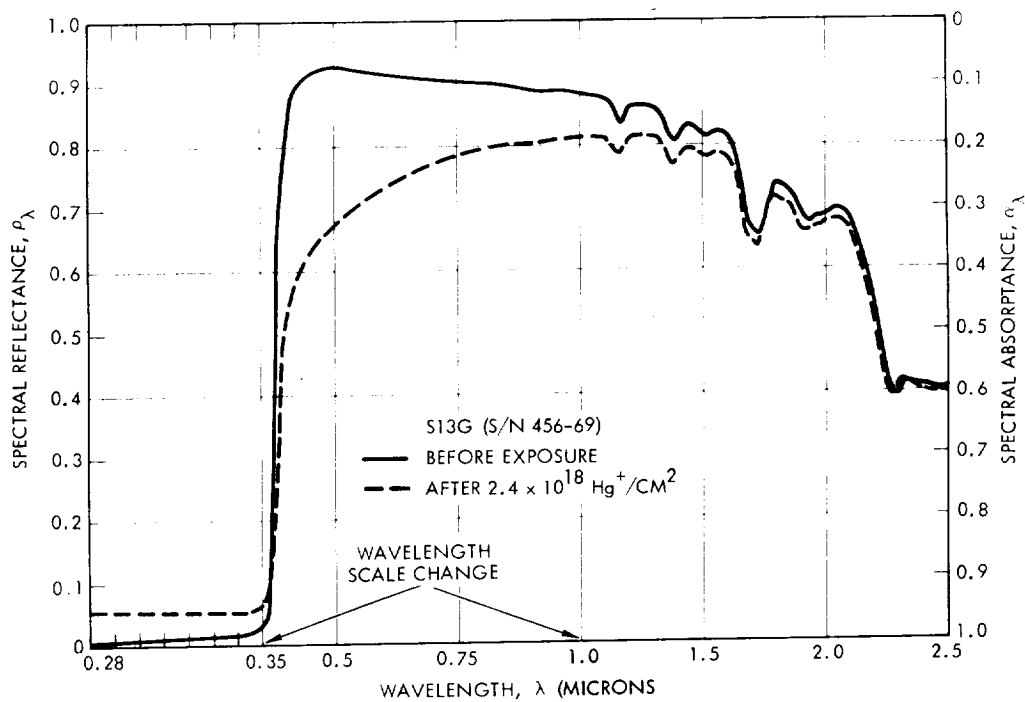


(b)

Figure 8-1. Spectral Reflectance of Gold and Z93 White Paint versus Wavelength Before and After Exposure to 3 kev Mercury Ions.

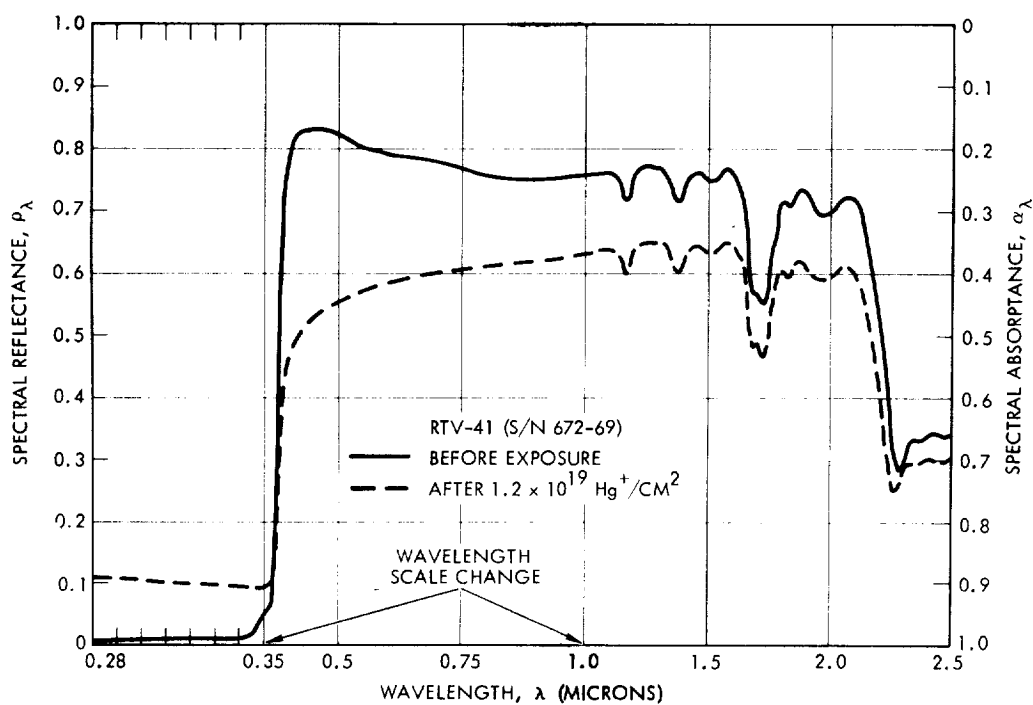


(c)

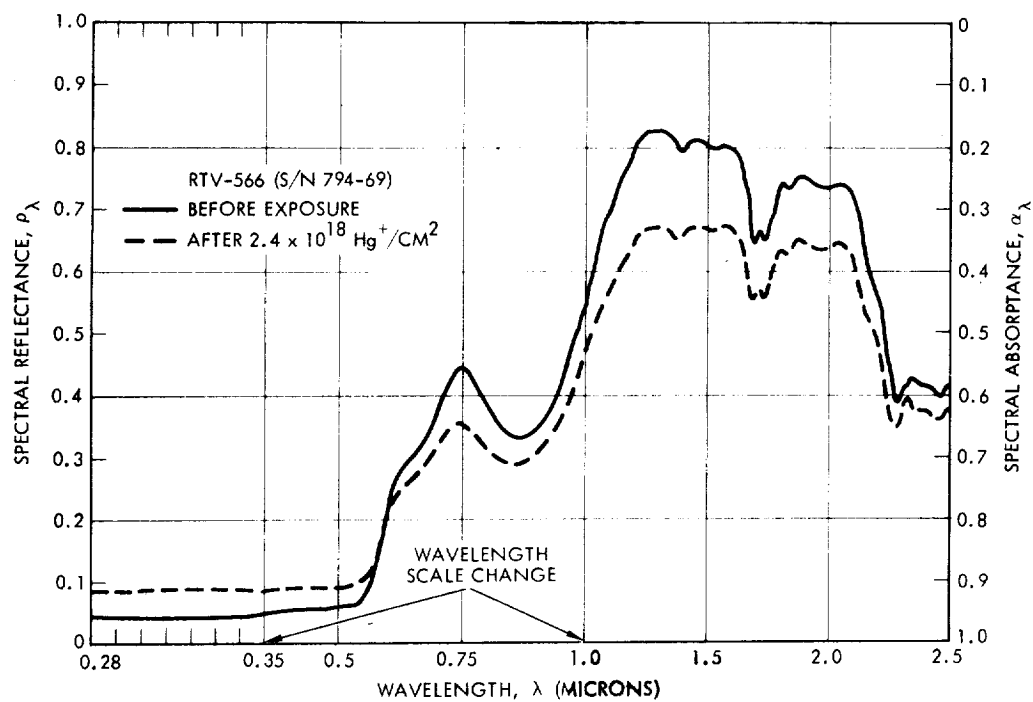


(d)

Figure 8-1. Spectral Reflectance of PV100 and S13G White Paints versus Wavelength Before and After Exposure to 3 keV Mercury Ions (Continued)

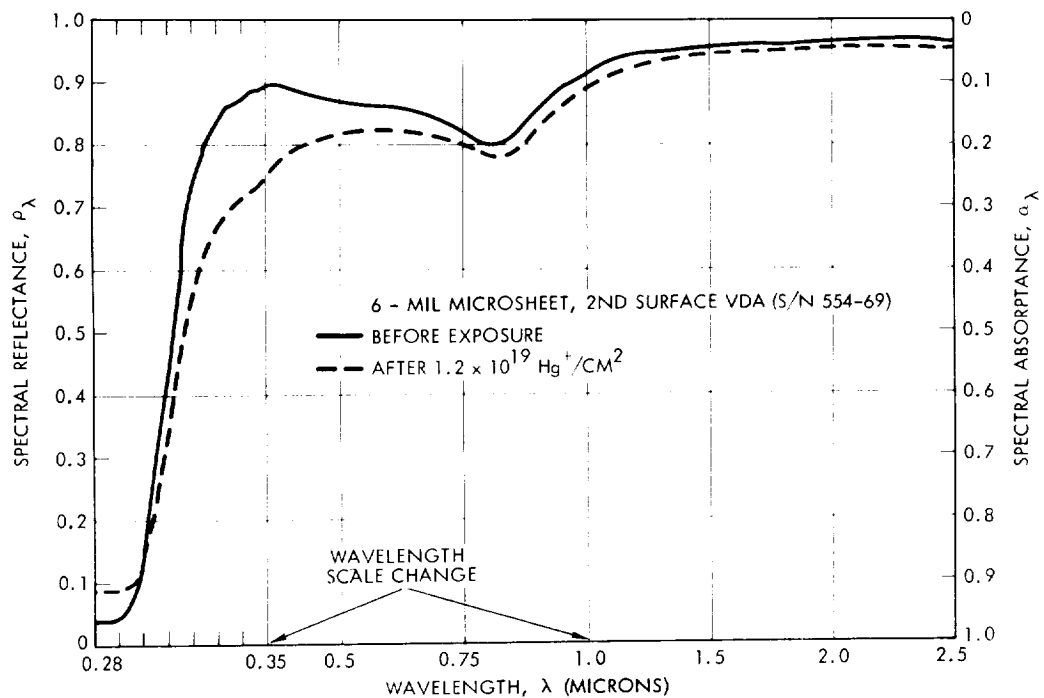


(e)



(f)

Figure 8-1. Spectral Reflectance of RTV41 and RTV566 versus Wavelength Before and After Exposure to 3 kev Mercury Ions (Continued)



(g)

Figure 8-1. Spectral Reflectance of 6-mil-thick Corning 0211 Microsheet With Second Surface Vacuum Deposited With Aluminum versus Wavelength Before and After Exposure to 3 kev Mercury Ions (Continued)

- (1) With the probable exception of degradation of their optical coatings, if any, damage to solar cell cover glass properties from normal incident ions will probably proceed at ion erosion rates; i. e., very slowly. Thus, thermophysical attention regarding the front surface of a solar array should focus on the materials exposed to the thruster exhaust by virtue of cover glass discontinuity and on propellant condensation effects. (However, later tests of glass erosion by off-normal ions, described in Section 5, suggest the need for more investigation of this area.)
- (2) On the rear surface of solar arrays, where only ϵ_H is of interest, ion damage will also proceed slowly for many, if not all, coatings.
- (3) Use of white paint as a low α_s/ϵ_H thermal control coating in areas exposed to the exhaust of ion engines should be avoided. Second surface quartz or glass mirrors appear to be a suitable substitute. [Second surface aluminized (or silvered) Teflon may also be a stable substitute (it does not degrade in UV as badly as Mylar); however, see Section 5 regarding ion effects on Teflon FEP].

8.3.2 Effect of Mercury Ions (Recent Experiments)

In situ measurements of surface thermal property degradation due to high energy mercury ion impingement were resumed in 1971. Based on results from the 1969 surface thermal property degradation measurements, five sample materials (Z93, S13G, and PV100 white paints, RTV41, and polished aluminum) were selected for further study. Five sets of these sample materials were exposed to mercury ion beams under the test conditions of Table 8-2 in an effort to establish scaling relationships on ion arrival rate and ion energy and to determine what effect, if any, sample temperature has on degradation rates.

Table 8-2. Summary of Nominal Test Conditions

Test Series	Ion Flux (ions/cm ² -sec)	Ion Energy (kev)	Sample Temperature (°C)	Total Accumulative Dose (ions/cm ²)
1†	1 x 10 ¹⁵	3	20	1 x 10 ¹⁹
2	6 x 10 ¹³	3	20	3 x 10 ¹⁸
3	6 x 10 ¹³	1.5	20	4 x 10 ¹⁸
4	1 x 10 ¹⁵	1.5	20	1 x 10 ¹⁹
5	1 x 10 ¹⁵	1.5	150	4 x 10 ¹⁹
6	6 x 10 ¹²	1.5	20, 50, 100*	3 x 10 ¹⁷

†From 1969 tests

*Exposed at 20°C and then heated.

Between nine and sixteen sets of exposures and in situ property measurements were made during each of the test series indicated in Table 8-2 except for Series I, which consisted of three exposures. As a consequence of the wider range of arrival rates and the fact that the present data have been taken at shorter exposure intervals, considerably more detail has been obtained during the recent tests concerning degradation as a function of accumulative ion dose.

In addition to the in situ measurements, corresponding pre- and post-exposure ex situ measurements of near-normal total emittance (ϵ_N) and post-exposure ex situ spectral reflectance measurements in the wavelength region between 0.28 and 2.5 microns were also made using the instruments

and techniques described in Appendix B. Pre-exposure spectral measurements were made on a single set of samples during the 1971 test series as a check on sample aging.

8.3.2.1 General Results

In situ measurements of hemispherical emittance (ϵ_H) showed little or no ϵ_H degradation of any of the five sample materials tested under the test conditions outlined in Table 8-2. Thus, as in 1969, xenon absorptance (α_x) is the property of most interest.

Xenon absorptance (α_x) degradation appears to be mainly a function of accumulative dose (ion arrival rate multiplied by accumulated exposure time) and possibly sample temperature. Figures 8-2 through 8-6 show α_x for each respective sample plotted as a function of accumulative dose. It can be seen from these plots that absorptance (α_x) for all 20°C runs with ion energies of 1.5 or 3.0 keV and ion fluxes of 6×10^{13} ions/cm²-sec or 1×10^{15} ions/cm²-sec fall along a common faired line for each material. It can be said, therefore, that this variation of ion energy had an insignificant effect on α_x degradation, and all five samples exhibited reciprocity over at least the indicated range of ion flux.

Except for polished aluminum, which showed no significant α_x degradation, all of the samples displayed similar crank-shaped curves (on semi-log paper) of α_x versus ion dose. In each case, sample absorptance values are acceptable until some accumulated ion dose is reached; thereafter, sample degradation continues as the dose is increased until saturation is finally reached. There are striking differences, however, in the magnitude of acceptable dose and the saturation absorptance values. In each case, saturation was reached by 10^{19} ions/cm².

The most dramatic curve is that of the Z93. Its initial degradation rate is so low that $\sim 4 \times 10^{16}$ ions/cm² are required to increase its absorptance to 0.2. The large subsequent value of the curve slope is the result of a continued linear degradation rate during the next decade of dose. This curve shape was completely missed in the 1969 measurements because of the longer exposure interval and higher arrival rate that was used then.

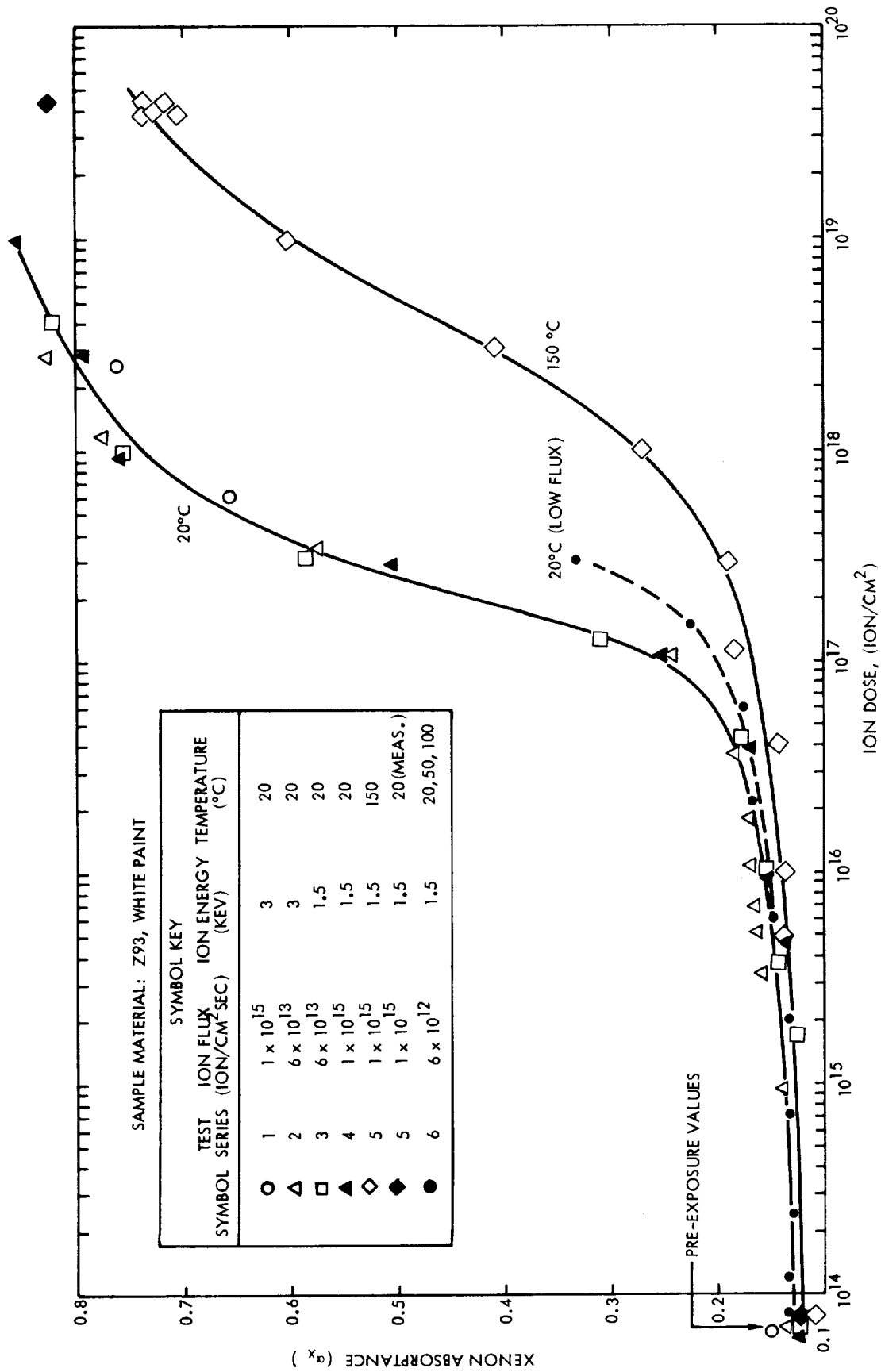


Figure 8-2. Degradation of Z93 White Paint from Exposure to Various Mercury Ion Beams

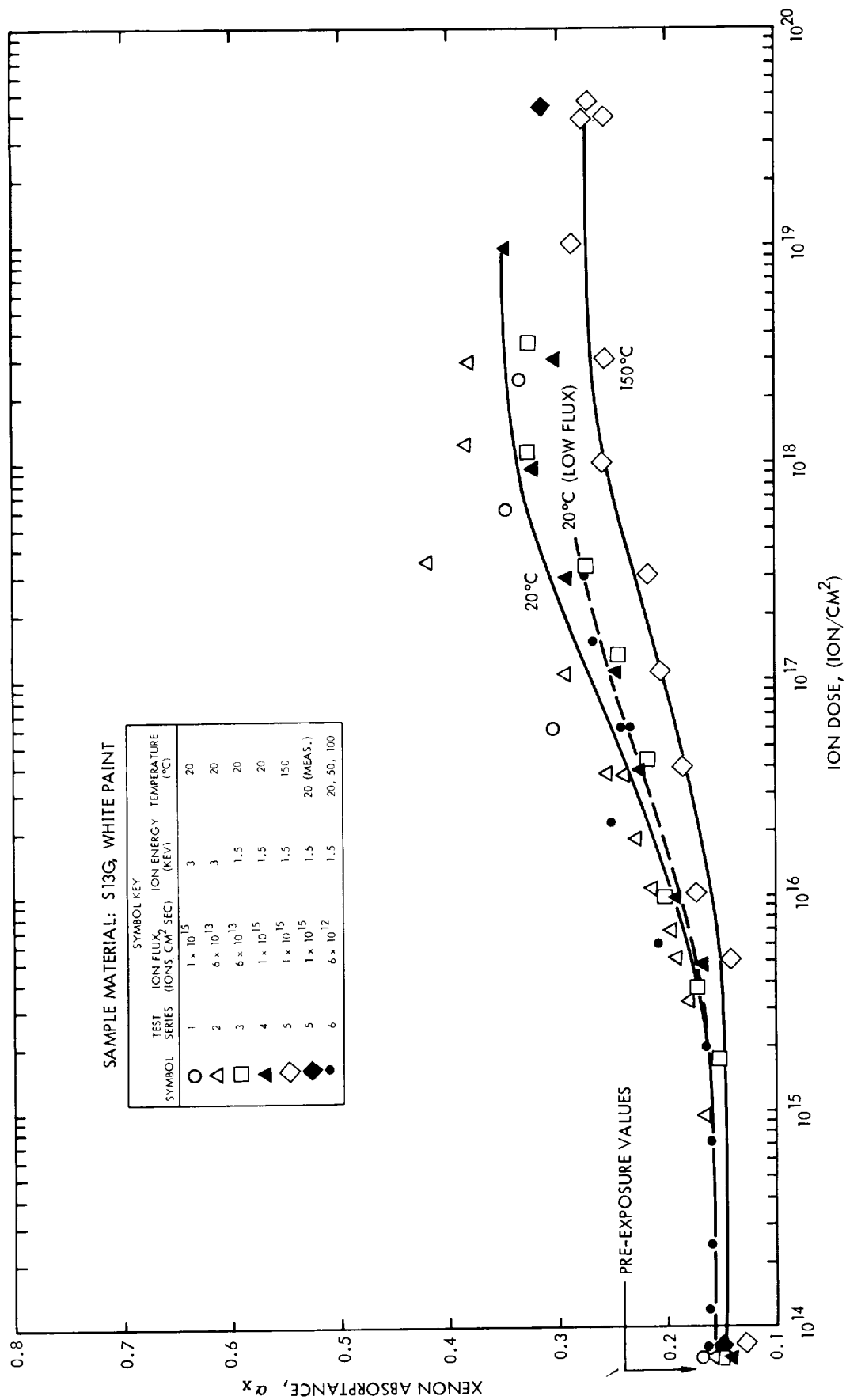


Figure 8-3. Degradation of S13G White Paint from Exposure to Various Mercury Ion Beams

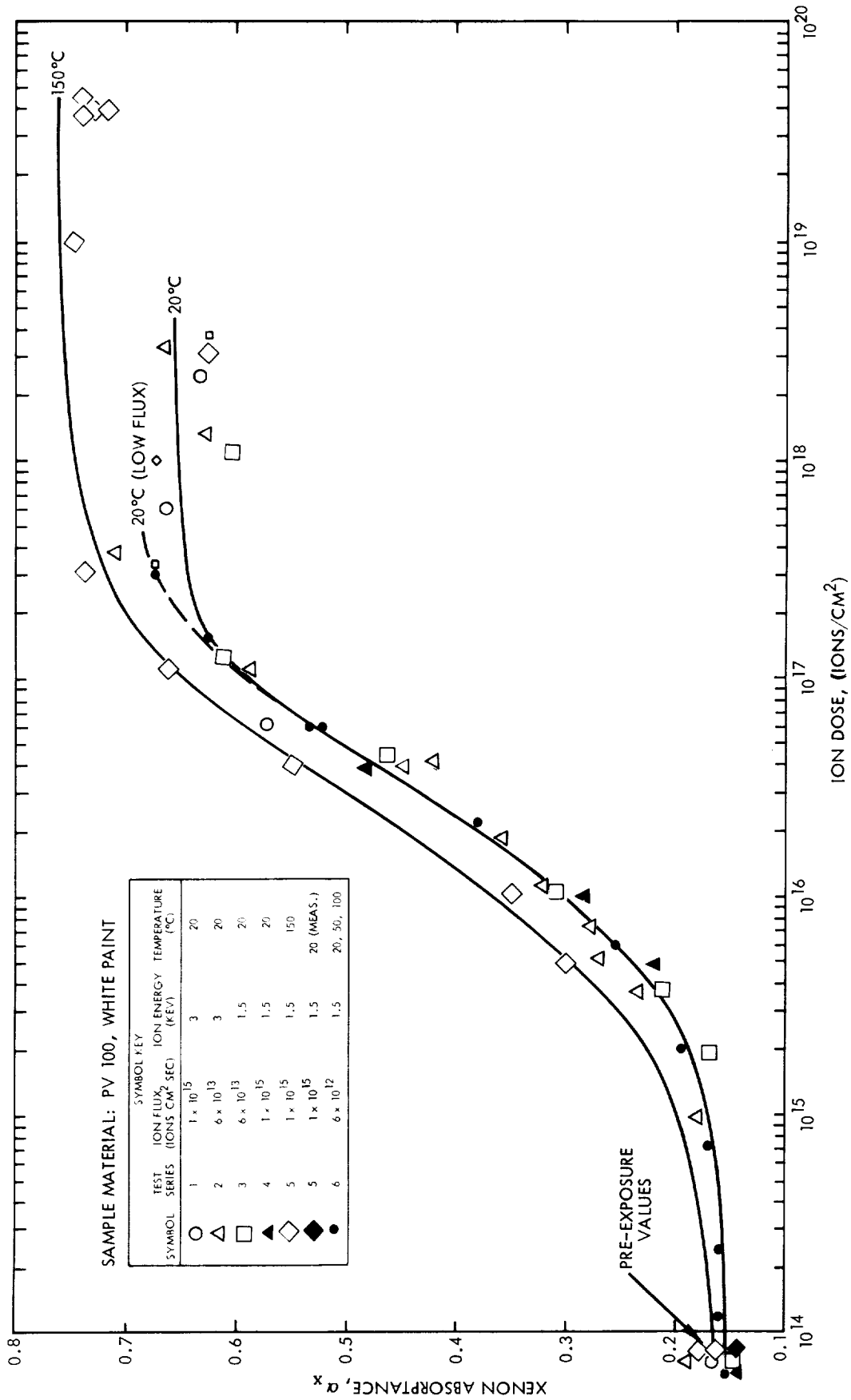


Figure 8-4. Degradation of PV100 White Paint from Exposure to Various Mercury Ion Beams

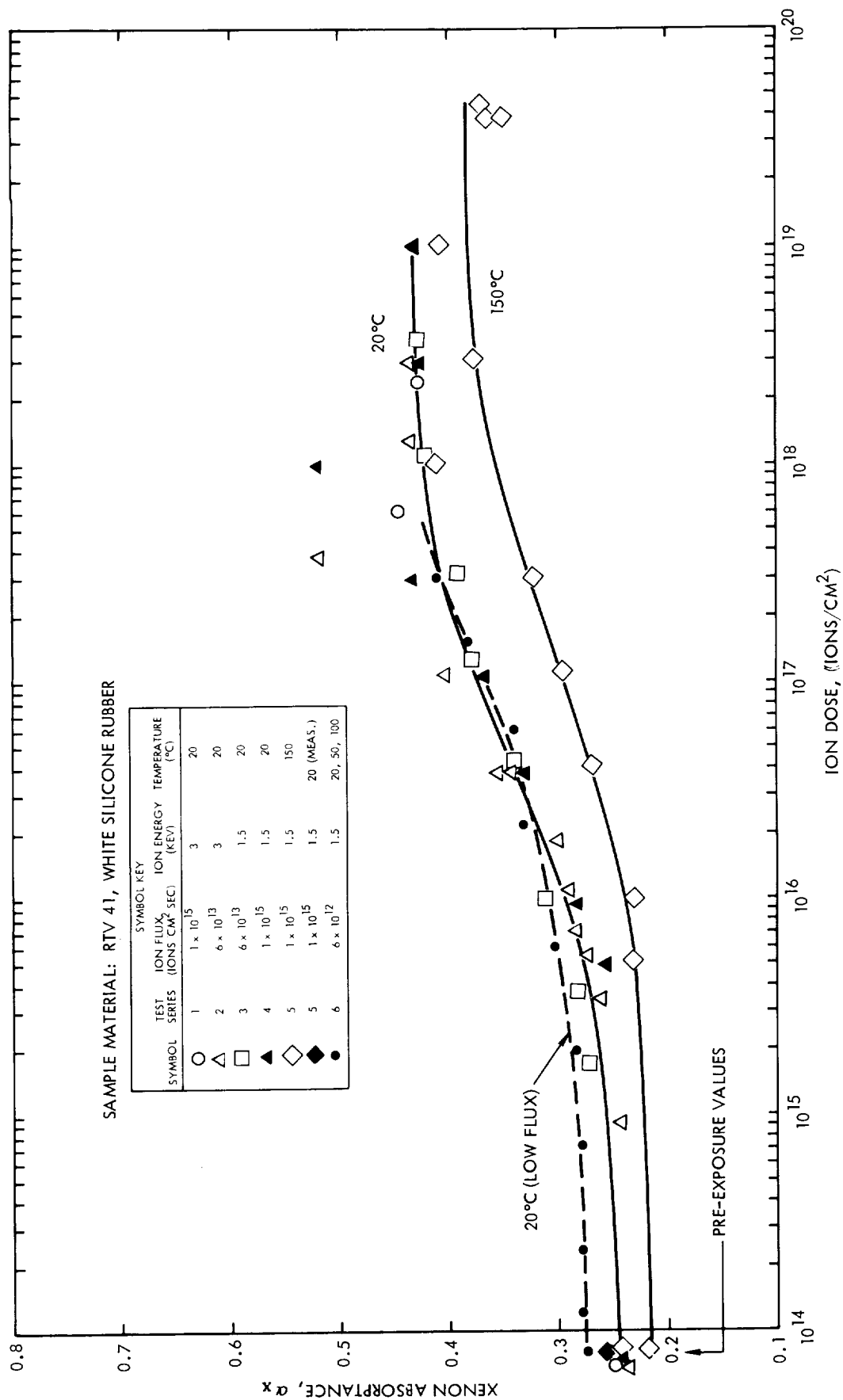


Figure 8-5. Degradation of RTV41 White Silicon Rubber from Exposure to Various Mercury Ion Beams

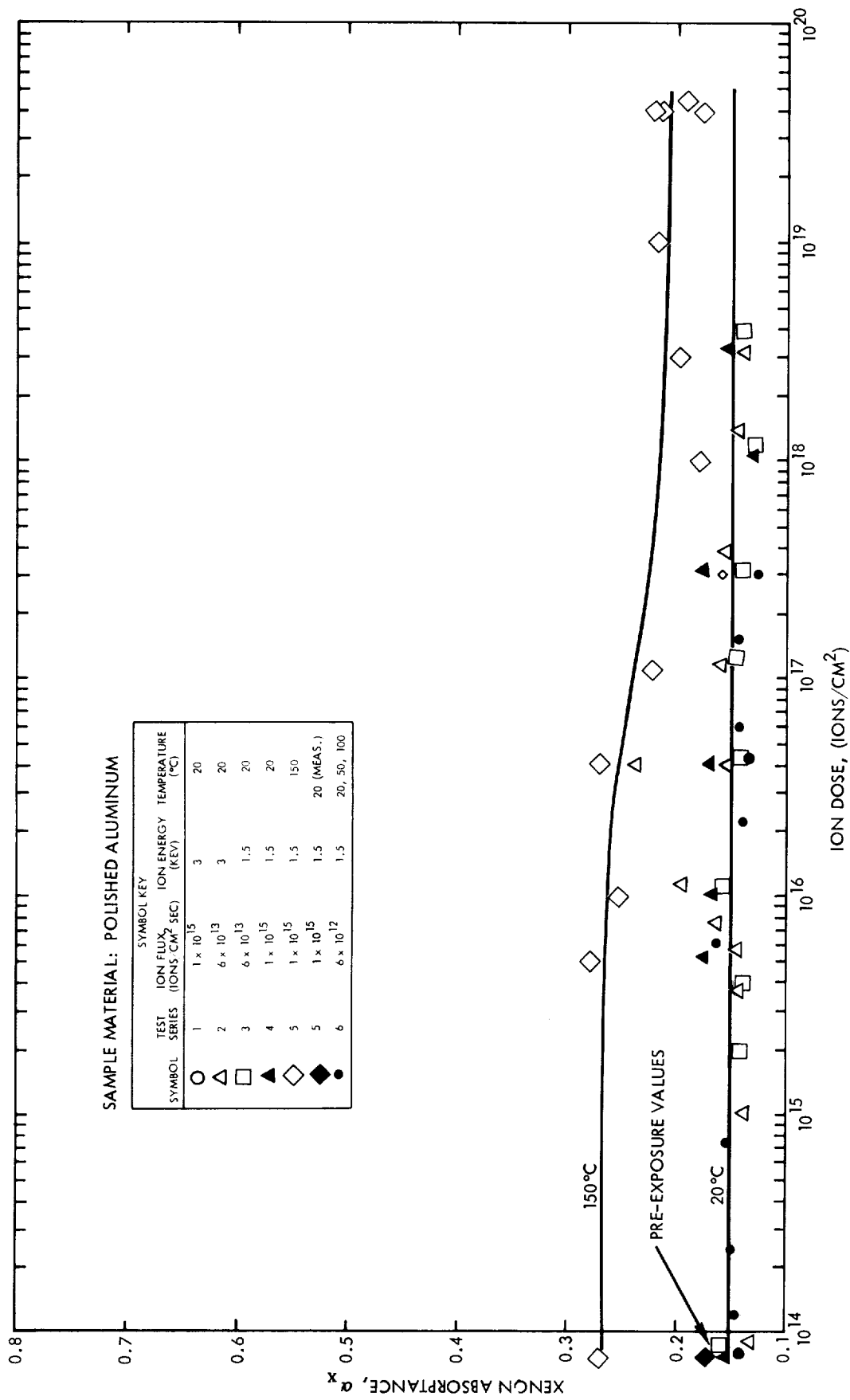


Figure 8-6. Degradation of Polished Aluminum (6061-T6) from Exposure to Various Mercury Ion Beams

8.3.2.2 Effect of Low Ion Flux

Test Series 6 with its considerably lower ion flux (6×10^{12} ions/cm²-sec) seems to have produced different α_x degradation results on at least three of the four white coatings than were obtained for the higher flux 20°C runs. The low flux series has therefore been accentuated in Figures 8-2 through 8-6 by a separate and dashed line. Interestingly enough, the PV 100 low ion flux degradation curve is identical to that of the higher fluxes until very high absorptance values are reached. This tends to discount the possibility that the low flux departure of the other samples might actually be due to an experimental error in accumulative dose, since all of the samples receive concurrent exposure. It should be noted in interpreting the low flux series of RTV 41 that the entire dashed line appears to be offset upward approximately 0.05, probably because its pre-exposure α_x was larger than average. If the dashed line were lowered by 0.05, the low flux departure for RTV 41 would then be in the same direction as for Z93 and S13G.

8.3.2.3 Effect of Sample Temperature

Test Series 5 was run with all five samples exposed and measured at approximately 150°C. The resulting α_x degradation data is plotted, along with pre- and post-series 20°C data (indicated by solid diamonds), in Figures 8-2 through 8-6. A separate solid line has been faired through the 150°C data to accentuate the apparent effect of temperature on α_x degradation rate. There are certain facts that make the 150°C lines questionable.

First of all, the 150°C plot for polished aluminum shows an unexplained decreasing α_x versus ion dose. Ion sputtering of polished metal eventually produces visible abrasion. Abrasion of a polished metal normally causes an increase in absorptance due to multiple reflections within the pits and cavities. The observed decrease in α_x might occur if there were initially a film of higher absorptance material on the sample's surface, and this film were gradually eroded away by the ion beam, but in situ emittance data do not indicate the presence of such a film.

Secondly, pre-exposure in situ α_x measurements made with the samples at approximately 20°C and at approximately 150°C disagreed somewhat. The 150°C values of PV100 and polished aluminum were higher and of RTV41, S13B, and Z93 were lower. In every case, the 20°C value

is closer to the results obtained for all other series than is the 150°C value. The final 150°C post exposure in situ α_x measurements were markedly lower than subsequent 20°C measurements. These initial and final 20°C data points for Series 5 are indicated in Figure 8-2 through 8-6 by the solid diamond symbol. The final, 20°C point is missing for RTV41 and polished aluminum because of malfunctioning that occurred on those two channels after the sample holder was cooled too rapidly from 150°C.

After the final ion beam exposure and while the samples were still hot, their properties were measured several times to determine if they were time variant. In particular, it was thought that the high temperature might be "annealing" the absorptance damage to the Z93, RTV41, and S13G samples. These measurements are represented by the cluster of data points near 4×10^{19} ions/cm². In fact, the variations between these measurements were small and the resulting slight trends were to higher absorptance with time, except S13G which was constant within the repeatability of the apparatus.

Comparison of 20°C and 150°C data points for Series 5 (solid diamonds versus open diamonds) reveals that in most cases the magnitude of the discrepancy is approximately proportional to the value of α_x . This suggests that much or even all of the apparent temperature effect shown by Figures 8-2 through 8-6 is actually due to a systematic error in the measurement apparatus or data reduction program. In situ emittance data does not, however, seem to show any similar discrepancy between hot and cold runs. Also, high temperature appears to retard α_x degradation of S13G, Z93, and RTV41 while accelerating degradation of PV100. Thus, the only thing that can be said with certainty at this point concerning the apparent temperature effect is that more analysis and/or testing is needed.

8.3.2.4 Thermal Annealing

Discovery of the possible retarding effect increased sample temperature appears to have on α_x degradation rates for Z93, S13G, and RTV41 motivated the addition of a temperature experiment to the Test Series 6. The objective of this experiment was to determine whether α_x degradation is annealable by subsequent heating in vacuum. The Series 6 samples, which had been exposed at 20°C for the low flux experiment, were heated while still in vacuum to approximately 50°C and remeasured several times over a period of about 24 hours. The samples were then

heated to approximately 100°C and, after about one-half hour, again remeasured. Shortly after the first set of measurements at 100°C was completed, the circulation bath heater burned out, thus precluding planned measurements versus time at 100°C and 150°C. Data that were obtained from the diffusion experiments are presented in Table 8-3.

Table 8-3 shows that no significant change in α_x occurred as a result of subsequent heating in vacuum.

As a supplement to the above experiment, the badly degraded Z93 sample from Test Series 2 was cut in half, and one half was heated to approximately 300°F in air for 2-1/2 hours. Visual comparison of the two halves after heating showed no apparent change. Thus, the absorptance damage to these samples does not appear to be temperature annealable.

8.3.2.5 Comparisons With Ex Situ Measurements

With but one exception, the ex situ total emittance measurements tended to verify the in situ emittance measurements by showing no measurable change in the emittance of any of the five samples due to

Table 8-3. Thermal Annealing Experiment Results*

Sample Temperature (°C)	PV100		RTV41		S13G		Z93		Polished Aluminum	
	Time (min)	α_x	Time (min)	α_x	Time (min)	α_x	Time (min)	α_x	Time (min)	α_x
19	—	0.67 ₄	—	0.41 ₁	—	0.27 ₇	—	0.33 ₅	—	0.12 ₈
50	40	0.65 ₄	28	0.42 ₄	0.7	0.25 ₉	6	0.30 ₅	58	0.13 ₆
50	150	0.70 ₂	141	0.40 ₂	133	0.27 ₂	125	0.32 ₉	158	0.11 ₇
50	293	0.67 ₀	287	0.40 ₃	281	0.27 ₃	275	0.33 ₅	300	0.14 ₃
50	1463	0.67 ₁	1455	0.39 ₈	1447	0.27 ₁	1440	0.32 ₇	1451	0.14 ₇
100	26	0.68 ₁	21	0.38 ₇	15	0.26 ₀	9	0.32 ₁	32	0.23 ₁
19	—	0.66 ₆	—	0.38 ₇	—	0.27 ₁	—	0.32 ₄	—	0.13 ₆

*Although the accuracy of the measuring instruments does not justify three significant figures, the third figure is retained depressed so as to indicate trends.

mercury ion impingement. The polished aluminum sample did exhibit an increase of ϵ_N of 0.027 after the 150°C run (Test Series 5). Since the 150°C series had an accumulative dose more than four times greater than any of the other series, the noted change in ϵ_N is most likely due to the extremely high ion fluence.

Post-exposure spectral reflectance measurements of samples from Test Series 2, 3, 4, 5 and 6 are superimposed with the corresponding pre-exposure distribution in Figures 8-7 through 8-11. The 25-band overlay that was developed in 1969 for our specific xenon lamp spectrum was used in conjunction with these reflectance distributions to compute the total absorptance α_x for each curve. Resulting ex situ values of α_x and $\Delta\alpha_x$ (difference between pre- and post-exposure α_x) are tabulated in Table 8-4 along with corresponding in situ values.

The pre-exposure ex situ spectrally computed α_x values of the five materials were obtained from one sample randomly selected from the stock of samples prepared in 1969. These values were all within 0.02 of the 1969 values of different samples from the same five batches except for RTV41, which differed (possibly due to aging) by 0.05.

A comparison of $\Delta\alpha_x$ as given by the in situ measurements with $\Delta\alpha_x$ as given by the ex situ measurements shows enough disagreement in a few cases to suggest that atmospheric annealing occurred. Such cases have been indicated in Table 8-4 by boxes. The most significant differences occurred after Test 5 at 150°C. Based on these results and visual inspection of the samples, it appears that for at least two of the samples (Z93 and PV100), elevated sample temperature during ion exposure (Series 5) increased the magnitude and/or rate of annealing that occurred when the samples were returned to the atmosphere. Of the Series 6 samples which were exposed at 20°C but were subsequently heated to 100°C while still in situ, only Z93 showed similar atmospheric annealing. While these annealing observations are probably of little interest in regard to spacecraft design, they may shed some light on the degradation mechanisms. They also demonstrate once again the need to make degradation measurements in situ.

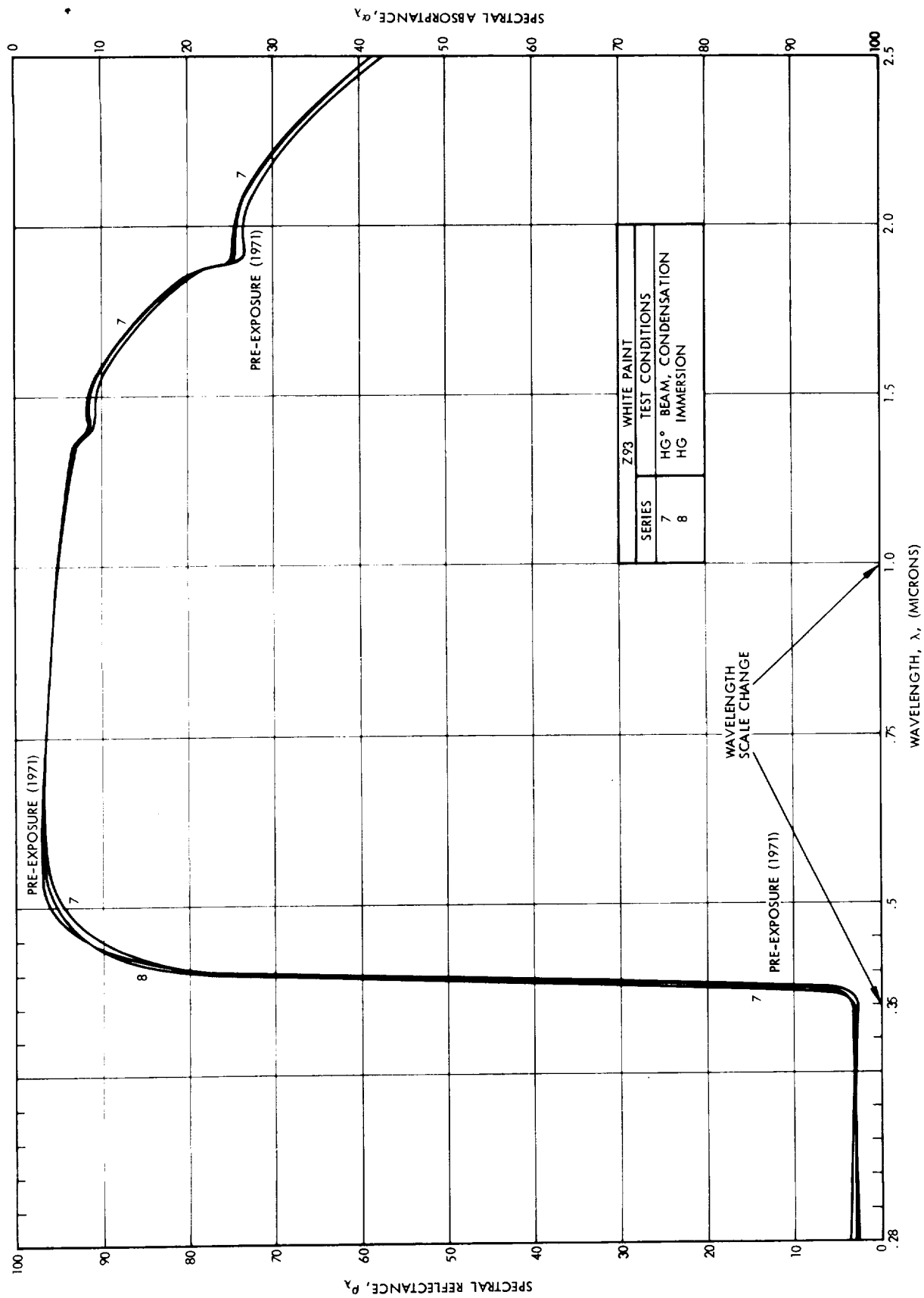


Figure 8-7. Spectral Distribution of Z93 White Paint Before and After Mercury Ion Beam Exposure

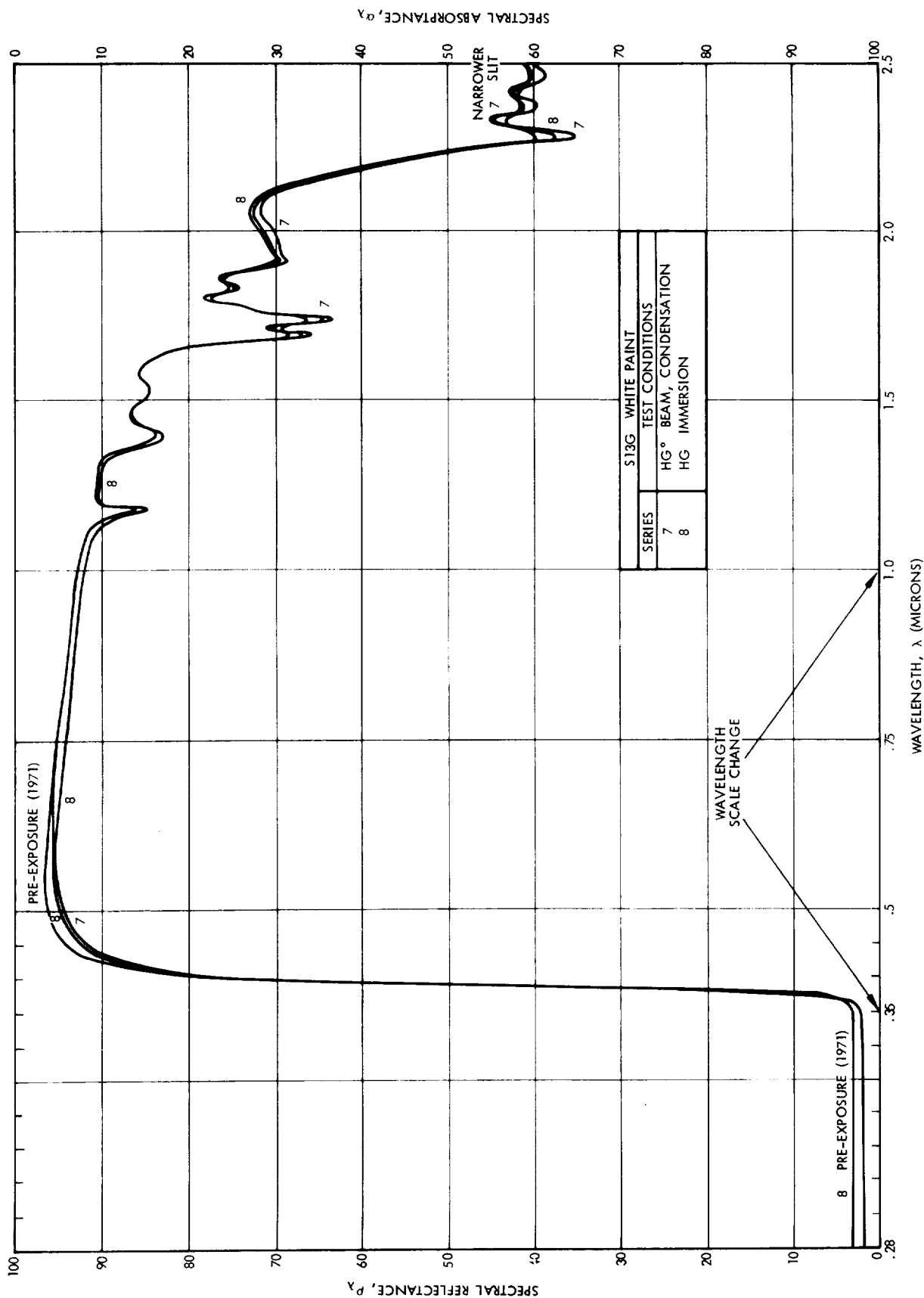


Figure 8-8. Spectral Distribution of S13G White Paint Before and After Mercury Ion Beam Exposure

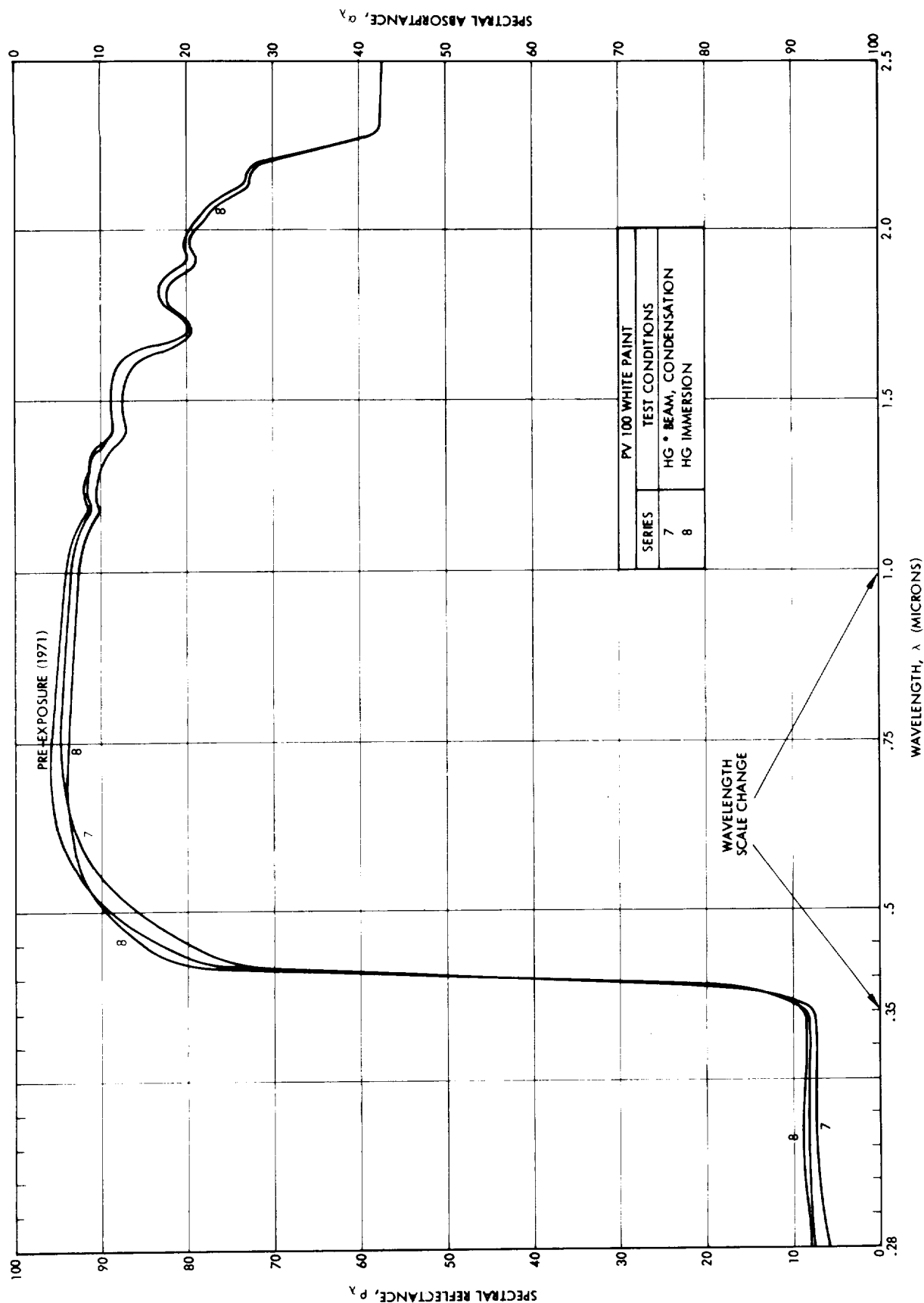


Figure 8-9. Spectral Distribution of PV100 White Paint Before and After Mercury Ion Beam Exposure

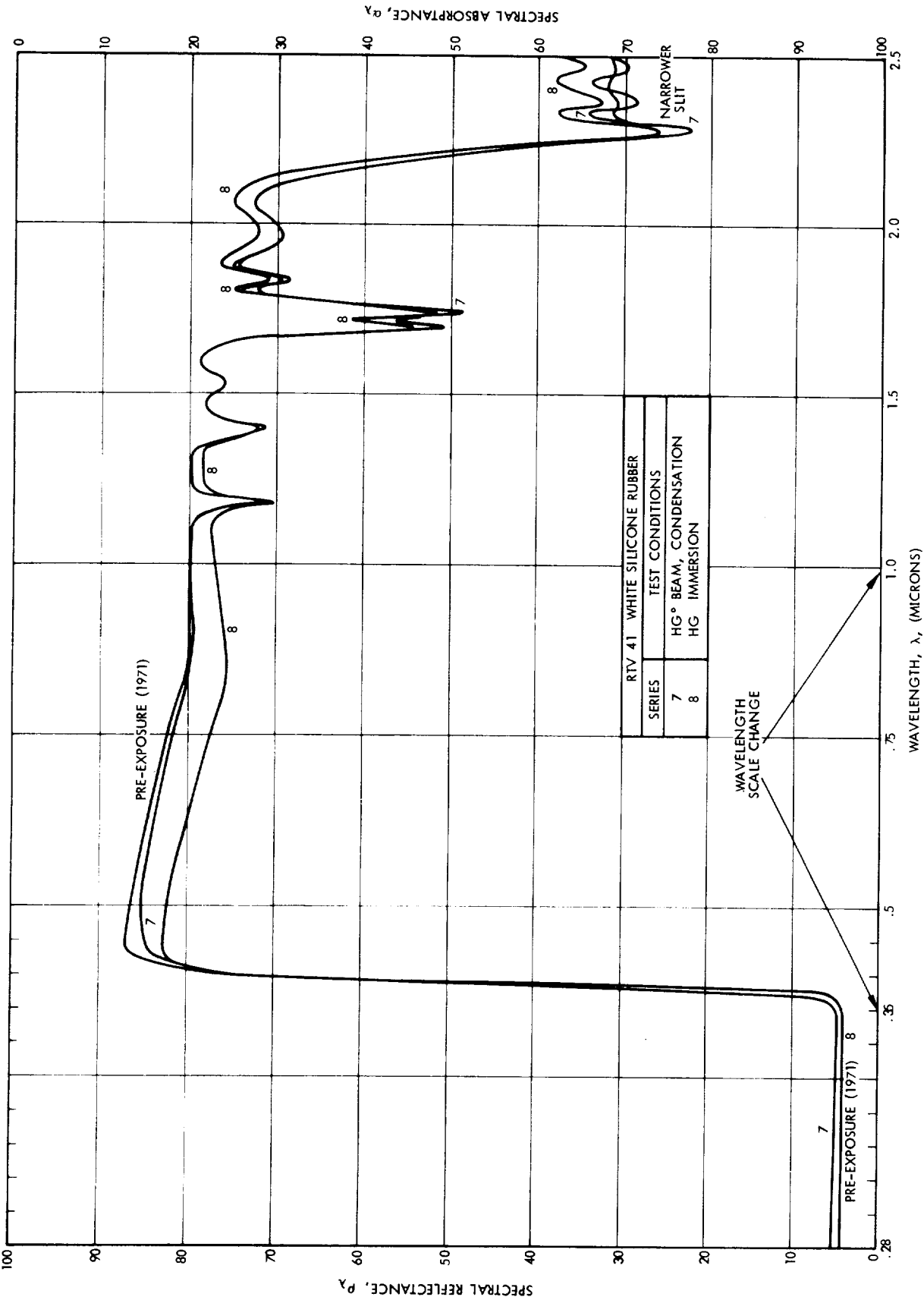


Figure 8-10. Spectral Distribution of RTV41 White Silicone Rubber Before and After Mercury Ion Beam Exposure

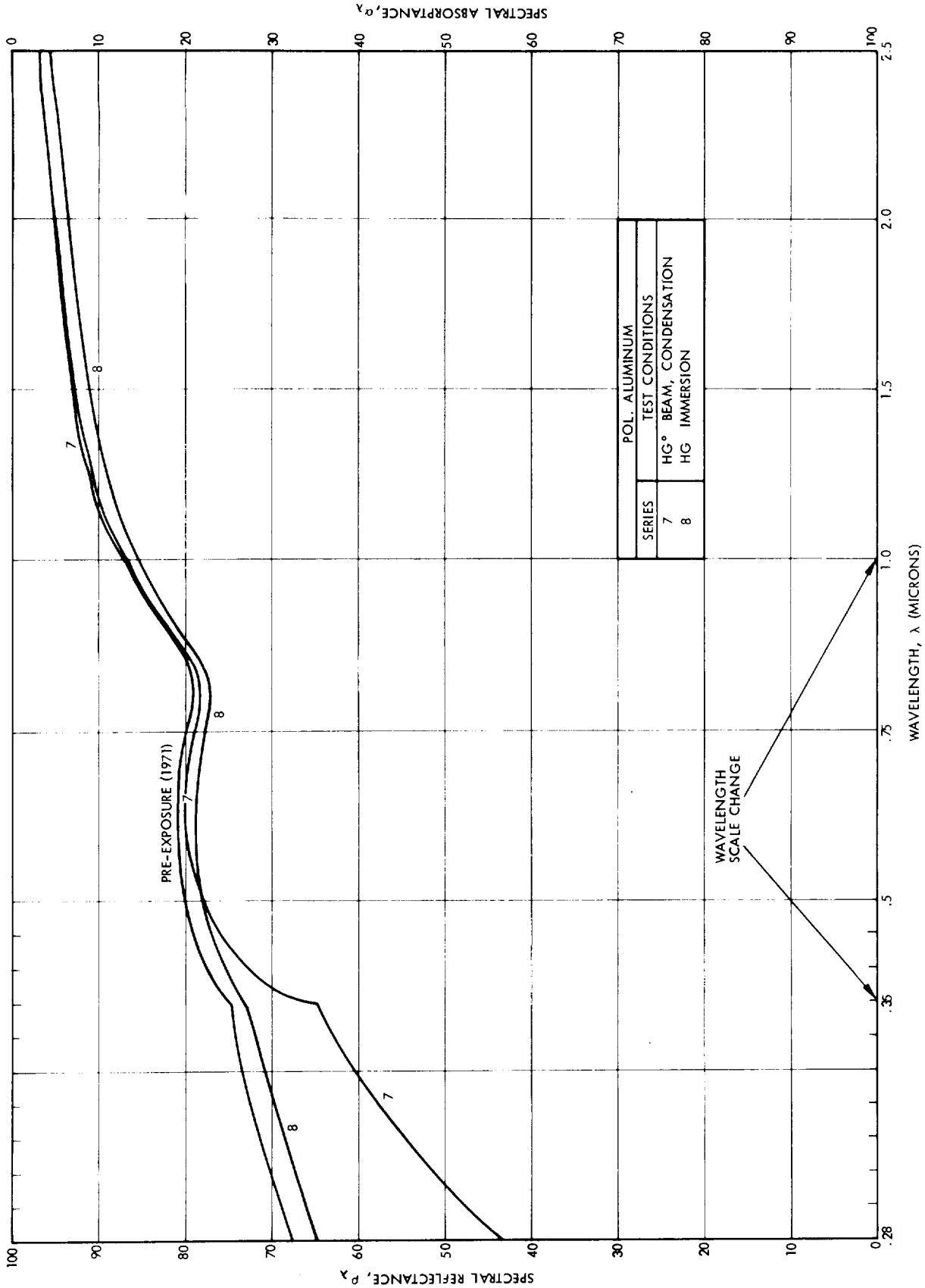


Figure 8-11. Spectral Distribution of Polished Aluminum (6061-T6) Before and After Mercury Ion Beam Exposure

Table 8-4. Comparison of In Situ and Ex Situ Total Absorptance Data†

Test Series			2	3	4	5	6
Total Dose (Ions/cm ²)			3×10^{18}	4×10^{18}	1×10^{19}	4×10^{19}	3×10^{17}
Ex Situ Delay Time*			3 hrs.	6 days	6 days	17 days	3 days
PV100	α_x , Initial	In Situ	0.19 ₃	0.14 ₈	0.14 ₂	0.14 ₅	0.15 ₄
		Ex Situ	0.21 ₁	0.12 ₁	0.12 ₁	0.12 ₁	0.12 ₁
	α_x , Final	In Situ	0.66 ₄	0.62 ₅	0.58 ₅	0.84 ₅	0.66 ₆
		Ex Situ	0.66 ₄	0.54 ₃	0.66 ₄	0.70 ₃	0.65 ₃
	$\Delta\alpha_x$	In Situ	0.47 ₁	0.47 ₁	0.44 ₃	0.70 ₀	0.51 ₂
		Ex Situ	0.54 ₃	0.42 ₂	0.54 ₃	0.58 ₂	0.53 ₂
RTV41	α_x , Initial	In Situ	0.24 ₂	0.27 ₃	0.24 ₁	0.25 ₄	0.27 ₆
		Ex Situ	0.23 ₂	0.23 ₂	0.23 ₂	0.23 ₂	0.23 ₂
	α_x , Final	In Situ	0.44 ₀	0.42 ₈	0.43 ₂	0.37 ₂	0.38 ₇
		Ex Situ	0.39 ₂	0.35 ₈	0.32 ₉	0.33 ₄	0.35 ₆
	$\Delta\alpha_x$	In Situ	0.19 ₈	0.15 ₅	0.19 ₁	0.11 ₈	0.11 ₁
		Ex Situ	0.16 ₀	0.12 ₅	0.09 ₇	0.10 ₂	0.12 ₄
S-13G	α_x , Initial	In Situ	0.16 ₀	0.15 ₇	0.14 ₆	0.15 ₃	0.16 ₄
		Ex Situ	0.12 ₂	0.12 ₂	0.12 ₂	0.12 ₂	0.12 ₂
	α_x , Final	In Situ	0.38 ₁	0.32 ₉	0.35 ₇	0.31 ₆	0.27 ₁
		Ex Situ	0.34 ₅	0.25 ₁	0.22 ₂	0.22 ₉	0.22 ₀
	$\Delta\alpha_x$	In Situ	0.22 ₁	0.17 ₂	0.20 ₁	0.16 ₃	0.10 ₇
		Ex Situ	0.22 ₃	0.12 ₉	0.10 ₀	0.10 ₇	0.09 ₈
Z-93	α_x , Initial	In Situ	0.12 ₃	0.12 ₆	0.12 ₁	0.12 ₆	0.13 ₃
		Ex Situ	0.10 ₂	0.10 ₂	0.10 ₂	0.10 ₂	0.10 ₂
	α_x , Final	In Situ	0.82 ₉	0.82 ₀	0.86 ₆	0.82 ₆	0.32 ₄
		Ex Situ	0.84 ₁	0.83 ₉	0.85 ₄	0.58 ₇	0.11 ₉
	$\Delta\alpha_x$	In Situ	0.70 ₆	0.69 ₄	0.74 ₅	0.70 ₀	0.19 ₁
		Ex Situ	0.73 ₉	0.73 ₇	0.75 ₂	0.48 ₅	0.01 ₇
Polished Aluminum	α_x , Initial	In Situ	0.13 ₂	0.15 ₇	0.15 ₉	0.17 ₀	0.14 ₀
		Ex Situ	0.15 ₄	0.15 ₄	0.15 ₄	0.15 ₄	0.15 ₄
	α_x , Final	In Situ	0.14 ₇	0.14 ₂	0.14 ₉	0.19 ₃	0.13 ₅
		Ex Situ	0.14 ₂	0.13 ₁	0.14 ₀	0.19 ₈	0.15 ₆
	$\Delta\alpha_x$	In Situ	0.01 ₅	-0.01 ₅	-0.01 ₀	-0.02 ₃	-0.00 ₄
		Ex Situ	-0.01 ₂	-0.02 ₃	-0.01 ₄	0.04 ₄	0.02 ₂

†Although the accuracy of the measuring instruments does not justify three significant figures, the third figure is retained depressed so as to indicate trends.

*Elapsed time between removal of the samples from vacuum and post-exposure ex situ measurements.

8.3.2.6 Conclusions

As was found in 1969, mercury ion impingement has little effect on sample emittance but strong influence on xenon (or solar) absorptance (α_x). Degradation of α_x appears to be mainly a function of accumulative ion dose and possibly sample temperature. Specifically:

- Z93 white paint appears to be a suitable low α/ϵ spacecraft thermal control coating in the presence of mercury ion beam exposure provided the accumulative dosage does not exceed 4×10^{16} ions/cm² during the required life.
- Polished aluminum is not significantly degraded at 20°C by exposure to mercury ion beam accumulated dosages of up to at least 5×10^{18} ions/cm². It may degrade somewhat when exposed at higher temperature (150°C).
- S13G white paint and RTV41 show insignificant degradation when exposed to mercury ion beam accumulated dosages of less than 4×10^{15} ions/cm².
- PV100 white paint begins degrading significantly when exposed to mercury ion beam accumulated dosages of 2×10^{15} ions/cm².
- No measurable change was found in the infrared hemispherical emittance of any of the samples after mercury ion beam exposure doses up to 4×10^{19} ions/cm².

Various questionable aspects of the high temperature data (Series 5 and 6) make it impossible to say with certainty at this time whether sample temperature has any significant effect on α_x degradation. If correct, the data seem to indicate that increased sample temperature during exposure retards α_x degradation of Z93, S13G, and RTV41, but accelerates α_x degradation of PV100.

No evidence of temperature "annealing" of absorptance damage was seen in a α_x versus time from beam exposure of 150°C samples, or α_x of samples exposed at 20°C and then heated. However, elevated sample temperature (150°C) during exposure to the ion beam does seem to increase the degree and/or rate of annealing of Z93 and PV100 that will occur once the samples are returned to the atmosphere.

Ion energies of 1.5 and 3.0 kev give essentially identical α_x degradation results. All five samples are dose rate independent for ion fluxes of

6×10^{13} ions/cm²-sec to at least 1×10^{15} ions/cm²-sec. Lower ion flux (6×10^{12} ions/cm²-sec) appears to retard α_x degradation of Z93, S13G, and RTV41, but accelerates degradation of PV100.

8.3.3 Effect of Mercury Atoms (Early Experiments)

During Phase II (1969), a brief set of experiments was performed using mercury atoms for bombarding the samples rather than mercury ions. Two sets of five sample materials were tested in situ before and after exposure to the mercury atom beam. The samples of the first set were all paints, Cat-a-lac black, 3M Velvet black, PV100 white, Z93 white, and S13G white. All in situ emittance data and the in situ absorptance data on the white paints appear to be valid; however, difficulties with low intensity operation of the solar simulator produced inconsistent absorptance data on the black paints. In situ and corresponding ex situ data for the first five samples are presented in Table 8-5. Ex situ data indicates that the black paints were unaffected by 4.425 hours exposure to approximately 10^{14} Hg atoms/cm²-sec at a sample temperature of approximately 22°C. Both in situ and ex situ data in Table 8-5 show a slight increase in the absorptance of the white paints.

Results for the second set of five sample materials (polished aluminum, gold-plated aluminum, 6-mil second surface aluminized microsheet, 20-mil second surface aluminized fused quartz, and RTV41 on aluminum) are given in Table 8-6. The impinging beam was again mercury atoms (neutrals) at a constant rate of about 1×10^{14} atoms/cm²-sec and the sample temperatures were again about 22°C. In general, it can be said that the absolute values of α_x and ϵ_H as determined in situ for all five samples are in excellent agreement with the corresponding ex situ values.

A comparison in Table 8-6 of in situ measurements of α_x or ϵ_H after various exposure times indicates that no significant change occurred with up to 3.37 hours of exposure on any of the five samples. Pre- and post-exposure ex situ measurements tend to substantiate this conclusion.

Results from these two sets of five samples should be considered in conjunction with Figure 8-12 which indicates that bulk condensation of mercury will not occur under the conditions of exposure employed. Thus, if an effect had been observed on any of the samples, it would have been

Table 8-5. Surface Thermal Degradation Test Results, Mercury Neutrals
(Sample Temperature $\sim 22^{\circ}\text{C}$, Beam Flux Density $\sim 1 \times 10^{14}$ atoms/cm²-sec)

Sample Material	Ex Situ † Pre-Exposure			In Situ Measurements †						Ex Situ † Post Exposure		
	$\alpha_x^{(a)}$	$\epsilon_N^{(b)}$	$\epsilon_H^{(c)}$	T = 0 hr		T = 1.725 hr		T = 4.425 hr		$\alpha_x^{(a)}$	$\epsilon_N^{(b)}$	$\epsilon_H^{(c)}$
				α_x	ϵ_H	α_x	ϵ_H	α_x	ϵ_H			
Cat-a-lac Black Paint	0.91 ₀	0.89 ₃	0.84 ₅	0.92 ₆	0.84 ₉	0.84 ₄	0.85 ₈	0.89 ₅	0.85 ₁	0.91 ₀	0.88 ₀	0.84 ₂
3M Black Paint	0.93 ₈	0.91 ₆	0.87 ₀	0.96 ₁	0.89 ₇	0.85 ₈	0.91 ₆	0.92 ₂	0.92 ₃	0.93 ₈	0.91 ₅	0.86 ₈
PV100 White Paint	0.11 ₅	0.87 ₁	0.82 ₇	0.17 ₇	0.81 ₄	0.17 ₅	0.81 ₄	0.18 ₂	0.80 ₇	0.12 ₂	0.87 ₃	0.82 ₈
Z93 White Paint	0.08 ₆	0.93 ₁	0.88 ₅	0.13 ₁	0.87 ₈	0.13 ₅	0.87 ₈	0.13 ₇	0.87 ₁	0.09 ₂	0.93 ₁	0.88 ₅
SI3G White Paint	0.11 ₂	0.91 ₄	0.86 ₆	0.17 ₀	0.88 ₅	0.17 ₀	0.88 ₆	0.17 ₁	0.87 ₂	0.12 ₀	0.91 ₄	0.86 ₆

(a) Measured on Gier Dunkle Mobile Solar Reflectometer.

(b) Measured on Gier Dunkle Quick Emittance Inspection Device.

(c) Calculated from Normal Emittance and Theoretical Correction given in Eckert and Drake, Heat and Mass Transfer, 2nd Edition.

† Third figure included to show trends; not fully significant.

Table 8-6. Surface Thermal Degradation Test Results, Mercury Neutrals
(Sample Temperature $\sim 22^{\circ}\text{C}$, Beam Flux Density $\sim 1 \times 10^{14}$ atoms/cm² sec)

Sample Material	Ex Situ Pre Exposure †			In Situ Measurements †								Ex Situ Post Exposure †		
	T = 0 hr			T = 0.333 hr		T = 2.37 hr		T = 3.37 hr						
	$\epsilon_{\text{S}}^{(\text{a})}$	$\epsilon_{\text{X}}^{(\text{a})}$	$\epsilon_{\text{N}}^{(\text{b})}$	$\epsilon_{\text{H}}^{(\text{c})}$	$\epsilon_{\text{Xe}}^{(\text{a})}$	$\epsilon_{\text{H}}^{(\text{a})}$	$\epsilon_{\text{Xe}}^{(\text{a})}$	$\epsilon_{\text{N}}^{(\text{a})}$	$\epsilon_{\text{Xe}}^{(\text{a})}$	$\epsilon_{\text{H}}^{(\text{a})}$	$\epsilon_{\text{S}}^{(\text{a})}$	$\epsilon_{\text{Xe}}^{(\text{a})}$	$\epsilon_{\text{N}}^{(\text{b})}$	$\epsilon_{\text{H}}^{(\text{c})}$
Polished 6061-T6 Aluminum	0.175	0.173	0.035	0.045	0.146*	0.058	0.147*	0.058	0.157*	0.060	0.184	0.169*	0.029	0.037
	0.161*	0.121*			0.056									
Gold Plating on Polished Aluminum	0.220	0.138	0.025	0.032	0.130*	0.053	0.170*	0.063	0.152*	0.069	0.224	0.162*	0.018	0.023
	0.160*	0.110*			0.056									
6-mil Microsheet 2nd Surface V D Aluminum	0.138	0.133	0.842	0.802	0.153	0.790	0.157	0.795	0.148	0.798	0.131	0.129	0.845	0.804
	0.151	0.789												
20-mil Quartz 2nd Surface V D Aluminum	0.118	0.114	0.811	0.778	0.139	0.765	0.139	0.773	0.142	0.776	0.113	0.124	0.809	0.775
	0.139	0.766												
RTV 41 Silicone Rubber	0.305	0.265	0.909	0.860	0.237	0.877	0.245	0.883	0.245	0.888	0.271	0.235	0.909	0.859
	0.236	0.874												

(a) Measured on Beckman (Modified DK2A).

(b) Measured on Gier Dunkle Quick Emittance Inspection Device.

(c) Calculated from normal emittance and theoretical correction given in Eckert and Drake, Heat and Mass Transfer, 2nd Edition.

† Third figure included to show data trends; not fully significant.

* Based on lens-out spectrum.

the result of fractional monolayer coverage, either as an adsorbed film or through reaction with the sample material. Reaction of mercury with the paint samples was not expected in light of chemical immersion tests which had previously been performed (Section 6). It is common knowledge that glass and mercury do not react at 22°C. Since gold's affinity for mercury is well known, it is somewhat surprising that only slight changes in its surface thermal properties were observed.

It appeared on the basis of these 1969 experiments that for the ten materials tested, neither chemical reaction with the mercury nor fractional monolayer mercury adsorption occurred. The obvious next step was to expose similar samples to mercury atoms under conditions which would result in bulk mercury condensation, re-evaporate the bulk mercury, and then look for sample property changes. Such an experiment was included in the more recent (1971) test series which is discussed in the following subsection.

8.3.4 Effect of Mercury Atoms (Recent Experiments)

During the Phase II (1969) experiments with mercury atoms, ten different sample materials showed only slight property changes after being exposed to a mercury atom beam under conditions that precluded bulk condensation of mercury. Mercury immersion tests of non-metallic samples were also conducted during Phase II as part of the chemistry effort with similar results (no apparent change), although quantitative surface thermal property measurements were not made on the Phase II immersion samples.

In the recent (1971) Phase III experiments with mercury atoms, five sample materials (Z93, PV100, S13G, polished aluminum, and RTV41) were subjected to sample temperature and atom arrival rate conditions that produced bulk condensation of mercury on the samples.

8.3.4.1 Exposure Conditions

After the samples were inserted into the 4- by 8-foot vacuum chamber, their surface thermal properties were measured in situ, first at 19°C and then at -58°C. At this time, it was determined that the RTV41 channel was malfunctioning. These pre-exposure measurements appear in the first two lines of Table 8-7.

Table 8-7. In Situ Results, Test Series 7 (Mercury Neutrals)

Conditions and Measured Temperature	PV100		RTV41		S13G		Z93		Polished Aluminum	
	ϵ_H	σ_x	ϵ_H	σ_x	ϵ_H	σ_x	ϵ_H	σ_x	ϵ_H	σ_x
Pre-Exposure, 19°C	0.804	0.151	Malfunctioning Channel	Malfunctioning Channel	0.869	0.157	0.903	0.125	0.044	0.136
Pre-Exposure, -58°C	0.754	0.155			0.830	0.163	0.876	0.118	0.078	0.133
After Condensation and Re-Evaporation of Hg., -32°C	0.768	0.350			0.850	0.250	0.910	0.251	0.083	0.172
After "No Hg" Exposure, -32°C	0.777	0.334			0.855	0.243	0.919	0.243	0.08	0.175
After Condensing Hg Layer of Uneven Thickness, -57°C	0.764	0.805			0.836	0.290	0.903	0.411	0.195	0.495
15 Hr After Re-evaporation of Hg Layer, -33°C	0.777	0.330			0.855	0.242	0.906	0.236	0.076	0.168

Then an initial attempt was made to produce a visible condensation of mercury on the -60°C samples. The samples were exposed for a total of 32 minutes of various boiler settings. No visible condensation was produced, probably for two reasons. First, many surfaces require higher mercury arrival rates to initiate condensation than to sustain layer growth. Subsequent beam experiments with these same samples confirmed that high arrival rates were required. Secondly, as has sometimes been observed in the past after boiler filling, the completely filled mercury boiler was delivering less mercury than its temperature calibration curve predicts.

The following day, a nonuniform deposit became visible following 16 minutes of exposure of the samples at -65°C. The deposit was a growing, approximately circular region centered between the PV100 and polished aluminum samples. Thus, these two samples condensed the most mercury, although by the time the exposure was terminated, mercury was visible over roughly one-half of the total sample holder area.

The sample holder was then warmed to confirm that the deposit would re-evaporate as expected. Within a half hour, the deposit was no longer

visible. Four hours later, during which time the samples were at approximately -32°C , the sample properties were remeasured. Results of this set of measurements are presented in Line 3 of Table 8-7. Significant increases occurred in the value measured for α_x on PV100, S13G, and Z93.

8.3.4.2 Non-Uniformity of Condensate

The circular pattern of the condensate on the sample holder suggests some type of an "imaging" effect. It is known from a separate experiment in which mercury was condensed uniformly on the copper surface of the QCM sample holder that the mercury beam itself is uniform. The most likely cause for non-uniformity is tantalum being evaporated by the engine (thermionic) cathode which had been held near its normal operating temperature to warm the discharge chamber and prevent mercury condensation in the chamber or manifold. (During ion beam tests, this minute flux of evaporated tantalum reaching samples is quickly removed by sputtering.) The location of the tantalum cathode behind the accelerator electrode gives a geometry that theoretically would produce a 3-inch-diameter image of the accelerator apertures at the sample plane. Thus, it is likely that the localized circular mercury deposit that was visually observed grew on tantalum atom nucleation sites. A small fraction of a monolayer of tantalum would have enhanced mercury nucleation significantly.

8.3.4.3 Possible Extraneous Effects

In situ measurements made before exposure and repeated after mercury had been condensed and then re-evaporated are shown in the second and third lines of Table 8-7. It can be seen that Z93, PV100, and S13G show a definite increase in α_x and even polished aluminum shows a slight increase. In light of the results from the 1969 immersion tests, the property changes indicated by the second and third lines of Table 8-7 were unexpected. Consequently, the possibility of extraneous or systematic effects was considered.

One possibility considered was that a significant quantity of tantalum was being evaporated by the engine (thermionic) cathode which, as mentioned above, had been held near its normal operating temperature

to warm the discharge chamber and prevent mercury condensation in the chamber or manifold. To test this hypothesis, the samples were "exposed" to the thruster for 18 minutes with the cathode current set at the maximum value used previously but with the mercury boiler cold. Comparison of the third and fourth lines in Table 8-7 shows that this exposure had no appreciable effect on the sample properties. Therefore, it is doubtful that the previous change can be attributed to the presence of tantalum on the samples.

Another potential systematic effect that can be eliminated from consideration as a possible cause of the noted property change is instrumentation dependence on sample temperature. This can be seen by comparing the first and second lines of Table 8-7. Both of these runs were pre-exposure runs but were made at different sample temperatures. Since it is known that α_x is a very weak function of temperature (over this range) for all of the samples, any temperature related systematic error in instrumentation would have been apparent. Moreover, the hemispherical emittance (ϵ_H) values which do show a slight change over this temperature range are in substantial agreement with other data available in the TRW Thermophysics section.

8.3.4.4 Measurements on Condensed Mercury

A subsequent exposure was made in an attempt at measuring ϵ_H and α_x while mercury was still condensed on the samples. The data appears in the fifth line of Table 8-7. Note that the PV100 and polished aluminum channels recorded the largest changes in surface properties. The visual observation that these samples were not completely covered is confirmed by the fact that the two channels gave different results. All of the channels showed increased α_x and the polished aluminum with initially low ϵ_H experienced increased emittance as well. Thus, all of the samples had at least some condensate and the topography of this mercury was rough.

The latter point deserves some discussion. Both theory and measurement indicate mercury has $\epsilon_H \approx 0.1$ and $\alpha_s \approx 0.2$. During Phase I of this program, analysis was made of the thermal effects of condensing mercury on deployed solar arrays. The results of this analysis, and the property values quoted above upon which those results depend, are

probably correct only for array temperatures above the freezing point of mercury (-38.9°C). At lower temperatures, the condensate is not smooth and both emittance and adsorptance increase, as they do when any smooth surface is roughened.

Finally, the condensed mercury was re-evaporated by warming the samples to -33°C . The next morning, the in situ sample property values were as shown in the last line of Table 8-7. These values are quite close to those taken prior to the second condensation of mercury (Line 4).

8.3.4.5 Additional Immersion Tests

Because of the apparent discrepancy between the in situ measurements (which showed a definite difference in α_x before and after mercury is condensed and then re-evaporated) and earlier immersion tests (which showed no visual change), an additional mercury immersion test was performed.

The new test employed specimens from the stock of surface thermal samples prepared during Phase II. All thermophysical experiments to date have used specimens from this stock. The immersion was performed in a glove bag which was continuously purged with 99.995 percent pure nitrogen, and it lasted for 18 hours. The main difference between this test and the original immersion test was that spectral reflectance measurements and total hemispherical infrared emittance measurements were made after completion of the recent test. Differences (Δ) between these post immersion measurements and the corresponding pre-exposure values are included in Table 8-8 (third line).

The first line of data in Table 8-8 is based on in situ measurements before and after test series 7 in which mercury was condensed and then re-evaporated. The $\Delta\alpha_x$ and $\Delta\epsilon_H$ indicated by the first line in Table 8-8 were obtained by taking the difference between the first and last lines in Table 8-7. The second line in Table 8-8 shows $\Delta\alpha_x$ and $\Delta\epsilon_H$ as determined from ex situ spectral and total measurements of these beam-exposed samples.

Comparison of the first two lines of data in Table 8-8 suggests that much of the damage (change in thermal properties) indicated by the in situ measurements was annealed by the atmosphere before the ex situ measurements were made. This effect is believed to have been occasionally

Table 8-8. Comparison of Thermal Property Changes*

Test Series	Measurement	PV100		RTV41		Si1G		Zn3		Polished Aluminum		Gold		Cat-a-lac Black		3M Black		RTV566	
		Δt_H	$\Delta \sigma_x$	Δt_H	$\Delta \sigma_x$	Δt_H	$\Delta \sigma_x$	Δt_H	$\Delta \sigma_x$	Δt_H	$\Delta \sigma_x$	Δt_H	$\Delta \sigma_x$	Δt_H	$\Delta \sigma_x$	Δt_H	$\Delta \sigma_x$	Δt_H	$\Delta \sigma_x$
7. 1lg ⁰ Beam Condensation	In Situ	-0.02 ₇	+0.17 ₉	†	†	-0.01 ₄	+0.08 ₅	+0.00 ₃	+0.11 ₁	+0.03 ₂	+0.03 ₂								
	Ex Situ	0.00 ₀	+0.01 ₁	+0.00 ₁	-0.00 ₃	-0.00 ₃	+0.00 ₇	-0.00 ₂	0.00 ₀	0.00 ₀	-0.01 ₅								
8. 1lg Immersion N ₂ Atmosphere	In Situ	0.00 ₀	+0.01 ₀	-0.00 ₄	-0.00 ₅	+0.00 ₃	-0.00 ₆	-0.00 ₃	-0.00 ₂	+0.00 ₄	+0.01 ₈	+0.11 ₅	-0.10 ₃	-0.00 ₂	0.00 ₀	-0.00 ₃	-0.00 ₇	-0.00 ₂	0.00 ₀

Although the accuracy of the measuring instruments does not justify three significant figures, the third figure is retained depressed so as to indicate trends.

† Not functioning Channel

observed before; see, for instance, Table 8-4. On the other hand, a Phase II (1969) experiment in which mercury ion beam damaged coatings were exposed to oxygen and then re-measured in situ did not indicate annealing of these badly damaged samples (see Table 8-1a.)

A comparison between the last two lines of data in Table 8-8 shows that the immersion tests did produce slight property changes whose polarity and magnitude are similar in most cases to those indicated by the ex situ measurements from the beam-condensation tests.

Deltas shown in Table 8-8 are total values; i. e., weighted integrated and averaged over the entire wavelength spectrum. Figures 8-12 through 8-16 show pre- and post-exposure spectral absorptance in the ultraviolet, visible, and near infrared regions. It was from these distributions that the ex situ $\Delta\alpha_x$ values of Table 8-8 were calculated using the xenon lamp energy distributions described in Appendix B. The spectral plots show that the damage is highly non-uniform with respect to wavelength. Thus, a tabulation of α_x for a few specific wavelengths where changes are maximum should render a better (more sensitive) comparison than can be obtained from Table 8-8. Such a tabulation is presented in Table 8-9.

Figures 8-12 through 8-16 and Table 8-9 show that the most dramatic change in α_x occurred in the ultraviolet region on the polished aluminum sample during the beam-condensation experiments (Test Series 7). The same type of change occurred but to a much lesser extent on the polished aluminum sample during the immersion tests. This difference suggests the existence of a thin protective surface layer which can be stripped or penetrated by the combination of vacuum, condensation, and dynamic effects of the beam but which remains more-or-less intact during immersion in liquid mercury in a nitrogen atmosphere. Interestingly enough, the damage imposed on polished aluminum (and possibly the other sample materials as well) by the mercury atom beam does not occur to any significant extent under conditions where mercury is not condensed on the sample. This statement is based on Table 8-6 which shows an ex situ $\Delta\alpha_x$ of +0.009 for polished aluminum after exposure to a beam of mercury atoms under conditions that prohibited bulk condensation. The spectral absorptance plot from which that data was calculated showed little or no change in the ultraviolet region.

Table 8-9. Summary Comparison of Ex Situ Delta α_x at Various Wavelengths

Test Series	Test Description	Wavelength (Microns)	Delta Absorbance ($\Delta\alpha_x$)*				
			PV100	RTV41	S13G	Z93	Polished Aluminum
7	Hg ^o Beam	0.28	+0.02 ₀	-0.01 ₀	+0.01 ₃	+0.00 ₅	+0.24 ₀
8	Hg Immersion	0.28	-0.00 ₂	0.00 ₀	0.00 ₀	-0.00 ₆	+0.03 ₀
7	Hg ^o Beam	0.50	+0.02 ₀	+0.02 ₀	+0.02 ₀	+0.01 ₅	+0.03 ₀
8	Hg Immersion	0.50	-0.00 ₆	+0.05 ₀	+0.01 ₅	+0.00 ₈	+0.03 ₀
7	Hg ^o Beam	2.00	0.00 ₀	0.00 ₀	+0.01 ₀	-0.01 ₄	0.00 ₀
8	Hg Immersion	2.00	0.00 ₀	+0.02 ₅	-0.00 ₂	-0.01 ₂	+0.02 ₀

*Although the accuracy of the measuring instruments does not justify three significant figures, the third figure is retained depressed so as to indicate trends.

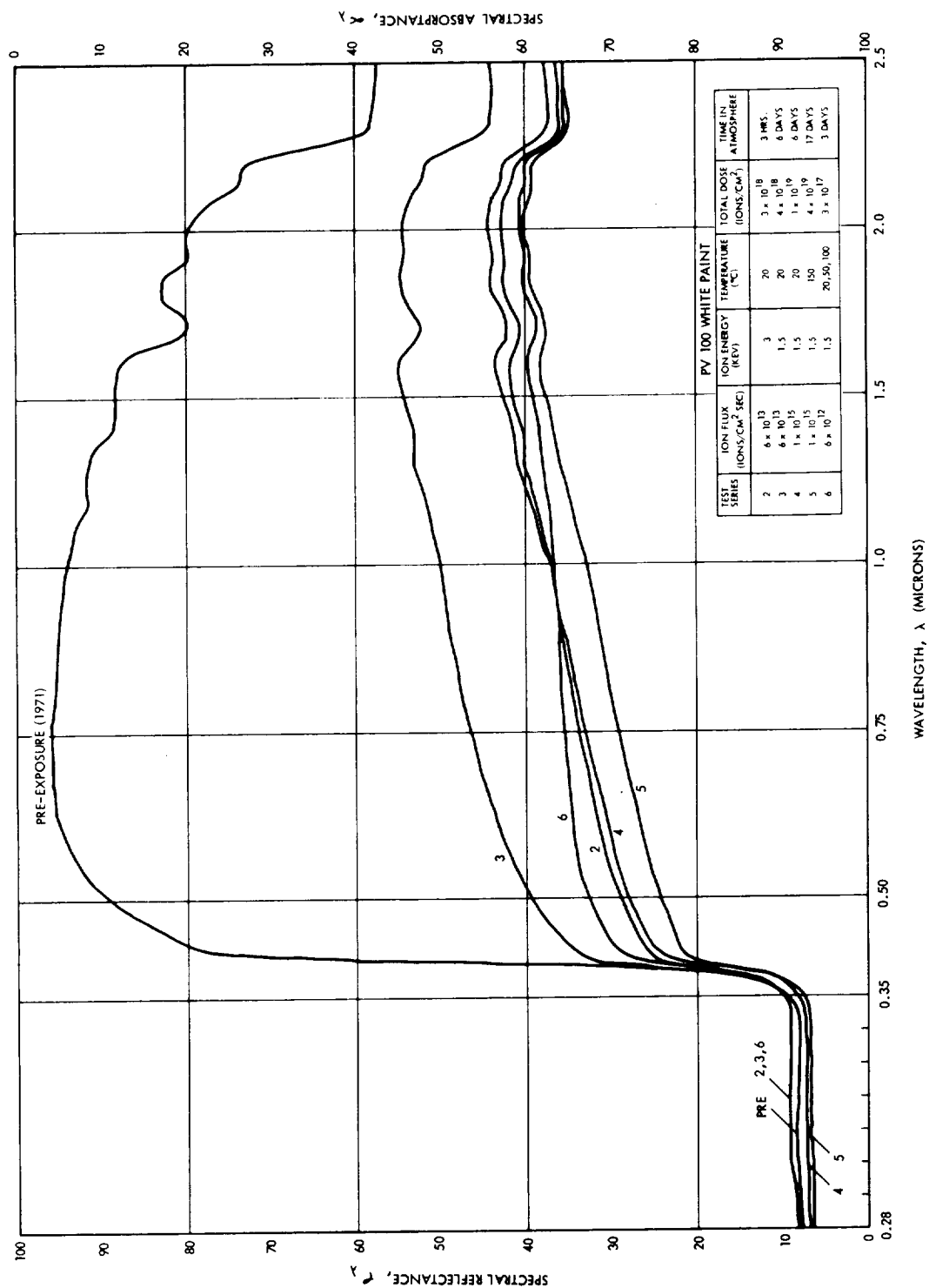


Figure 8-12. Spectral Distribution of PV100 White Paint Before and After Exposure to a Mercury Atom Beam (7) and Immersion in Liquid Mercury (8)

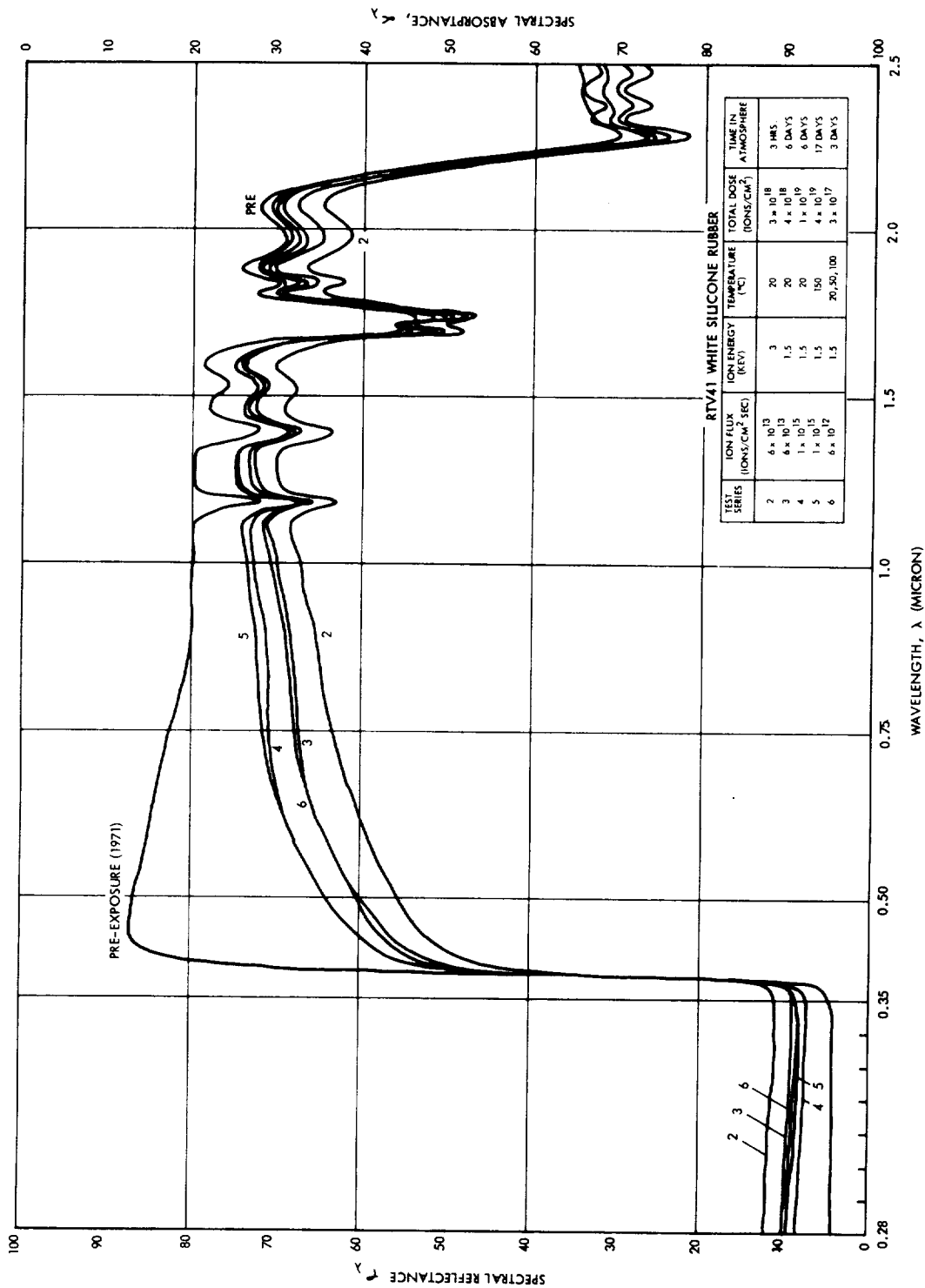


Figure 8-13. Spectral Distribution of RTV41 White Silicone Rubber Before and After Exposure to a Mercury Atom Beam (7) and Immersion in Liquid Mercury (8)

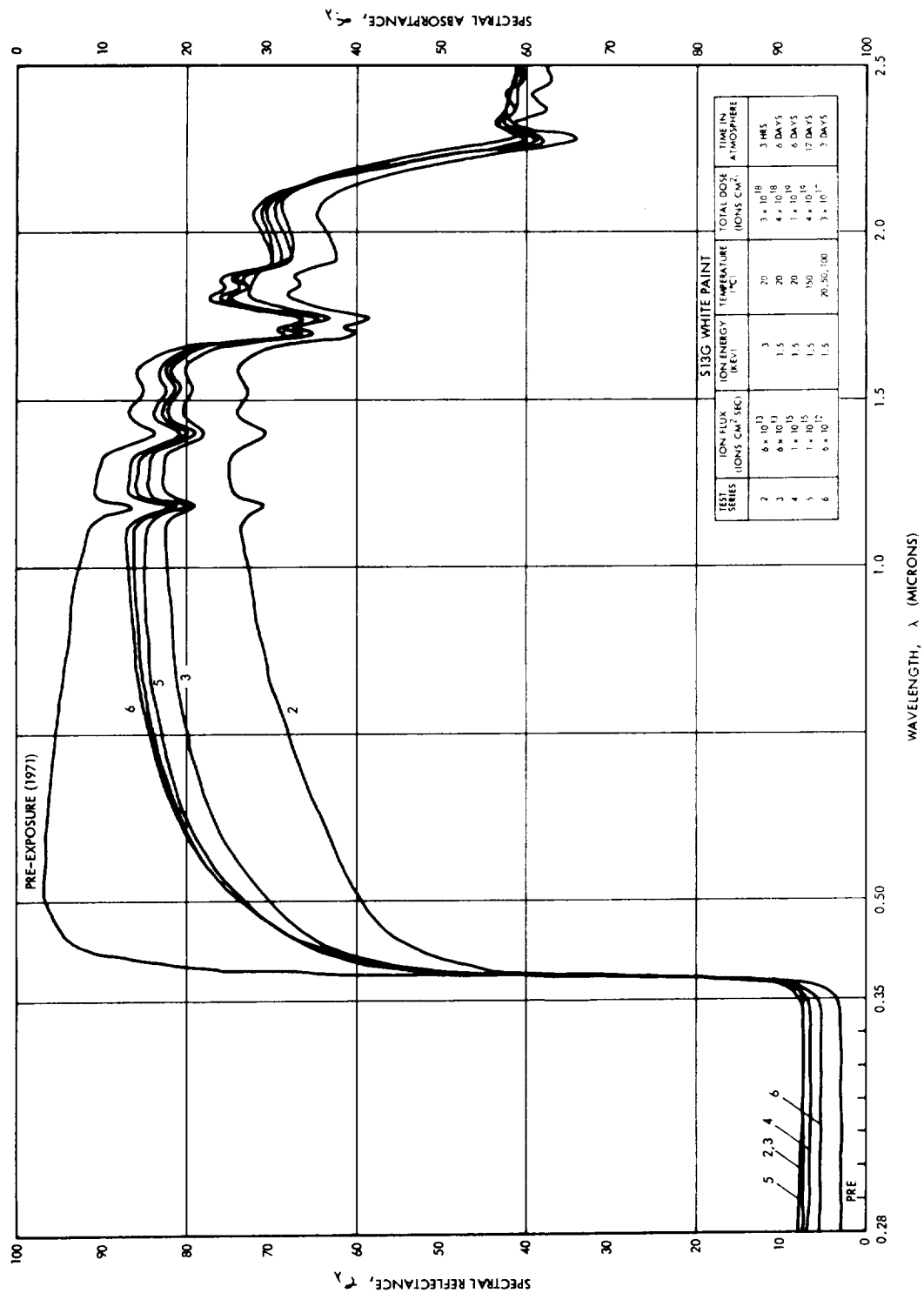


Figure 8-14. Spectral Distribution of S13G White Paint Before and After Exposure to a Mercury Atom Beam (7) and Immersion in Liquid Mercury (8)

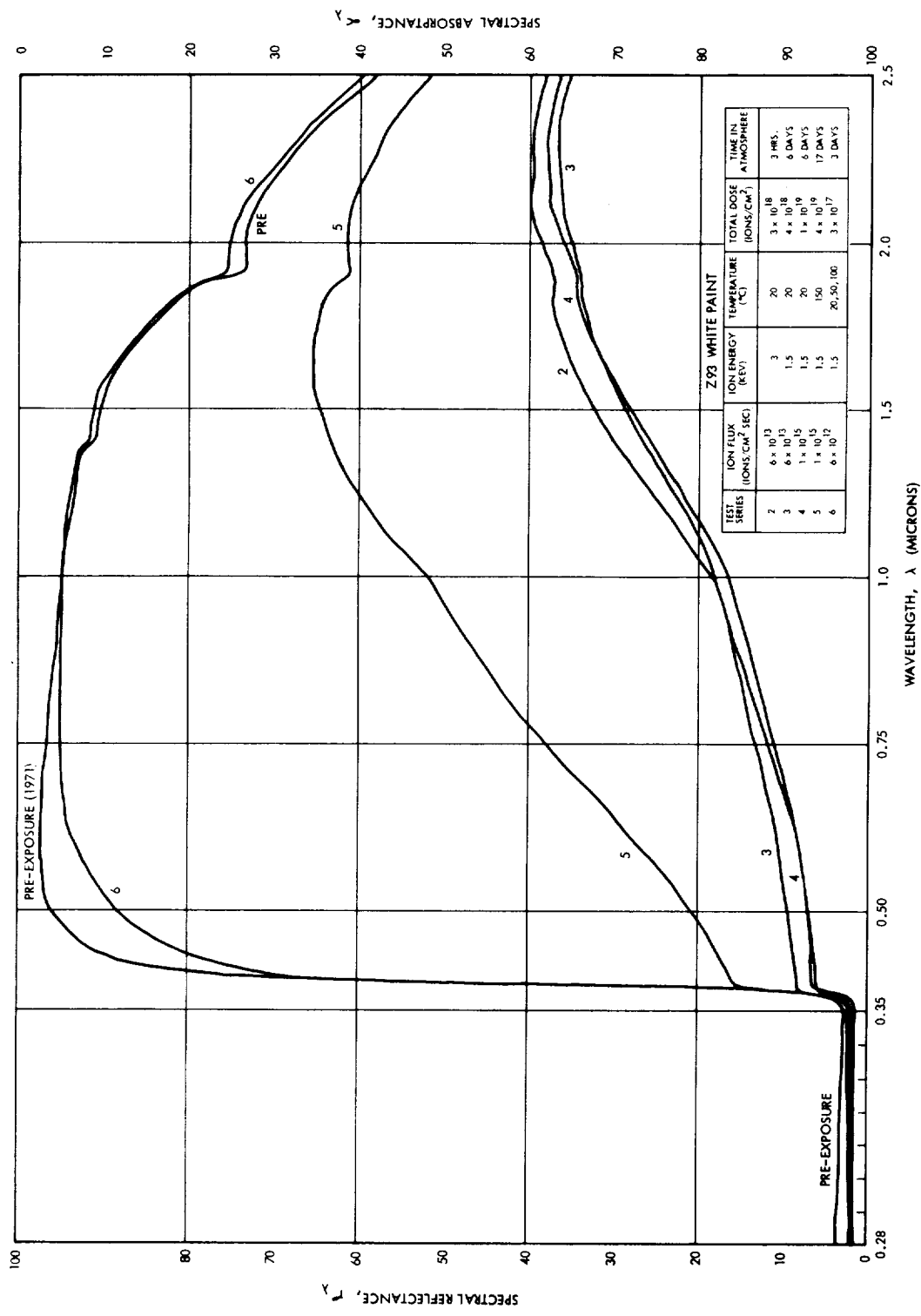


Figure 8-15. Spectral Distribution of Z93 White Paint Before and After Exposure to a Mercury Atom Beam (7) and Immersion in Liquid Mercury (8)

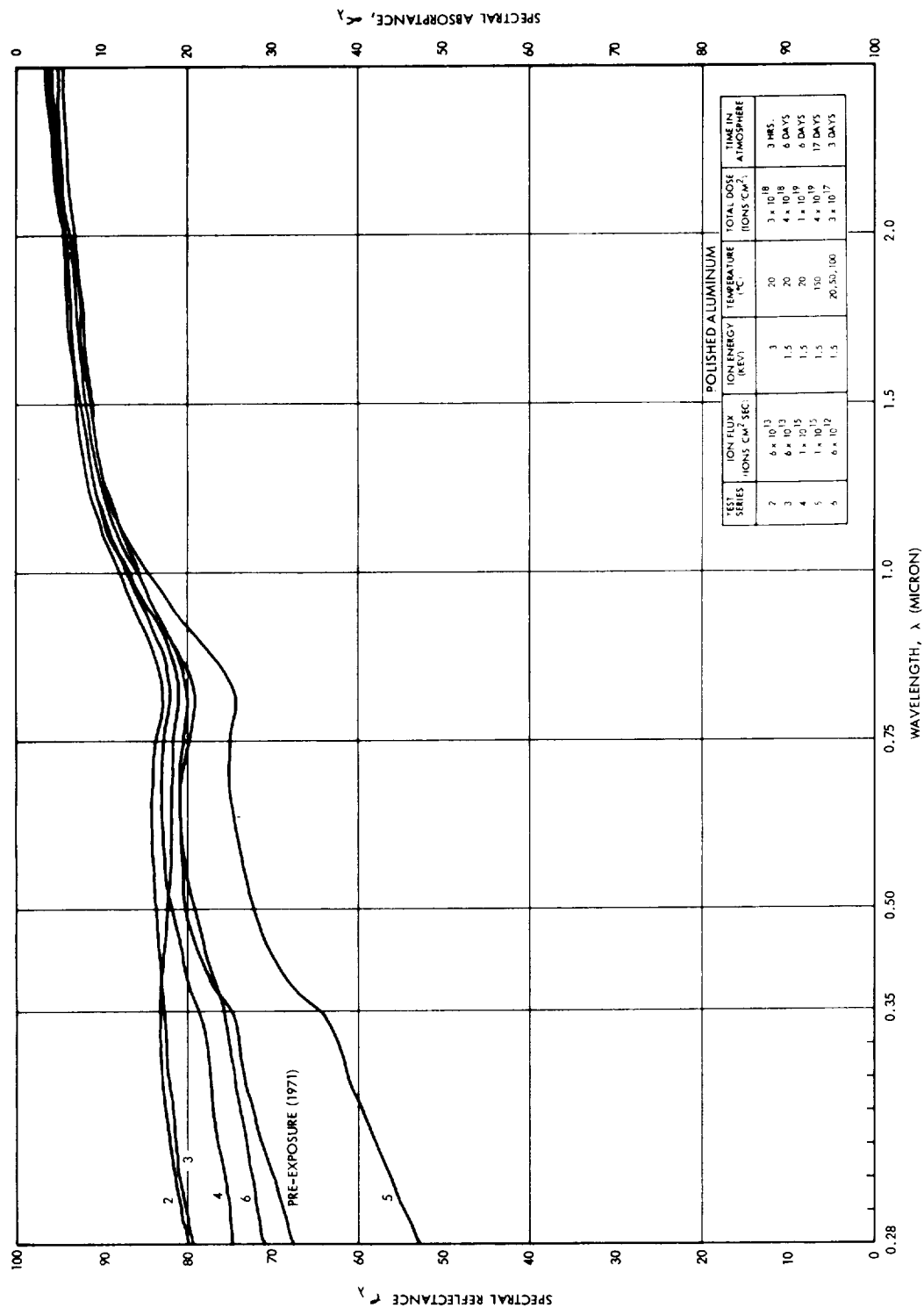


Figure 8-16. Spectral Distribution of Polished Aluminum Before and After Exposure to a Mercury Atom Beam (7) and Immersion in Liquid Mercury (8)

Much of the remaining apparent change in ex situ α_x shown by Figures 8-12 through 8-16 and Table 8-9 can be attributed to sample-to-sample variations and measurement non-repeatability.

8.3.4.6 Conclusions

If the in situ total deltas of Table 8-8 are reliable, as we believe they are, then bulk condensation and re-evaporation of mercury in vacuum can impose measurable changes on the surface thermal properties of most of the samples tested. Much of the effect apparently disappears when the samples are returned to the atmosphere. However, since atom beam damage was not expected and the mercury condensation was not uniform, the experiment obviously should be repeated. Unfortunately, contract resources and time did not permit further repetitions.

8.4 COMPARISONS TO DATA FROM OTHER LABORATORIES

8.4.1 Total Property Damage

An interesting comparison of the results of mercury ion degradation from this program with previous work is shown in Figure 8-17 taken from Reference 10. This figure was originally presented in Reference 11 as a summary of test of light particle bombardment induced damage to zinc oxide pigmented potassium silicate paint. Additional data were added by Lockheed when it was reprinted in Reference 10. It should be noted that the in situ measurements of Hg^+ damage employed a xenon spectrum whereas the other data on Figure 8-17 were computed from spectral measurements and the solar spectrum. If true $\Delta\alpha_s$ for the solar spectrum were available for the Hg^+ damage case, one would expect greater degradation than shown, since the solar spectrum contains more energy in the ultraviolet where greater degradation occurs. This would shift the curve to the left, closer to the mass of other data presented. The good agreement of present test data with that for various energies of hydrogen ions would, of itself, indicate similar degradation mechanisms are responsible for property changes of Z93 type material.

8.4.2 Spectral Damage

Pre- and post-exposure spectral reflectance plots of samples exposed to beams of mercury ions provide another basis of comparison with thermal coatings testing performed in other laboratories¹²⁻¹⁴.

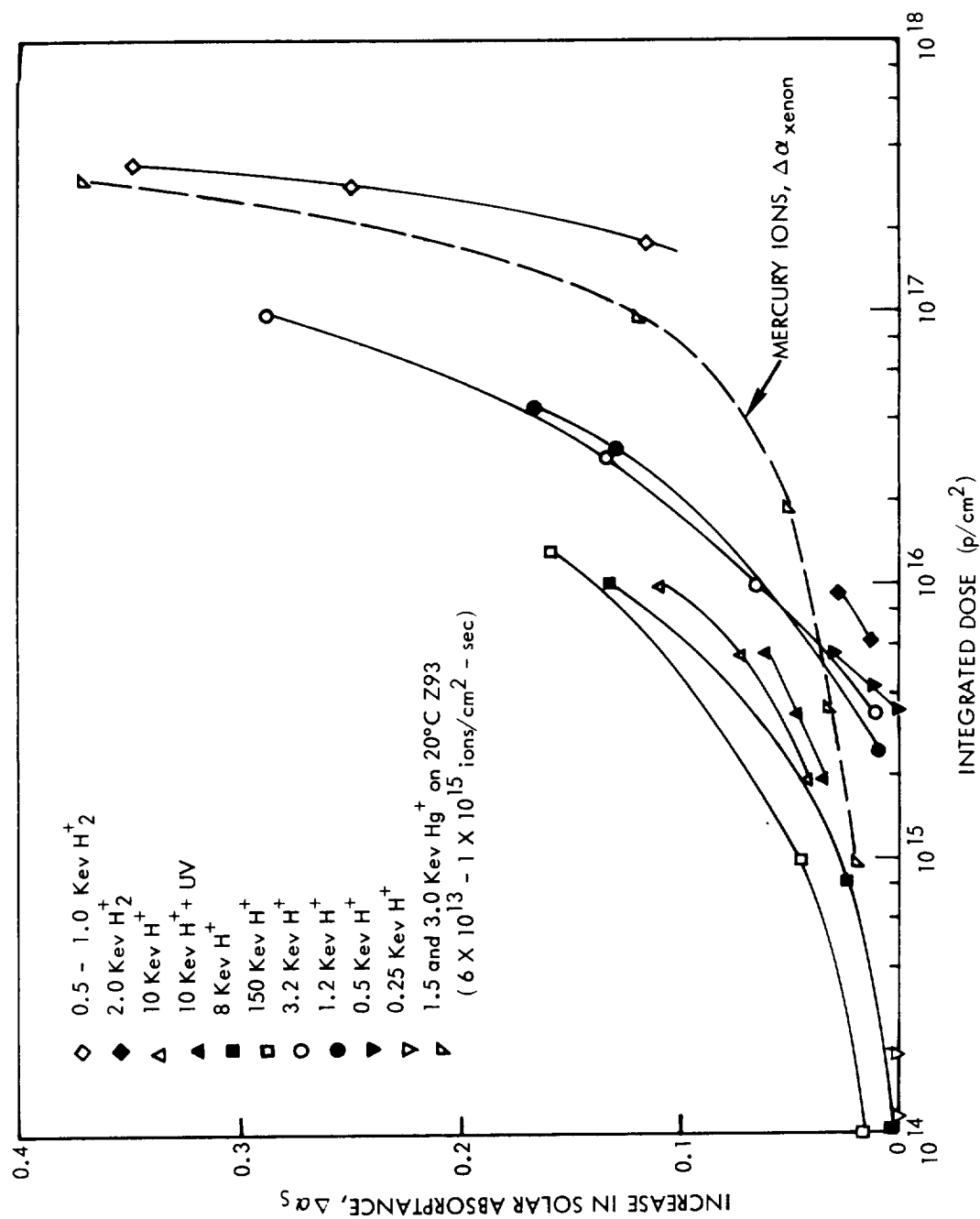


Figure 8-17. Change in Solar Absorbance ($\Delta\alpha_s$) as a Function of Proton Integrated Dose for ZnO/K₂SiO₃ Paints (After Reference 19) and Change in Absorbance ($\Delta\alpha_x$) of Z93 by Hg⁺

It should be noted, however, that total fluences in this current work are far above those traditionally used in charged particle testing. These fluences were purposely selected to identify potential problem areas and to discover maximum tolerable ion doses as an aid to design of spacecraft employing electro-static propulsion.

Also, the experimentors of References 12 to 14 have observed significant O₂ related recovery of charged particle and ultraviolet degradation of the thermal coatings. Tests made under the present program also show similar results in this regard for some samples. Thus, the post-exposure ex situ spectral data reported to date should be considered primarily as qualitative information.

In general, the magnitude of the Hg⁺ caused degradation is much greater than that reported for smaller doses of H⁺ and H₂⁺. With one exception, it is also more spectrally uniform than that caused by either ultraviolet radiation or light ions. This degradation appears grey rather than the short wavelength or yellow degradation usually obtained. The one exception is the Z93 sample of Test Series No. 6 (see Figure 8-7). Interestingly, the exposure rate and dose of Test Series No. 6 was smaller than the others and closer to that used in the light ion work. However, Figures 8-8 through 8-11 show that the Series No. 6 spectral damage to the other paint samples (S13G, PV100, RTV41) extends well beyond one micron.

Both the lack of significant (and rapid) bleaching and the "grey" degradation suggest that the dominant degradation mechanism for the mercury ion impingement may be different than for hydrogen ion impingement. As suggested above, another possibility is that these differences are associated with the difference in the magnitude of damage produced in the Hg⁺ and H⁺ tests. This question could be resolved by attempting to heal samples which had received smaller Hg⁺ doses and then making spectral measurements.

8.4.3 Summary

Both spectral and total degradation data from the current program have been compared to data appearing in the literature. With one exception, the spectral data indicate more uniform (less wavelength

dependent) degradation than either ultraviolet or hydrogen ion data from other experimenters. However, the good agreement of total property degradation as function of ion fluence with other data suggests similar degradation mechanisms are responsible for property changes. The total property data are considered adequate for the engineering objectives of this program, but in situ spectral data would be very helpful if more basic scientific valuations of ion effects are to be performed in future studies.

8.5 REFERENCES (Section 8)

1. "Solar Radiation-Induced Damage to Optical Properties of ZnO-type Pigments", NAS 8-18114 June, 1967, Lockheed Palo Alto Res. Lab. Tech Summary, 27 June 1966 - March 1967.
2. G. V. Jorgenson, "Effects of Simulated Solar-Wind Bombardment on Spacecraft Thermal Control Surfaces", AIAA Paper No. 65-647 presented at the AIAA Thermophysics Specialist Conference at Monterey, California, September 13, 1965.
3. G. V. Jorgenson, "Solar-Wind Damage to Spacecraft Thermal Control Coatings", AIAA Journal, 5, pp. 1204-5, 1967.
4. G. K. Wehner, "Solar-Wind Bombardment of a Surface in Space", from Symposium on Thermal Radiation of Solids, NASA SP-55, pp. 345-349 1964.
5. R. M. Van Vliet, Passive Temperature Control in the Space Environment, MacMillan Company, New York, pp. 210-217 and 229-235, 1965.
6. J. F. Friichtenicht, J. T. Bevans, J. T. McNamara, and W. D. Miller, "Final Report of a Study of Micrometeoroid Damage to Thermal Control Materials", prepared under Contract No. NAS 8-20120 for the George Marshall Space Flight Center, October, 1966.
7. H. F. MacMillan, A. F. Sklensky, and L. A. McKellar, "Apparatus for Spectral Bidirectional Reflectance Measurements during Ultraviolet Irradiation in Vacuum", Progress in Astronautics and Aeronautics, 18, "Thermophysics and Temperature Control of Spacecraft and Entry Vehicles", pp. 129-149; Editor: G. B. Heller, Monterey Conference, September 13 - 15, 1965, Academic Press, 1966.
8. "Solar-Radiation-Induced Damage to Optical Properties of ZnO-type Pigments", NAS 8-18114, June 1967, Lockheed Palo Alto Res. Lab. Tech. Summary, 27 June 1966 - 27 March 1967.

9. W. D. Miller and E. E. Luedke, "In Situ Solar Absorptance Measurement, An Absolute Method", Effects of the Space Environment on Materials, II, pp. 75-84, Society of Aerospace Materials and Process Engineers, 11th National Symposium and Exhibit, St. Louis, April 1967.
10. "Study of Environmental Effects upon Particulate Radiation Induced Absorption Bands in Spacecraft Thermal Control Coatings Pigments", Lockheed Report 6-78-68-45, Contract No. NAS 2-4353. Final Report for 22 May 1967 to 27 January 1969.
11. E. R. Streed, "An Experimental Study of the Combined Space Environmental Effects on a Zinc-Oxide-Potassium-Silicate Coating", AIAA Paper 67-339, April 17-20, 1967.
12. L. B. Fogdall, et al., "Ultraviolet and Electron Radiation Effects on Reflectance and Emittance Properties of Thermal Control Coatings", AFML-TR-70-156, July 1970.
13. S. A. Greenberg, et al., "Damage Mechanisms in Thermal Control Coating Systems", AFML-TR-67-294, September 1967.
14. J. E. Gilligan and G. A. Zerlaut, "The Space Environment Stability Problem in White Pigment Coatings", Institute of Environmental Sciences 1971 Proceedings, pp. 447-457, April 26-30, 1971.

9. OVERALL CONCLUSIONS AND RECOMMENDATIONS FOR FUTURE WORK

9.1 INTRODUCTION

The individual sections contain detailed conclusions and recommendations for future work. Highlights of these findings are given here, section by section.

9.2 SPACECRAFT DESIGN IMPLICATIONS

Particulate contamination has a major impact on the design of electric spacecraft. Spacecraft surfaces should be restricted from the exhaust hemisphere whenever possible, but this is not always possible and does not necessarily eliminate all contamination problems. The data and theory of this report can guide selection of materials and determination of acceptable angles and distances between sensitive spacecraft surfaces and the thrusters.

Development of thruster baffling schemes, though not completely straightforward, offers some hope in solving some kinds of contamination problems. Work on baffle technology deserves a high priority.

9.3 ION ENGINE EFFLUENTS

Although mathematical descriptions of ion engine effluents are given, they may be very unreliable at large angles which is the usual region of interest. Experimental investigations of the high angle emissions of typical thrusters should receive the highest priority.

9.4 DEPOSITION AND EFFECTS OF THIN FILMS

Propellant condensation can be predicted satisfactorily using "worst case" assumptions. It is found that propellant condensation is a potential problem only on very cold surfaces as may occur on missions distant from the sun. Theoretical analysis of the optical effects of thruster metal deposition indicates that extremely thin films can be very troublesome. If true, thruster metal deposition will be the most important of all contamination problems on most electric spacecraft designs. Direct experimental confirmation of these analyses is badly needed.

9.5 ION EROSION

The erosion rates of 18 spacecraft surface materials by 1 and 3 keV Hg^+ were measured as a function of angle of ion incidence. These data permit calculation of the erosion lifetime of a surface and its strength as a secondary source of contaminants. Because erosion proceeds slowly, only very thin films or targets receiving rather large ion doses might be completely removed by sputtering.

Future ion erosion work should explore topographical effects on the optical properties of lenses and solar cell cover glasses. Additional sample materials, lower ion energies, use of cesium as well as mercury, and variation of target temperature are other areas for future work.

9.6 CHEMICAL EFFECTS OF PROPELLANTS

Except for Teflon FEP and Kapton surfaces receiving cesium propellant, the organic materials tested appear to be reasonably chemically stable toward both mercury and cesium ions and atoms. However, materials subject to severe basic hydrolysis should not be used in areas where moisture may survive until cesium ion thruster operation commences.

Cesium beam experiments are clearly indicated for Teflon FEP and Kapton.

9.7 METALLURGICAL EFFECTS OF PROPELLANTS

The propellant/spacecraft metal reactions which have received experimental attention are mercury/solder, mercury/silver, and cesium/solder. Gold is also expected to be attacked by the propellants. Solder was found to be severely affected by immersion in liquid mercury and in liquid cesium. However, mercury atom beam exposures of room temperature solder lap shear tensile specimens did not produce measurable changes in joint strength. The reaction between liquid mercury and silver is quite slow, and therefore probably not a problem.

Future metallurgical work should include mercury beam exposures of cold solder lap specimens, cesium beam/solder tests, and tests on gold.

9.8 DAMAGE OF THERMAL CONTROL COATINGS

The in situ property degradation measurement technique and apparatus developed under this program have been demonstrated to perform as designed, and a considerable quantity of data has been obtained. Pre-exposure in situ values of α_X and ϵ_H are in good agreement with corresponding values obtained by integrating ex situ spectral data. In some instances post-exposure ex situ values are clearly in disagreement with corresponding in situ values. The need for making degradation measurements in situ is thus confirmed.

Basically, three types of in situ tests were conducted. In the first type, samples were bombarded with mercury atoms with sample temperatures and atom arrival rates that disallowed bulk condensation of mercury. Similar samples were later bombarded with mercury neutrals under conditions that caused bulk condensation. In the third type, test samples were exposed to a beam of mercury ions.

The non-condensing mercury atom experiments showed no measurable effect on either α_X or ϵ_H for any of the sample materials tested (Catalac black paint, 3M black paint, PV100 white paint, Z93 white paint, S13G white paint, RTV41 silicone rubber, polished 6061-T6 aluminum, gold plated polished aluminum, 6 mil microsheet with second surface VDA, and 20 mil quartz with second surface VDA). The samples were exposed at room temperature for up to 4.425 hours with a beam flux density of 1×10^{14} atoms/cm² sec.

Only four samples (PV100, S13G, Z93, and polished aluminum) were exposed to the mercury beam with condensation, but of these four all showed an increase in α_X . This was a somewhat surprising result, since neither mercury immersion tests nor subsequent ex situ measurements showed much, if any, change. The possibility of experimental errors during the in situ test has not been fully eliminated but based on checks that have been made, it is believed that the in situ values are essentially correct and that the ex situ results were influenced by atmospheric "healing." The immersion test results may have been similarly affected, or it may be that immersion testing fails in some important respect to simulate mercury atom beam impinging in vacuum on a cold sample.

Damage imposed by mercury ions is more severe than that imposed by mercury atoms. This is particularly true for the white paints, most notably Z93 at high ion doses. Degradation occurs mainly in α_X with ϵ_H being essentially unaffected by exposure to accumulative mercury ion doses of up to 4×10^{19} ions/cm². Degradation of α_X is a strong function of accumulative ion doses (flux density multiplied by exposure time). Flux densities between 6×10^{13} and 1×10^{15} ions/cm² sec and ion energies between 1.5 and 3 keV gave essentially identical results. Lowering the flux density by another factor of 10 (6×10^{12} ions/cm² sec) had only a weak influence on the α_X versus accumulative ion dose curve. Similarly, sample temperatures (during exposure) appear to have a weak influence in most cases. Because of slight sample to sample variations and random data scatter, many more runs would be required in order to accurately define these relatively weak influences.

Future work should include additional tests of the effects of condensing mercury atoms, tests with additional materials (e.g., DC92-007 white paint, silvered Teflon, aluminized Kapton, GSFC MS-74 white paint, Al₂O₃/SiO₂/VDA, Kynar), measurement of α and ϵ of frozen Hg and Cs, tests with smaller Hg⁺ energy and arrival rate, tests with cesium beams, and investigation of the effects of angle of ion incidence and low sample temperature.

10. NEW TECHNOLOGY

The use of the large diameter space-charge-neutralized beam of an ion engine to simultaneously bombard many metallic and dielectric samples for the purpose of measuring their rates of erosion and changes in surface properties is believed to be new technology. A description of this scheme and some typical results are given in Section 5. Of course, the same techniques could be employed for study of ion erosion of many ionic species by substituting other vapors or gases for mercury.

—

—

—

APPENDIX A EXPERIMENTAL FACILITY

The Spacecraft Surface Contamination Experimental Facility (SSCEF), developed during Phases I and II, was used for all atom and ion beam experiments reported herein. This is a 4- by 8-foot vacuum chamber especially designed to accommodate a number of different experiments on the effects of mercury and cesium ion and atom beams on spacecraft surface materials. Figure A-1 gives an overview of the SSCEF.

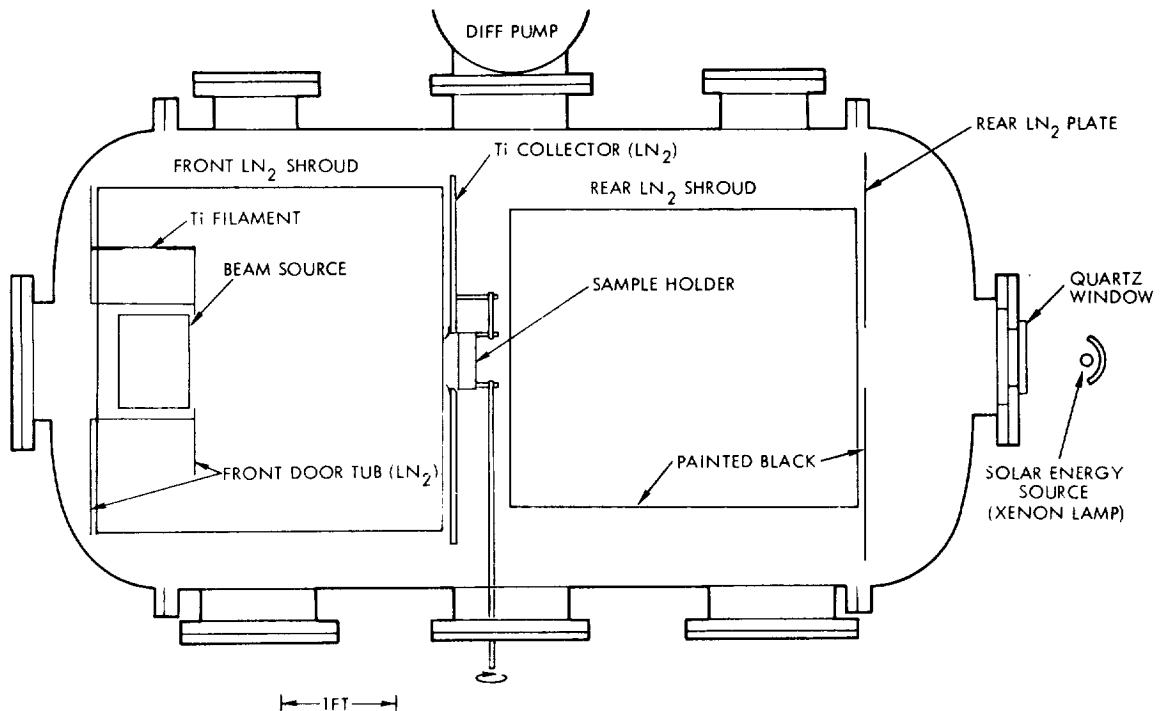


Figure A-1. Schematic Diagram of Spacecraft Surface Contamination Experimental Facility

The mercury beam source is a 15-cm electron bombardment NASA/Lewis-type thruster with a refractory metal cathode and heatable propellant tank. The design electrode potentials for this thruster are +3 kv on the screen grid and -2 kv on the accelerator grid; however, to obtain ± 3 percent beam uniformity over the 6- x 6-inch sample area some 30 inches distant, the accelerator grid is usually operated in excess of -4 kv. Ion beam uniformity is verified before and after each sample exposure by an array of five Faraday cup probes mounted on a movable

sample shutter (see Figure B-7) which is used to start and terminate sample exposures.

As with any ion engine, the "ion beam" is in fact a streaming plasma. The presence of plasma neutralizing electrons in the beam prevents dielectric targets from obtaining a significant surface charge during ion bombardment. As soon as a surface begins to accumulate excess positive charge, plasma electrons are attracted and collected.

In some experiments the plasma electrons are secondaries from ion impacts on the collector while in others a thermionic refractory metal wire is immersed in the beam near the thruster. The latter technique is recommended.

The beam collector is an LN_2 -cooled, high-purity titanium circular plate with a square cut out at its center through which the samples view the beam source. Titanium was chosen as the collector material to minimize the release of occluded and absorbed gases as it is slowly sputtered away. A second advantage is that the Ti atoms sputtered from the collector deposit on other LN_2 -cooled surfaces and getter residual gases which do not cryopump (carbon monoxide and hydrogen). This continuous adsorption pumping can be supplemented by heating Ti sublimation filaments deployed between the flanges of the LN_2 -cooled, spool-shaped front door "tub". Pressure in the experimental chamber does not exceed 5×10^{-8} torr during operation with 750 watts of Hg^+ beam power. Chamber pressure is even lower when the beam is off. This gas is primarily CO and H_2 . The ratio of beam particles to gas particles arriving at the sample surfaces exceeds 50. An experiment with an aluminum-coated quartz crystal microbalance demonstrated that the chamber pressure must exceed 1×10^{-6} torr of carbon monoxide before the ion beam erosion rate of Al is inhibited.¹

The roughing pump line to the chamber contains a zeolite trap. Trap bakeout is thermally managed in a way that requires the trapped vapors to go into the pumps. During pump down, the system is switched off the roughing pumps and onto the diffusion pump at about 100 microns. This practice further reduces the possibility of mechanical pump oil entering the chamber.

The diffusion pump is charged with DC-704 oil and is continuously trapped with an optically opaque LN_2 trap.

In addition to minimizing the arrival rate of residual gases in the SSCEF, careful attention was given the matter of extraneous metal atoms arriving at the sample plane. Metal atoms can originate at the beam source itself and come from chamber wall sputtering.

Extraneous atoms originating at the 15-cm electron bombardment thruster are tantalum from the thermionic tantalloy engine cathode and molybdenum from accelerator grid sputtering. Both of these fluxes are small compared with the mercury ion flux. The cathode is hairpin-shaped with its axis coincident with the thruster axis. Thus, it has only a small view factor with the samples. Further, these atoms must pass through the ~50 percent opaque grid system to reach the sample area. Accelerator grid erosion is a bigger source of extraneous atoms. However, the arriving flux of Mo is estimated² to be ~1/500 that of the Hg^+ .

Copper is sputtered from the cylindrical LN_2 liner between the front door tub and the collector and is shadow-shielded from the sample area. These shields are mounted on the collector around the sample area. Figure A-2 is a closeup with the sample area blanked off with white paper. The forward (most prominent) shield set shadows the sample area from copper sputtered from the liner. The inner set of shields precisely defines the sample area and prevents ions from striking the sides of the cut-out in the 5/8-inch thick titanium collector plate. In their absence, sputtered titanium would reach the samples. Both sets of shields have their inside edges beveled to make the edge area, and therefore, the quantity of copper sputtered onto the samples, negligible.

Not shown in Figure A-2 is a Faraday cup (j_+) probe which is mounted just outside the shields. It monitors arriving ion current density during sample exposures when the j_+ probes on the shutter cannot be used.

Mercury atom beams were also supplied by the 15-cm thruster. The refractory metal cathode and electromagnet were powered to prevent propellant from condensing in the thruster. The intensity of the atom flux emitted was controlled by electronically regulating the temperature

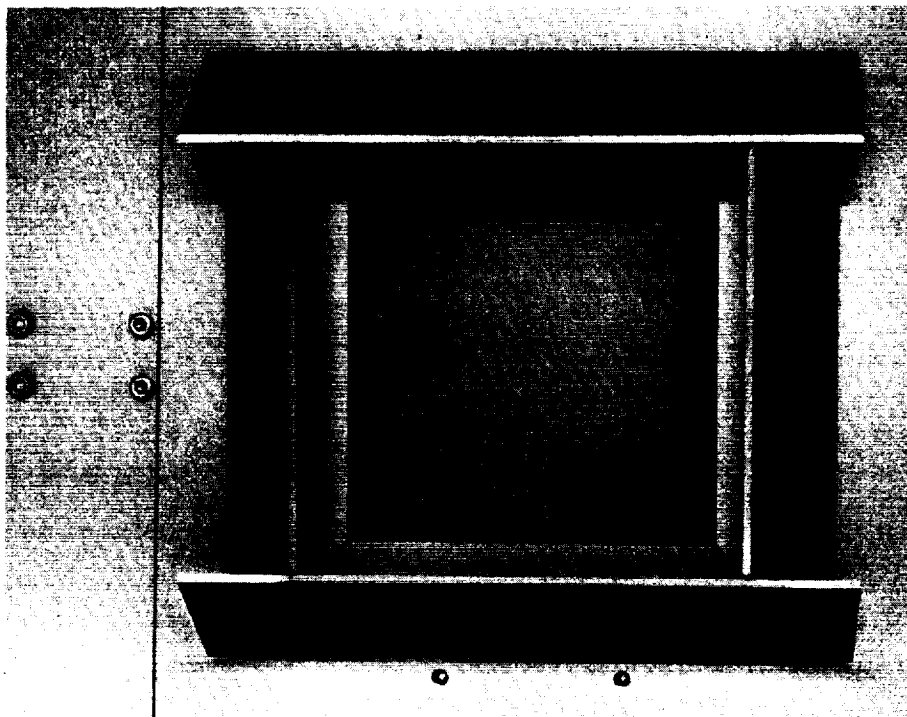


Figure A-2. Closeup Photograph of Collector Plate
Sample-Area-Cut-Out Sputtering Shields

of the isothermal mercury boiler. Data from lengthy gravimetric calibrations² of boiler efflux versus temperature were used to determine the rate of boiler efflux. Arrival rate at the sample plane was calculated based on boiler efflux and an assumed cosine distribution from the accelerator grid.

REFERENCES (APPENDIX A)

1. D. F. Hall, "Evaluation of Electric Propulsion Beam Divergence Effects on Spacecraft," 08965-6013-R0-00, Final Report Contract No. NAS7-575, TRW Systems, Redondo Beach, California, September 1969.
2. D. F. Hall, "Electrostatic Propulsion Beam Divergence Effects on Spacecraft Surfaces," Final Report, Vol. I, JPL Contract No. 952350, TRW Systems, Redondo Beach, California, August 1970.

APPENDIX B THERMOPHYSICS INSTRUMENTATION

1. EX SITU MEASUREMENTS

During Phase II (in 1969), pre-exposure spectral reflectance distributions of two samples of each of eleven materials were measured between 0.28 and 2.5 microns on a modified Beckman DK2A double beam ratio recording photo spectrometer¹ and between 2.0 and 26.0 microns on a Gier Dunkle Heated Cavity Reflectometer². These pre-exposure data were presented in total in Appendix B of Reference 3 and are considered to be representative of the respective sample batches that were prepared in 1969 and from which all test samples have been obtained. Similar post-exposure measurements were made on some samples and the results are presented with and compared to corresponding in situ data in Sections 8.3.2.5 and 8.3.4.5. During the more recent test series (1971), one more of the original unexposed samples of several of the materials was re-measured on the ex situ instruments as a check on aging. With the possible exception of RTV41, which has always showed considerable sample to sample variation, no aging effects were detected.

From the reflectance functions described above, values of total absorptance for different light sources were calculated assuming opacity ($\alpha_t = 1 - \rho_t$). The total reflectance was computed by integrating the spectral reflectance function over the range of wavelengths after weighting with the spectral intensity function of the light source. These data reductions were manually performed using an equal energy band method. Values for total solar absorptance α_s were obtained using a 25-band overlay based on the Johnson zero-air-mass solar curve⁴. Inasmuch as relatively little solar energy lies outside the range of 0.28 to 2.5 microns, this calculation is principally from the DK2A data. Similarly, values for total xenon absorptance α_x (or α_{Xe}) were obtained using a 25-band overlay with each band representing 4 percent of the total integrated energy under the measured spectral distribution of the Christie xenon lamp unit (described below). During runs requiring low thermal flux density, the Christie lens system was removed. This gave rise to a different spectral distribution, and a separate overlay was made for this configuration also. All initial ex-situ data are tabulated in Table B-1.

Table B-1. Summary of Results of Pre-Exposure
Ex Situ Measurements†

Sample No.		α_s (a)	α_x (a)	ϵ_N (b)	ϵ_H (c)
454-69	Gold Plated Aluminum	0.220	0.160*	0.010	0.013
455-69	Gold Plated Aluminum	0.196	0.140*	0.010	0.013
456-69	S13G White Paint	0.190	0.148	0.903	0.853
457-69	S13G White Paint	0.188	0.142	0.899	0.850
458-69	PV100 White Paint	0.188	0.142	0.866	0.823
459-69	PV100 White Paint	0.190	0.139	0.864	0.820
460-69	Z93 White Paint	0.159	0.117	0.918	0.869
461-69	Z93 White Paint	0.162	0.117	0.923	0.873
462-69	Polished Aluminum	0.181	0.166*	0.018	0.023
463-69	Polished Aluminum	0.169	0.155*	0.021	0.027
464-69	3M Black Paint	0.982	0.982	0.909	0.858
465-69	3M Black Paint	0.986	0.986	0.918	0.866
554-69	6-mil Microsheet†	0.138	0.133	0.817	0.785
555-69	6-mil Microsheet†	0.142	0.135	--	--
556-69	20-mil Quartz†	0.118	0.114	0.779	0.751
557-69	20-mil Quartz†	0.118	0.114	--	--
613-69A	Cat-a-lac Black	0.956	0.956	0.872	0.828
613-69B	Cat-a-lac Black	0.954	0.954	0.868	0.825
672-69	RTV 41	0.305	0.265	0.892	0.846
673-69	RTV 41	0.327	0.291	0.887	0.843
794-69	RTV 566	0.652	--	--	--
795-69	RTV 566	0.652	--	--	--

†Accuracy within ± 0.02 in α and ± 0.03 in ϵ ; repeatability ± 0.005 ; therefore third figure shows data trends.

†Vacuum deposited aluminum on second surface.

*Based on lens-out spectrum.

(a) Measured on modified Beckman DK2A.

(b) Measured on Gier Dunkle Heated Cavity Reflectometer.

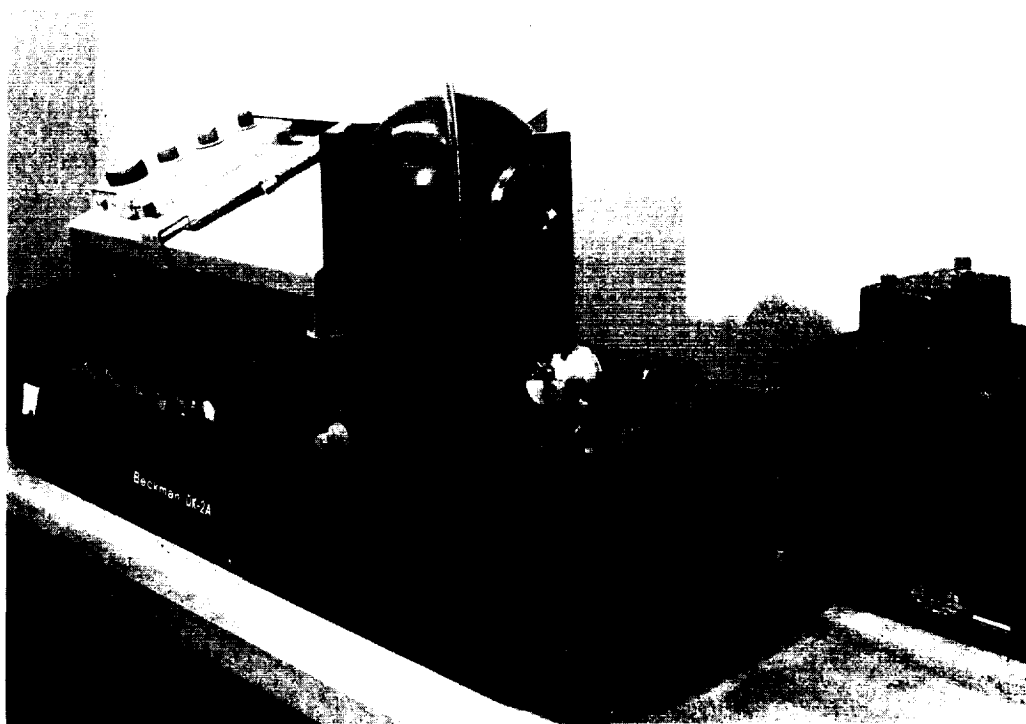
(c) Calculated from normal emittance and theoretical correction given in Eckert and Drake, Heat and Mass Transfer, 2nd Edition.

In addition to absorptance values, the infrared emittance normal to the sample surface is computed from the infrared reflectance data using a black-body spectral curve for the given sample temperature. This calculation relies principally on the heated-cavity reflectometer data.

Typically, ex situ quick inspection total measurements of α_s and ϵ_N were made on each sample before and after exposure to the ion engine exhaust. These measurements were made with the sample in place on the sample holders using a Gier Dunkle Model MS 250 Mobile Solar Reflectometer for α_s and a Gier Dunkle Model DB100 Mobile Infrared Emittance Inspection Device⁵ for ϵ_N .

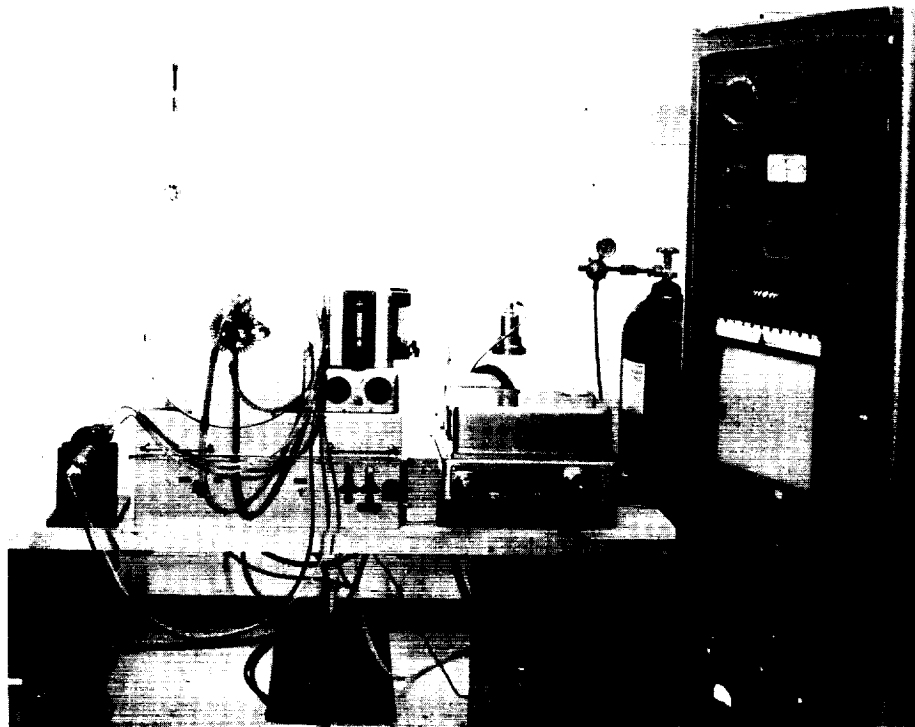
Photographs of the various ex situ instruments are presented in Figures B-1 through B-4.

The quantity ϵ_H shown in Table B-1 is total hemispherical infrared emittance, and is calculated from the value of ϵ_N using the method of Eckert and Drake⁶. Hemispherical infrared emittance is directly measured in situ using the calorimetric sample holder described below.



80544-62

Figure B-1. Beckman DK2A Photo Spectrometer with TRW Modified Integrating Sphere



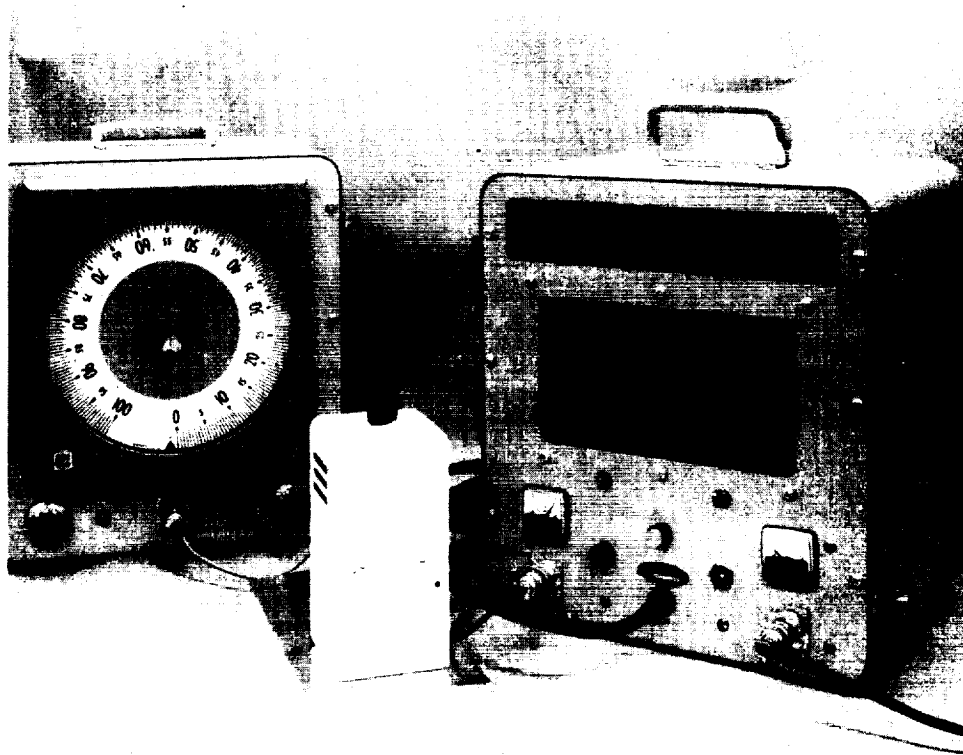
77583-62

Figure B-2. Gier-Dunkle Heated Cavity Reflectometer



31636-67

Figure B-3. Mobile Quick Emittance Device (Gier Dunkle Model DB100)



31635-67

Figure B-4. Mobile Quick Alpha Device (Gier Dunkle
Model MS250)

2. IN SITU EXPERIMENTAL DESIGN

The SSCEF, described in Appendix A, was used to measure the effects of electrostatic rocket exhaust particles on thermal control coatings. A special surface thermal sample holder, described below, was loaded through the center port of the facility as shown in Figure A-1. The samples were exposed to exhaust particle beams and then rotated 180 degrees for property measurements, which employed illumination from a xenon lamp shining through a quartz window in the rear door of the tank. The interior surfaces of the rear section of the chamber were painted with 3M type 401-C-10 Velvet Black paint, and maintained at the LN_2 temperature.

Figure B-5 is a photograph of the surface thermal sample holder in place behind the titanium beam collector. It is turned toward the solar simulator, in the measurement position. The holder accepts up to five separate samples for simultaneous exposure to propellant beams. In this

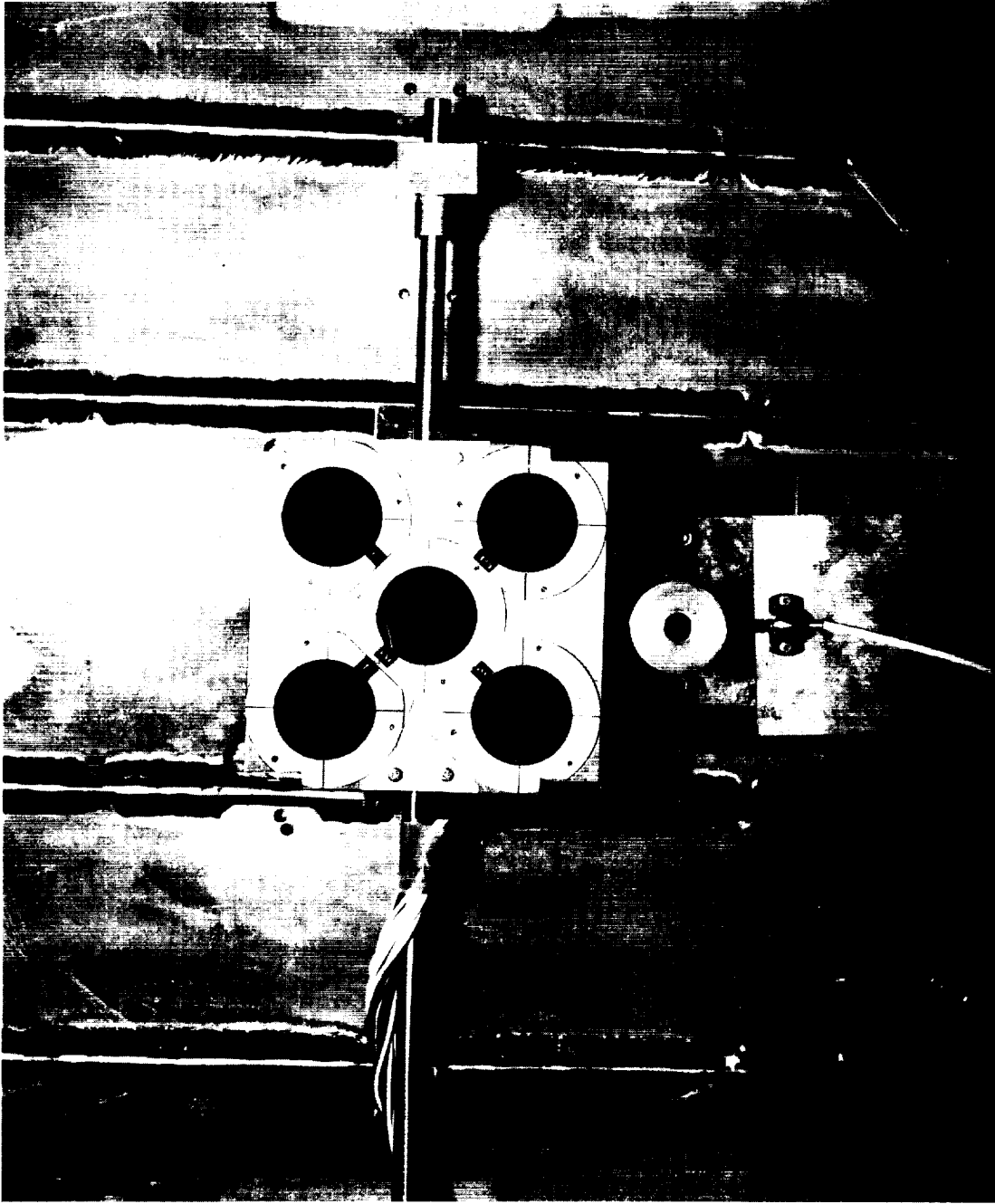


Figure B-5. Surface Thermal Sample Holder in Measurement Position.
Radiometer appears below sample holder.

photograph, each sample happens to be black paint. The holder can rotate 180 degrees in the collector-mounted bracket (at the right in Figure B-5) into the propellant beam exposure position, as shown in Figure B-6. The "window frame" around the sample area is a set of carefully designed shields which prevent foreign metal particles from arriving at the samples. They are discussed in Appendix A.

Since the thruster cannot be turned on and off rapidly, the sample shutter shown in Figure B-7 is used to initiate and terminate beam exposures. The shutter is actuated through a rotary motion feed-through in less than two seconds. In the closed position it is a few inches in front of the sample plane, and its thermal design permits thruster operation when closed without significant outgassing in the direction of the samples.

The critical elements of the experiment are discussed below.

2.1 In Situ Measurement Method

An electrical substitution method was selected for the in situ measurements because of its high accuracy, wide range of linearity, and ability to maintain almost constant sample temperature during exposure and measurement. This method provides an absolute measurement of sample hemispherical emittance and an absorptance measurement relative to the spectrum of the solar simulator used.

Figure B-8 illustrates the construction of one of the five identical measurement units. The sample is attached to a very thin electrical heater of the same diameter as the sample (1.75 inches). Cemented to the other side of the heater is a very thin equal diameter thermopile-type heat flux meter which in turn is permanently bonded to a water cooled plate. An annular shaped aluminum ring surrounds and lies flush with the sample to minimize edge radiation and protect electrical connections from ion beam erosion. Clearance between the sample edge and the ion shield is approximately 0.01 inch.

During property measurements, the samples view only an LN_2 cooled shroud and a quartz port through which a xenon lamp solar simulator beam can be projected. With the solar simulation beam off, the electrical power to each sample heater is adjusted so that the corresponding heat meter is nulled. Under this condition, almost all of the measured electrical

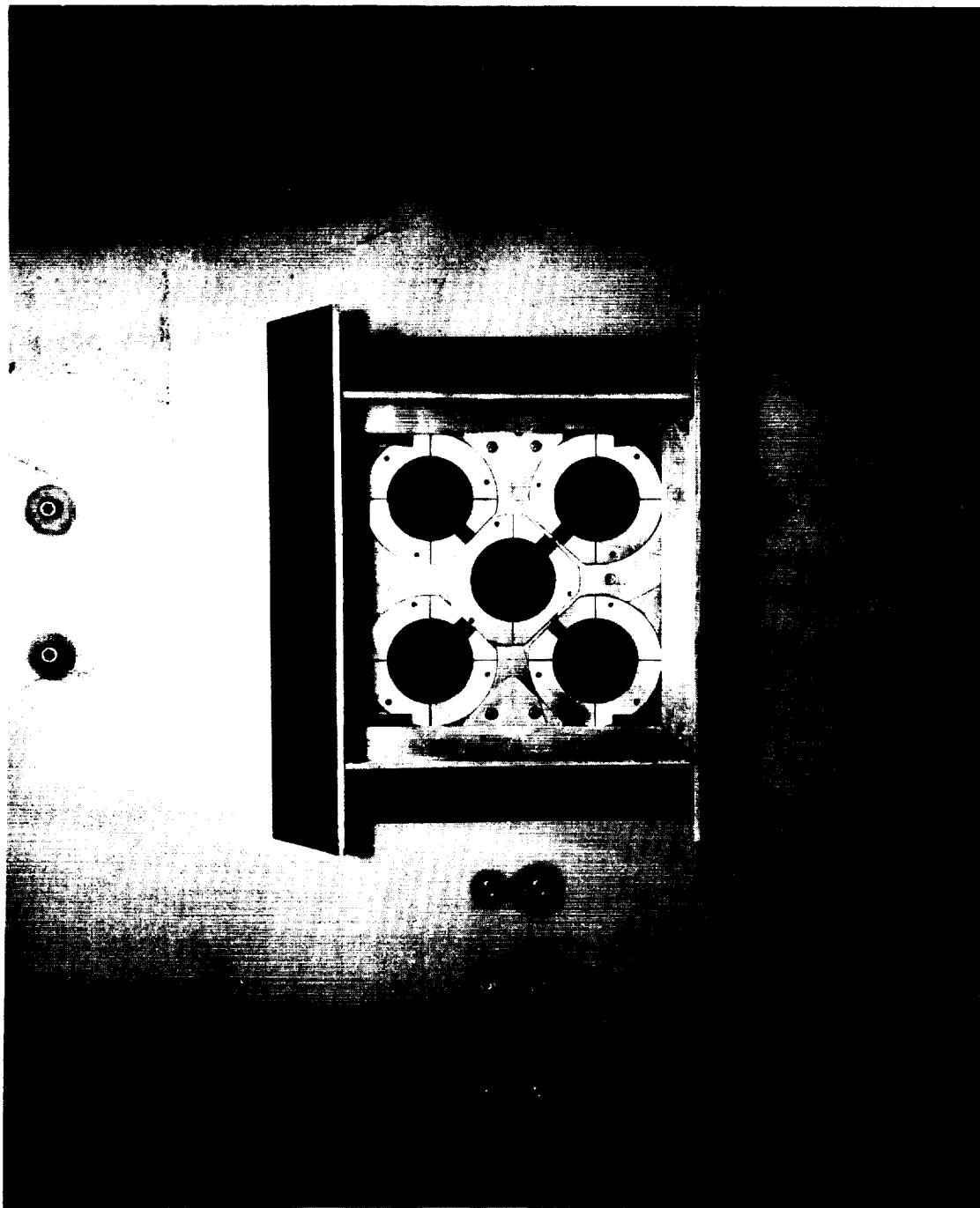


Figure B-6. Closeup of Sputtering Shields and Surface
Thermal Sample Holder

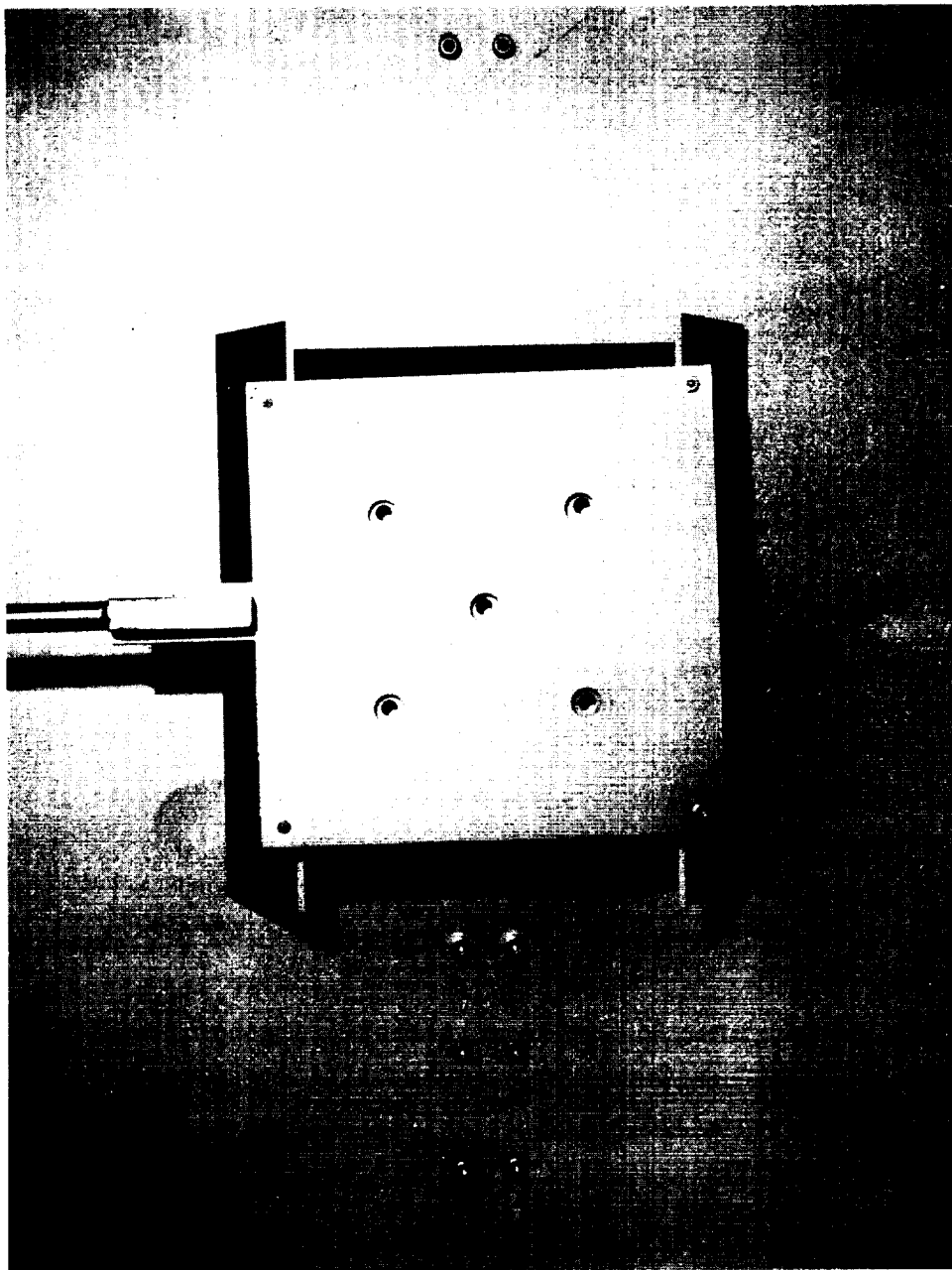


Figure B-7. Photo of Sample Shutter in Closed Position. Five Faraday cups for current density measurement are visible.

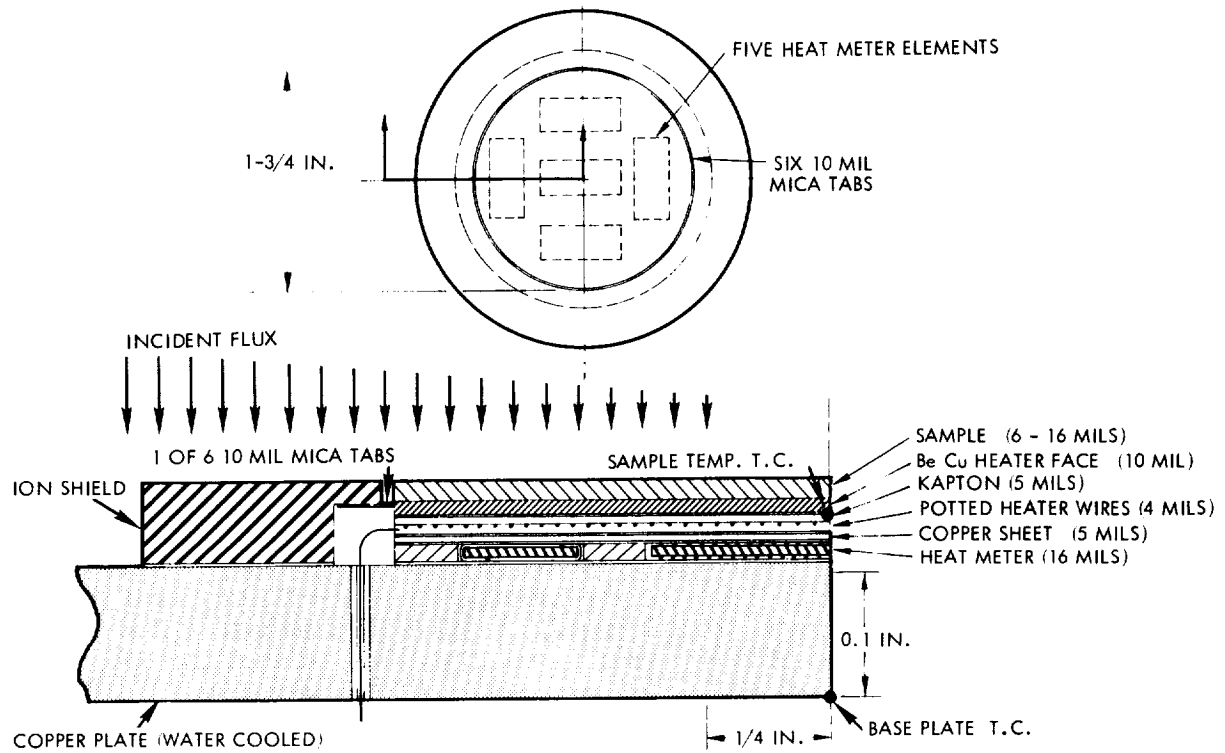


Figure B-8. Cross Section of One Surface Thermal Property Measurement Unit

power to a sample heater is emitted by its sample. A small amount of the power (which can be computed and corrected for) is lost by radiation from the edge and conduction through the lead wires. The temperature of each sample is measured by a thermocouple placed between the sample and the heater, and a correction is made for the small temperature drop through the sample. Since sample area is known and temperature and emittance power are measured, total hemispherical emittance is computed from the heat balance equation:

$$\epsilon_H = \frac{Q_e}{A\sigma[T_e^4 - T_W^4]} \quad (B-1)$$

where

Q_e = electrical power to the heater during emittance measurement

A = sample area

σ = Stefan-Boltzman constant

T_e = sample temperature during emittance measurement, $^{\circ}\text{K}$

T_W = temperature of chamber walls, $^{\circ}\text{K}$

After the emittance readings are taken, the xenon lamp is turned on and the power to each sample heater is reduced until the heat meters are again nulled. The new electrical power dissipation and sample temperature readings are taken and corrected as before. In addition, the incident flux density (G) of the solar simulator beam is measured with a radiometer before and after illuminating each sample position. (The radiometer appears below the sample assembly in Figure B-5.) Sample absorptivity with respect to xenon spectrum can then be computed from the new heat balance equation:

$$\alpha_{Xe} = \frac{\epsilon_H A \sigma [T_a^4 - T_W^4] - Q_a}{AG} \quad (\text{B-2})$$

where

Q_a = electrical power to the heater during absorptance measurement

T_a = sample temperature during absorptance measurement.

It is estimated that the in situ measurements are accurate to within ± 0.03 (absolute number) in emittance and ± 0.05 (absolute number) in absorptance. These estimates are based on a detailed error analysis⁷ of a similar sample holder configuration and agreement obtained between in situ and ex situ measurements to date.

2.2 Heat Meters

Successful performance of the sample holder unit hinges on proper design of the heat meters. These units must be extremely thin to both minimize edge effects and reduce thermal resistance in the normal direction. The heat flux density during sample exposure to ion beams is

typically 500 mw/cm^2 and can be as high as 1 watt/cm^2 . Thus, unless the thermal resistance between the sample surface and the water cooled plate is small, sample temperature during exposure would vary strongly with beam power and even elevate enough to affect sample properties. Stabilization time during measurement is also reduced by minimizing the thermal resistance.

In spite of its thinness and low thermal resistance, the heat meter must produce a measurable signal ($2\text{-}3 \mu\text{v}$) for a heat flow that (ideally) is negligible compared to the heat radiated by the sample. This was accomplished by utilizing a thermopile with approximately 365 junction pairs in each heat meter.

The junctions were formed by first winding 0.002-inch-diameter constantan wire on 0.007-inch-thick 1/4-inch-wide Texolite (epoxy impregnated fiberglass) with 0.006 center to center wire spacing. Wires on one edge and approximately 1/3 of the 1/4 inch width on both sides were then silver-plated so as to form the two silver-constantan junction pairs per turn of wire with the silver plating forming low-resistance connections from top to bottom. Five 3/4-inch-long strips were mounted individually in 1/4 by 3/4-inch cut-outs in a 0.010-inch-thick 1.75-inch-diameter Texolite wafer, as shown in Figure B-8. The five windings were then connected in series and the wafer and strips were potted with TBS758 silicone rubber to form a 0.016-inch-thick heat meter.

Calibration measurements were made by reading the heat meter output for a black sample of known emittance with no electrical power applied to the sample heater. These measurements indicate that the heat meter sensitivity is approximately 3.95 mv/watt . An automatic controller was able to maintain null within $\pm 4 \mu\text{v}$. The uncertainty of heat flow through the heat meter was therefore approximately 0.001 watt. This is quite small, even when compared to the approximately 0.037 watt emitted from a 1.75-inch-diameter low emissivity ($\epsilon_H = 0.05$) sample at 20°C . In fact, the heat meters are so sensitive that minor fluctuations in cooling water temperature and/or pressure introduced noise ($20\text{-}50 \mu\text{v}$) in the heat meter output signal. This problem was solved by installing a thermally insulated constant-head gravity-feed cooling system.

2.3 Solar Simulator

A Christie model UF 30K projector with a 1600-watt xenon short arc lamp and a fused quartz lens assembly provided the simulated solar radiation beam. In order to obtain sufficiently high beam flux density (150 mw/cm^2) at the sample plane to accurately measure α_{Xe} on low $\alpha_{\text{Xe}}/\epsilon_{\text{H}}$ samples (such as white paints or second surface mirrors), the simulator beam had to be focused down to approximately a 10-inch-diameter circle at the target plane. As a result, the beam was spatially and spectrally nonuniform, so only the center 2-inch-diameter core was used for measurement purposes. This center core was accurately aimed first at the radiometer, then at one of the five samples, and then back at the radiometer using a telescope sight rigidly attached to the simulator. The simulator was mounted on an adjustable platform shown in Figure B-9. Cross hairs in the telescope were "sighted in" during beam intensity calibration measurements so that at the sample plane the line of sight through the telescope intersected the simulator beam axis. Sighting aids placed on each sample holder (see Figure B-5) were used to accurately position the center of the beam onto the center of each sample.

Low beam flux densities (3 mw/cm^2) at the sample plane were obtained by removing the entire projection lens assembly. A permanent clamp was placed on the lens assembly to assure that it would be replaced in the same position each time. Intermediate flux densities were obtained by introducing 60 mesh brass wire screens with the lens assembly in place. Minor intensity adjustments were also made by varying the lamp current.

2.3.1 Spectral Distribution Measurement

Spectral distribution of the solar simulator beam was measured between 0.26 and 2.9 microns using a Beckman DK2A double beam spectrophotometer using essentially the method described in Reference 8. Magnesium oxide diffusing plates were interposed in both beams to reduce directional effects. An NBS calibrated tungsten-halogen lamp was used as the reference source. Neither insertion of wire screens in the beam nor variation of the xenon arc lamp current had any significant effect on the measured spectral distribution. Removal of the lens assembly, however, resulted in a considerably different spectral distribution. Figures B-10 and B-11 show the normalized spectral distribution with lens in

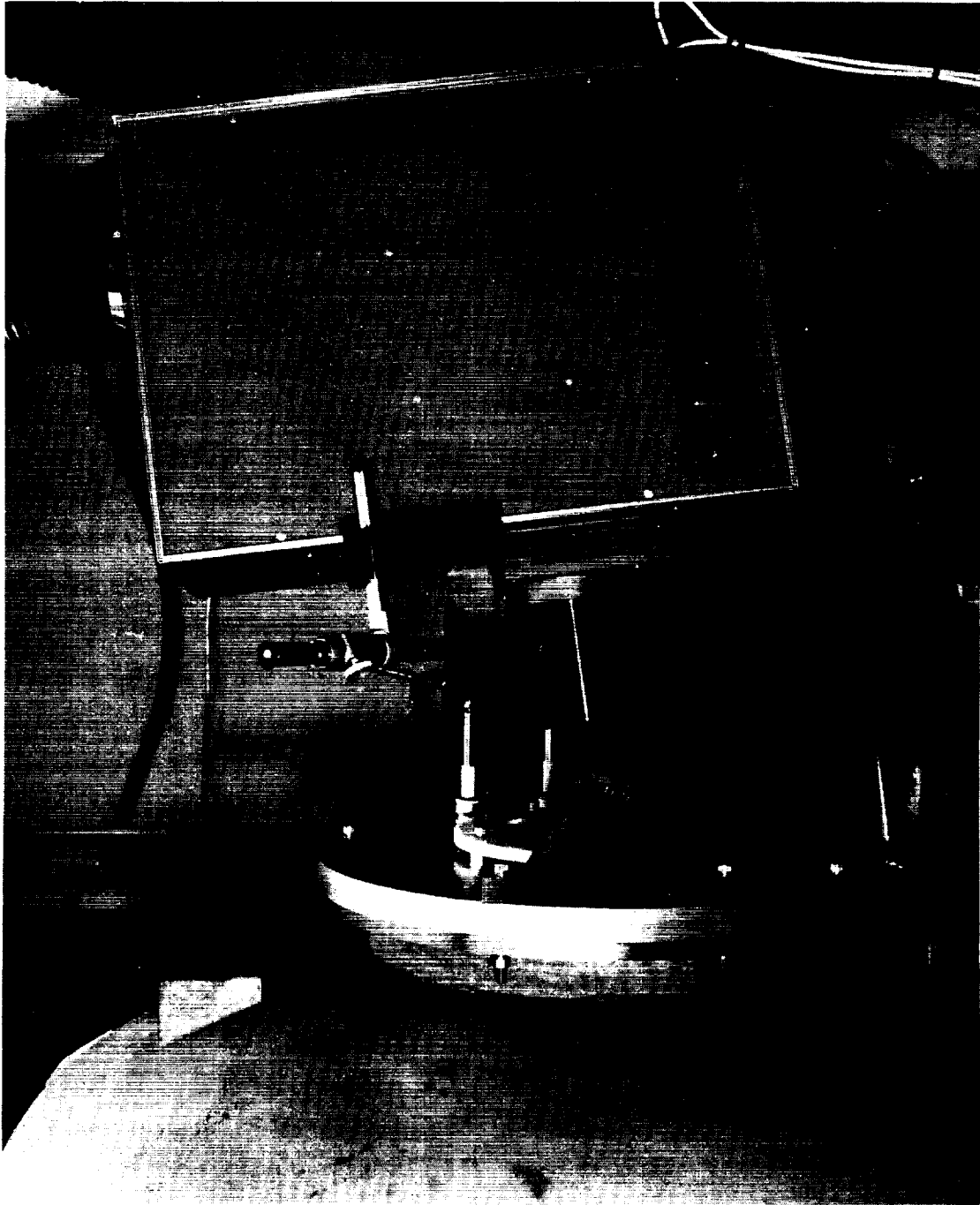


Figure B-9. Solar Simulator on Adjustable Mount

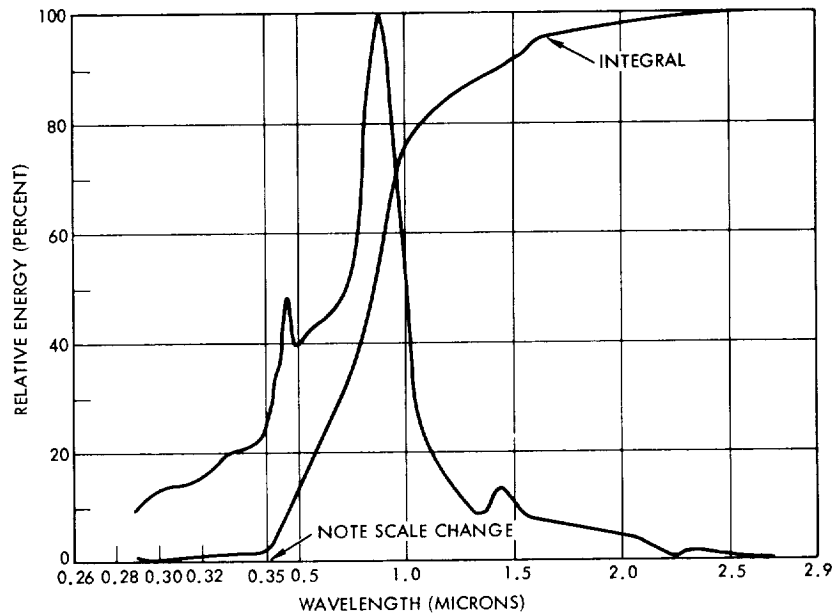


Figure B-10. Normalized Spectral Distribution Provided at the Sample by the Christie Xenon Arc System with the Lens in Place

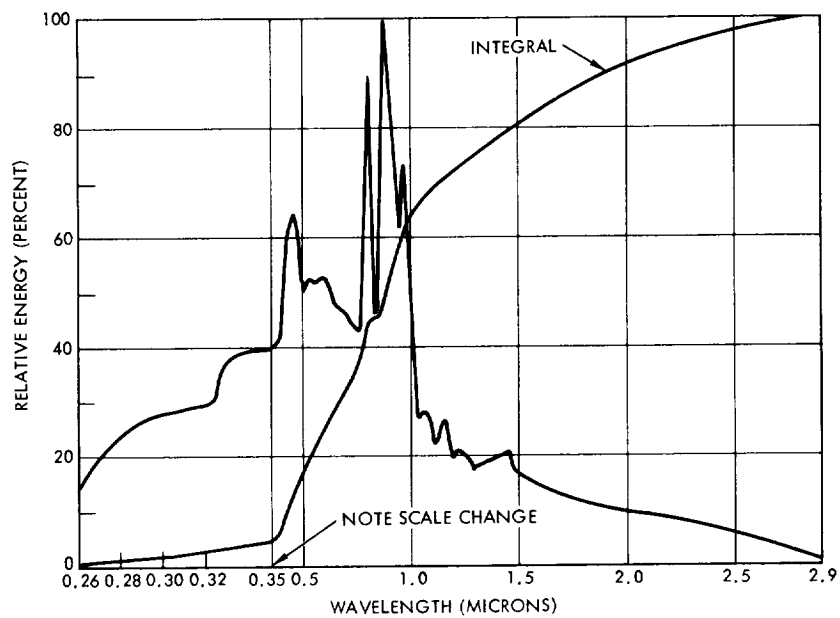


Figure B-11. Normalized Spectral Distribution Provided at the Sample by the Christie Xenon Arc System with the Lens Removed

and lens out respectively. Lens configuration is indicated in in-situ data tables by footnotes.

2.3.2 Spacial Distribution Measurement

Flux density distribution throughout the center 4-inch diameter of the beam was mapped with and without the projection lens assembly in place by traversing the beam in the x and y directions across the radiometer. With the lens out the distribution is flat. Figure B-12 shows the lens-in distribution. The flux density drops off about 10 percent symmetrically from the center of the beam to a radius corresponding to the edge of a sample. Table B-2 shows the integration of this curve to obtain the appropriate correction factor, 0.94, for the total flux incident on the sample based on the radiometer reading on the beam axis.

2.3.3 Reference Radiometer

The TRW EC-1 was selected as the reference radiometer. This is an electrically compensated radiometer which consists of two identical foils housed in identical enclosures. One foil is exposed to the unknown beam

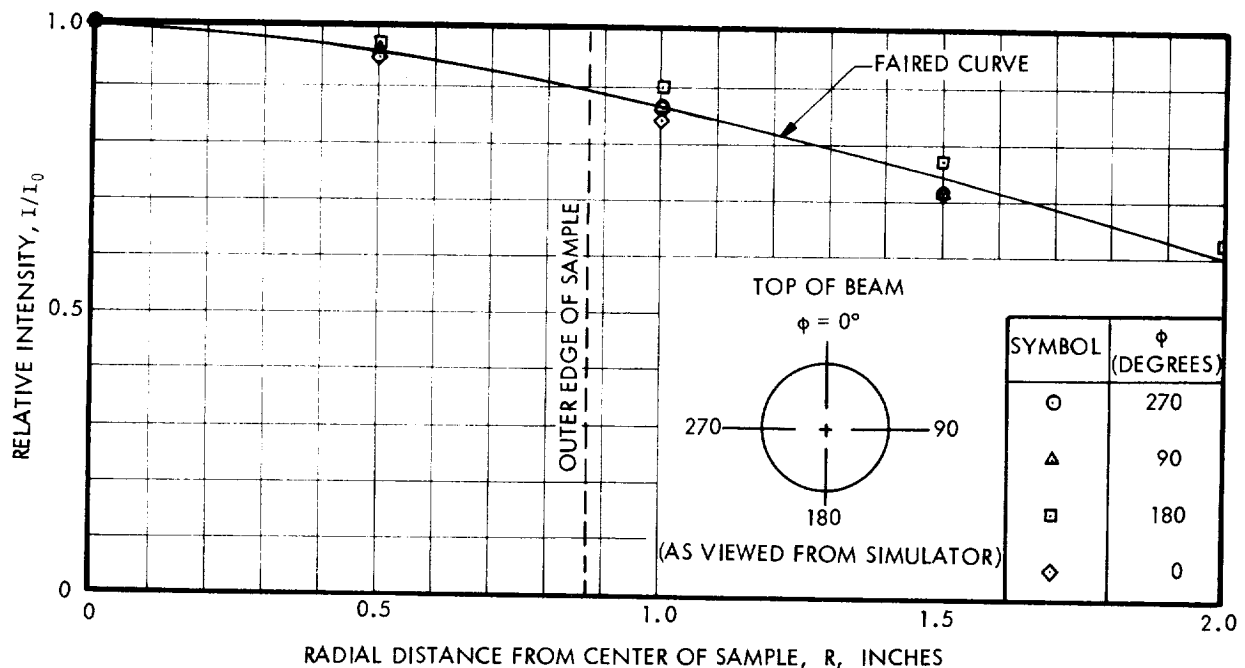


Figure B-12. Total Intensity Distribution at 60.3 inches from the Front Face of the Christie Lamp Housing

Table B-2. Computation of Effective Beam Intensity

(\bar{R}) (inches)	(I/I_0)	ΔR (inches)	$(\bar{R})(I/I_0)(\Delta R)$
0.05	0.995	0.10	0.004975
0.15	0.990	0.10	0.01485
0.25	0.982	0.10	0.02455
0.35	0.975	0.10	0.034125
0.45	0.960	0.10	0.04320
0.55	0.949	0.10	0.052195
0.65	0.940	0.10	0.0611
0.75	0.912	0.10	0.0684
0.8375	0.899	0.075	0.05647
SUM		0.875	0.349865
$\frac{I_{\text{effective}}}{I_{\text{center}}} = \frac{2\sum(\bar{R})(I/I_0)(\Delta R)}{R_{\text{max}}^2} = \frac{(2)(0.349865)}{(0.875)^2} = 0.94$			

intensity through a 1.3-cm-diameter quartz window. The other foil is heated electrically at a rate that will just null a differential thermocouple operating between the two foils. The beam intensity can be determined approximately from the measured electrical power, the window aperture area, the absorptance of the receiving foil, and the transmittance of the window. For greater accuracy however, several identical instruments have been calibrated in vacuum against a laboratory standard radiometer whose calibration is traceable to the National Bureau of Standards.

Figure B-5 shows the radiometer as installed within the chamber. The radiometer aperture is in the same plane as the samples.

2.4 ELECTRONICS

The in situ electrical and temperature measurements are made with a Darcy Model 440 digital voltmeter (DVM) with low noise mV option (random variation $\pm 2 \mu\text{V}$) through a specially designed signal switching console. Switch S2 in the console circuit, shown in Figure B-13, permits switching an electronic controller (which automatically nulls its input

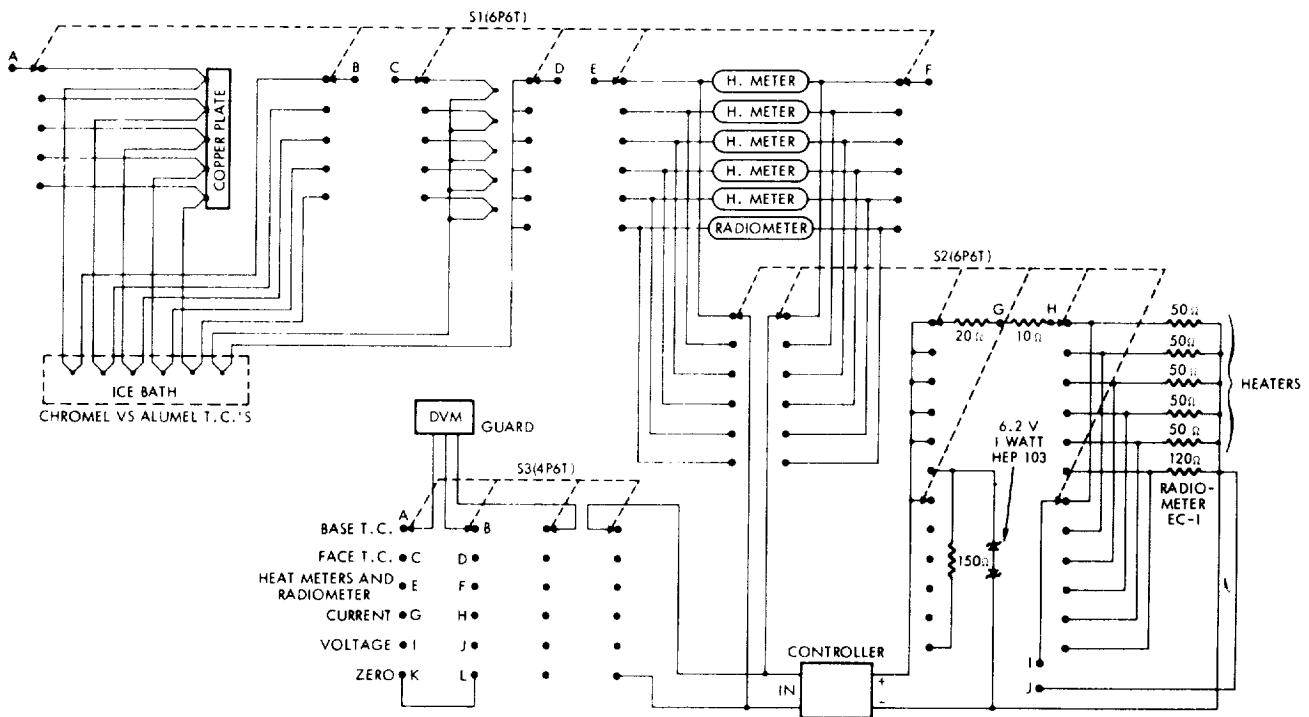


Figure B-13. Schematic Diagram of Signal and Controller Switch Console

signal) between samples and radiometer. Switch S1 selects which of the five sample units or radiometer signal sets will be available to the DVM, and S3 switches the DVM through the signal set. Figure B-14 shows the entire electronics rack including the switching console, and an HP 425A microvoltmeter which is part of the electronic controller. Also visible in the figure is the vacuum port cover which supports the sample holder package and electrical hermetic seal pass-throughs.

During in situ property measurements, the DVM readings are recorded by hand in a systematic way on specially prepared data sheets. Sample, run, beam exposure, and solar simulator configuration codes are also recorded. Immediately following data recording, the data is punched onto paper tape with a nearby teletypewriter. The teletypewriter is then connected to a timesharing digital computer which has the data reduction program in memory. Within seconds after the paper data tape is read into a computer file, values of α_X , ϵ_H and several instrument diagnostic numbers are computed for each sample. This rapid procedure for data reduction

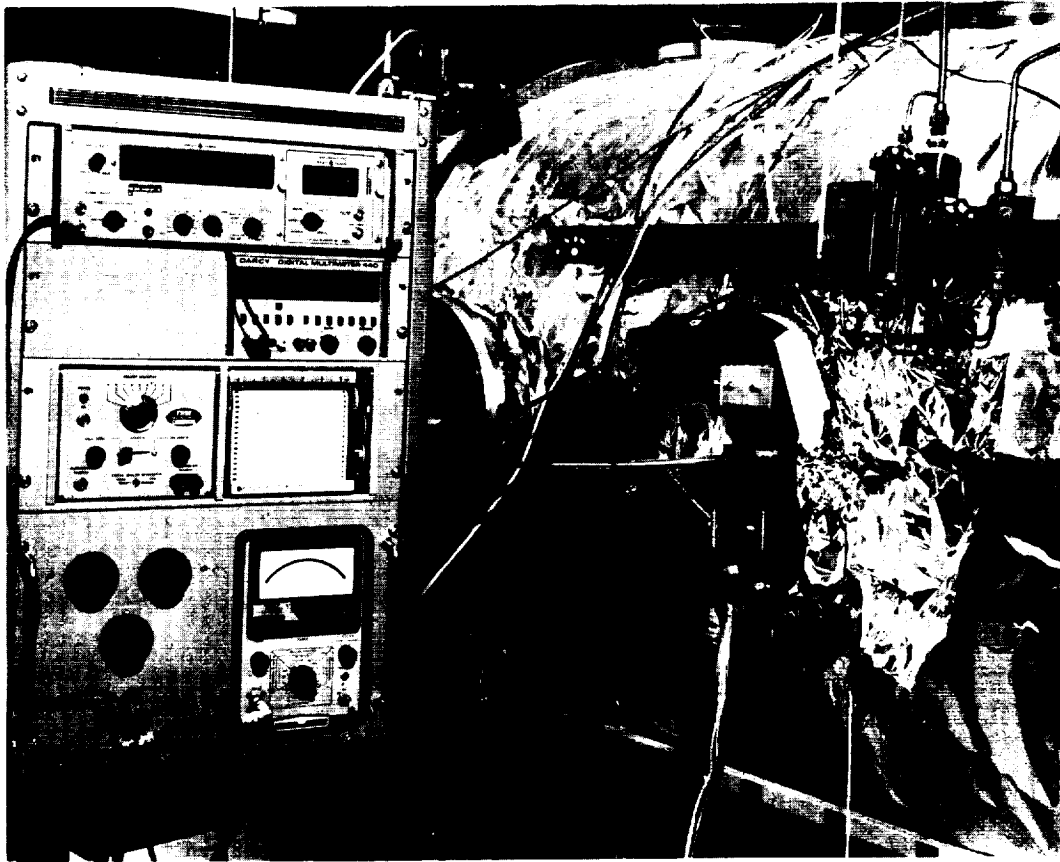


Figure B-14. Exterior View of Port Plate, Electronics, and Water Cooling System

permits the sequence of experimental steps to be modified in response to current results while the experiment is in progress. For instance, if a property measurement seems questionable, it is repeated before going on; when an 0.3-hour atom beam exposure had little effect, a much larger period was chosen for the next exposure.

REFERENCES (APPENDIX B)

1. W.D. Miller, and E. E. Luedke, "In Situ Solar Absorptance Measurements, An Absolute Method," Effects of the Space Environment on Materials; Vol. II, pp. 75-84, Society of Aerospace Material and Processing Engineers, 11th National Symposium and Exhibit, St. Louis, April 1967.
2. R. V. Dunkle, et al., "Heat Cavity Reflectometer for Angular Reflectance Measurements," Progress in International Research on Thermodynamics and Transport Properties; pp. 541-67, American Society of Mechanical Engineers, 1962.

3. D. F. Hall, "Electrostatic Propulsion Beam Divergence Effects on Spacecraft Surfaces," Final Report, Vol. 1, JPL Contract 952350, Doc. No. 11985-6001-RO-00, TRW Systems, Redondo Beach, Calif., August 1970.
4. F. S. Johnson, "The Solar Constant," J. Metrology, Vol. II, pp. 431-439, 1954.
5. K. E. Nelson, E. E. Luedke, and J. T. Bevans, "A Device for the Rapid Measurements of Total Emittance," Journal of Spacecraft and Rockets, pp. 758-760, Vol. 3, 1966.
6. Eckert and Drake, Heat and Mass Transfer, 2nd Edition, McGraw-Hill Book Co., New York, New York, 1959.
7. D. F. Hall, "Evaluation of Electric Propulsion Beam Divergence Effects on Spacecraft," 08965-6013-RO-00, Final Report, Contract No. NAS7-575, TRW Systems, Redondo Beach, Calif., September 1969.
8. F. Crum, "Modification of a Beckman Spectrophotometer for Direct Measurement of Spectral Energy Distribution of Light Sources," Applied Optics Vol. 2, pp. 237-242, 1963.